

Study of anomalous gauge boson self-couplings and the role of spin-1 polarizations

RAFIQUL RAHAMAN
Roll. no. 13RS033

Supervisor: Dr. Ritesh K. Singh



DEPARTMENT OF PHYSICAL SCIENCES
INDIAN INSTITUTE OF SCIENCE EDUCATION AND RESEARCH, KOLKATA
MOHANPUR, NADIA, WB-741246, INDIA

*A dissertation submitted to IISER Kolkata
for the partial fulfilment of the requirements for the Degree of
Doctor of Philosophy*

July 2020

I dedicate this thesis to

My Parents

DECLARATION OF AUTHORSHIP

Date: 03/07/2020

I, **Rafiqul Rahaman** with Registration No. **13RS033** dated 26/12/2013, a student of Department of Physical Sciences of the PhD Program of IISER Kolkata, hereby declare that this thesis is my own work and, to the best of my knowledge, it neither contains materials previously published or written by any other person, nor it has been submitted for any degree/diploma or any other academic award anywhere before.

I also declare that all copyrighted material incorporated into this thesis is in compliance with the Indian Copyright (Amendment) Act, 2012 and that I have received written permission from the copyright owners for my use of their work.

Rafiqul Rahaman

Department of Physical Sciences

Indian Institute of Science Education and Research Kolkata

Mohanpur 741246, West Bengal, India

CERTIFICATE FROM SUPERVISOR

Date: 03/07/2020

This is to certify that the thesis entitled "**Study of anomalous gauge boson self-couplings and the role of spin-1 polarizations**" submitted by Mr. **Rafiqul Rahaman** with Registration No. **13RS033** dated 26/12/2013, a student of Department of Physical Sciences of the PhD Program of IISER Kolkata, is based upon his own research work under my supervision. This is also to certify that neither the thesis nor any part of it has been submitted for any degree/diploma or any other academic award anywhere before. In my opinion, the thesis fulfils the requirement for the award of the degree of Doctor of Philosophy.

Dr. Ritesh K. Singh

Associate Professor

Department of Physical Sciences

Indian Institute of Science Education and Research Kolkata

Mohanpur 741246, West Bengal, India

ACKNOWLEDGMENTS

I can not forget the people who have their contributions directly or indirectly in the long journey of my Ph.D. Without their support, I can not imagine myself writing my Ph.D. thesis now. I will try to acknowledge their contribution to my Ph.D. in the best possible way.

First of all, I would like to thank Maa and Abba for their unconditional love and support. It is impossible to mention their contributions in a few words, but it is worth mentioning the crucial ones. They supported my educational aspirations and passionate cultivation of my curiosities through their persistent emotional, financial aid, even in their empty stomach. They unconditionally support me to fulfil my dream of becoming a scientist, a selfish one based on the fact that we have a poor financial condition from the very beginning. I could not forget the contribution of my brother Majibul, who had to quit school after his Madhyamik and join work to keep our stomach full. It is not enough just to thank him for his unconditional love, along with emotional and financial support. I would like to thank my other brother and sisters, for their love and support. I especially thank Mabo, my late grandmother, for her words of encouragement and praise. I thank my uncles, aunts, and cousins for their love and support.

Secondly, I would like to acknowledge my Ph.D. supervisor Dr. Ritesh K. Singh, who directly contributed to my Ph.D. In the long journey of my Ph.D., he gave me his valuable times for discussions. He kept his calm down with patience to many of my irritating stupid questions. He is more like a friend than a guide during any interaction. He is the coolest person I ever met. He continued discussing with me even on his own and his family member's health issues. For his guidance and suggestions, I could publish articles in peer-reviewed journals. My thirst for knowledge has increased gradually through discussions with him. Once again, I thank Dr. Ritesh to boost my quest to unravel the mysteries of the Universe.

Next, I would like to thank all my teachers throughout my school and college. I would like to thank my school headmaster Dr. Ganguly for his support and encouragement to science. I would especially like to acknowledge my science and mathematics teachers late Bumba Da, Samsul Sir, Natu Da, who not only encourage my interests through support and praise but also did not take fees from me during my high school. I especially thank Dr. Mainak Gupta, who seeded the interests of quantum mechanics and relativity in me in college. I

also thank Dr. Kumar Rao, with whom I did my master's thesis in particle physics and later chose to do a Ph.D. in the same area. I would like to acknowledge Asuthosh College in Kolkata for inviting me and giving me the opportunity to complete my B.Sc. with free food and lodging. I would like to thank the Department of Science and Technology (DST), Government of India, for support through stipend during my B.Sc. and M.Sc. I would like to express my sincere gratitude to my research collaborators Subhasish Behera, Dr. Rashidul Islam, Dr. Mukesh Kumar, Prof. Poulouse, Dr. Satendra Kumar, and Dr. Adam Falkowski for wonderful collaborations.

I am grateful to the Department of Science and Technology (DST), Government of India, for support through DST-INSPIRE Fellowship for my doctoral program, INSPIRE CODE IF140075, 2014. I am grateful to IISER Kolkata for financial assistance to attend the APS April meeting in the United States. I am also thankful to CEFIPRA for giving me funds to visit LPT Orsay for collaborative work. I would like to thank the taxpayers of India for their contribution to fellowship.

Lastly, I would like to thank my friends Momidul and Mosayeb for their company during high school. I would like to thank my friends Rakesh, Vivek, Deep, and Anirban, for their support and company. Late-night gossips, tea break gossips in various topics like social, political, science, etc., with them has chased away the monotony of life during my Ph.D. I would especially like to thank Atanu for his company and various discussions. I would like to thank my seniors Soumitra, Priyasri, Ipsita, Swati, Biswarup, Soumen, Gopal, Ankan, and Santanu, for their advice. I also thank my juniors Sayak, Soumik, Anurag, Chiranjib, Subhojit, Avijit, Srijita, Debangana, Dipanjan, Pandey, Souraj, Sajal, Souradip, Arkayan, and Chiranjit for keeping a vibrant and joyful environment in the workplace. I would like to thank Bimal kaka, in whose shop we take tea, have breakfast and gossip/discuss everything.

Rafiqul Rahaman

ABSTRACT

The prime goal of this thesis is to study anomalous gauge boson self couplings, triple gauge boson couplings in particular, with the help of spin polarization observables of the gauge bosons Z and W^\pm in the presence of beam polarizations where ever possible. The neutral triple gauge boson couplings, i.e., ZZZ , $ZZ\gamma$, $Z\gamma\gamma$, are studied in $ZZ/Z\gamma$ ($2lq\bar{q}/2l\gamma$) production at an e^+e^- collider with and without beam polarization. Some of these anomalous couplings are also studied in ZZ ($4l$) production at the LHC. In the charge sector the anomalous gauge boson couplings, i.e., WWZ , $WW\gamma$ have been studied at an e^+e^- collider in W^+W^- ($l^-\bar{\nu}_l q'\bar{q}$) production. The WWZ anomalous couplings are also studied in ZW^\pm production at LHC in $3l+\cancel{E}_T$ channel. All the analyses at an e^+e^- collider have been performed for center-of-mass (CM) energy of 500 GeV and integrated luminosity of 100 fb^{-1} . The analyses at the LHC are performed at 13 TeV CM energy of pp collisions. The cross sections and polarization asymmetries, along with other asymmetries (forward-backward, azimuthal), are used to obtain simultaneous limits on the anomalous couplings using Markov-Chain-Monte-Carlo (MCMC) method in each process. The polarization asymmetries can distinguish between CP -even and CP -odd couplings and help to put tighter constraints on the couplings. The polarization of the initial e^- and e^+ beam, in case of e^+e^- collider, are used to increase the signal to background ratio, putting tighter constraints on the anomalous couplings. The polarization asymmetries are instrumental in the measurement of anomalous couplings should a deviation from the SM be observed.

List of Publications (included in this thesis)

1. **R. Rahaman** and R. K. Singh, “On polarization parameters of spin-1 particles and anomalous couplings in $e^+e^- \rightarrow ZZ/Z\gamma$ ”, *Eur. Phys. J.* **C76** no. 10, (2016) 539, [arXiv:1604.06677 \[hep-ph\]](#).
2. **R. Rahaman** and R. K. Singh, “On the choice of beam polarization in $e^+e^- \rightarrow ZZ/Z\gamma$ and anomalous triple gauge-boson couplings”, *Eur. Phys. J.* **C77** no. 8, (2017) 521, [arXiv:1703.06437 \[hep-ph\]](#).
3. **R. Rahaman** and R. K. Singh, “Anomalous triple gauge boson couplings in ZZ production at the LHC and the role of Z boson polarizations”, *Nuclear Physics B* **948** (2019) 114754, [arXiv:1810.11657 \[hep-ph\]](#).
4. **R. Rahaman** and R. K. Singh, “Probing the anomalous triple gauge boson couplings in $e^+e^- \rightarrow W^+W^-$ using W polarizations with polarized beams”, *Phys. Rev. D* **101** no. 7, (2020) 075044, [arXiv:1909.05496 \[hep-ph\]](#)
5. **R. Rahaman** and R. K. Singh, “Unravelling the anomalous gauge boson couplings in ZW^\pm production at the LHC and the role of spin-1 polarizations”, *JHEP* **04** (2020) 075, [arXiv:1911.03111 \[hep-ph\]](#).

List of Publications (not included in this thesis)

1. Subhasish Behera, Rashidul Islam, Mukesh Kumar and Poullose Poullose and **Rafiqul Rahaman**, “Fingerprinting the Top quark FCNC via anomalous Ztq couplings at the LHeC”, *Phys. Rev.* **D100** no. 1, (2019) 015006, [arXiv:1811.04681 \[hep-ph\]](#).
2. S. Kumar, P. Poullose, **R. Rahaman**, and R. K. Singh, “Measuring Higgs self-couplings in the presence of VVH and VVHH at the ILC”, *Int. J. Mod. Phys.* **A34** no. 18, (2019) 1950094, [arXiv:1905.06601 \[hep-ph\]](#).

UNIT, SYMBOLS AND ABBREVIATIONS

We use the natural unit system, i.e., $\hbar = c = 1$ throughout.

Symbol	Name	Unit
\sqrt{s}	CME	GeV
\mathcal{L}	Luminosity	fb^{-1}
σ	cross section	pb/fb

SM	Standard Model
QFT	Quantum field theory
BSM	Beyond the SM
QED	Quantum electro dynamics
QCD	Quantum chromo dynamics
CP	Charge and parity
EFT	Effective field theory
EM	Electromagnetic
ED	Extra dimension
UED	Universal extra dimension
KK	Kaluza-Klein
DM	Dark matter
EW	Electroweak
EWSB	Electroweak symmetry breaking
SUSY	Supersymmetry
2HDM	Two-Higgs-doublet-model
C2HDM	Complex 2HDM
MSSM	Minimal supersymmetric SM
NCSM	Non commutative extension of the SM
GUT	Grand unified theory

LEP	Large Electron–Positron Collider
LHC	Large Hadron Collider
ILC	International Linear Collider
LHeC	Large Hadron electron Collider
CM	Centre-of-mass
aTGC	Anomalous triple gauge boson couplings
MCMC	Markov-Chain–Monte-Carlo
SDM	Spin density matrix
C.L.	Confidence level
BCI	Bayesian confidence interval
LO	Leading order
NLO	Next to LO
NNLO	Next to NLO
pb	Pico barn
fb	Femto barn
GeV	Giga electron volt

Contents

List of Figures	xxi
List of Tables	xxxii
1 Introduction	1
1.1 The Standard Model of particle physics	2
1.1.1 The interactions in the SM electroweak theory	8
1.1.2 Summary of the SM	12
1.2 Problems in the SM with possible solutions	12
1.3 EFT and anomalous gauge boson couplings.	15
1.3.1 BSM contributions to aTGC	21
1.3.2 Probe of the aTGC	22
1.4 Outline of the thesis	23
2 Polarization parameters of spin-1 particles.	25
2.1 Polarization density matrix	26
2.2 Polarization asymmetries	34
2.3 Spin-spin correlations	39
2.4 Summary	40
3 The probe of aTGC in $e^+e^- \rightarrow ZZ/Z\gamma$ and the role of Z boson polarizations.	41
3.1 Anomalous Lagrangian and their probe	44
3.1.1 Helicity formalism and polarizations of Z	46
3.1.2 Parametric dependence of observables	48
3.1.3 Sensitivity of observables to anomalous couplings	50
3.2 Likelihood mapping of parameter space	55
3.2.1 MCMC analysis for $e^+e^- \rightarrow ZZ$	56
3.2.2 MCMC analysis for $e^+e^- \rightarrow Z\gamma$	61

3.2.3	Separability of benchmark aTGCs	64
3.3	Summary	66
4	The role of beam polarizations along with Z boson polarizations to probe aTGC in $e^+e^- \rightarrow ZZ/Z\gamma$.	67
4.1	Beam polarizations and polarization observables.	68
4.2	Effect of beam polarization on the sensitivity	71
4.3	Average likelihood and best choice of beam polarization.	74
4.4	Results with beam polarizations combined with their opposite values	79
4.5	Summary	83
5	The probe of aTGC in ZZ production at the LHC and the role of Z boson polarizations	85
5.1	The signal and background	87
5.2	Probe of the anomalous couplings.	91
5.2.1	Effect of aTGC in kinematic distributions	91
5.2.2	Sensitivity of observables to the couplings	94
5.2.3	Simultaneous limits on the aTGC	95
5.2.4	Role of the polarization asymmetries in parameter extraction	96
5.3	Summary	98
6	The probe of aTGC in $e^+e^- \rightarrow W^+W^-$ and the role of W boson polarizations along with beam polarizations	99
6.1	Observables and effect of beam polarizations	103
6.2	Probe of the anomalous couplings.	105
6.2.1	Sensitivity of observables on anomalous couplings and their binning	107
6.2.2	Effect of beam polarizations to the limits on aTGC	111
6.2.3	On the choice of beam polarizations	119
6.3	Summary	121
7	The probe of aTGC in $W^\pm Z$ productions at the LHC and the role of Z/W boson polarizations	123
7.1	Signal cross sections and their sensitivity to anomalous couplings	124
7.2	The asymmetries	130
7.3	Probe of the anomalous couplings.	134
7.3.1	Limits on the couplings	136

7.3.2 The role of asymmetries in parameter extraction	139
7.4 Summary	141
8 Conclusions and outlooks	143
Appendices	147
A The Standard Model Feynman rules in the electroweak theory.	149
B Helicity amplitudes and polarization observables in $e^+e^- \rightarrow ZZ/Z\gamma$	151
B.1 Helicity amplitudes	151
B.1.1 For the process $e^+e^- \rightarrow ZZ$	151
B.1.2 For the process $e^+e^- \rightarrow Z\gamma$	153
B.2 Polarization observables	154
B.2.1 For the process $e^+e^- \rightarrow ZZ$	154
B.2.2 For the process $e^+e^- \rightarrow Z\gamma$	156
C Polarization observables of Z boson in ZZ production at the LHC	159
C.1 Expressions of observables	159
C.2 Note on linear approximation	161
D The helicity amplitudes in $e^+e^- \rightarrow W^+W^-$ in SM+aTGC	163
E The fitting procedures of the observables and their SM values in WZ^\pm productions at the LHC	169
E.1 The SM values of the asymmetries and the corresponding polarizations.	169
E.2 Fitting procedure for obtaining observables as a function of couplings	171
F HEP packages that are used in this thesis	173
Bibliography	175

List of Figures

1.1	Beta decay ($d \rightarrow u$ conversion) with W^- (a) exchange and effective four-point interaction (b).	15
1.2	Triple gauge boson vertex with $V = Z/\gamma$. Anomalous contributions are shown by the shaded blob.	17
1.3	Triangular diagram with a heavy fermion F contributing to neutral aTGC.	21
1.4	Contributions to anomalous ZZZ (<i>upper-row</i>) and WWZ (<i>lower-row</i>) vertex from 2HDM with $i \neq j \neq k$ in <i>left-top</i> and $i \neq j$ for rest.	22
1.5	Contributions to anomalous WWV^* ($V = Z/\gamma$) vertex with off-shell V in a universal extra dimension.	23
2.1	Schematic diagram for the production of a particle A and it's decay to D_1 and D_2 . The dashed line separates the production part and the decay part.	26
2.2	The reference frame showing the fermions decay angles in the V rest frame. The direction of V in the Lab frame (\vec{P}_V) defines the z' -axis (the prime is due to not being the colliding beam direction). The directions of decayed fermions are shown with \vec{P}'_f and $\vec{P}'_{f'}$ and they are in the decay plane shown by the upper transparent layer (light blue colour). The incoming particle B_1 and B_2 are in the xz plane shown by intermediated transparent layer (light red colour). The azimuthal angle ϕ of f is measured w.r.t the xz plane. The co-ordinate system is right-handed, which defines the y' -axis.	34
2.3	The momentum configuration of the particles are shown in the Lab frame. The decay plane spanned by \vec{P}'_f and $\vec{P}'_{f'}$ makes an angle ϕ with the xz plane.	37

2.4	The SM values (analytic) of asymmetries $A_{x^2-y^2}$ (<i>solid/green line</i>) and A_{zz} (<i>dashed/blue line</i>) as a function of beam energy in the e^+e^- collider for ZZ (<i>top-left-panel</i>), $Z\gamma$ (<i>top-right-panel</i>) and W^+W^- (<i>bottom-panel</i>) processes. The data points with error bar correspond to 10^4 events generated by MAD-GRAPH5_aMC@NLO.	38
3.1	Feynman diagram for a general anomalous triple gauge boson vertex with $V = Z/\gamma$	44
3.2	Feynman diagrams for the production of ZZ or $Z\gamma$ at e^+e^- collider.	46
3.3	Sensitivity of the cross section and asymmetries to anomalous couplings for the process $e^+e^- \rightarrow ZZ$ with $\sqrt{s} = 500$ GeV and $\mathcal{L} = 100$ fb $^{-1}$	51
3.4	Sensitivity of the cross section and asymmetries to anomalous couplings for the process $e^+e^- \rightarrow Z\gamma$ with $\sqrt{s} = 500$ GeV, $\mathcal{L} = 100$ fb $^{-1}$, and $10^\circ \leq \theta_\gamma \leq 170^\circ$	52
3.5	1σ sensitivity contours ($\Delta\chi^2 = 1$) for cross section and asymmetries obtained by varying two parameters at a time and keeping the others at zero for the ZZ process at $\sqrt{s} = 500$ GeV and $\mathcal{L} = 100$ fb $^{-1}$	54
3.6	1σ sensitivity contours ($\Delta\chi^2 = 1$) for cross section and asymmetries obtained by varying two parameters at a time and keeping the others at zero for the $Z\gamma$ process at $\sqrt{s} = 500$ GeV, $\mathcal{L} = 100$ fb $^{-1}$, and $10^\circ \leq \theta_\gamma \leq 170^\circ$	54
3.7	Two-dimensional marginalized contours showing most correlated observable for each parameter of the process $e^+e^- \rightarrow ZZ$. The upper transparent layer (<i>blue</i>) contours correspond to aTGC, while the lower layer (<i>green</i>) contours correspond to SM. The darker shade shows 68 % contours, while the lighter shade is for 95 % contours.	58
3.8	Two-dimensional marginalized contours showing correlation between A_{zz} and σ in the ZZ process. The rest of the details are the same as in Fig. 3.7.	59
3.9	One-dimensional marginalized posterior distribution for the parameters of the process $e^+e^- \rightarrow ZZ$. <i>Solid (green)</i> lines are for SM and <i>dashed (blue)</i> lines are for aTGC hypothesis. The values of the parameters for the benchmark points are shown by vertical lines for reference.	59
3.10	Two-dimensional marginalized contours showing correlations between parameters of the process $e^+e^- \rightarrow ZZ$. The other details are the same as in Fig. 3.7.	60

- 3.11 Two-dimensional marginalized contours showing most correlated observables for each parameter of the process $e^+e^- \rightarrow Z\gamma$ for two benchmark points. The rest of the details are the same as in Fig. 3.7. 63
- 3.12 Posterior one-dimensional marginalized distributions for parameters of the process $e^+e^- \rightarrow Z\gamma$ for SM (*green/solid*) and aTGC (*blue/dashed*) points. Vertical lines denote the values of the benchmark points. 64
- 3.13 Two-dimensional contours for all pairs of the parameters in the process $e^+e^- \rightarrow Z\gamma$. The Upper transparent layers (*blue*) are for aTGC and the lower layers (*green*) for the SM showing the 68 % BC (*dark shades*) and 95 % BC (*light shades*) contours. 65
- 3.14 Likelihood ratio for the separability of benchmark points for ZZ (left) and $Z\gamma$ (right) final state: SM *pseudo data* are in solid (*green*) and aTGC *pseudo data* are in dotted (*blue*) lines. 65
- 4.1 Feynman diagram for production of Z boson and its decay to a pair of fermions. 69
- 4.2 The SM cross section (in fb) for the process $e^+e^- \rightarrow ZZ/Z\gamma$ as a function of longitudinal beam polarizations η_3 (for e^-) and ξ_3 (for e^+) at $\sqrt{s} = 500$ GeV. 70
- 4.3 Effect of beam polarizations on sensitivity of cross section σ , A_{xy} and \tilde{A}_{yz} in the process $e^+e^- \rightarrow ZZ$ for anomalous couplings $\vec{f} = \{+3, +3, +3, +3\} \times 10^{-3}$ at $\sqrt{s} = 500$ GeV and $\mathcal{L} = 100$ fb $^{-1}$ 72
- 4.4 Likelihood $L(\{\mathcal{O}\}, \vec{f}; \eta_3, \xi_3)$ for three different benchmark anomalous couplings at $\sqrt{s} = 500$ GeV and $\mathcal{L} = 100$ fb $^{-1}$ in ZZ process. 73
- 4.5 The log of average likelihood, $\log[L(V_{\vec{f}}, \{\mathcal{O}\}; \eta_3, \xi_3)]$ as a function of beam polarization is shown for the ZZ process at $\sqrt{s} = 500$ GeV and $\mathcal{L} = 100$ fb $^{-1}$. The dot at the centre is the (0,0) point, while cross mark at $P_{ZZ} = (+0.16, -0.16)$ is the minimum likelihood point and hence the best choice of beam polarizations for ZZ process. 75
- 4.6 Same as Fig. 4.5 but for the $Z\gamma$ process. The plus mark at $P_{Z\gamma} = (+0.09, -0.10)$ is the lowest likelihood point and hence the best choice of beam polarizations for $Z\gamma$ process. 76

- 4.7 The log of average likelihood, $\log[L(V_{\{f,\tilde{h}\}},\{\mathcal{O}\};\eta_3,\xi_3)]$, is shown considering both the processes ZZ and $Z\gamma$ at $\sqrt{s} = 500$ GeV, $\mathcal{L} = 100$ fb $^{-1}$. The *asterisk mark* at $P_{best} = (+0.12, -0.12)$ is the combined best choice for beam polarizations while the other points are for ZZ (*cross mark*) and $Z\gamma$ (*plus mark*). 77
- 4.8 Two dimensional marginalised contours at 95 % confidence level (C.L.) from MCMC in ZZ production in f_4^γ - f_4^Z and f_5^γ - f_5^Z planes for unpolarized case, best choice for ZZ process and combined best choice of beam polarization including both processes. 78
- 4.9 Two dimensional marginalised contours at 95 % C.L. from MCMC in $Z\gamma$ production in h_1^γ - h_1^Z and h_3^γ - h_3^Z planes for unpolarized case, best choice for $Z\gamma$ process and combined best choice of beam polarization including both processes. 78
- 4.10 The log of average likelihood, $\log[L(V_{\vec{p}},\{\mathcal{O}\};\eta_3,\xi_3)]$ as a function of beam polarization ($\pm\eta_3, \pm\xi_3$) is shown for the ZZ (*left-panel*) and $Z\gamma$ (*right-panel*) process for $\sqrt{s} = 500$ GeV and $\mathcal{L} = 100$ fb $^{-1}$. The dots (\bullet) on the plots are the choice of polarizations for obtaining simultaneous limits given in Table 4.3 and Figs. 4.11 & 4.12. 80
- 4.11 All the one dimensional marginalised projections and two dimensional marginalised contours at 95 % C.L. in triangular array from MCMC in ZZ production for $\sqrt{s} = 500$ GeV and $\mathcal{L} = 100$ fb $^{-1}$ for different beam polarizations ($\pm\eta_3, \pm\xi_3$). 81
- 4.12 All the one dimensional marginalised projections and two dimensional marginalised contours at 95 % C.L. in triangular array from MCMC in $Z\gamma$ production for $\sqrt{s} = 500$ GeV and $\mathcal{L} = 100$ fb $^{-1}$ for different beam polarizations ($\pm\eta_3, \pm\xi_3$). 82
- 5.1 Representative Feynman diagrams for ZZ pair production at the LHC in the SM ($q\bar{q}$ and gg initiated) as well as in aTGC ($q\bar{q}$ initiated) at tree level together with NLO in QCD. 87
- 5.2 The differential distributions of m_{ZZ} in the ZZ production at the LHC at $\sqrt{\hat{s}} = 13$ TeV in LO, NLO and NNLO obtained using MATRIX. In the *left-panel* $q\bar{q}$ initiated results are shown, while in the *right-panel* $q\bar{q} + gg$ initiated results are shown. 89

- 5.3 The differential distributions of m_{4l} (*left-panel*) and $\Delta R(\mu^+, \mu^-)$ (*right-panel*) in the ZZ production at the LHC at $\sqrt{s} = 13$ TeV and $\mathcal{L} = 300$ fb $^{-1}$ at NLO in QCD. The *light-shaded* region with maximum heights (green shaded), the *dark-shaded* region (blue shaded) and the *light-shaded* region with smallest heights (grey shaded) correspond to $q\bar{q}$ SM contribution, gg SM contributions and the background, respectively. The aTGC contributions are shown with different line types (colours). 92
- 5.4 m_{4l} vs ΔR scattered plot (*left*) and m_{4l} distribution for $\Delta R(l^+, l^-) \geq 0.2$ (*right*) in ZZ production at the LHC at $\sqrt{s} = 13$ TeV for the SM and for aTGC with $f_4^\gamma = 0.002$ 93
- 5.5 The sensitivity of the cross section and the polarization observables to the anomalous couplings at $\sqrt{s} = 13$ TeV and $\mathcal{L} = 300$ fb $^{-1}$ in ZZ production at the LHC. 94
- 5.6 Two dimensional marginalised contours at 95 % BCI from MCMC using the cross section σ along with polarization asymmetries (pol.) at $\sqrt{s} = 13$ TeV for various luminosities in ZZ production at the LHC. 96
- 5.7 Comparison of σ vs ($\sigma +$ pol.) in two dimensional marginalised contours from MCMC for aTGC benchmark $f_i^V = 0.002$ in $f_4^\gamma - f_4^Z$ panel and $f_5^\gamma - f_5^Z$ panel at $\sqrt{s} = 13$ TeV for various luminosities in ZZ production at the LHC. 97
- 6.1 Feynman diagrams of $e^+e^- \rightarrow W^+W^-$, (a) t -channel and (b) s -channel with anomalous W^+W^-V ($V = \gamma, Z$) vertex contribution shown by the shaded blob. 103
- 6.2 The production cross section $\sigma_{W^+W^-}$ in pb (*left-panel*) and the polarization asymmetry A_x (*right-panel*) in the SM as a function of longitudinal beam polarizations η_3 (for e^-) and ξ_3 (for e^+) at $\sqrt{s} = 500$ GeV. The asterisks mark represent the unpolarized points and the number near it correspond to the SM values for corresponding observables with unpolarized beams. . . . 104
- 6.3 The WWV vertex showing anomalous contribution represented the shaded blob on top of SM. The momentum P is incoming to the vertex, while q and \bar{q} are outgoing from the vertex. 105

- 6.4 The cross section σ including the decays in pb (*left-panel*) and the asymmetry A_{zz} (*right-panel*) in the SM and aTGC with all anomalous couplings ($c_i^{\mathcal{L}}$) at 0.05 as a function of \sqrt{s} for the SM analytic (*solid/blue*) and aTGC analytic (*dashed/green*) with unpolarized beams. The *crossed* (black) points and *boxed* (red) points with errorbars correspond to results from MadGraph5. The errorbars are given for number of events of 10^4 107
- 6.5 The one parameter sensitivities of the cross section σ , A_{fb} and 8 polarization asymmetries (A_i) on g_4^Z (*left-panel*) and on $\Delta\kappa^\gamma$ (*right-panel*) for $\sqrt{s} = 500$ GeV, $\mathcal{L} = 100 \text{ fb}^{-1}$ with unpolarized beams. 108
- 6.6 The cross section σ (*left-top*), A_z (*right-top*), A_x (*left-bottom*) and A_y (*right-bottom*) as a function of $\cos\theta$ of W^- in 8 bin for $\sqrt{s} = 500$ GeV. The *dotted* (blue) lines correspond to the SM unpolarized values, *solid* (red) lines correspond to the unpolarized aTGC values, *dashed* (black) lines represent the polarized SM values, and *dashed-dotted* (green) lines represent polarized aTGC values of observables. For aTGC, only one anomalous coupling has been assumed non-zero and others kept at zero in each *panel*. 109
- 6.7 The one parameter sensitivities of A_x on g_4^Z (*left-panel*) and of A_z on $\Delta\kappa^\gamma$ (*right-panel*) in 8 bins at $\sqrt{s} = 500$ GeV, $\mathcal{L} = 100 \text{ fb}^{-1}$ with $c_\theta = \cos\theta_{W^-}$ with unpolarized beams. 110
- 6.8 The $\chi^2 = 4$ contours in the *left-panel* and 95 % C.L. contours from simultaneous analysis in the *right-panel* in the $\lambda^\gamma - \lambda^Z$ plane using the binned cross sections (σ) alone in *dotted* (black) lines, just binned polarizations asymmetries (Pol.) in *dashed* (blue) lines and the bin cross section together with binned polarization asymmetries ($\sigma + \text{Pol.}$) in *solid* (green) lines for $\sqrt{s} = 500$ GeV, $\mathcal{L} = 100 \text{ fb}^{-1}$ 110

- 6.9 The $\chi^2 = 4$ contours of the unbinned cross sections $\sigma = \sigma(+\eta_3, +\xi_3)$ in *solid/green* lines, $\bar{\sigma} = \sigma(-\eta_3, -\xi_3)$ in *big-dashed/black* lines, $\sigma_T = \sigma(+\eta_3, +\xi_3) + \sigma(-\eta_3, -\xi_3)$ in *dotted/blue* line, $\sigma_A = \sigma(+\eta_3, +\xi_3) - \sigma(-\eta_3, -\xi_3)$ in *dash-dotted/red* line and the combined χ^2 of σ and $\bar{\sigma}$ in *dashed/magenta* lines for polarization $(\eta_3, \xi_3) = (+0.6, -0.6)$ on $\lambda^\gamma - \lambda^Z$ plane are shown in the *left-panel*. The 95 % C.L. contours from simultaneous analysis in $\lambda^\gamma - \lambda^Z$ plane for the beam polarization $(+0.6, -0.6)$, $(-0.6, +0.6)$ and their combined one $(\pm 0.6, \mp 0.6)$ are shown in the *right-panel* using all the binned observables, i.e., in Binned case. The analyses are done for $\sqrt{s} = 500$ GeV and $\mathcal{L} = 50$ fb $^{-1}$ luminosity to each beam polarization set. 112
- 6.10 The 95 % BCI limits on the anomalous couplings $c_i^{\mathcal{L}}$ for a set of fixed choices of beam polarizations for $\sqrt{s} = 500$ GeV, $\mathcal{L} = 100$ fb $^{-1}$ using the binned observables. 114
- 6.11 The 95 % C.L. contours from simultaneous analysis in $\lambda^\gamma - \lambda^Z$ plane (*left-panel*) and $\lambda^\gamma - \lambda^Z$ plane (*right-panel*) for a set of fixed choices of beam polarizations for $\sqrt{s} = 500$ GeV, $\mathcal{L} = 100$ fb $^{-1}$ using the binned observables. 114
- 6.12 The pictorial visualisation of 95 % BCI limits (a) : on the anomalous couplings $c_i^{\mathcal{L}}$ in the *left-panel*, (b) : on $c_i^{\mathcal{O}}$ in the *right-top-panel* and (c) : on $c_i^{\mathcal{L}_g}$ in the *right-bottom-panel* for $\sqrt{s} = 500$ GeV, $\mathcal{L} = 100$ fb $^{-1}$ using the binned observables. The numerical values of the limits can be read of in Tables 6.4 & 6.5. 118
- 6.13 The marginalised 1D projections for the couplings λ^γ , Δg_1^Z and $\Delta \kappa^Z$ in the *top-panel* and 2D projection at 95 % C.L. on $\lambda^\gamma - \lambda^Z$, $\Delta g_1^Z - \widetilde{\kappa^Z}$ and $\Delta \kappa^\gamma - \Delta \kappa^Z$ planes in *bottom-panel* from MCMC for a set of choice of beam polarizations are shown for $\sqrt{s} = 500$ GeV, $\mathcal{L} = 100$ fb $^{-1}$ using the binned observables in the effective vertex formalism. The legend labels are same as in Figs. 6.12 & 6.14. 119
- 6.14 All the marginalised 1D projections and 2D projections at 95 % C.L. from MCMC in triangular array for the effective operators (TeV $^{-2}$) for a set of choice of beam polarizations for $\sqrt{s} = 500$ GeV, $\mathcal{L} = 100$ fb $^{-1}$ using the binned observables. 120
- 6.15 The averaged likelihood $L_{Av} = L(V_{f^p}; \eta_3, \xi_3)$ in log scale as a function of $(\pm \eta_3, \pm \xi_3)$ in the effective vertex formalism for $\sqrt{s} = 500$ GeV, $\mathcal{L} = 100$ fb $^{-1}$. 121

- 7.1 Sample of Born level Feynman diagrams for ZW^+ production in the $e^+e^-\mu^+\nu_\mu$ channel at the LHC. The diagrams for ZW^- can be obtained by charge conjugation. The shaded blob represents the presence of anomalous WWV couplings on top of SM. 125
- 7.2 The differential distributions of m_{3l} (*top-row*) and $p_T(Z)$ (*bottom-row*) in the ZW^+ (*left-column*) and ZW^- (*right-column*) production in the $e^+e^-\mu^\pm + \cancel{E}_T$ channel at the LHC for $\sqrt{s} = 13$ TeV at LO, NLO and NNLO obtained using MATRIX [229–234, 247, 249] for CMS fiducial phase-space. 126
- 7.3 The differential distributions of m_{3l} and $p_T(Z)$ in the W^+Z production in the $e^+e^-\mu^+\nu_\mu$ channel at the LHC at $\sqrt{s} = 13$ TeV and $\mathcal{L} = 35.9$ fb $^{-1}$ at NLO in the SM and five benchmark anomalous couplings. 127
- 7.4 The sensitivity of cross sections to the five benchmark aTGC as a function of the lower cut on m_{3l} and $p_T(Z)$ in the ZW^\pm production at the LHC at $\sqrt{s} = 13$ TeV and $\mathcal{L} = 35.9$ fb $^{-1}$ 128
- 7.5 The sensitivity of the asymmetry $A_{\Delta\phi}$ on the five benchmark aTGC as a function of the lower cut on $p_T(Z)$ in the ZW^\pm productions at the LHC at $\sqrt{s} = 13$ TeV and $\mathcal{L} = 35.9$ fb $^{-1}$. The legend labels are same as in Fig. 7.4. 130
- 7.6 The sensitivity of some polarization asymmetries of W^+ (ZW^+) on some benchmark aTGC for three scenarios: with absolute truth (**Abs. True**) information of neutrino in *solid*/blue lines, with the close to true reconstructed solution of neutrino (**Reco. True**) in *dotted*/red lines and with the smaller $|p_z(\nu)|$ to be the true solution (**Small $|p_z(\nu)|$**) in *dash-dotted*/blue lines as a function of the lower cut on $p_T(Z)$ (*top-left-panel*) and m_{3l} (*top-right-panel*) at $\sqrt{s} = 13$ TeV and $\mathcal{L} = 100$ fb $^{-1}$. The scatter plot of the total χ^2 for about 100 aTGC points using all the asymmetries of W^\pm for **Reco. True** in x -axis with **Small $|p_z(\nu)|$** in y -axis is shown in the *bottom-panel*. 133
- 7.7 The $\chi^2 = 4$ contours are shown in the $\Delta\kappa^Z - \widetilde{\kappa}^Z$ plane with different asymmetries and their combinations in the *left-panel*, various combinations of the cross sections and asymmetries in the *right-panel* for $\sqrt{s} = 13$ TeV and $\mathcal{L} = 100$ fb $^{-1}$. The contour for $A_{\Delta\phi} + A_i^Z + A_i^W$ (*thick-solid*/black line) is repeated in both *panel* for comparison. 135
- 7.8 All the marginalised 1D projections and 2D projections at 95 % BCI from MCMC in triangular array for the effective vertices ($c_i^{\mathcal{L}}$) for various luminosities at $\sqrt{s} = 13$ TeV using all the observables. 138

- 7.9 The marginalised 2D projections at 95 % BCI from MCMC in the Δg_1^Z - $\Delta \kappa^Z$, λ^Z - $\widetilde{\lambda}^Z$, and $\Delta \kappa^Z$ - $\widetilde{\kappa}^Z$ planes are shown in *solid/red* when the effective vertex factors ($c_i^{\mathcal{L}}$) are treated independent, while shown in *dashed/green* when the operators are treated independent ($c_i^{\mathcal{L}^s}$) for luminosities $\mathcal{L} = 1000 \text{ fb}^{-1}$ (two inner contours) and $\mathcal{L} = 100 \text{ fb}^{-1}$ (two outer contours) at $\sqrt{s} = 13 \text{ TeV}$ using all the observables. 139
- 7.10 The two parameter 95 % C.L. contours in the c_{WWW}/Λ^2 - c_W/Λ^2 plane (*left-panel*) and c_W/Λ^2 - c_B/Λ^2 plane (*right-panel*) for our estimate in *solid/green* lines, for CMS $ZW + WW$ in *dashed/black* lines and for CMS ZW in *dotted/blue* lines at $\sqrt{s} = 13 \text{ TeV}$ and $\mathcal{L} = 35.9 \text{ fb}^{-1}$ using all the observables. 139
- 7.11 The marginalised 1D projections for the couplings Δg_1^Z , λ^Z , $\Delta \kappa^Z$, and $\widetilde{\kappa}^Z$ in *top-panel* and 2D projections at 95 % BCI on Δg_1^Z - $\widetilde{\kappa}^Z$, λ^Z - $\widetilde{\lambda}^Z$, $\Delta \kappa^Z$ - $\widetilde{\kappa}^Z$, and $\Delta \kappa^Z$ - $\widetilde{\lambda}^Z$ planes in *bottom-panel* from MCMC with observables σ_i (*dotted/red* line), $\sigma_i + A_{\Delta\phi} + A_i^Z$ (*dashed/blue* line) and $\sigma_i + A_{\Delta\phi} + A_i^Z + A_i^W$ (*solid/green* line) for aTGC-Bench couplings $\{\Delta g_1^Z, \lambda^Z, \Delta \kappa^Z, \widetilde{\lambda}^Z, \widetilde{\kappa}^Z\} = \{0.01, 0.01, 0.1, 0.01, 0.1\}$ at $\sqrt{s} = 13 \text{ TeV}$ and $\mathcal{L} = 100 \text{ fb}^{-1}$ 140
- B.1 Schematic diagram for $e^-e^+ \rightarrow ZV$ kinematics. 152
- D.1 Schematic diagram for $e^-e^+ \rightarrow W^-W^+$ kinematics. 164
- E.1 The simulated data (in x -axis) vs. fitted values (in y -axis) for the cross section in the two diagonal bins (*top-panel*) and the polarization asymmetries A_z and A_{xz} (*bottom-panel*) in ZW^+ production in $e^+e^-\mu^+\nu_\mu$ channel at the LHC at $\sqrt{s} = 13 \text{ TeV}$ 172

List of Tables

1.1	The gauge quantum numbers of the SM fields in the $SU(3)_C \otimes SU(2)_L \otimes U(1)_Y$ gauge group.	4
1.2	Value of axial coupling a_f and vector couplings v_f to the Z boson given in Eq. (1.1.42) & (1.1.43).	10
2.1	Total number of polarization parameters and correlator in spin- s and spin- s' production system.	40
3.1	List of tightest limits on anomalous couplings of Eq. (3.0.1) available in literature.	43
3.2	Dependence of the polarization observables on the anomalous coupling in ZZ final state.	49
3.3	Dependence of the polarization observables on the anomalous coupling in $Z\gamma$ final state.	49
3.4	List of tightest limits on anomalous couplings at 1σ level and the corresponding observable obtained for $\sqrt{s} = 500$ GeV and $\mathcal{L} = 100 \text{ fb}^{-1}$	53
3.5	List of observables shown for the process $e^+e^- \rightarrow ZZ$ for the benchmark point SM with $\sqrt{s} = 500$ GeV: theoretical values (column 2), MadGraph5 simulated value for $\mathcal{L} = 100 \text{ fb}^{-1}$ (column 3), 68 % (column 4) and 95 % (column 5) Bayesian confidence intervals (BCI).	57
3.6	List of observables shown for the process $e^+e^- \rightarrow ZZ$ for the benchmark point aTGC with $\sqrt{s} = 500$ GeV. The rest of the details are the same as in Table 3.5.	57
3.7	The list of best-fit points, posterior 68 % and 95 % BCI for the parameters for the process $e^+e^- \rightarrow ZZ$ for both SM and aTGC benchmark points.	60

3.8	List of observables shown for the process $e^+e^- \rightarrow Z\gamma$ for the SM point with $\sqrt{s} = 500$ GeV and $\mathcal{L} = 100$ fb $^{-1}$. The rest of the details are the same as in Table 3.5.	62
3.9	List of observables shown for the process $e^+e^- \rightarrow Z\gamma$ for the aTGC point with $\sqrt{s} = 500$ GeV and $\mathcal{L} = 100$ fb $^{-1}$. The rest of the details are the same as in Table 3.5.	62
3.10	The list of best-fit points, posterior 68 % and 95 % BCI for the parameters for the process $e^+e^- \rightarrow Z\gamma$ for both benchmark points.	62
4.1	List of simultaneous limits on the anomalous couplings obtained for $\sqrt{s} = 500$ GeV and $\mathcal{L} = 100$ fb $^{-1}$ for different η_3 and ξ_3 from MCMC in ZZ process. 76	76
4.2	List of simultaneous limits on the anomalous couplings obtained for $\sqrt{s} = 500$ GeV and $\mathcal{L} = 100$ fb $^{-1}$ for different η_3 and ξ_3 from MCMC in Z γ process. 77	77
4.3	List of simultaneous limits at 95 % C.L. on the anomalous couplings (10^{-3}) obtained for $\sqrt{s} = 500$ GeV and $\mathcal{L} = 100$ fb $^{-1}$ for different beam polarization ($\pm\eta_3, \pm\xi_3$) from MCMC in ZZ and Z γ processes.	80
5.1	The theoretical estimates and experimental measurements of the ZZ production cross section at $\sqrt{s} = 13$ TeV at the LHC. The uncertainties in the theoretical estimates come from scale variation.	88
5.2	One parameter limits (10^{-3}) at 95 % C.L. on anomalous couplings in ZZ production at the LHC at $\sqrt{s} = 13$ TeV for various luminosities.	95
5.3	Simultaneous limits (10^{-3}) at 95 % C.L. on anomalous couplings in ZZ production at the LHC at $\sqrt{s} = 13$ TeV for various luminosities from MCMC. 95	95
6.1	The list of tightest limits obtained on the anomalous couplings of dimension-6 operators in Eq. (6.0.1) and effective vertices in Eq. (6.0.2) in $SU(2) \times U(1)$ gauge (except g_4^Z and g_5^Z) at 95% C.L. from experiments.	102
6.2	The dependence of observables (numerators) on the form factor couplings in the form of $c_i^{\mathcal{L}}$ (linear), $(c_i^{\mathcal{L}})^2$ (quadratic) and $c_i^{\mathcal{L}} c_j^{\mathcal{L}}$, $i \neq j$ (interference) in the process $e^+e^- \rightarrow W^+W^-$. Here, $V \in \{\gamma, Z\}$. The “✓” (<i>checkmark</i>) represents the presence and “—” (<i>big-dash</i>) corresponds to absence.	106

- 6.3 The list of analyses performed in the present work and set of observables used with different kinematical cuts to obtain simultaneous limits on the anomalous couplings at $\sqrt{s} = 500$ GeV, $\mathcal{L} = 100$ fb⁻¹ with unpolarized beams. The rectangular volumes of couplings at 95% BCI are shown in the last column for each analyses (see text for details). 110
- 6.4 List of posterior 95 % BCI of anomalous couplings $c_i^{\mathcal{L}}$ (10^{-2}) of the Lagrangian in Eq. (6.0.2) at $\sqrt{s} = 500$ GeV, $\mathcal{L} = 100$ fb⁻¹ for a chosen set of longitudinal beam polarizations η_3 and ξ_3 from MCMC in Binned case. The limits for the best choice of beam polarization within technological reach, i.e., ($\pm 0.8, \mp 0.6$) are marked in **bold**. The pictorial visualisation for these 95 % BCI of $c_i^{\mathcal{L}}$ is shown in Fig. 6.12 in the *left-panel*. The one parameter ($1P$) limits (10^{-2}) at 95 % BCI with unpolarized beams are given in the last column for comparison. The notations used here are ${}_{low}^{high} \equiv [low, high]$ with *low* being lower limit and *high* being upper limit. 116
- 6.5 The list of posterior 95 % BCI of anomalous couplings $c_i^{\mathcal{O}}$ (TeV⁻²) of effective operators in Eq. (6.0.1) and their translated limits on the couplings $c_i^{\mathcal{L}_g}$ (10^{-2}) for $\sqrt{s} = 500$ GeV, $\mathcal{L} = 100$ fb⁻¹ in Binned case for a chosen set of longitudinal beam polarizations η_3 and ξ_3 from MCMC. The pictorial visualisations for these 95 % BCI of $c_i^{\mathcal{O}}$ and $c_i^{\mathcal{L}_g}$ are shown in Fig. 6.12 in *right-top* and *right-bottom* panel, respectively. Rest details are same as in Table 6.4. 117
- 7.1 The theoretical estimates and experimental measurements of the cross sections of ZW^\pm productions in the $e^+e^-\mu^\pm\nu_\mu/\bar{\nu}_\mu$ channel at $\sqrt{s} = 13$ TeV at the LHC for CMS fiducial phase-space. The uncertainties in the theoretical estimates are due to scale variation. 125
- 7.2 The sensitivity of the cross sections on the five benchmark aTGC in the four bins (see Eq. (7.1.3)) of m_{3l} and $p_T(Z)$ in the ZW^\pm productions at the LHC at $\sqrt{s} = 13$ TeV and $\mathcal{L} = 35.9$ fb⁻¹. 129
- 7.3 The list of optimized lower cuts (opt. cut) on $(m_{3l}, p_T(Z))$ for various asymmetries to maximize the sensitivity to the anomalous couplings. 135

- 7.4 The list of simultaneous limits from MCMC at 95 % BCI on the effective vertex couplings $c_i^{\mathcal{L}}$ and the effective operator couplings $c_i^{\mathcal{O}}$ along with translated limits on effective vertices $c_i^{\mathcal{L}_g}$ for various luminosities. The notations for $c_i^{\mathcal{L}}$, $c_i^{\mathcal{O}}$, and $c_i^{\mathcal{L}_g}$ are given in Eqs. (6.0.4), (6.0.3), and (6.0.5), respectively. 137
- E.1 The SM values with MC error of the polarization asymmetries of Z and W and their corresponding polarizations along with the other asymmetries in ZW^\pm production in the $e^+e^-\mu^\pm + \cancel{E}_T$ channel are shown for event selection cuts (sel.cut) given in Eq. (7.1.2) and optimized cuts (opt.cut) given Table 7.3. 170

1

Introduction

Contents

1.1	The Standard Model of particle physics.	2
1.1.1	The interactions in the SM electroweak theory	8
1.1.2	Summary of the SM	12
1.2	Problems in the SM with possible solutions.	12
1.3	EFT and anomalous gauge boson couplings.	15
1.3.1	BSM contributions to aTGC	21
1.3.2	Probe of the aTGC	22
1.4	Outline of the thesis	23

The Standard Model (SM) [1–9] of particle physics is one of the most remarkably successful fundamental theories to describe the governing principle of elementary constituents of matter and their interactions in the Universe. It explains almost all the phenomena observed in Nature at a small length scale. The theoretical predictions of the SM are being confirmed time and again with a spectacular accuracy with the discovery of many fundamental particles and interactions. The particle spectrum of the SM is complete with the discovery of its last milestone, the Higgs boson at the Large Hadron Collider (LHC) [10, 11] in 2012. However, the SM is too far from being a final theory (theory of everything) as it has many issues within the theoretical framework, such as the hierarchy of mass scales, the strong CP problem, and it is unable to address some experimental facts, such as neutrino oscillation, dark matter, baryogenesis, and many more. Many theories, with SM as a subset, have been postulated to address the unresolved issues predicting new particles and new interactions, i.e., new physics beyond the SM (BSM). Searches for such new physics are going on at the LHC with higher energy and higher luminosity, but sadly one has not found anything beyond

the SM [12–16] till date except few fluctuations (e.g., see Refs. [17–19]). One could expect that the new physics scale is too heavy to be directly explored by the current LHC, and they may leave some footprints in the available energy range. They will modify the structure of the SM interactions or bring some new interactions often through higher-dimensional operators with the SM fields. These new vertices and/or the extra contributions to the SM vertices are termed as anomalous in the sense that they are not present in the SM at leading order. The electroweak sector will get affected by the anomalous bosonic self couplings, which alter the paradigm of electroweak symmetry breaking (EWSB) [20–23]. To test the SM (or BSM) predictions for the EWSB mechanism, precise measurements of the Higgs couplings with all other gauge bosons, Higgs self-couplings, and gauge boson self-couplings are necessary.

This thesis is focused on the study of gauge boson self couplings, in particular, anomalous triple gauge boson couplings (aTGC). The anomalous gauge boson couplings which carry information of high scale new physics in the electroweak sector can be modelled through effective field theory (EFT) in a model independent way. In EFT, one can preserve the SM gauge symmetry or just consider the Lorentz invariance. Both approaches serve as an open-minded method of describing low energy impacts of new physics at much higher energy scales. There are lots of studies of the aTGC in the literature on the theoretical side as well as in various experiments in various ways with cross sections and some asymmetries. Innovative techniques with more observables are required to probe many unknown anomalous couplings parameters in experiments. Our strategy, here, is to use the polarizations of gauge bosons to probe the aTGC and we will see that they give significant contributions in pinning down the aTGC.

Before going to the main contents, we give a brief introduction of the SM which is very important to understand the aTGC. We will close the introduction chapter by giving a description of the aTGC in the EFT approach followed by contributions from some of the BSM scenarios.

1.1 The Standard Model of particle physics

The SM relies on the framework of quantum field theory (QFT), where the fundamental particles are treated as discrete excitations of an underlying dynamical field. The SM is constructed by postulating a set of underlying symmetries and considering the most general renormalizable Lagrangian with the field contents. The symmetry of the SM is based on the *local* gauge transformation, i.e., separately valid at each space-time point x , under

$SU(3)_C \otimes SU(2)_L \otimes U(1)_Y$ group, which describe the fundamental forces in Nature: the strong, the weak and the electromagnetic interactions excluding the gravity. Each gauge symmetry manifestly gives rise to gauge boson mediators for each interaction. The particle content of the SM in the matter sector, all with spin 1/2, are the six quarks, endowed with both color ($SU(3)_C$) and electroweak charges ($SU(2)_L \otimes U(1)_Y$), six leptons with no color but with electroweak charges. The matter fermions (quarks and leptons) are present in three generations with identical quantum number but different masses with the pattern

$$\begin{aligned} \text{Leptons } (l) & : \begin{pmatrix} \nu_l \\ l^- \end{pmatrix} = \begin{pmatrix} \nu_e & \nu_\mu & \nu_\tau \\ e^- & \mu^- & \tau^- \end{pmatrix} \quad \text{and} \\ \text{Quarks } (q) & : \begin{pmatrix} q_u \\ q_d \end{pmatrix} = \begin{pmatrix} u & c & t \\ d & s & b \end{pmatrix}. \end{aligned} \quad (1.1.1)$$

The mediators (gauge bosons) of the strong, weak and electromagnetic forces are, of spin 1; eight massless gluons (g) for strong interaction, three massive gauge boson (W^+ , W^- and Z) for the weak interaction and one massless photon (A) for the electromagnetic interaction. While the color ($SU(3)_C$) symmetry is conserved, the electroweak ($SU(2)_L \otimes U(1)_Y$) symmetry is broken leaving some of its generators to be massive. The electroweak gauge symmetry is spontaneously broken by the celebrated Brout-Englert-Higgs-Kibble (BEHK) mechanism, which generates mass terms for the massive vector bosons by the spin-0 Higgs field (Φ). The quantum excitation of the Higgs field gives rise to the particle Higgs boson (h).

The weak interaction in the SM is chiral, i.e., the left chiral and the right chiral fermion fields given by

$$\psi_{L/R} = \frac{1}{2}(1 \mp \gamma_5)\psi = P_{L/R}\psi \quad (1.1.2)$$

transform differently under $SU(2)_L$ group. Due to the chirality, each of the three fermion generations come with five different representation as q_L , q_{uR} , q_{dR} , l_L , and l_R , shown in Table 1.1 along with their quantum numbers. The left-handed fields transform as doublet, while the right-handed fields transform as singlet under the $SU(2)_L$ group. All quarks, having three color degrees of freedom, transform as triplet under the $SU(3)_C$ subgroup equally for left-handed and right-handed fields. The leptons remain singlet under the $SU(3)_C$.

The gauge field mediators arise naturally when the local gauge invariance is imposed on

Table 1.1. The gauge quantum numbers of the SM fields in the $SU(3)_C \otimes SU(2)_L \otimes U(1)_Y$ gauge group.

Field/ Quantum number	$SU(3)_C$	$SU(2)_L$	$U(1)_Y$	T_3	$Q_{EM} = T_3 + Y$
$q_L = \begin{pmatrix} q_u \\ q_d \end{pmatrix}_L$	3	2	$+\frac{1}{6}$	$+\frac{1}{2}$ $-\frac{1}{2}$	$+\frac{2}{3}$ $-\frac{1}{3}$
q_{uR}	3	1	$+\frac{2}{3}$	0	$+\frac{2}{3}$
q_{dR}	3	1	$-\frac{1}{3}$	0	$-\frac{1}{3}$
$l_L = \begin{pmatrix} \nu_l \\ l^- \end{pmatrix}_L$	1	2	$-\frac{1}{2}$	$+\frac{1}{2}$ $+\frac{1}{2}$	0 -1
l_R	1	1	-1	0	-1
$\Phi = \begin{pmatrix} \Phi^+ \\ \Phi^0 \end{pmatrix}$	1	2	$+\frac{1}{2}$	$+\frac{1}{2}$ $-\frac{1}{2}$	+1 0

the free Lagrangian. For example, the free quantum electrodynamic (QED) Lagrangian

$$\mathcal{L}_0 = i\bar{\psi}(x)(\not{\partial} - m)\psi(x) \quad (\not{\partial} = \gamma^\mu \partial_\mu) \quad (1.1.3)$$

is invariant under the *local*¹ $U(1)$ transformations

$$\psi(x) \xrightarrow{U(1)} \psi'(x) \equiv \exp\{iQ\theta(x)\}\psi(x) \quad (1.1.4)$$

if

$$\partial_\mu \rightarrow \mathcal{D}_\mu \equiv \partial_\mu - ieQA_\mu(x), \quad A_\mu(x) \rightarrow A'_\mu(x) \equiv A_\mu(x) + \frac{1}{e}\partial_\mu\theta(x), \quad (1.1.5)$$

i.e., introducing a new spin-1 field $A_\mu(x)$ which is realized as photon in Nature. The local gauge invariance, thus, of a Lagrangian demands a gauge field or gauge mediator. For the $A_\mu(x)$ to be a free propagating field one needs to add the gauge invariant kinetic term for it as

$$\mathcal{L}_{kin} = -\frac{1}{4}F_{\mu\nu}(x)F^{\mu\nu}(x), \quad (1.1.6)$$

where $F_{\mu\nu} = \partial_\mu A_\nu - \partial_\nu A_\mu$ is the usual electro magnetic field strength tensor. A possible mass term of $A_\mu(x)$ of the form $m_A^2 A^\mu A_\mu$ is forbidden as it breaks the gauge invariance. The total

¹Local or space-time dependence is required as the space time dependent phase of charged fields should not be observable.

gauge invariant QED Lagrangian

$$\mathcal{L}_{QED} = i\bar{\psi}(x)(\not{\partial} - m)\psi(x) - \frac{1}{4}F_{\mu\nu}(x)F^{\mu\nu}(x) \quad (1.1.7)$$

gives the well known Maxwell equations:

$$\partial_\mu F^{\mu\nu} = J^\nu, \quad j^\nu = -eQ\bar{\psi}\gamma^\nu\psi. \quad (1.1.8)$$

The electromagnetic (EM) current j^ν couple to the photon field A_ν with the interaction term:

$$\mathcal{L}_{QED(int)} = A_\nu J^\nu = eQA_\nu(x)\bar{\psi}(x)\gamma^\nu\psi(x). \quad (1.1.9)$$

The electromagnetic interaction and the weak interaction are unified as the electroweak theory under the gauge group $SU(2)_L \otimes U(1)_Y$. For the $U(1)_Y$ abelian gauge symmetry a B_μ field with generator Y (hypercharge) is introduced (similar to A_μ in QED case); for the $SU(2)_L$ non abelian gauge symmetry, three ($2^2 - 1 = 3$) gauge fields W_μ^a with three generators $T^a = \sigma^a/2$ are required. The strong interaction, however, remain unbroken requiring eight ($3^2 - 1 = 8$) gauge field G_μ^c with eight generators $\mathbb{T}^a = \lambda^a/2$ for the $SU(3)_C$ gauge invariance. The *local* gauge invariance of the full $SU(3)_C \otimes SU(2)_L \otimes U(1)_Y$ symmetry require the co-variant derivative \mathcal{D}_μ in Eq. (1.1.5) to be

$$\mathcal{D}_\mu = \partial_\mu - ig'YB_\mu - ig\frac{1}{2}\sigma^a W_\mu^a - ig_s\frac{1}{2}\lambda^a G_\mu^a. \quad (1.1.10)$$

Here g' , g and g_s are the couplings constant in $U(1)_Y$, $SU(2)_L$ and $SU(3)_C$ subgroup, respectively. The σ^a and λ^a are Pauli matrices (see Eq. (A.0.1)) and eight Gell-Mann matrices, respectively. The non-Lorentz indices a on the gauge field W and G run on $SU(2)_L$ flavour space and the color space, respectively. The generators Y , T^a , and the \mathbb{T}^a follow the algebra:

$$[\mathbb{T}^a, \mathbb{T}^b] = if^{abc}\mathbb{T}^c, \quad [T^a, T^b] = i\epsilon^{abc}T^c, \quad [\mathbb{T}^a, T^b] = [\mathbb{T}^a, Y] = [T^a, Y] = 0. \quad (1.1.11)$$

The gauge invariant matter Lagrangian of the SM is given by

$$\mathcal{L}_{matter} = i\bar{q}_L\not{\partial}q_L + i\bar{l}_L\not{\partial}l_L + i\bar{q}_{uR}\not{\partial}q_{uR} + i\bar{q}_{dR}\not{\partial}q_{dR} + i\bar{l}_R\not{\partial}l_R, \quad (1.1.12)$$

where $\mathcal{D}^{(L)}$, $\mathcal{D}^{(qR)}$, and $\mathcal{D}^{(lR)}$ are given by (according to Table 1.1),

$$\begin{aligned}\mathcal{D}_\mu^{(L)} &= \partial_\mu - ig' Y B_\mu - ig \frac{1}{2} \sigma^a W_\mu^a, \\ \mathcal{D}_\mu^{(qR)} &= \partial_\mu - ig' Y B_\mu - ig_s \frac{1}{2} \lambda^a G_\mu^a, \\ \mathcal{D}_\mu^{(lR)} &= \partial_\mu - ig' Y B_\mu.\end{aligned}\tag{1.1.13}$$

The Lagrangian with kinetic terms for the gauge fields is

$$\mathcal{L}_{gauge} = -\frac{1}{4g'^2} B^{\mu\nu} B_{\mu\nu} - \frac{1}{4g^2} W_a^{\mu\nu} W_{\mu\nu}^a - \frac{1}{4g_s^2} G_a^{\mu\nu} G_{\mu\nu}^a\tag{1.1.14}$$

with the field strength tensors given by

$$G_{\mu\nu}^a = g_s (\partial_\mu G_\nu^a - \partial_\nu G_\mu^a + g_s f^{abc} G_\mu^b G_\nu^c),\tag{1.1.15}$$

$$W_{\mu\nu}^a = g (\partial_\mu W_\nu^a - \partial_\nu W_\mu^a + g \epsilon^{abc} W_\mu^b W_\nu^c),\tag{1.1.16}$$

$$B_{\mu\nu} = g' (\partial_\mu B_\nu - \partial_\nu B_\mu).\tag{1.1.17}$$

The mass terms for the gauge fields can not be added by hand as they break the gauge invariance. Fermion masses can also not be added as they would generate left-chiral and right-chiral mixing breaking the gauge invariance explicitly. A scalar doublet under $SU(2)$, the Higgs scalar field (quantum number given in Table 1.1),

$$\Phi = \begin{pmatrix} \Phi^+ \\ \Phi^0 \end{pmatrix}\tag{1.1.18}$$

comes to rescue by generating mass of the heavy gauge bosons by spontaneous symmetry breaking (SSB). The gauge invariant Higgs Lagrangian is given by,

$$\mathcal{L}_{Higgs} = (\mathcal{D}_\mu^{(lL)} \Phi)^\dagger (\mathcal{D}_\mu^{(lL)} \Phi) - \mu^2 \Phi^\dagger \Phi - \lambda (\Phi^\dagger \Phi)^2.\tag{1.1.19}$$

The potential

$$V(\Phi) = \mu^2 \Phi^\dagger \Phi + \lambda (\Phi^\dagger \Phi)^2\tag{1.1.20}$$

get a non-vanishing vacuum expectation value (VEV) for $\mu^2 < 0$ as,

$$\langle \Phi \rangle = \frac{v}{\sqrt{2}} = \frac{1}{\sqrt{2}} \sqrt{\frac{-\mu^2}{\lambda}},\tag{1.1.21}$$

which break the $SU(2)_L \otimes U(1)_Y$ symmetry spontaneously down to $U(1)$ electro magnetic with generator $Q_{EM} = T_3 + Y$. The scalar field Φ , after removing the would-be Goldstone boson, can be expressed as,

$$\Phi = \frac{1}{\sqrt{2}} \begin{pmatrix} 0 \\ \mathbf{v} + h \end{pmatrix}, \quad (1.1.22)$$

h being the excitation around the minima. The h turn out to be a physical degree of freedom, the Higgs boson with mass

$$m_h = \sqrt{2\lambda}\mathbf{v}. \quad (1.1.23)$$

After the SSB the kinetic term $(\mathcal{D}_\mu \Phi)^\dagger (\mathcal{D}_\mu \Phi)$ of the Higgs field gives the mass terms of the physical gauge bosons W^\pm and Z as,

$$\mathcal{L}_{mass} = \frac{1}{4}g^2\mathbf{v}^2 W^{\pm\mu} W_\mu^\mp + \frac{1}{8}(g^2 + g'^2)\mathbf{v}^2 Z^\mu Z_\mu + 0 \times (A^\mu A_\mu) \quad (1.1.24)$$

after rewriting the gauge field in their mass basis as,

$$\begin{aligned} W^\pm &= \frac{1}{\sqrt{2}}(W_1 \mp iW_2), \\ Z^\mu &= \cos\theta_W W_3^\mu - \sin\theta_W B^\mu, \\ A^\mu &= \sin\theta_W W_3^\mu + \cos\theta_W B^\mu \end{aligned} \quad (1.1.25)$$

with

$$\tan\theta_W = \frac{g'}{g}. \quad (1.1.26)$$

The θ_W , called the weak mixing angle, represents a rotation angle from the ‘‘interaction’’ basis (where fields have well- defined transformation properties under the gauge symmetry), W_3^μ and B^μ , into their mass basis for the vector bosons, Z^μ and A^μ . The W and Z , thus, acquire masses as,

$$m_W = \frac{1}{2}g\mathbf{v}, \quad m_Z = \frac{1}{2}\sqrt{(g^2 + g'^2)}\mathbf{v}, \quad (1.1.27)$$

while the photon A^μ remain massless. The θ_W provides a relation between the vector boson masses with the parameter

$$\rho = \frac{m_W^2}{m_Z^2 \cos^2\theta_W} = 1 \quad (1.1.28)$$

at the tree level. The fermions also get their masses after SSB via the Yukawa terms given

by,

$$\mathcal{L}_{Yukawa} = -Y_{ij}^u \overline{q_{Li}} q_{uRj} \tilde{\Phi} - Y_{ij}^d \overline{q_{Li}} q_{dRj} \Phi - Y_{ij}^l \overline{l_{Li}} l_{Rj} \Phi + h.c., \quad \tilde{\Phi} = i\sigma_2 \Phi^*. \quad (1.1.29)$$

The Yukawa matrix Y_{ij} are in general 3×3 matrix of dimensionless couplings, and can be chosen in diagonal basis as,

$$Y^u = \text{diag}(y_u, y_c, y_t), \quad Y^d = \text{diag}(y_d, y_s, y_b), \quad Y^l = \text{diag}(y_e, y_\mu, y_\tau) \quad (1.1.30)$$

without any loss of generality. After SSB, the \mathcal{L}_{Yukawa} generates the mass terms

$$\mathcal{L}_{Yukawa(mass)} = -\frac{y_l^V}{\sqrt{2}} \bar{l}_L l_R - \frac{y_q^V}{\sqrt{2}} \bar{q}_L q_R \quad (1.1.31)$$

with the fermion masses given by,

$$m_l = \frac{y_l^V}{\sqrt{2}}, \quad m_q = \frac{y_q^V}{\sqrt{2}}. \quad (1.1.32)$$

The total SM Lagrangian is thus given by,

$$\mathcal{L}_{SM} = \mathcal{L}_{matter} + \mathcal{L}_{gauge} + \mathcal{L}_{Higgs} + \mathcal{L}_{Yukawa}. \quad (1.1.33)$$

The SM Lagrangian needs the gauge fixing of the field strength tensors required to have a finite propagator and also the ghost term for the s -matrix to remain unitary. The gauge fixing terms and the ghosts do not appear in the physical observables.

1.1.1 The interactions in the SM electroweak theory

The matter part \mathcal{L}_{matter} in Eq. (1.1.12) and gauge part \mathcal{L}_{gauge} in Eq. (1.1.14) of the SM Lagrangian generates interactions between the gauge bosons and fermions as well as the gauge bosons themselves, which are discussed in the next subsection. The relevant Feynman rules for this thesis in the electroweak sector (excluding quartic gauge couplings) are given in appendix A for completeness.

1.1.1.a Charged and neutral current interactions

The neutral current and the charge current interactions of the fermions with the electroweak gauge bosons arise from the Lagrangian \mathcal{L}_{matter} in Eq. (1.1.12) and they are given by,

$$\mathcal{L}_{int} = -ig' B_\mu \sum_{j=L,R} Y_j \bar{\psi}_j \gamma^\mu \psi_j - ig \bar{\psi}_L \gamma^\mu T^a W_\mu^a \psi_L, \quad (1.1.34)$$

where ψ represents the fermion field given in Table 1.1. The terms containing in the $SU(2)_L$ matrix

$$\frac{1}{2} \sigma^a W_\mu^a = \frac{1}{2} \begin{pmatrix} W_\mu^3 & \sqrt{2} W_\mu^+ \\ \sqrt{2} W_\mu^- & -W_\mu^3 \end{pmatrix} \quad (1.1.35)$$

give the charged current interactions

$$\mathcal{L}_{CC} = \frac{g}{2\sqrt{2}} \left\{ W_\mu^+ [\bar{u} \gamma^\mu (1 - \gamma_5) d + \bar{\nu}_e \gamma^\mu (1 - \gamma_5) e] + h.c. \right\} \quad (1.1.36)$$

for a single family of quarks and leptons, see Eq. (1.1.1). Gauge symmetry thus brings the universality of the quarks and leptons interacting with the charge gauge bosons W^\pm . For the quarks, the mass basis (diagonal Yukawa matrix) are not the same as the interaction basis. When one writes the weak eigenstates of the quarks in their mass basis, a unitary matrix V , called the Cabibbo-Kobayashi-Maskawa (CKM) matrix, arises in the quark charged current interaction as,

$$\mathcal{L}_{CC(CKM)} = \frac{g}{2\sqrt{2}} \left\{ W_\mu^+ \sum_{i,j} \bar{q}_{ui} \gamma^\mu (1 - \gamma_5) V_{ij} q_{dj} + h.c. \right\}. \quad (1.1.37)$$

The CKM matrix V couples any up-type quark (q_u) to all down-type quarks (q_d).

The interaction term \mathcal{L}_{int} in Eq. (1.1.34) also contains the interactions of fermions with the neutral gauge fields W_μ^3 and B_μ , which are related to the physical neutral gauge bosons Z_μ and A_μ , as given in Eq. (1.1.25). The neutral interactions in terms of the physical gauge bosons are given by,

$$\mathcal{L}_{NC} = - \sum_{j=L,R} \bar{\psi}_j \gamma^\mu \left\{ A_\mu \left[g \frac{\sigma^3}{2} \sin \theta_W + g' Y_j \cos \theta_W \right] + Z_\mu \left[g \frac{\sigma^3}{2} \cos \theta_W - g' Y_j \sin \theta_W \right] \right\} \psi_j. \quad (1.1.38)$$

To recover the QED interaction in Eq. (1.1.9) containing the A_μ term in the above equation,

one needs to impose the conditions

$$g \sin \theta_W = g' \cos \theta_W = e, \quad Y = Q - T^3, \quad (1.1.39)$$

where Q denote the charge operator as,

$$Q_L = \begin{pmatrix} Q_{u/\nu} & 0 \\ 0 & Q_{d/e} \end{pmatrix}, \quad Q_R = Q_{u/\nu}, Q_{d/e}. \quad (1.1.40)$$

The first identity relates the observable EM coupling e to the couplings of the unified electroweak theory. The second identity provides the hypercharges of the fermions in terms of their electric charges and weak iso-spin, given in Table 1.1. A hypothetical right handed neutrino would not interact with W^\pm boson as both of it's electric charge and weak hypercharge will be zero. The neutral current interaction containing the Z boson is given by,

$$\mathcal{L}_{NC(Z)} = \frac{e}{2 \sin \theta_W \cos \theta_W} Z_\mu \sum_{j=L,R} \bar{\psi}_j \gamma^\mu (\sigma^3 - 2 \sin^2 \theta_W Q_j) \psi_j \quad (1.1.41)$$

which can be simplified as,

$$\mathcal{L}_{NC(Z)} = \frac{g_Z}{2} Z_\mu \sum_f \bar{f} \gamma^\mu (v_f - a_f \gamma_5) f, \quad g_Z = \frac{g}{\cos \theta_W}, \quad (1.1.42)$$

where axial coupling a_f and vector couplings v_f are given by,

$$a_f = T_f^3, \quad v_f = T_f^3 - 2Q_f \sin^2 \theta_W. \quad (1.1.43)$$

The values of a_f and v_f of all the fermions can be deduced from the Table 1.1 and they are given in Table 1.2.

Table 1.2. Value of axial coupling a_f and vector couplings v_f to the Z boson given in Eq. (1.1.42) & (1.1.43).

	q_u	q_d	ν_l	l
a_f	$\frac{1}{2}$	$-\frac{1}{2}$	$\frac{1}{2}$	$-\frac{1}{2}$
v_f	$\frac{1}{2} - \frac{4}{3} \sin^2 \theta_W$	$-\frac{1}{2} + \frac{2}{3} \sin^2 \theta_W$	$\frac{1}{2}$	$-\frac{1}{2} + 2 \sin^2 \theta_W$

1.1.1.b Gauge self couplings

The gauge part \mathcal{L}_{gauge} in Eq. (1.1.14) of the electroweak theory generates cubic and quartic interactions among the gauge bosons in the following form:

$$\mathcal{L}_{WWV} = ig_{WWV} \left[(W_{\mu\nu}^+ W^{-\mu} - W^{+\mu} W_{\mu\nu}^-) V^\nu + W_\mu^+ W_\nu^- V^{\mu\nu} \right], \quad (1.1.44)$$

$$\begin{aligned} \mathcal{L}_{W^4/W^2V^2} &= -\frac{g^2}{2} \left[(W_\mu^+ W^{-\mu})^2 - W_\mu^+ W^{+\mu} W_\nu^- W^{-\nu} \right] \\ &- g_{WWV_1V_2} \left[W_\mu^+ W^{-\mu} V_{1\nu} V_2^\nu - W_\mu^+ V_1^\mu W_\nu^- V_2^\nu \right], \end{aligned} \quad (1.1.45)$$

with $V = Z/A$ and

$$\begin{aligned} W_{\mu\nu}^\pm &= \partial_\mu W_\nu^\pm - \partial_\nu W_\mu^\pm, \quad V_{\mu\nu} = \partial_\mu V_\nu - \partial_\nu V_\mu, \\ g_{WW\gamma} &= -g \sin\theta_W, \quad g_{WWZ} = -g \cos\theta_W, \\ g_{WWZZ} &= (g \cos\theta_W)^2, \quad g_{WWAA} = (g \sin\theta_W)^2, \quad g_{WWAZ/WWZA} = g^2 \sin\theta_W \cos\theta_W. \end{aligned} \quad (1.1.46)$$

There are no gauge couplings among only the neutral gauge bosons in the SM at tree level. However, higher order corrections can generate neutral triple gauge boson vertex and also can contribute to the existing tree level cubic and quartic gauge boson self couplings. Higher dimensional effective operators of the SM fields and new physics effect can produce triple and quartic gauge boson couplings beyond the SM tree level structures, which we will discuss in section 1.3.

1.1.1.c Higgs couplings

The Lagrangian \mathcal{L}_{Higgs} includes Higgs self couplings as well as Higgs to gauge boson couplings in the form:

$$\mathcal{L}_{Higgs(int)} = -\frac{m_h^2}{2\nu} h^3 - \frac{m_h^2}{8\nu^2} h^4 + m_W^2 W_\mu^- W^{+\mu} \left(\frac{2h}{\nu} + \frac{h^2}{\nu^2} \right) + \frac{1}{2} m_Z^2 Z_\mu Z^\mu \left(\frac{2h}{\nu} + \frac{h^2}{\nu^2} \right). \quad (1.1.47)$$

The Higgs (h) couples to the gauge bosons proportional to their masses. There are no hAA nor $hhAA$ couplings present in the SM, as the h has zero EM charge and should not couple to EM force carrier. Another way of looking the absence is that the photon is massless,

and hence its coupling to Higgs is zero. The fermion couples to the Higgs through the Lagrangian \mathcal{L}_{Yukawa} in the form:

$$\mathcal{L}_{Yukawa(int)} = -\frac{h}{v} [m_l \bar{l}_L l_R + m_q \bar{q}_L q_R]. \quad (1.1.48)$$

The Higgs to fermion couplings are also proportional to the fermion masses.

1.1.2 Summary of the SM

The SM beautifully accommodates the electroweak and the strong interactions under the $SU(3)_C \otimes SU(2)_L \otimes U(1)_Y$ gauge group predicting or explaining almost all the experimental facts. All the theoretical predictions of the SM, such as the weak neutral current; existence and masses of W and Z bosons; the existence of τ , c , b , and t were discovered at various colliders with spectacular accuracy. The particle spectrum of the SM got completed with the discovery of the last milestone, the Higgs boson, at the LHC in 2012. The ρ parameter (in Eq. (1.1.28)), predicted to be 1 by the SM, was confirmed with great accuracy at colliders. It receives a small perturbative correction, however, related to a broken $SU(2)_L \times SU(2)_R$ ‘‘custodial’’ symmetry of the Higgs potential [24]. However, the SM is believed to be not a complete theory for various issues, which are discussed in the next section.

1.2 Problems in the SM with possible solutions

Although the SM is a highly successful theory, it suffers various problems within the theoretical framework. It is also unable to explain many observed phenomena. The SM requires a large number of arbitrary free parameters (19 free parameters [25]), too much for a fundamental theory believed by most physicists. The other fundamental problems are discussed below.

Gauge problem The SM has three separate gauge couplings; they do not unify at high scale after running. We do not have an explanation for the electroweak part only being chiral. The SM includes but does not explain the charge quantization, i.e., why electric charges are multiple of $e/3$. One possible solution includes grand unified theory (GUT) which predicts the existence of magnetic monopole and decay of the proton (e.g., see Refs. [26, 27]) not observed yet.

Fermion problem The SM contains three generations of fermions, whereas e^- , u , d alone from the first generation make up all the visible matter in the Universe. There is no suitable explanation of the existence of the other heavier fermions. More ever, the mass of the fermions are input by hand or from the experiment; they do not originate from the SM. Possible solutions are given as an extension of the SM, such as the model of composite fermions, the model of radiative hierarchies where the fermion masses are generated at the loop-level [28, 29], model of extra dimension [30–32], etc.

Higgs mass hierarchy The Higgs mass gets divergent corrections from the top quark loop as

$$m_H^2 = (m_H^2)_0 + \mathcal{O}(\Lambda_{uv}^2), \quad (1.2.1)$$

where the Λ_{uv} is the energy scale of a ultraviolet complete theory, e.g., the Planck scale (or the grand unification scale). Thus, the natural scale of m_H is $\mathcal{O}(\Lambda_{uv})$, which is much larger than the observed values of $m_H = 125$ GeV. There must be an incredibly unnatural fine tuning to cancel the quadratic corrections to the tree level mass or bare mass. One solution could be to forget about the elementary Higgs field and consider the dynamical generation of mass: technicolor and composite Higgs model are in favour to this [33, 34]. Various other models of SM extension (e.g., extra dimension) also shed light on it. The most compelling solution is the supersymmetry (SUSY) for the hierarchy problem. In SUSY, each fermion and boson have their bosonic and fermionic superpartner: the quadratic divergent from the fermionic loop of the Higgs mass cancels way by the bosonic superpartner loop. The superpartners have not been observed yet, but not ruled out.

Strong CP problem In the current mathematical formulation of quantum chromodynamics (QCD), CP can be violated by including the term $\theta \times G_{\mu\nu} \tilde{G}^{\mu\nu}$ ($\tilde{G}_{\mu\nu} = 1/2 \epsilon_{\mu\nu\alpha\beta} G^{\alpha\beta}$ is the dual field) in to the Lagrangian. This would induce electric dipole moment to neutron (n), but the very small value of this put a stringent limit on θ to be $\mathcal{O}(10^{-10})$ [35]. Thus, QCD does not violate CP ; whereas, there is no explanation for that in the SM. There are several extensions of the SM to solve the strong CP problem. The most well-known solution is the Peccei–Quinn mechanism involving a new pseudo-scalar (imposing a $U(1)$ global symmetry) particle named axion [36, 37]. The axions are being searched at various experiments, but no evidence of its existence has been found yet [38, 39].

Neutrino oscillation In the SM, the neutrinos are massless. However, compelling evidences [40–44] are there for neutrino oscillation suggesting small neutrino mass and mixing. The SM does not provide any mechanism for neutrino mass and their mixing. The most popular mechanism for the small neutrino mass is the seesaw mechanism [45–47], where two or more right-handed neutrinos with large Majorana mass are assumed. The right-handed neutrino induces a very small mass to the left-handed neutrino reciprocal to the heavy mass. Many derivatives of the seesaw mechanism exist, such as type I, type II, inverse, etc [48] of which inverse seesaw mechanism has obtained great interest nowadays [49].

Dark matter To the current belief in accordance with astrophysical and cosmological data, dark matter (DM) is one of the main ingredients (about 26 %) of the Universe [50, 51]. The SM does not provide any fundamental particles that could be good dark matter candidates. There are plenty of models with extension to the SM postulating candidates for dark matter [52–54] with extra dimension [55], supersymmetry, axion, inverse seesaw [56], etc.

Baryogenesis The Universe is made out of mostly the matter (baryon). According to the SM, the matter and anti-matter should be present in equal amounts, resulting in zero baryon number. No sufficient mechanism exists in the SM to explain the matter dominance over anti-matter. One solution for this is to break baryon number symmetry in a GUT theory with mediating a massing X boson or heavy Higgs (H^0) boson [57].

The various models which address the issues of the problems mentioned above predict new particles along with new interactions. However, no new resonance beyond the SM has been observed until now at the current reach of energy. We could thus expect that the new physics, undoubtedly necessary, could be standing at a higher energy scale; these new physics may leave their footprint to the low energy available to us. They will modify the interactions among the SM particles or bring new interactions among them. Precision study of these modified or new interactions, which are called anomalous, in a way, could reveal new physics scenario. The anomalous interactions can be studied considering a given model and also can be modelled by higher dimensional effective operators formed by the SM fields, which goes by the name of effective field theory (EFT). Our aim here is to study the anomalous gauge boson couplings focusing on the EWSB. In the next section, we give a brief description of EFT for the anomalous gauge boson self-interactions with contributions from some of the BSM models.

1.3 EFT and anomalous gauge boson couplings

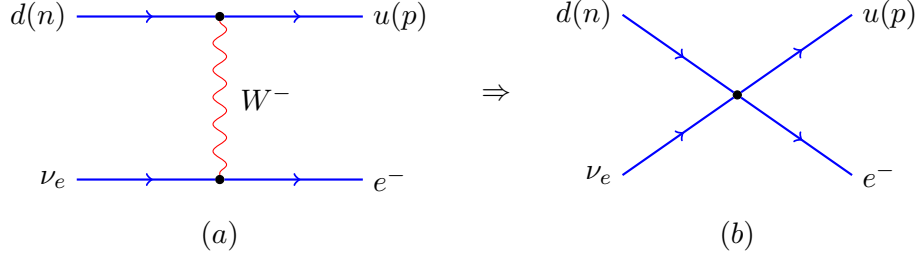


Figure 1.1. Beta decay ($d \rightarrow u$ conversion) with W^- (a) exchange and effective four-point interaction (b).

To begin with the EFT, let us start with the classic example of Fermi's theory of weak interaction (beta decay) at low energy. Fermi was able to describe the beta decay $n(udd) \rightarrow p(uud) + e^- + \bar{\nu}_e$ with high level accuracy with a four-point fermion interaction with a coupling constant G_F . The beta decay is proceeded via the exchange of the W^- boson at the symmetry breaking scale (VEV). In the low energy, the W^- can not be produced (extreme off-shell W^- is produced) and this interaction effectively boils down to a four-point contact interaction. The tree level amplitude for the diagram (a) in Fig. 1.1 is

$$\mathcal{M}_W = \left(\frac{-ig}{\sqrt{2}} \right) V_{ud} (\bar{u} \gamma^\mu P_L d) \left(\frac{-ig_{\mu\nu}}{p^2 - m_W^2} \right) (e^- \gamma^\nu P_L \nu_e) \quad (1.3.1)$$

with V_{ud} being the CKM mixing matrix element and p being the momentum transfer of the W^- propagator. In low energy, i.e., $p \ll m_W$, the W propagator can be expanded as,

$$\frac{1}{p^2 - m_W^2} = -\frac{1}{m_W^2} \left(1 + \frac{p^2}{m_W^2} + \frac{p^4}{m_W^4} + \dots \right) \quad (1.3.2)$$

with different order of expansion w.r.t p/m_W . Retaining only the first term, we obtain the amplitude in Eq. (1.3.1) as,

$$\mathcal{M}_W = \frac{i}{m_W^2} \left(\frac{-ig}{\sqrt{2}} \right) V_{ud} (\bar{u} \gamma^\mu P_L d) (e^- \gamma_\mu P_L \nu_e) + \mathcal{O}\left(\frac{1}{m_W^4}\right) \quad (1.3.3)$$

which resembles the amplitude for the four-point interaction vertex shown in Fig. 1.1(b) as [58],

$$\mathcal{M}_{4f} = -\frac{G_F}{\sqrt{2}} V_{ud} (\bar{u} \gamma^\mu (1 - \gamma_5) d) (e^- \gamma_\mu (1 - \gamma_5) \nu_e). \quad (1.3.4)$$

One can easily identify the Fermi constant (G_F) as,

$$\frac{G_F}{\sqrt{2}} \equiv \frac{g^2}{8m_W^2}. \quad (1.3.5)$$

Thus the effective Lagrangian

$$\mathcal{L} = \frac{-4G_F}{\sqrt{2}} V_{ud} (\bar{u}\gamma^\mu P_L d) (\bar{e}^- \gamma_\mu P_L \nu_e) \quad (1.3.6)$$

is the low energy limit of the SM. The EFT does not have the dynamical W ; however, the effect of W exchange in the SM is incorporated by the dimension-6 four-fermion operator. New physics beyond the SM can also provide the four-fermion contact interaction contributing to the Fermi constant G_F . Flavour changing processes such as $\mu \rightarrow e$ through weak current can also be parametrized by a four fermion contact interaction at low energy.

In EFT, one adds higher dimensional effective operators suppressed by an energy cut-off (Λ) with the SM fields and obtain the interactions after symmetry breaking [59]. Thus, EFT acts as a bridge between heavy scale new physics and low energy experimental observations. In EFT, there are two main approaches to follow: top-down and bottom-up. In the top-down approach, a high energy theory is known (GUT like), and the low energy effective operators are obtained by integrating out the heavy scale associated with the theory. This approach is thus, model dependent. The heavy scale gets encoded into the Wilson coefficient or the coupling constants of the remnant interactions. In the bottom-up approach, however, a fundamental theory at high energy is unknown, but one uses the known symmetry and particles of the SM and construct higher dimension operators to model the effects of new physics in a model independent way. In the above example, Fermi modelled the weak interaction by four-fermion contact interactions, which falls under the bottom-up approach. We integrated out the W boson to get the effective four-fermion operator at low energy, which falls under the top-down approach. In both the way, the effective Lagrangian incorporating the effective higher dimension operators is taken as,

$$\mathcal{L}_{eft} = \mathcal{L}_{SM} + \sum_{D \geq 4} \sum_i \frac{c_i^{(D)}}{\Lambda^{D-4}} \mathcal{O}_i^{(D)} \quad (1.3.7)$$

encapsulating all the desired operators ($\sum_i \mathcal{O}_i$) at given order (D) of Λ . Here, $c_i^{(D)}$ are the coefficients of the dimension- D operator $\mathcal{O}_i^{(D)}$. Avoiding the baryon number and lepton

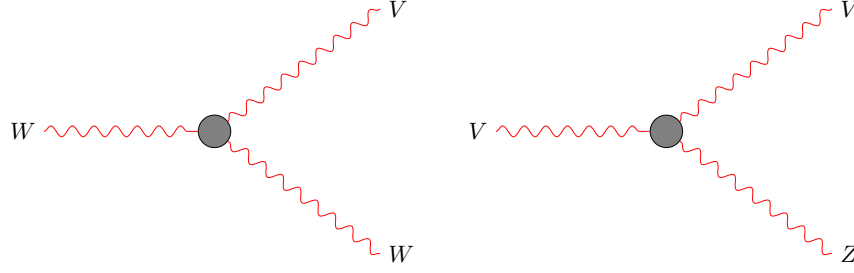


Figure 1.2. Triple gauge boson vertex with $V = Z/\gamma$. Anomalous contributions are shown by the shaded blob.

number violation the effective Lagrangian becomes [59]

$$\mathcal{L}_{eft} = \mathcal{L}_{SM} + \sum_i \frac{c_i^{(6)}}{\Lambda^2} \mathcal{O}_i^{(6)} + \sum_i \frac{c_i^{(8)}}{\Lambda^4} \mathcal{O}_i^{(8)} + \dots, \quad (1.3.8)$$

which encapsulates only the even order effective operators. As we go to higher and higher order, the effect of them become lower and lower in the low energy. Almost all of the studies available in literature contain operators only up to order Λ^{-4} , of which most of them contain only up to Λ^{-2} . A complete list of dimension-6 operators (a total of 80) respecting the SM gauge group has been given by Buchmuller *et al.* in Ref [59] in gauge sector, fermion sector, and gauge with fermions.

The kinetic terms of the gauge fields in the SM Lagrangian (Eq. (1.1.14)) generate interactions of triple gauge bosons WWV ($V = Z/\gamma$) and quartic gauge bosons $WWVV$ due to the non abelian nature of $SU(2)_L$ symmetry as given in Eqs. (1.1.44) & (1.1.45). There are no gauge boson vertices among the neutral gauge bosons, i.e., ZZZ , $ZZ\gamma$, $Z\gamma\gamma$, and $\gamma\gamma\gamma$ are not present in the SM. As we stated earlier, heavy scale new physics may induce new gauge boson vertices and also modify the SM gauge boson vertices through the effective higher dimension operators. The new or modified form factors (a function of the momentum of the gauge bosons) are called anomalous. In the SM, there could be some extra contributions to the gauge boson vertices through higher order loop corrections. For example, a triangular diagram with top-quark running in the loop can provide some of the anomalous triple gauge boson couplings. In this thesis, we focus on the study of the anomalous triple gauge boson vertices (see Fig. 1.2) in the charge sector as well as in the neutral sector with terms up to dimension-6 in a model independent way.

To the lowest order (i.e., upto dimension-6), the operators in HISZ basis [60] contributing

to WWV couplings, respecting the SM gauge symmetry, are [61, 62]

$$\begin{aligned}
\mathcal{O}_{WWW} &= \text{Tr}[W_{\mu\nu}W^{\nu\rho}W_{\rho}^{\mu}], \\
\mathcal{O}_W &= (\mathcal{D}_{\mu}\Phi)^{\dagger}W^{\mu\nu}(\mathcal{D}_{\nu}\Phi), \\
\mathcal{O}_B &= (\mathcal{D}_{\mu}\Phi)^{\dagger}B^{\mu\nu}(\mathcal{D}_{\nu}\Phi), \\
\mathcal{O}_{\widetilde{WWW}} &= \text{Tr}[\widetilde{W}_{\mu\nu}W^{\nu\rho}W_{\rho}^{\mu}], \\
\mathcal{O}_{\widetilde{W}} &= (\mathcal{D}_{\mu}\Phi)^{\dagger}\widetilde{W}^{\mu\nu}(\mathcal{D}_{\nu}\Phi),
\end{aligned} \tag{1.3.9}$$

where $\widetilde{W}^{\mu\nu}$ is the dual of $W^{\mu\nu}$ given by $\widetilde{W}_{\mu\nu} = 1/2\epsilon_{\mu\nu\rho\sigma}W^{\rho\sigma}$ ($\epsilon^{0123} = +1$). Among these operators \mathcal{O}_{WWW} , \mathcal{O}_W and \mathcal{O}_B are CP -even, while $\mathcal{O}_{\widetilde{WWW}}$ and $\mathcal{O}_{\widetilde{W}}$ are CP -odd. In the neutral sector, however, there are no dimension-6 operators contributing to the neutral triple gauge boson couplings ZVV ; they appear only at dimension-8. The dimension-8 operators in HISZ basis under the SM gauge group contributing to the anomalous ZVV are [63],

$$\begin{aligned}
\mathcal{O}_{BW} &= i\Phi^{\dagger}(B_{\mu\nu}/g')(W^{\mu\rho}/g)\{\mathcal{D}_{\rho}, \mathcal{D}^{\nu}\}\Phi, \\
\mathcal{O}_{WW} &= i\Phi^{\dagger}(W_{\mu\nu}W^{\mu\rho}/g^2)\{\mathcal{D}_{\rho}, \mathcal{D}^{\nu}\}\Phi, \\
\mathcal{O}_{BB} &= i\Phi^{\dagger}(B_{\mu\nu}B^{\mu\rho}/g'^2)\{\mathcal{D}_{\rho}, \mathcal{D}^{\nu}\}\Phi, \\
\mathcal{O}_{\widetilde{BW}} &= i\Phi^{\dagger}(\widetilde{B}_{\mu\nu}/g')(W^{\mu\rho}/g)\{\mathcal{D}_{\rho}, \mathcal{D}^{\nu}\}\Phi.
\end{aligned} \tag{1.3.10}$$

The first three operators are CP -odd; the last one is CP -even.

The above operators are invariant under the $SU(2) \otimes U(1)$ gauge group. In order to establish the SM couplings and/or to capture new physics irrespective of any symmetry, one has to go beyond the SM gauge symmetry. In this way, one can only consider the Lorentz invariance and $U(1)_{EM}$ symmetry to construct more general form factors as a function of the momentum involved in a given vertex. In the form factor formalism, the effective WWV and ZVV Lagrangian are given by [64],

$$\begin{aligned}
\mathcal{L}_{WWV} &= ig_{WWV} \left[g_1^V (W_{\mu\nu}^+ W^{-\mu} - W^{+\mu} W_{\mu\nu}^-) V^{\nu} + ig_4^V W_{\mu}^+ W_{\nu}^- (\partial^{\mu} V^{\nu} + \partial^{\nu} V^{\mu}) \right. \\
&\quad - ig_5^V \epsilon^{\mu\nu\rho\sigma} (W_{\mu}^+ \partial_{\rho} W_{\nu}^- - \partial_{\rho} W_{\mu}^+ W_{\nu}^-) V_{\sigma} + \frac{\lambda^V}{m_W^2} W_{\mu}^{+\nu} W_{\nu}^{-\rho} V_{\rho}^{\mu} \\
&\quad \left. + \frac{\widetilde{\lambda}^V}{m_W^2} W_{\mu}^{+\nu} W_{\nu}^{-\rho} \widetilde{V}_{\rho}^{\mu} + \kappa^V W_{\mu}^+ W_{\nu}^- V^{\mu\nu} + \widetilde{\kappa}^V W_{\mu}^+ W_{\nu}^- \widetilde{V}^{\mu\nu} \right]
\end{aligned} \tag{1.3.11}$$

and

$$\begin{aligned}
\mathcal{L}_{ZVV} = \frac{e}{m_Z^2} & \left[- \left[f_4^\gamma (\partial_\mu F^{\mu\beta}) + f_4^Z (\partial_\mu Z^{\mu\beta}) \right] Z_\alpha (\partial^\alpha Z_\beta) + \left[f_5^\gamma (\partial^\sigma F_{\sigma\mu}) + f_5^Z (\partial^\sigma Z_{\sigma\mu}) \right] \widetilde{Z}^{\mu\beta} Z_\beta \right. \\
& - \left[h_1^\gamma (\partial^\sigma F_{\sigma\mu}) + h_1^Z (\partial^\sigma Z_{\sigma\mu}) \right] Z_\beta F^{\mu\beta} - \left[h_3^\gamma (\partial_\sigma F^{\sigma\rho}) + h_3^Z (\partial_\sigma Z^{\sigma\rho}) \right] Z^\alpha \widetilde{F}_{\rho\alpha} \\
& - \left\{ \frac{h_2^\gamma}{m_Z^2} \left[\partial_\alpha \partial_\beta \partial^\rho F_{\rho\mu} \right] + \frac{h_2^Z}{m_Z^2} \left[\partial_\alpha \partial_\beta (\square + m_Z^2) Z_\mu \right] \right\} Z^\alpha F^{\mu\beta} \\
& + \left\{ \frac{h_4^\gamma}{2m_Z^2} \left[\square \partial^\sigma F^{\rho\alpha} \right] + \frac{h_4^Z}{2m_Z^2} \left[(\square + m_Z^2) \partial^\sigma Z^{\rho\alpha} \right] \right\} Z_\sigma \widetilde{F}_{\rho\alpha} \Big], \tag{1.3.12}
\end{aligned}$$

respectively. In the SM $g_1^V = 1$, $\kappa^V = 1$ and other couplings are zero, see Eq. (1.1.44). In the charge sector, the couplings g_1^V , κ^V and λ^V are CP -even (both C and P -even), while g_4^V (odd in C , even in P), $\widetilde{\kappa}^V$ and $\widetilde{\lambda}^V$ (even in C , odd in P) are CP -odd. The g_5^V is, however, both C and P -odd making it CP -even. In the neutral sector, the couplings f_4^V , h_1^V , h_2^V correspond to the CP -odd form factors, while f_5^V , h_3^V , h_4^V correspond to the CP -even ones. We note that although the Lagrangian in Eq. (1.3.12) provides a $Z\gamma\gamma$ couplings as given in Fig. 1.2, this does not appear in a two on-shell photons production process as it is forbidden by Yang-Landau theorem [65, 66].

The couplings of the form factors in Eq. (1.3.11) & Eq. (1.3.12) are related to the couplings of the operators in Eq. (1.3.9) & Eq. (1.3.10), respectively when $SU(2) \otimes U(1)$ gauge invariance is assumed. The relations between form factor couplings and operator couplings in the charge sector are given by [61, 62, 67],

$$\begin{aligned}
\Delta g_1^Z &= c_W \frac{m_W^2}{2\Lambda^2}, \\
g_4^V &= g_5^V = \Delta g_1^\gamma = 0, \\
\lambda^\gamma &= \lambda^Z = \lambda^V = c_{WWW} \frac{3g^2 m_W^2}{2\Lambda^2}, \\
\widetilde{\lambda}^\gamma &= \widetilde{\lambda}^Z = \widetilde{\lambda}^V = c_{\widetilde{WWW}} \frac{3g^2 m_W^2}{2\Lambda^2}, \\
\Delta \kappa^\gamma &= (c_W + c_B) \frac{m_W^2}{2\Lambda^2}, \\
\Delta \kappa^Z &= (c_W - c_B \tan^2 \theta_W) \frac{m_W^2}{2\Lambda^2}, \\
\widetilde{\kappa}^\gamma &= c_{\widetilde{W}} \frac{m_W^2}{2\Lambda^2}, \\
\widetilde{\kappa}^Z &= -c_{\widetilde{W}} \tan^2 \theta_W \frac{m_W^2}{2\Lambda^2}. \tag{1.3.13}
\end{aligned}$$

It is clear from above that some of the vertex factor couplings are dependent on each others in the SM gauge symmetry and they are

$$\begin{aligned}\Delta g_1^Z &= \Delta k^Z + \tan^2 \theta_W \Delta k^\gamma, \\ \tilde{\kappa}^Z + \tan^2 \theta_W \tilde{\kappa}^\gamma &= 0 .\end{aligned}\tag{1.3.14}$$

In the neutral sector the relations are [63]

$$\begin{aligned}\frac{f_5^Z}{m_Z^2} &= 0, \\ \frac{f_5^\gamma}{m_Z^2} &= \frac{v^2}{4c_w s_w} \frac{C_{\tilde{B}W}}{\Lambda^4}, \\ \frac{f_4^Z}{m_Z^2} &= \frac{v^2 (c_w^2 C_{WW} + 2c_w s_w C_{BW} + 4s_w^2 C_{BB})}{2c_w s_w \Lambda^4}, \\ \frac{f_4^\gamma}{m_Z^2} &= -\frac{v^2 (-c_w s_w C_{WW} + C_{BW} (c_w^2 - s_w^2) + 4c_w s_w C_{BB})}{4c_w s_w \Lambda^4}\end{aligned}\tag{1.3.15}$$

and

$$\begin{aligned}\frac{h_3^Z}{m_Z^2} &= \frac{v^2}{4c_w s_w} \frac{C_{\tilde{B}W}}{\Lambda^4}, \\ h_4^Z &= h_3^\gamma = h_4^\gamma = h_2^Z = h_2^\gamma = 0, \\ \frac{h_1^Z}{m_Z^2} &= \frac{v^2 (-c_w s_w C_{WW} + C_{BW} (c_w^2 - s_w^2) + 4c_w s_w C_{BB})}{4c_w s_w \Lambda^4}, \\ \frac{h_1^\gamma}{m_Z^2} &= -\frac{v^2 (s_w^2 C_{WW} - 2c_w s_w C_{BW} + 4c_w^2 C_{BB})}{4c_w s_w \Lambda^4}\end{aligned}\tag{1.3.16}$$

with the relation

$$f_5^\gamma = h_3^Z \quad \text{and} \quad h_1^Z = -f_4^\gamma.\tag{1.3.17}$$

Here v is the VEV and $c_w = \cos \theta_W$, $s_w = \sin \theta_W$.

One can follow both effective operator approach and effective vertex approach to study the anomalous gauge boson couplings. We follow both the approach for studying the charge sector couplings; while, we study only the vertex factors in the neutral sector. In this thesis, we restrict ourselves to only dimension-6 operators or form factors with a partial contribution up to Λ^{-4} . We take the quadratic contribution of dimension-6 form factors/ operators to compare our results with current LHC constraints.

1.3.1 BSM contributions to aTGC

In the top down approach of the EFT, one has a high scale model which may provide triple gauge boson couplings in the low energy through loops. Some simplified fermionic models [68], the Minimal Supersymmetric SM (MSSM) [69, 70] and Little Higgs model [71] provide some of the CP -even structure of the neutral aTGC. Some CP -odd couplings in the neutral sector can be generated in the MSSM [69] (at two loops), in complex two Higgs doublet model (C2HDM) [68, 72, 73]. Besides these, a non-commutative extension of the SM (NCSM) [74, 75] can also provide an anomalous coupling structure in the neutral sector with a possibility of a trilinear $\gamma\gamma\gamma$ coupling as well [74]. In the charge sector, aTGC may be obtained in MSSM [76–78], extra dimension [79, 80], Georgi-Machacek model [81], etc. by integrating out the heavy degrees of freedom.

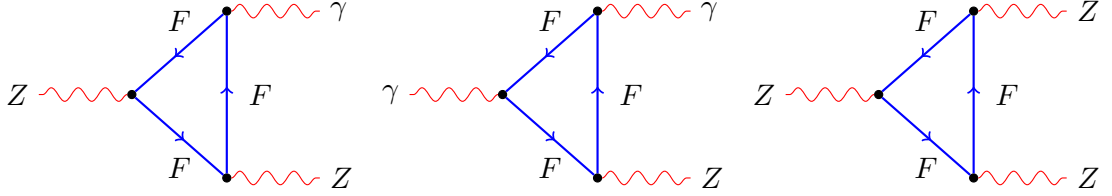


Figure 1.3. Triangular diagram with a heavy fermion F contributing to neutral aTGC.

We discuss some of the explicit models providing some of the aTGC. As a simplest example, a heavy fermion in a toy model can contribute to some of the triple gauge boson couplings in the neutral sector. For example, the Lagrangian [82]

$$\mathcal{L}_{VF\bar{F}} = -eQ_F A^\mu \bar{F} \gamma_\mu F - \frac{e}{2s_w c_w} Z^\mu \bar{F} (\gamma_\mu g_{VF} - \gamma_\mu \gamma_5 g_{AF}) F \quad (1.3.18)$$

with a heavy fermion F can generate f^γ , f^Z , h_3^γ and h_3^Z couplings in the Lagrangian \mathcal{L}_{ZVV} in Eq. (1.3.12) through the triangular diagrams shown in Fig. 1.3 with the F running in loops. The contributions to aTGC are [82]

$$h_3^Z = -f_5^\gamma = -N_F \frac{e^2 Q_F g_{VF} g_{AF}}{96\pi^2 s_w^2 c_w^2} \frac{m_Z^2}{m_F^2}, \quad (1.3.19)$$

$$h_3^\gamma = -N_F \frac{e^2 Q_F g_{AF}}{48\pi^2 s_w c_w} \frac{m_Z^2}{m_F^2}, \quad (1.3.20)$$

$$f_5^Z = -N_F \frac{e^2 g_{AF} (5g_{VF}^2 + g_{AF}^2)}{960\pi^2 s_w^3 c_w^3} \frac{m_Z^2}{m_F^2}. \quad (1.3.21)$$

Here Q_F is the electric charge, m_F is the mass of F , N_F is the number of flavour. Other

couplings are zero in this model. The heavy fermion, if associates with a iso-spin partner to form a $SU(2)$ doublet, will provide WWZ and $WW\gamma$ couplings as well.

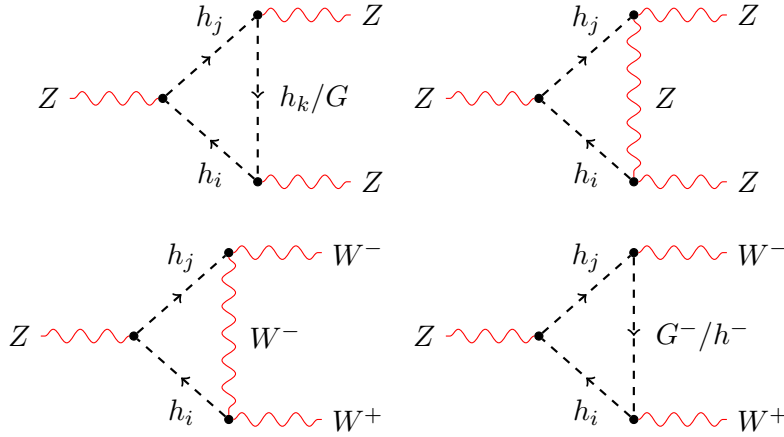


Figure 1.4. Contributions to anomalous ZZZ (*upper-row*) and WWZ (*lower-row*) vertex from 2HDM with $i \neq j \neq k$ in *left-top* and $i \neq j$ for rest.

The two-Higgs-doublet model (2HDM) is another example of a detail and renormalizable model containing the SM where the anomalous ZZZ vertex along with WWZ vertex can be generated [68, 72, 73]. The Feynman diagrams in Fig. 1.4 with the neutral Higgs bosons (h_i , $i = 1, 2, 3$) or Goldstone boson (G), after integrated out, will provide ZZZ (CP -even/odd, *upper-row*) and WWZ vertex (*lower-row*). In another example, anomalous WWZ and $WW\gamma$ vertices ($\Delta\kappa^V$ in particular) can be generated at loop level in a universal extra dimension (UED) from the Feynman diagrams given in Fig. 1.5 with the Kaluza–Klein (KK) excited modes ($A^{(n)}/Z^{(n)}/W^{(n)}/H^{(n)}/h^{(n)}/f_i^{(n)}$) running in loops as discussed in Ref. [80].

1.3.2 Probe of the aTGC

It is important to probe the aTGC for the precision measurements in a collider. The aTGC predominantly appear in various di-boson ($ZZ/Z\gamma/WW/WZ$) production processes; a detailed and careful study of these processes may reveal new physics through probing the aTGC. The aTGC not only change the total cross section in those processes, they affect the distribution of various kinematical variables, such as transverse momentum, invariant mass, etc. They also modify the angular distributions of the daughter particles of the final state gauge bosons. Some of the asymmetries based on the angular distribution of the decay products are related to the various polarizations of the gauge bosons. So, by studying the cross sections, distribution of kinematical variables, polarizations of gauge bosons, angular asymmetries of the decay products, etc., one could probe the aTGC in a particle collider. There has been a lot of studies of the aTGC in the neutral sector [82–106] as well as in

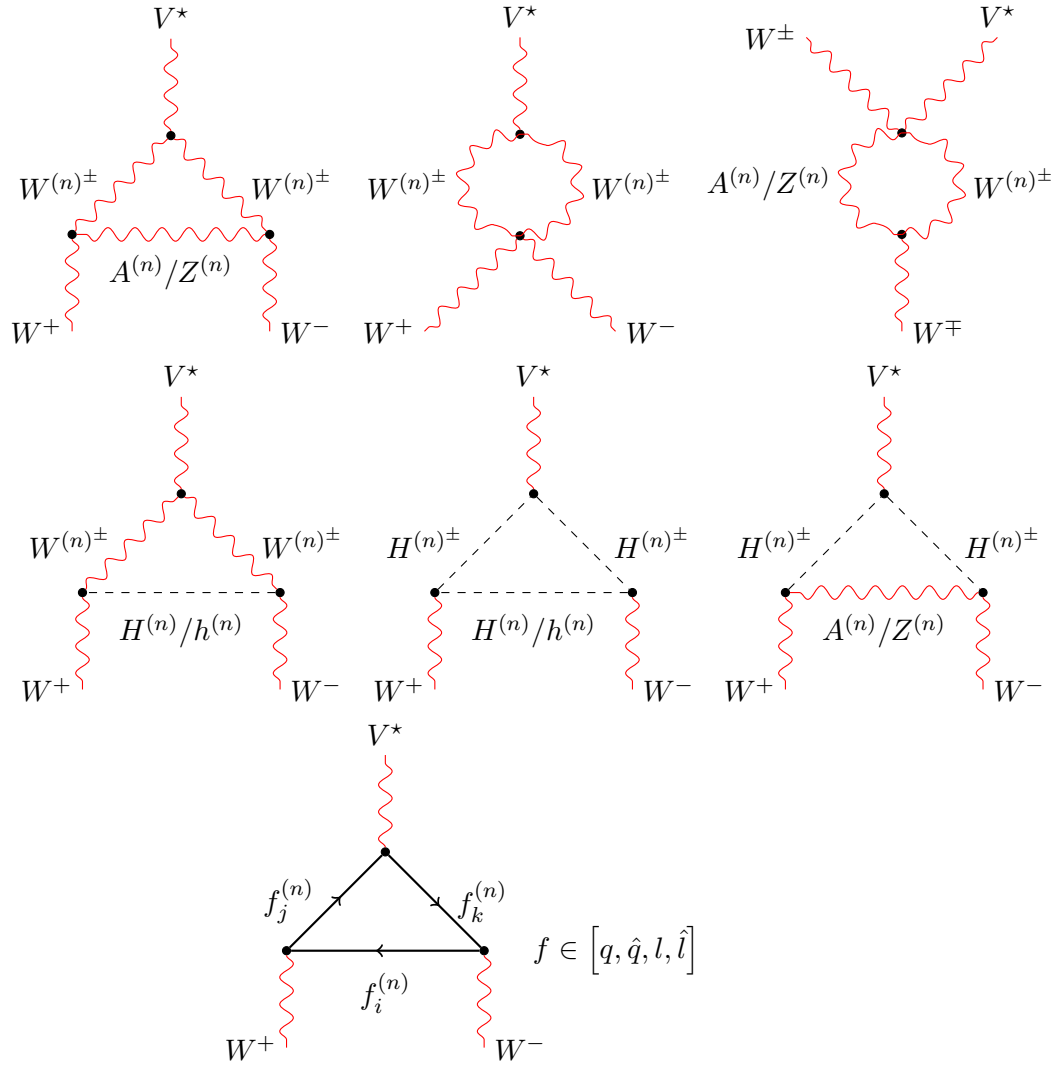


Figure 1.5. Contributions to anomalous WWV^* ($V = Z/\gamma$) vertex with off-shell V in a universal extra dimension.

the charge sector [64, 102, 107–114, 114, 115, 115–132] in different processes. The direct measurements of the aTGC have been performed at various colliders for neutral sector in Refs. [133–148] and for the charge sectors in Refs. [143, 149–170].

1.4 Outline of the thesis

We organise the rest of the thesis as follows: We employ the polarizations of the gauge boson involved in the anomalous couplings along with the cross sections to study the aTGC. First, we introduce the polarization observables of a general spin-1 particle in chapter 2. The thesis then divided into two parts on the basis of neutral aTGC and charged aTGC. First, we study the neutral aTGC, and then we move on to the charged aTGC. In chapter 3, we study the sensitivities of the polarization observables to the aTGC in the neutral sector and obtain limits

on them in $ZZ/Z\gamma$ productions in a e^+e^- collider. In chapter 4, we examine the effect of beam (e^+ , e^-) polarizations on the sensitivity of observables to aTGC in the same processes of $e^+e^- \rightarrow ZZ/Z\gamma$. In chapter 5, we restrict to ZZ production process at the LHC and investigate the role of Z polarizations. Next in chapter 6, we study the WWV anomalous couplings in $e^+e^- \rightarrow W^+W^-$ process by employing the W polarizations along with the beam polarizations. In chapter 7, we study the WWZ anomalous couplings in $W^\pm Z$ production at the LHC and investigate the role of Z and reconstructed W polarizations. We conclude in chapter 8 followed by the outlooks of the thesis. We keep some important supplementary materials in the appendices for completeness of the main chapters. In appendix A, we give some of the Feynman rules of the electroweak theory necessary for the chapters. In appendix B, we give the helicity amplitudes in $e^+e^- \rightarrow ZZ/Z\gamma$ process for SM+aTGC along with the expressions for observables. The semi-analytic expressions for the observables in ZZ production are given in appendix C. The helicity amplitudes for SM+aTGC in $e^+e^- \rightarrow W^+W^-$ process are given in appendix D. In appendix E, we give the SM values of the asymmetries and corresponding polarizations along with the numerical fitting procedures for them in ZW^\pm production process. In appendix F, we give some brief descriptions of some HEP packages that we have used in this thesis.

2 Polarization parameters of spin-1 particles

Contents

2.1 Polarization density matrix	26
2.2 Polarization asymmetries	34
2.3 Spin-spin correlations	39
2.4 Summary	40

The cross section of a process is an important observable to detect new physics through excess rate compared to the SM or through new resonance. Kinematical distributions and cuts may increase the signal to background ratio for a new physics. But the cross section may not be sensitive to some new physics parameters or may not be sufficient when a large number of new physics parameters have to be measured. In this scenario, one needs as many observables as possible.

One can construct observables related to the polarizations of a particle and use them along with total rate and other kinematical observables to study new physics. A spin- s particle offers a total of $(2s + 1)^2 - 1 = 4s(s + 1)$ observables related to polarizations of the particle. The polarization density matrix of the spin- s particle is a $(2s + 1) \times (2s + 1)$ hermitian, unit-trace matrix that can be parametrized by $4s(s + 1)$ real parameters. These parameters are different kinds of polarizations. For example, a spin-1/2 fermion has three polarization parameters called longitudinal, transverse, and normal polarizations (see for example [171, 172]). Similarly, for a spin-1 particle we have a total of eight such parameters [98, 149, 172–176]; three of them are vectorial like in the spin-1/2 case and the other five are tensorial [172, 175] as will be described in Section 2.1 in detail. These polarization parameters can be calculated analytically from the production process as well as from the angular asymmetries

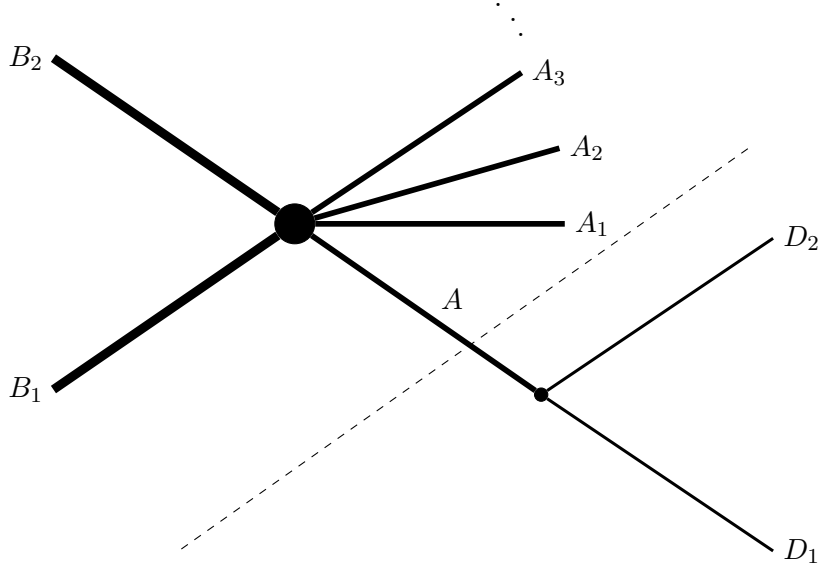


Figure 2.1. Schematic diagram for the production of a particle A and its decay to D_1 and D_2 . The dashed line separates the production part and the decay part.

of the decayed products of the particle.

The polarization observables of spin-1 particles have been used earlier to study new physics. The polarization asymmetries of Z and W were used to study the anomalous gauge boson couplings [98, 99, 106, 118, 149, 177, 178], Higgs-gauge boson interaction [176, 179], FCNC interaction [180], dark matter [181], the top quark mass structure [182, 183], special interactions of massive particles [184, 185], and dark matter along with heavy resonance [186]. In the next sections, we discuss the polarizations of a general spin- s particle with special focus on the spin-1 case.

2.1 Polarization density matrix

To begin with, let us consider the production and decay of an unstable particle A of spin- s in a general process of $B_1 B_2 \rightarrow A A_1 A_2 \dots A_{n-1}$ with $A \rightarrow D_1 D_2$, as shown in Fig. 2.1. The differential rate for such a process is given by [172],

$$\begin{aligned}
 d\sigma &= \sum_{\lambda, \lambda'} \left[\frac{1}{I_{B_1 B_2}} \rho'(\lambda, \lambda') (2\pi)^4 \delta^4 \left(p_{B_1} + p_{B_2} - p_A - \sum_i^{n-1} p_{A_i} \right) \frac{d^3 p_A}{(2\pi)^3 2E_A} \prod_i^{n-1} \frac{d^3 p_{A_i}}{(2\pi)^3 2E_{A_i}} \right] \\
 &\times \left[\frac{1}{\Gamma_A} \frac{(2\pi)^4}{2m_A} \Gamma'(\lambda, \lambda') \delta^4 (p_A - p_{D_1} - p_{D_2}) \frac{d^3 p_{D_1}}{(2\pi)^3 2E_{D_1}} \frac{d^3 p_{D_2}}{(2\pi)^3 2E_{D_2}} \right] \quad (2.1.1)
 \end{aligned}$$

after using the narrow width approximation of the unstable particle A , allowing the factoring out the production part (1^{st} square-bracket) from the decay (2^{nd} square-bracket). Here, the flux factor $I_{B_1 B_2}$ is given by $I_{B_1 B_2} = 4\sqrt{(p_{B_1} \cdot p_{B_2})^2 - m_{B_1}^2 m_{B_2}^2}$, Γ_A is the total decay width of A with $\Gamma_A \ll m_A$, m_i are the mass of i^{th} particles. The λ and λ' are the helicities of the particle A and they are given by $\lambda, \lambda' \in \{-s, -s+1, \dots, s\}$. The helicities of the particles A_i are suppressed, i.e., helicities are summed over the remaining final state particle and averaged over the initial particles. The phase-space integration can be performed in any reference frame without any loss of generality. To get the decay distribution of A , we perform the phase-space integration in the rest frame of A . We integrate the production part in the first square bracket in Eq. (2.1.1) and expresses it as,

$$\rho(\lambda, \lambda') = \frac{1}{I_{B_1 B_2}} \int \rho'(\lambda, \lambda') (2\pi)^4 \delta^4 \left(p_{B_1} + p_{B_2} - p_A - \sum_i^{n-1} p_{A_i} \right) \frac{d^3 p_A}{(2\pi)^3 2E_A} \prod_i^{n-1} \frac{d^3 p_{A_i}}{(2\pi)^3 2E_{A_i}}, \quad (2.1.2)$$

with $\rho'(\lambda, \lambda') = \mathcal{M}(\lambda) \mathcal{M}^\dagger(\lambda')$, $\mathcal{M}(\lambda)$ being the helicity amplitude with helicity λ . The $\rho(\lambda, \lambda')$, which is a $(2s+1) \times (2s+1)$ matrix, is called the production density matrix. The total integrated production cross section, without any cuts, will be given by the sum of diagonal terms, i.e.,

$$\sigma_A = \text{Tr}[\rho(\lambda, \lambda')] = \sum_\lambda \rho(\lambda, \lambda). \quad (2.1.3)$$

Only the diagonal elements enter into the total rate, while all the elements in certain combinations have the information for the polarizations of the particle. Thus the normalized production density matrix will contain only the information of polarizations of the particle and can be equated to the spin density matrix (SDM) of spin- s particles. We rewrite $\rho(\lambda, \lambda') = \sigma_A P_A(\lambda, \lambda')$, $P_A(\lambda, \lambda')$ is the polarization density matrix. In a similar way, we can integrate the decay part in second square bracket in Eq. (2.1.1) and write it as,

$$\begin{aligned} & \int \frac{1}{\Gamma_A} \frac{(2\pi)^4}{2m_A} \Gamma'(\lambda, \lambda') \delta^4(p_A - p_{D_1} - p_{D_2}) \frac{d^3 p_{D_1}}{(2\pi)^3 2E_{D_1}} \frac{d^3 p_{D_2}}{(2\pi)^3 2E_{D_2}} \\ &= \frac{B_{D_1 D_2} (2s+1)}{4\pi} \Gamma_A(\lambda, \lambda') d\Omega_{D_i}, \quad i = 1, 2, \end{aligned} \quad (2.1.4)$$

where $B_{D_1 D_2}$ is the branching fraction for $A \rightarrow D_1 D_2$. The matrix $\Gamma_A(\lambda, \lambda')$ is the decay density matrix normalized to unit trace; $d\Omega_{D_i} = \sin \theta_{D_i} d\theta_{D_i} d\phi_{D_i}$ is the measure of solid angle of the daughter D_1/D_2 . Now, combining the production density matrix in Eq. (2.1.2) and the decay density matrix in Eq. (2.1.4), the decay angular distribution of either of the daughter

D_1/D_2 becomes

$$\frac{1}{\sigma} \frac{d\sigma}{d\Omega_{D_i}} = \frac{2s+1}{4\pi} \sum_{\lambda, \lambda'} P_A(\lambda, \lambda') \Gamma_A(\lambda, \lambda'), \quad (2.1.5)$$

where $\sigma = \sigma_A B_{D_1 D_2}$ is the total cross section for the whole process. Below, we discuss the polarization density matrix in terms of SDM.

An SDM represents a state of an ensemble of particles. To understand a SDM, let us begin with a pure quantum mechanical spin state of a spin- s particle which can be expressed as,

$$|\Psi_s\rangle = \sum_{\lambda=-s}^s c_\lambda |s, s_z = \lambda\rangle. \quad (2.1.6)$$

In this spin state, the mean value of an arbitrary operator \hat{A} will be given by,

$$\langle \hat{A} \rangle_{\Psi_s} = \langle \Psi_s | \hat{A} | \Psi_s \rangle = \sum_{\lambda, \lambda'} c_{\lambda'}^* A_{\lambda, \lambda'} c_\lambda, \quad (2.1.7)$$

where $A_{\lambda, \lambda'}$ is the matrix element in the given helicity basis. For a non-pure state (e.g., state in scattering processes) with incoherent mixture of some pure state $|\Psi^{(i)}\rangle$ each with a probability $p^{(i)}$ ($\sum_i p^{(i)} = 1$), the mean value of \hat{A} will be given by,

$$\langle \hat{A} \rangle_{\Psi_s} = \sum_{\lambda, \lambda'} A_{\lambda, \lambda'} \sum_i p^{(i)} c_{\lambda'}^{(i)*} c_\lambda^{(i)}. \quad (2.1.8)$$

The SDM of the non-pure ensemble is thus

$$\rho_s(\lambda, \lambda') = \sum_i p^{(i)} c_{\lambda'}^{(i)*} c_\lambda^{(i)}. \quad (2.1.9)$$

This density matrix has unit trace, i.e.

$$\sum_\lambda \rho_s(\lambda, \lambda) = 1; \quad (2.1.10)$$

it is a hermitian matrix, i.e.

$$\rho_s^*(\lambda, \lambda') = \rho_s(\lambda', \lambda); \quad (2.1.11)$$

the diagonal elements are positive semi-definite, i.e.

$$\rho_s(\lambda, \lambda) \geq 0. \quad (2.1.12)$$

A number of $(2s+1)^2 - 1$ real parameters can completely specify the unit traced hermitian

density matrix ρ_s .

The SDM can be expressed with irreducible spin tensors up to rank $2s$, i.e., identity matrix, linear (spin-1/2), bilinear (spin-1), trilinear (spin-3/2) combinations of standard spin matrices. The SDM can be represented in terms of spherical tensor operators or can be given in Cartesian form. The properties of the density matrix will then be specified by the expansion coefficients. In the spherical tensor form, the SDM can be expanded as [173],

$$\rho_s = \frac{1}{2s+1} \sum_{L,M} (2L+1) (t_M^L)^* T_M^L, \quad (2.1.13)$$

where T_L^M is the spherical tensor operator with rank L satisfying $0 \leq L \leq 2s$, $-L \leq M \leq L$; t_L^M are multi-pole parameters which are generalization of the vector polarizations. We, however, are interested in the Cartesian form of SDM. In Cartesian system, the SDM of spin-1/2 particles, which is 2×2 , can always be expressed as,

$$\rho_{1/2} = \frac{1}{2} (\mathbb{I}_{2 \times 2} + \vec{p} \cdot \vec{\sigma}), \quad (2.1.14)$$

where σ_i are the Pauli spin matrices (Eq. (A.0.1)). The \vec{p} represents the mean polarization of the ensemble, i.e.,

$$\vec{p} = \text{Tr}[\rho_{1/2} \vec{\sigma}]. \quad (2.1.15)$$

For spin-1 particles, the SDM can be expressed, with 3×3 identity matrix and linear combination along with a spin-tensor with bilinear combinations of spin-1 matrices, as [172, 173],

$$\rho_1(\lambda, \lambda') = \frac{1}{3} \left[\mathbb{I}_{3 \times 3} + \frac{3}{2} \vec{p} \cdot \vec{S} + \sqrt{\frac{3}{2}} T_{ij} (S_i S_j + S_j S_i) \right], \quad (2.1.16)$$

where S_i are the spin basis for spin-1 given by,

$$S_x = \frac{1}{\sqrt{2}} \begin{pmatrix} 0 & 1 & 0 \\ 1 & 0 & 1 \\ 0 & 1 & 0 \end{pmatrix}, \quad S_y = \frac{i}{\sqrt{2}} \begin{pmatrix} 0 & -1 & 0 \\ 1 & 0 & -1 \\ 0 & 1 & 0 \end{pmatrix}, \quad S_z = \begin{pmatrix} 1 & 0 & 0 \\ 0 & 0 & 0 \\ 0 & 0 & -1 \end{pmatrix}. \quad (2.1.17)$$

Here $\vec{p} = \{p_x, p_y, p_z\}$ is a 3-component vector and the T_{ij} are the elements of a 2^{nd} -rank symmetric traceless tensor, i.e.,

$$T_{ij} = T_{ji}, \quad \sum_i T_{ii} = 0 \quad (2.1.18)$$

leading to five independent elements. The parameters p_i and T_{ij} are all real and independent of each other. We note that the tensor part here, in Eq. (2.1.16), is absent for spin-1/2 case since $\sigma_i\sigma_j + \sigma_j\sigma_i = 2\delta_{ij}\mathbb{I}_{2\times 2}$ and $\sum_i T_{ii}\sigma_i^2 = 0$. Likewise, any higher rank (e.g., rank-3 $T_{ijk}S_iS_jS_k$) tensor evaluate to zero due to spin-1 symmetry. The multi-pole parameters in the spherical tensor operator representation of the SDM can be related to the Cartesian vector and tensor polarizations. The \vec{p} measures the mean spin vector as,

$$\vec{p} = \langle \hat{s} \rangle \quad (2.1.19)$$

and T_{ij} measures the mean rank-2 spin tensor as,

$$T_{ij} = \frac{1}{2} \sqrt{\frac{3}{2}} \left\{ \langle \hat{s}_i \hat{s}_j + \hat{s}_j \hat{s}_i \rangle - \frac{4}{3} \delta_{ij} \right\}. \quad (2.1.20)$$

Thus, three p_i are the vector polarizations and five T_{ij} are the tensor polarizations of a spin-1 particle. The degrees of vector polarization \vec{p} , and tensor polarization T , are

$$p = \sqrt{\vec{p}^2}; \quad 0 \leq p \leq 1 \quad (2.1.21)$$

and

$$T = \sqrt{\sum_{ij} (T_{ij})^2}; \quad 0 \leq T \leq 1. \quad (2.1.22)$$

The overall degree of polarization, which is proportional to it's distance to the unpolarized state, is given by,

$$\begin{aligned} d_{pol.} &= \frac{1}{\sqrt{2s}} \sqrt{(2s+1)\text{Tr}[\rho_s^2] - 1}, \\ &= \sqrt{\frac{3}{4}p^2 + T^2} (\leq 1). \end{aligned} \quad (2.1.23)$$

For an example, if the particle is such that it's spin is quantized along the z -axis and p_+ , p_0 , p_- be the probabilities of finding the particle with spin projections 1, 0, -1 , respectively along the quantization axis, then the measure of polarizations would be

$$p_x = p_y = 0, \quad p_z = (p_+ - p_-), \quad T_{ij} = 0 \text{ if } i \neq j, \quad T_{xx} = T_{yy} = -\frac{1}{2}T_{zz}, \quad T_{zz} = \frac{1}{\sqrt{6}}(1 - 3p_0). \quad (2.1.24)$$

The degrees of vector and tensor polarizations are then given by¹,

$$p = |p_+ - p_-|, \quad T = \frac{1}{2}|1 - 3p_0|. \quad (2.1.25)$$

For spin-3/2 case, the 4×4 SDM can be expressed in the Cartesian basis extending the spin-1 SDM by a 3-rank tensor with spin-3/2 matrices as [187],

$$\rho_{3/2} = \frac{1}{4} \left[\mathbb{I}_{4 \times 4} + 4\vec{p} \cdot \vec{\Sigma} + \frac{4}{3} T_{ij}^{(2)} \Sigma_{ij} + \frac{4}{3} T_{ijk}^{(3)} \Sigma_{ijk} \right] \quad (2.1.26)$$

with

$$\Sigma_{ij} = \frac{1}{2} (\Sigma_i \Sigma_j + \Sigma_j \Sigma_i) - \frac{5}{4} \delta_{ij}, \quad (2.1.27)$$

$$\begin{aligned} \Sigma_{ijk} = \frac{1}{6} & \left[(\Sigma_i \Sigma_j \Sigma_k + \Sigma_i \Sigma_k \Sigma_j + \Sigma_j \Sigma_i \Sigma_k + \Sigma_j \Sigma_k \Sigma_i + \Sigma_k \Sigma_i \Sigma_j + \Sigma_k \Sigma_j \Sigma_i) \right. \\ & \left. - \frac{5}{12} (\delta_{ij} \Sigma_k + \delta_{jk} \Sigma_i + \delta_{ki} \Sigma_j) \right]. \end{aligned} \quad (2.1.28)$$

Here, $T^{(2)}$ and $T^{(3)}$ are the rank-2 and rank-3 spin tensors, respectively related to the tensor polarizations. The spin-3/2 matrices, Σ_i are given by,

$$\begin{aligned} \Sigma_x &= \frac{1}{2} \begin{pmatrix} 0 & \sqrt{3} & 0 & 0 \\ \sqrt{3} & 0 & 2 & 0 \\ 0 & 2 & 0 & \sqrt{3} \\ 0 & 0 & \sqrt{3} & 0 \end{pmatrix}, \quad \Sigma_y = \frac{i}{2} \begin{pmatrix} 0 & -\sqrt{3} & 0 & 0 \\ \sqrt{3} & 0 & -2 & 0 \\ 0 & 2 & 0 & -\sqrt{3} \\ 0 & 0 & \sqrt{3} & 0 \end{pmatrix}, \\ \Sigma_z &= \frac{1}{2} \begin{pmatrix} 3 & 0 & 0 & 0 \\ 0 & 1 & 0 & 0 \\ 0 & 0 & -1 & 0 \\ 0 & 0 & 0 & -3 \end{pmatrix}. \end{aligned} \quad (2.1.29)$$

The degree of polarization can be calculated similar to the case of spin-1 case, see Ref. [187] for details.

We now focus on the case of a spin-1 particle; let us call it V . The production density matrix of the spin-1 particle (V), when normalized, contains only the information of polarizations of the particle, thus can be equated to its SDM given in Eq. (2.1.16). The normalized

¹Although p and T are independent, they have their upper limit according to Eq. (2.1.23)

production density matrix is called the polarization density matrix which takes the form

$$\rho_1(\lambda, \lambda') = P_V(\lambda, \lambda') = \begin{bmatrix} \frac{1}{3} + \frac{p_z}{2} + \frac{T_{zz}}{\sqrt{6}} & \frac{p_x - ip_y}{2\sqrt{2}} + \frac{T_{xz} - iT_{yz}}{\sqrt{3}} & \frac{T_{xx} - T_{yy} - 2iT_{xy}}{\sqrt{6}} \\ \frac{p_x + ip_y}{2\sqrt{2}} + \frac{T_{xz} + iT_{yz}}{\sqrt{3}} & \frac{1}{3} - \frac{2T_{zz}}{\sqrt{6}} & \frac{p_x - ip_y}{2\sqrt{2}} - \frac{T_{xz} - iT_{yz}}{\sqrt{3}} \\ \frac{T_{xx} - T_{yy} + 2iT_{xy}}{\sqrt{6}} & \frac{p_x + ip_y}{2\sqrt{2}} - \frac{T_{xz} + iT_{yz}}{\sqrt{3}} & \frac{1}{3} - \frac{p_z}{2} + \frac{T_{zz}}{\sqrt{6}} \end{bmatrix} \quad (2.1.30)$$

after expansion of the Eq. (2.1.16). The dynamic of a reaction decides the values of the polarizations \vec{p} and T_{ij} . For a given reaction one has to relate Eq. (2.1.2) to Eq. (2.1.16) to measure the polarization parameters. For the process shown in Fig. 2.1, one can calculate the polarization parameters p_i and T_{ij} in the following way. We first calculate the production density matrix in Eq. (2.1.2) using helicity amplitudes of the production process and compare it after normalization to the polarization density matrix $P_V(\lambda, \lambda')$ in Eq. (2.1.30) as,

$$\begin{aligned} P_V(\lambda, \lambda') &= \frac{1}{\sigma_V} \rho(\lambda, \lambda'), \\ &= \frac{1}{\sigma_V} \begin{bmatrix} \rho(+, +) & \rho(+, 0) & \rho(+, -) \\ \rho(0, +) & \rho(0, 0) & \rho(0, -) \\ \rho(-, +) & \rho(-, 0) & \rho(-, -) \end{bmatrix}. \end{aligned} \quad (2.1.31)$$

Thus, the polarization parameters can be extracted from the polarization matrix elements as,

$$\begin{aligned} p_x &= \frac{[(\rho(+, 0) + \rho(0, +)) + (\rho(0, -) + \rho(-, 0))]}{\sqrt{2}\sigma_V}, \\ p_y &= \frac{i[(\rho(0, +) - \rho(+, 0)) + (\rho(-, 0) - \rho(0, -))]}{\sqrt{2}\sigma_V}, \\ p_z &= \frac{[\rho(+, +) - \rho(-, -)]}{\sigma_V}, \\ T_{xy} &= \frac{i\sqrt{6}[\rho(-, +) - \rho(+, -)]}{4\sigma_V}, \\ T_{xz} &= \frac{\sqrt{3}[(\rho(+, 0) + \rho(0, +)) - (\rho(0, -) + \rho(-, 0))]}{4\sigma_V}, \\ T_{yz} &= \frac{i\sqrt{3}[(\rho(0, +) - \rho(+, 0)) - (\rho(-, 0) - \rho(0, -))]}{4\sigma_V}, \\ T_{xx} - T_{yy} &= \frac{\sqrt{6}[\rho(-, +) + \rho(+, -)]}{2\sigma_V}, \\ T_{zz} &= \frac{\sqrt{6}}{2} \left[\frac{\rho(+, +) + \rho(-, -)}{\sigma_V} - \frac{2}{3} \right], \\ &= \frac{\sqrt{6}}{2} \left[\frac{1}{3} - \frac{\rho(0, 0)}{\sigma_V} \right]. \end{aligned} \quad (2.1.32)$$

Using the traceless property of T_{ij} , i.e., $T_{xx} + T_{yy} + T_{zz} = 0$, along with the values of T_{zz} and $T_{xx} - T_{yy}$ from above, one can calculate T_{xx} and T_{yy} separately, although they will not be independent parameters. Instead of considering T_{xx} and T_{yy} separately we consider $T_{xx} - T_{yy}$ as an independent tensor polarization. These polarization parameters can also be obtained from the angular information of the decayed products of the particle V , which is discussed in the next section.

The polarization parameters p_i and T_{ij} depend on the choice of reference frame; they possess different values in different frame. The above formulation of polarizations is based on the helicity frame, which is equivalent to the centre-of-mass frame (CM) of colliding beams in a given process. For an e^+e^- collider, the observables are calculated in the CM frame, while for hadronic collider such as the LHC, the observables are calculated in the laboratory (Lab) frame as well as in CM frame if possible. In the case of hadronic collider, the CM frame and Lab frame are not the same due to the involvement of parton distribution functions (PDFs). The production density matrix (in Eq. (2.1.2)) and hence the polarization density matrix (in Eq. (2.1.30)) receive an effective total rotation comprising boost and angular rotations leaving the trace invariant going from CM to Lab frame. Due to the rotation of polarization density matrix, its elements p_i and T_{ij} get transformed as [173, 188, 189],

$$\begin{aligned} p_i^{Lab} &= \sum_j R_{ij}^Y(\omega) p_j^{CM}, \\ T_{ij}^{Lab} &= \sum_{k,l} R_{ik}^Y(\omega) R_{jl}^Y(\omega) T_{kl}^{CM}, \end{aligned} \quad (2.1.33)$$

where

$$\begin{aligned} \cos \omega &= \cos \theta_{CM} \cos \theta_{Lab} + \gamma_{CM} \sin \theta_{CM} \sin \theta_{Lab}, \\ \sin \omega &= \frac{m}{E} (\sin \theta_{CM} \cos \theta_{Lab} - \gamma_{CM} \cos \theta_{CM} \sin \theta_{Lab}). \end{aligned} \quad (2.1.34)$$

Here, R_{ij}^Y is the usual rotational matrix w.r.t. y -direction and $\gamma_{CM} = 1/\sqrt{1-\beta_{CM}^2}$ with β_{CM} being boost of the CM frame. The quantities m and E are the mass and energy of the particle V , respectively.

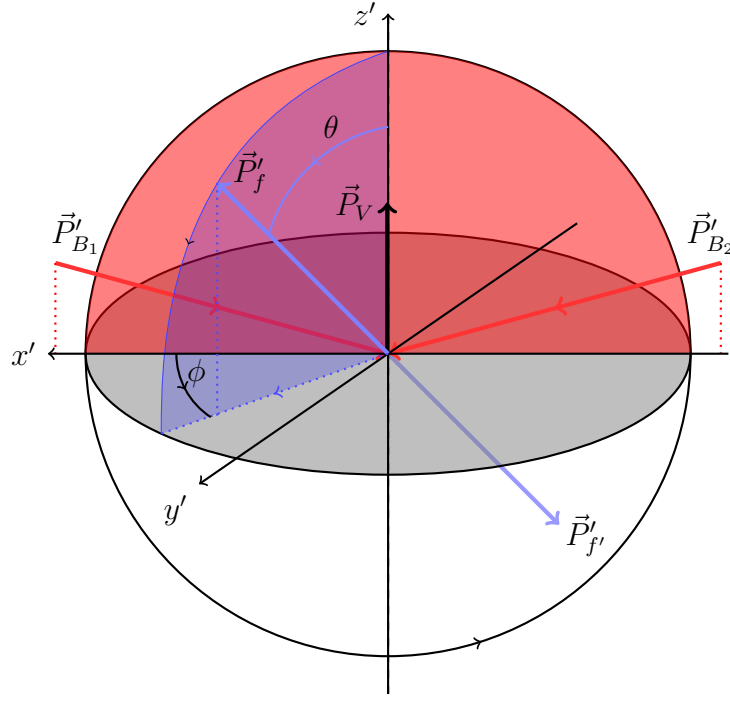


Figure 2.2. The reference frame showing the fermions decay angles in the V rest frame. The direction of V in the Lab frame (\vec{P}_V) defines the z' -axis (the prime is due to not being the colliding beam direction). The directions of decayed fermions are shown with \vec{P}'_f and $\vec{P}'_{f'}$, and they are in the decay plane shown by the upper transparent layer (light blue colour). The incoming particle B_1 and B_2 are in the xz plane shown by intermediated transparent layer (light red colour). The azimuthal angle ϕ of f is measured w.r.t the xz plane. The co-ordinate system is right-handed, which defines the y' -axis.

2.2 Polarization asymmetries

For the spin-1 particle V to be decayed to a pair of fermions ff' via the interaction vertex

$$Vff' : \gamma^\mu (L_f P_L + R_f P_R), \quad P_{L/R} = \frac{1}{2} (1 \mp \gamma_5), \quad (2.2.1)$$

the decay density matrix (normalized to one) is given by [172]²,

$$\Gamma_V(\lambda, \lambda') = \begin{bmatrix} \frac{1+\delta+(1-3\delta)\cos^2\theta+2\alpha\cos\theta}{4} & \frac{\sin\theta(\alpha+(1-3\delta)\cos\theta)}{2\sqrt{2}} e^{i\phi} & (1-3\delta)\frac{(1-\cos^2\theta)}{4} e^{i2\phi} \\ \frac{\sin\theta(\alpha+(1-3\delta)\cos\theta)}{2\sqrt{2}} e^{-i\phi} & \delta + (1-3\delta)\frac{\sin^2\theta}{2} & \frac{\sin\theta(\alpha-(1-3\delta)\cos\theta)}{2\sqrt{2}} e^{i\phi} \\ (1-3\delta)\frac{(1-\cos^2\theta)}{4} e^{-i2\phi} & \frac{\sin\theta(\alpha-(1-3\delta)\cos\theta)}{2\sqrt{2}} e^{-i\phi} & \frac{1+\delta+(1-3\delta)\cos^2\theta-2\alpha\cos\theta}{4} \end{bmatrix}. \quad (2.2.2)$$

²Same choice of polarization vectors, as in polarization density matrix in Eq. (2.1.30), are used.

Here θ, ϕ are the polar and the azimuthal orientation of the final state fermion f , in the rest frame of V with it's would be momentum along z -direction, see Fig. 2.2. The parameters α , called analysing power, and δ are given by,

$$\alpha = \frac{2(R_f^2 - L_f^2) \sqrt{1 + (x_1^2 - x_2^2)^2 - 2(x_1^2 + x_2^2)}}{12L_f R_f x_1 x_2 + (R_f^2 + L_f^2)[2 - (x_1^2 - x_2^2)^2 + (x_1^2 + x_2^2)]}, \quad (2.2.3)$$

$$\delta = \frac{4L_f R_f x_1 x_2 + (R_f^2 + L_f^2)[(x_1^2 + x_2^2) - (x_1^2 - x_2^2)^2]}{12L_f R_f x_1 x_2 + (R_f^2 + L_f^2)[2 - (x_1^2 - x_2^2)^2 + (x_1^2 + x_2^2)]}, \quad (2.2.4)$$

with $x_1 = m_f/m_V$, $x_2 = m_{f'}/m_V$. For massless final state fermions, $x_1 \rightarrow 0$, $x_2 \rightarrow 0$; one obtains $\delta \rightarrow 0$ and $\alpha \rightarrow (R_f^2 - L_f^2)/(R_f^2 + L_f^2)$. Using the expression of $P(\lambda, \lambda')$ from Eq. (2.1.30) and $\Gamma(\lambda, \lambda')$ from Eq. (2.2.2), the angular distribution in Eq. (2.1.5) of the fermion f becomes

$$\begin{aligned} \frac{1}{\sigma} \frac{d\sigma}{d\Omega} &= \frac{3}{8\pi} \left[\left(\frac{2}{3} - (1-3\delta) \frac{T_{zz}}{\sqrt{6}} \right) + \alpha p_z \cos\theta + \sqrt{\frac{3}{2}}(1-3\delta) T_{zz} \cos^2\theta \right. \\ &+ \left(\alpha p_x + 2\sqrt{\frac{2}{3}}(1-3\delta) T_{xz} \cos\theta \right) \sin\theta \cos\phi \\ &+ \left(\alpha p_y + 2\sqrt{\frac{2}{3}}(1-3\delta) T_{yz} \cos\theta \right) \sin\theta \sin\phi \\ &\left. + (1-3\delta) \left(\frac{T_{xx} - T_{yy}}{\sqrt{6}} \right) \sin^2\theta \cos(2\phi) + \sqrt{\frac{2}{3}}(1-3\delta) T_{xy} \sin^2\theta \sin(2\phi) \right]. \end{aligned} \quad (2.2.5)$$

The above nice differential angular distribution is the *master equation* that is used to probe all the polarization parameters of the particle V from the data in a real experiment or in a Monte-Carlo event simulator. Using partial integration w.r.t θ and ϕ of the Eq. (2.2.5) one can construct several asymmetries which relate all the polarization parameters of V .

The asymmetries to probe the polarization parameters are given below. We can obtain p_x from the left-right asymmetry as,

$$\begin{aligned} A_x &= \frac{1}{\sigma} \left[\int_{-\frac{\pi}{2}}^{\frac{\pi}{2}} \frac{d\sigma}{d\phi} d\phi - \int_{\frac{\pi}{2}}^{\frac{3\pi}{2}} \frac{d\sigma}{d\phi} d\phi \right], \\ &= \frac{3\alpha p_x}{4} \equiv \frac{\sigma(\cos\phi > 0) - \sigma(\cos\phi < 0)}{\sigma(\cos\phi > 0) + \sigma(\cos\phi < 0)}. \end{aligned} \quad (2.2.6)$$

The polarization parameters p_y and p_z are obtained from up-down and forward-backward

asymmetry, respectively as

$$\begin{aligned} A_y &= \frac{1}{\sigma} \left[\int_0^\pi \frac{d\sigma}{d\phi} d\phi - \int_\pi^{2\pi} \frac{d\sigma}{d\phi} d\phi \right], \\ &= \frac{3\alpha p_y}{4} \equiv \frac{\sigma(\sin\phi > 0) - \sigma(\sin\phi < 0)}{\sigma(\sin\phi > 0) + \sigma(\sin\phi < 0)}, \end{aligned} \quad (2.2.7)$$

$$\begin{aligned} A_z &= \frac{1}{\sigma} \left[\int_0^{\frac{\pi}{2}} \frac{d\sigma}{d\theta} d\theta - \int_{\frac{\pi}{2}}^\pi \frac{d\sigma}{d\theta} d\theta \right], \\ &= \frac{3\alpha p_z}{4} \equiv \frac{\sigma(\cos\theta > 0) - \sigma(\cos\theta < 0)}{\sigma(\cos\theta > 0) + \sigma(\cos\theta < 0)}. \end{aligned} \quad (2.2.8)$$

All other polarization parameters are obtained from the following up-down-left-right mixed asymmetries:

$$\begin{aligned} A_{xy} &= \frac{1}{\sigma} \left[\left(\int_0^{\frac{\pi}{2}} \frac{d\sigma}{d\phi} d\phi + \int_\pi^{\frac{3\pi}{2}} \frac{d\sigma}{d\phi} d\phi \right) - \left(\int_{\frac{\pi}{2}}^\pi \frac{d\sigma}{d\phi} d\phi + \int_{\frac{3\pi}{2}}^{2\pi} \frac{d\sigma}{d\phi} d\phi \right) \right], \\ &= \frac{2}{\pi} \sqrt{\frac{2}{3}} (1 - 3\delta) T_{xy} \equiv \frac{\sigma(\sin 2\phi > 0) - \sigma(\sin 2\phi < 0)}{\sigma(\sin 2\phi > 0) + \sigma(\sin 2\phi < 0)}, \end{aligned} \quad (2.2.9)$$

$$\begin{aligned} A_{xz} &= \frac{1}{\sigma} \left[\left(\int_{\theta=0}^{\frac{\pi}{2}} \int_{\phi=-\frac{\pi}{2}}^{\frac{\pi}{2}} \frac{d\sigma}{d\Omega} d\Omega + \int_{\theta=\frac{\pi}{2}}^\pi \int_{\phi=\frac{\pi}{2}}^{\frac{3\pi}{2}} \frac{d\sigma}{d\Omega} d\Omega \right) \right. \\ &\quad \left. - \left(\int_{\theta=0}^{\frac{\pi}{2}} \int_{\phi=\frac{\pi}{2}}^{\frac{3\pi}{2}} \frac{d\sigma}{d\Omega} d\Omega + \int_{\theta=\frac{\pi}{2}}^\pi \int_{\phi=-\frac{\pi}{2}}^{\frac{\pi}{2}} \frac{d\sigma}{d\Omega} d\Omega \right) \right] \\ &= \frac{2}{\pi} \sqrt{\frac{2}{3}} (1 - 3\delta) T_{xz} \equiv \frac{\sigma(\cos\theta \cos\phi > 0) - \sigma(\cos\theta \cos\phi < 0)}{\sigma(\cos\theta \cos\phi > 0) + \sigma(\cos\theta \cos\phi < 0)}, \end{aligned} \quad (2.2.10)$$

$$\begin{aligned} A_{yz} &= \frac{1}{\sigma} \left[\left(\int_{\theta=0}^{\frac{\pi}{2}} \int_{\phi=0}^\pi \frac{d\sigma}{d\Omega} d\Omega + \int_{\theta=\frac{\pi}{2}}^\pi \int_{\phi=\pi}^{2\pi} \frac{d\sigma}{d\Omega} d\Omega \right) \right. \\ &\quad \left. - \left(\int_{\theta=0}^{\frac{\pi}{2}} \int_{\phi=\pi}^{2\pi} \frac{d\sigma}{d\Omega} d\Omega + \int_{\theta=\frac{\pi}{2}}^\pi \int_{\phi=0}^\pi \frac{d\sigma}{d\Omega} d\Omega \right) \right] \\ &= \frac{2}{\pi} \sqrt{\frac{2}{3}} (1 - 3\delta) T_{yz} \equiv \frac{\sigma(\cos\theta \sin\phi > 0) - \sigma(\cos\theta \sin\phi < 0)}{\sigma(\cos\theta \sin\phi > 0) + \sigma(\cos\theta \sin\phi < 0)}, \end{aligned} \quad (2.2.11)$$

$$\begin{aligned} A_{x^2-y^2} &= \frac{1}{\sigma} \left[\left(\int_{-\frac{\pi}{4}}^{\frac{\pi}{4}} \frac{d\sigma}{d\phi} d\phi + \int_{\frac{3\pi}{4}}^{\frac{5\pi}{4}} \frac{d\sigma}{d\phi} d\phi \right) - \left(\int_{\frac{\pi}{4}}^{\frac{3\pi}{4}} \frac{d\sigma}{d\phi} d\phi + \int_{\frac{5\pi}{4}}^{\frac{7\pi}{4}} \frac{d\sigma}{d\phi} d\phi \right) \right] \\ &= \frac{1}{\pi} \sqrt{\frac{2}{3}} (1 - 3\delta) (T_{xx} - T_{yy}) \equiv \frac{\sigma(\cos 2\phi > 0) - \sigma(\cos 2\phi < 0)}{\sigma(\cos 2\phi > 0) + \sigma(\cos 2\phi < 0)}, \end{aligned} \quad (2.2.12)$$

$$\begin{aligned} A_{zz} &= \frac{1}{\sigma} \left[\left(\int_0^{\frac{\pi}{3}} \frac{d\sigma}{d\theta} d\theta + \int_{\frac{2\pi}{3}}^\pi \frac{d\sigma}{d\theta} d\theta \right) - \int_{\frac{\pi}{3}}^{\frac{2\pi}{3}} \frac{d\sigma}{d\theta} d\theta \right], \\ &= \frac{3}{8} \sqrt{\frac{3}{2}} (1 - 3\delta) T_{zz} \equiv \frac{\sigma(\sin 3\theta > 0) - \sigma(\sin 3\theta < 0)}{\sigma(\sin 3\theta > 0) + \sigma(\sin 3\theta < 0)}. \end{aligned} \quad (2.2.13)$$

While extracting the polarization asymmetries in a collider/event generator, we have to

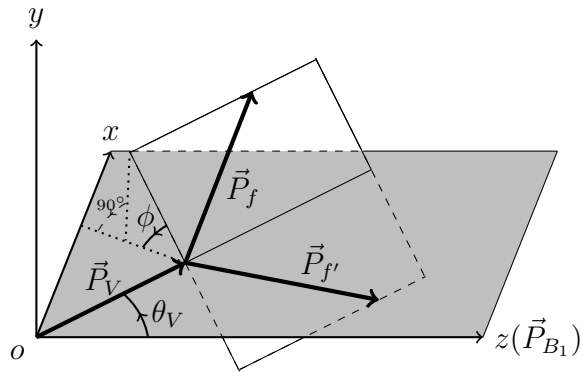


Figure 2.3. The momentum configuration of the particles are shown in the Lab frame. The decay plane spanned by \vec{P}_f and $\vec{P}_{f'}$ makes an angle ϕ with the xz plane.

make sure that the analysis is done in the rest frame of V . The initial beam defines the z -axis in the Lab, while the production plane of V defines the xz plane, i.e. $\phi = 0$ plane, see Fig. 2.3. While boosting to the rest frame of V , we keep the xz plane invariant. The polar and the azimuthal angles of the decay products of V are measured with respect to the *would-be* momentum of the particle V .

Thus, the polarization parameters of a spin-1 particle can be obtained at two levels: At the production level and the level of decay products. As a demonstration of the two methods of obtaining polarization parameters, we look at three processes: $e^+e^- \rightarrow ZZ$, $e^+e^- \rightarrow Z\gamma$ and $e^+e^- \rightarrow W^+W^-$ in the SM. The polarization parameters are constructed both at the production level using Eq. (2.1.32) and at the decay level using Eqs. (2.2.6)-(2.2.13). The asymmetries $A_{x^2-y^2}$, A_{zz} are calculated analytically from the production part and shown as a function of beam energy in Fig. 2.4 with lines. For the same processes with $ZV \rightarrow f\bar{f}q\bar{q}$ and $W^+W^- \rightarrow l^-\bar{\nu}_l q_u \bar{q}_d$, we generate events using MADGRAPH5_aMC@NLO [190] with different values of beam energies. The polarization asymmetries were constructed from these events and are shown in Fig. 2.4 with points. The statistical error bars shown correspond to 10^4 events. We observe agreement between the asymmetries calculated at the production level (analytically) and the decay level (using event generator). Any possible new physics in the production process of Z and W boson is expected to change the cross section, kinematical distributions and the values of the polarization parameters/asymmetries. We intend to use these asymmetries to probe the standard and BSM physics.

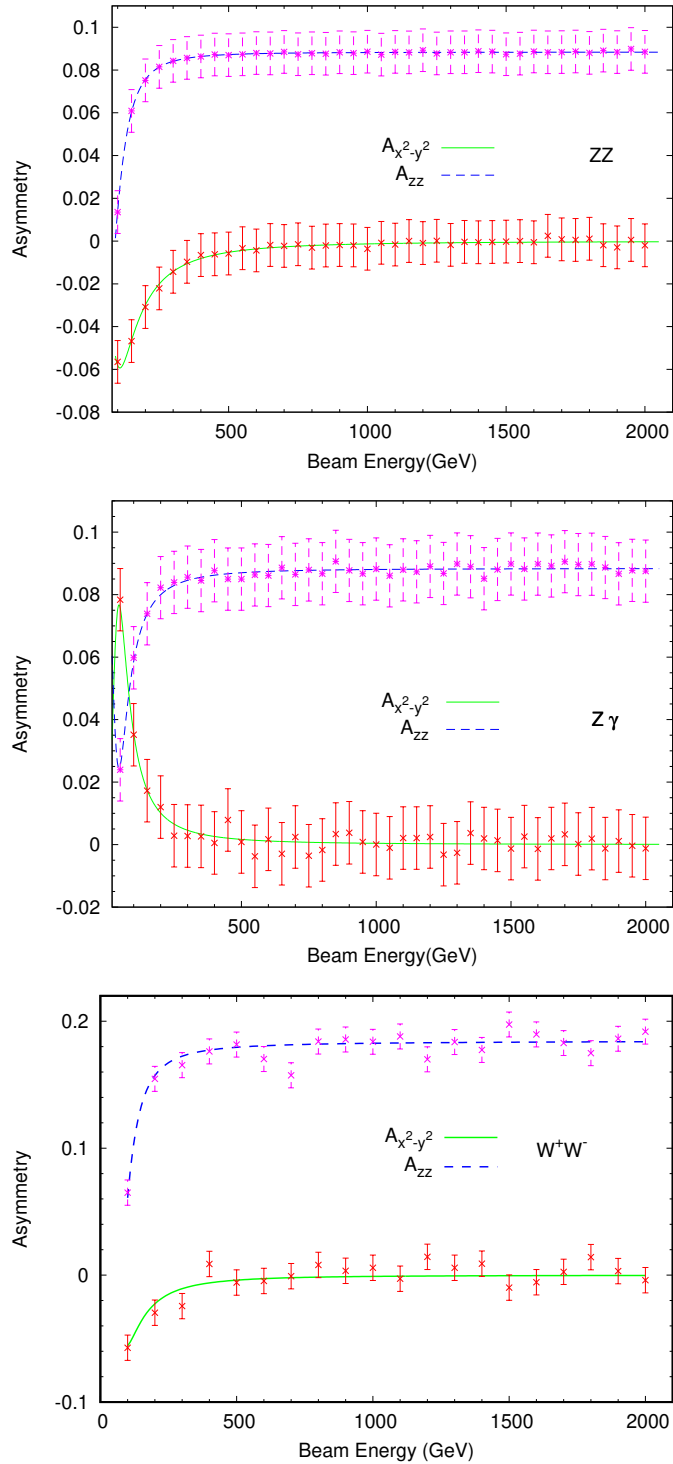


Figure 2.4. The SM values (analytic) of asymmetries $A_{x^2-y^2}$ (solid/green line) and A_{zz} (dashed/blue line) as a function of beam energy in the e^+e^- collider for ZZ (top-left-panel), Z γ (top-right-panel) and W⁺W⁻ (bottom-panel) processes. The data points with error bar correspond to 10^4 events generated by MADGRAPH5_aMC@NLO.

2.3 Spin-spin correlations

The spin of two particles produced in a reaction could be correlated even if they do not get produced polarized individually. In the SM the two top quarks are not produced polarized in top quark pair production at the LHC; but their spins are correlated [191, 192]. In a two going to two body reaction, if two particles with spin s and s' are produced, there will be $4s(s+1)$ and $4s'(s'+1)$ individual polarizations and $4s(s+1) \times 4s'(s'+1)$ spin-spin correlator giving a total of $(2s+1)^2(2s'+1)^2 - 1$ number of spin observables. For example, in a vector boson pair ($VV, V = W/Z$) production there are a total of $8 + 8 + 8 \times 8 = 80$ spin observables. The spin-spin correlator can be obtained by constructing asymmetries from the double angular distribution of the two particles' decay products. These spin-spin correlators can be sensitive to new physics signals and can be used to probe them at collider [124, 193, 194].

As an example of spin-spin correlation, one may consider top quark pair production and their leptonic decays. For spin-1/2 case, the polarization density matrix (expanding Eq. (2.1.14)) and decay density matrix are given by [172],

$$\rho_{1/2} = \frac{1}{2} \begin{bmatrix} 1 + p_z & p_x - ip_y \\ p_x + ip_y & 1 - p_z \end{bmatrix}, \quad (2.3.1)$$

$$\Gamma_{1/2}(\lambda, \lambda') = \begin{bmatrix} \frac{1 + \alpha \cos \theta}{2} & \frac{\alpha \sin \theta}{2} e^{i\phi} \\ \frac{\alpha \sin \theta}{2} e^{-i\phi} & \frac{1 - \alpha \cos \theta}{2} \end{bmatrix}. \quad (2.3.2)$$

Thus, according to Eq. 2.1.5, the top-decayed leptons will have angular distribution as,

$$\frac{1}{\sigma} \frac{d\sigma}{d\Omega} = \frac{1}{4\pi} \left[1 + \alpha p_x \sin \theta \cos \phi + \alpha p_y \sin \theta \sin \phi + \alpha p_z \cos \theta \right] \quad (2.3.3)$$

in the rest frame of their respective mother top quark. The double $\cos \theta$ distribution of the two leptons will be given by,

$$\frac{1}{\sigma} \frac{d^2\sigma}{d\Omega_1 d\Omega_2} = C_N \left[1 + \alpha_t p_z(t) \cos \theta_1 + \alpha_{\bar{t}} p_z(\bar{t}) \cos \theta_2 + \alpha_t \alpha_{\bar{t}} C_{\bar{t}\bar{t}} \cos \theta_1 \cos \theta_2 + \dots \right] \quad (2.3.4)$$

with C_N as an overall normalization constant and $C_{\bar{t}\bar{t}}$ being one of the spin-spin correlator of

Table 2.1. Total number of polarization parameters and correlator in spin- s and spin- s' production system.

s, s'	example	total spin observables = $(2s + 1)^2(2s' + 1)^2 - 1$
$\frac{1}{2}, \frac{1}{2}$	t, \bar{t}	$3 + 3 + 3 \times 3 = 15$
$\frac{1}{2}, 1$	t, W	$3 + 8 + 3 \times 8 = 35$
$1, 1$	Z, Z	$8 + 8 + 8 \times 8 = 80$

t and \bar{t} . The spin-spin correlator $C_{t\bar{t}}$ can be obtained from an asymmetry constructed as,

$$\begin{aligned}
A_{z_1 z_2} &= \frac{1}{\sigma} \left[\left(\int_{\theta_1=0}^{\frac{\pi}{2}} d\theta_1 \int_{\theta_2=0}^{\frac{\pi}{2}} \frac{d\sigma}{d\theta_1 d\theta_2} d\theta_2 + \int_{\theta_1=\frac{\pi}{2}}^{\pi} d\theta_1 \int_{\theta_2=\frac{\pi}{2}}^{\pi} \frac{d\sigma}{d\theta_1 d\theta_2} d\theta_2 \right) \right. \\
&\quad \left. - \left(\int_{\theta_1=0}^{\frac{\pi}{2}} d\theta_1 \int_{\theta_2=\frac{\pi}{2}}^{\pi} \frac{d\sigma}{d\theta_1 d\theta_2} d\theta_2 + \int_{\theta_1=\frac{\pi}{2}}^{\pi} d\theta_1 \int_{\theta_2=0}^{\frac{\pi}{2}} \frac{d\sigma}{d\theta_1 d\theta_2} d\theta_2 \right) \right], \\
&= (C_N \alpha_t \alpha_{\bar{t}}) C_{t\bar{t}} \equiv \frac{\sigma(\cos \theta_1 \cos \theta_2 > 0) - \sigma(\cos \theta_1 \cos \theta_2 < 0)}{\sigma(\cos \theta_1 \cos \theta_2 > 0) + \sigma(\cos \theta_1 \cos \theta_2 < 0)}. \quad (2.3.5)
\end{aligned}$$

All other spin-spin correlator can be obtained in a similar way. The total number of spin observables for a general spin s and s' system of particle(both of them being either 1 or 1/2) are listed in Table 2.1.

2.4 Summary

A spin-1 particle offers eight polarization parameters providing eight more observables in addition to the total production cross section to probe new physics. The polarization observables can discriminate among various new physics models. In a given new physics model, these polarization parameters can discriminate between different couplings, such as vector-like, tensor-like, CP -even, CP -odd, etc. The polarization asymmetries A_y , A_{xy} and A_{yz} probe CP -odd couplings, while others probe CP -even couplings in a reaction, which will be discussed in detail in the next chapters in the context of anomalous triple gauge boson couplings. We use these polarization asymmetries of Z and W along with the cross sections of their production to study anomalous triple gauge boson couplings in the neutral sector as well as in the charge sector in the next chapters.

3 The probe of aTGC in $e^+e^- \rightarrow ZZ/Z\gamma$ and the role of Z boson polarizations

Contents

3.1 Anomalous Lagrangian and their probe.	44
3.1.1 Helicity formalism and polarizations of Z	46
3.1.2 Parametric dependence of observables	48
3.1.3 Sensitivity of observables to anomalous couplings	50
3.2 Likelihood mapping of parameter space	55
3.2.1 MCMC analysis for $e^+e^- \rightarrow ZZ$	56
3.2.2 MCMC analysis for $e^+e^- \rightarrow Z\gamma$	61
3.2.3 Separability of benchmark aTGCs	64
3.3 Summary	66

The contents in this chapter are based on the published article in Ref. [98].

The possible trilinear gauge boson interactions in electroweak theory are WWZ , $WW\gamma$, $ZZ\gamma$, ZZZ , $\gamma\gamma Z$, and $\gamma\gamma\gamma$, out of which the SM, after EWSB, provides only WWZ and $WW\gamma$ self-couplings. Other interactions among neutral gauge bosons are not possible at the tree level in the SM, and hence they are anomalous. Thus any deviation from the SM prediction, either in strength or the tensorial structure, would be a signal of BSM physics. In this chapter, we focus on the precise measurement of the neutral triple gauge boson couplings, in a model independent way, at the proposed International Linear Collider (ILC) [195–197]. Different

parametrization for the neutral aTGC exists in the literature for effective form factors [64, 107, 198] as well as effective operators [63, 199, 200]. We follow the effective form factor approach for the neutral aTGC discussed in Ref. [64]. The neutral aTGC have been widely studied in the literature [82–106] for various colliders: in e^+e^- collider [83, 85, 93–95, 97–101, 104, 105], $e\gamma$ collider [86, 91, 92], $\gamma\gamma$ collider [96], hadron collider [84, 88, 90, 102, 103, 106] and both e^+e^- and hadron collider [82, 87, 89]. For these effective anomalous vertices one can write an effective Lagrangian and they have been given in [82, 85, 86, 104] up to differences in conventions and parametrizations. The Lagrangian corresponding to the anomalous form factors in the neutral sector in [64] is given by [82],

$$\begin{aligned}
\mathcal{L}_{ZVV} = & \frac{g_e}{m_Z^2} \left[- \left[f_4^\gamma (\partial_\mu F^{\mu\beta}) + f_4^Z (\partial_\mu Z^{\mu\beta}) \right] Z_\alpha (\partial^\alpha Z_\beta) + \left[f_5^\gamma (\partial^\sigma F_{\sigma\mu}) + f_5^Z (\partial^\sigma Z_{\sigma\mu}) \right] \tilde{Z}^{\mu\beta} Z_\beta \right. \\
& - \left[h_1^\gamma (\partial^\sigma F_{\sigma\mu}) + h_1^Z (\partial^\sigma Z_{\sigma\mu}) \right] Z_\beta F^{\mu\beta} - \left[h_3^\gamma (\partial_\sigma F^{\sigma\rho}) + h_3^Z (\partial_\sigma Z^{\sigma\rho}) \right] Z^\alpha \tilde{F}_{\rho\alpha} \\
& - \left\{ \frac{h_2^\gamma}{m_Z^2} \left[\partial_\alpha \partial_\beta \partial^\rho F_{\rho\mu} \right] + \frac{h_2^Z}{m_Z^2} \left[\partial_\alpha \partial_\beta (\square + m_Z^2) Z_\mu \right] \right\} Z^\alpha F^{\mu\beta} \\
& + \left. \left\{ \frac{h_4^\gamma}{2m_Z^2} \left[\square \partial^\sigma F^{\rho\alpha} \right] + \frac{h_4^Z}{2m_Z^2} \left[(\square + m_Z^2) \partial^\sigma Z^{\rho\alpha} \right] \right\} Z_\sigma \tilde{F}_{\rho\alpha} \right], \tag{3.0.1}
\end{aligned}$$

where $\tilde{Z}_{\mu\nu} = 1/2\epsilon_{\mu\nu\rho\sigma} Z^{\rho\sigma}$ ($\epsilon^{0123} = +1$) with $Z_{\mu\nu} = \partial_\mu Z_\nu - \partial_\nu Z_\mu$ and similarly for the photon tensor $F_{\mu\nu}$. The $g_e = e = \sqrt{4\pi\alpha_{EM}}$ is the electro magnetic coupling constant. The couplings f_4^V , h_1^V , h_2^V correspond to the CP -odd tensorial structures, while f_5^V , h_3^V , h_4^V correspond to the CP -even ones. Further, the terms corresponding to h_2^V and h_4^V are of mass dimension-8, while the others are dimension-6 in the Lagrangian. In [95] the authors have pointed out one more possible dimension-8 CP -even term for $Z\gamma Z$ vertex, given by,

$$\mathcal{L}_{aTGC} \supset \frac{g_e h_5^Z}{2m_Z^4} (\partial^\tau F^{\alpha\lambda}) \tilde{Z}_{\alpha\beta} \partial_\tau \partial_\lambda Z^\beta.$$

In our present work, however, we shall restrict ourselves to the dimension-6 subset of the Lagrangian given in Eq. (3.0.1). Besides the form factors, one can study the neutral aTGC with the dimension-8 operators given in Eq. (1.3.10) as independent and translate the results to the dimension-6 form factors using relations in Eqs. (1.3.15) & (1.3.16).

In the theoretical side, the tensorial structure for some of these anomalous couplings can be generated at higher order loop within the framework of a renormalizable theory. For example, a fermionic triangular diagram can generate CP -even couplings in the SM, some

Table 3.1. List of tightest limits on anomalous couplings of Eq. (3.0.1) available in literature.

Limits on couplings	Experiment
$-1.2 \times 10^{-3} < f_4^\gamma < +1.3 \times 10^{-3}$	$pp \rightarrow ZZ \rightarrow 4l$
$-1.2 \times 10^{-3} < f_4^Z < +1.0 \times 10^{-3}$	13 TeV
$-1.2 \times 10^{-3} < f_5^\gamma < +1.3 \times 10^{-3}$	35.9 fb ⁻¹
$-1.2 \times 10^{-3} < f_5^Z < 1.3 \times 10^{-3}$	CMS [146]
$-3.7 \times 10^{-4} < h_3^\gamma < +3.7 \times 10^{-4}$	$pp \rightarrow Z\gamma \rightarrow v\bar{v}\gamma$
$-3.2 \times 10^{-4} < h_3^Z < +3.3 \times 10^{-4}$	13 TeV
$-4.4 \times 10^{-7} < h_4^\gamma < +4.3 \times 10^{-7}$	36.1 fb ⁻¹
$-4.5 \times 10^{-7} < h_4^Z < +4.4 \times 10^{-7}$	ATLAS [148]

simplified fermionic model [68], the Minimal supersymmetric SM (MSSM) [69, 70] and Little Higgs model [71]. On the other hand, CP -odd couplings can be generated at 2 loop in the MSSM [69]. A CP -violating ZZZ vertex has been studied in 2HDM in Ref. [68, 72, 73]. Besides this, a non-commutative extension of the SM (NCSM) [74, 75] can also provide an anomalous coupling structure in the neutral sector with a possibility of a trilinear $\gamma\gamma\gamma$ coupling as well [74]. We note that the dimension-8 operators which contribute to the trilinear couplings also contribute to quartic gauge boson couplings $WWVV$, $ZZZ\gamma$, $ZZ\gamma\gamma$ which appear in triple gauge boson production [201, 202] and vector boson scattering [203], for example. A complete study of these operators will require one to include all these processes involving triple gauge boson couplings as well as quartic gauge boson couplings. In the effective form factor approach as we study in this paper, however, the triple and the quartic gauge boson couplings are independent of each other and can be studied separately.

On the experimental side, the anomalous Lagrangian in Eq. (3.0.1) has been explored at the Large Electron-Positron collider (LEP) [133–137], the Tevatron [138–140], and the LHC [141–148]. The tightest bounds on f_i^V ($i = 4, 5$) [146] and on h_j^V ($j = 3, 4$) [148] comes from the CMS and ATLAS collaboration, respectively (see Table 3.1). For the ZZ process the total rate has been used [141], while for the $Z\gamma$ process both the cross section and the p_T distribution of γ has been used [142–145] for obtaining the limits. All these analyses vary one parameter at a time to find the 95 % confidence limits on the form factors. For the $Z\gamma$ process the limits on the CP -odd form factors, h_1^V , h_2^V , are comparable to the limits on the CP -even form factors, h_3^V , h_4^V , respectively.

To put simultaneous limits on all the form factors, one would need as many observables

as possible, like differential rates, kinematic asymmetries, etc. Interestingly the Z being a spin-1 particle it offers eight polarization observables beyond the total cross section which are discussed in chapter 2 in details. In this chapter, we investigate all anomalous couplings (up to dimension-6 operators) of Eq. (3.0.1) in the processes $e^+e^- \rightarrow ZZ/Z\gamma$ with the help of the total cross section and the eight polarization asymmetries of the final state Z boson.

3.1 Anomalous Lagrangian and their probe

The effective Lagrangian for the anomalous trilinear gauge boson interactions in the neutral sector is given in Eq. (3.0.1), which includes both dimension-6 and dimension-8 operators as found in the literature. For the present work we restrict our analysis to dimension-6 operators only. Thus, the anomalous Lagrangian of our interest is

$$\begin{aligned} \mathcal{L}_{ZVV}^{dim-6} = & \frac{g_e}{m_Z^2} \left[- \left[f_4^\gamma (\partial_\mu F^{\mu\beta}) + f_4^Z (\partial_\mu Z^{\mu\beta}) \right] Z_\alpha (\partial^\alpha Z_\beta) + \left[f_5^\gamma (\partial^\sigma F_{\sigma\mu}) + f_5^Z (\partial^\sigma Z_{\sigma\mu}) \right] \tilde{Z}^{\mu\beta} Z_\beta \right. \\ & \left. - \left[h_1^\gamma (\partial^\sigma F_{\sigma\mu}) + h_1^Z (\partial^\sigma Z_{\sigma\mu}) \right] Z_\beta F^{\mu\beta} - \left[h_3^\gamma (\partial_\sigma F^{\sigma\rho}) + h_3^Z (\partial_\sigma Z^{\sigma\rho}) \right] Z^\alpha \tilde{F}_{\rho\alpha} \right]. \quad (3.1.1) \end{aligned}$$

This yields anomalous vertices ZZZ through $f_{4,5}^Z$ couplings, γZZ through $f_{4,5}^\gamma$ and $h_{1,3}^Z$ couplings and $\gamma\gamma Z$ through $h_{1,3}^\gamma$ couplings. There is no $\gamma\gamma\gamma$ vertex in the above Lagrangian. We

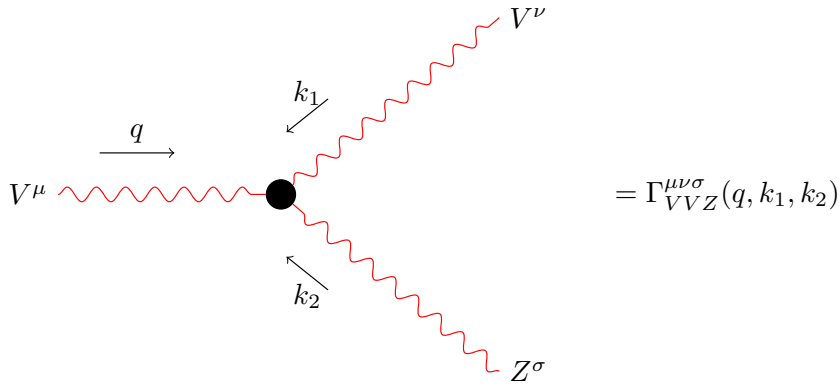


Figure 3.1. Feynman diagram for a general anomalous triple gauge boson vertex with $V = Z/\gamma$.

use FeynRules [204] to obtain the vertex tensors and they are given by,

$$\begin{aligned} \Gamma_{\gamma ZZ}^{\mu\nu\sigma}(q, k_1, k_2) = & \frac{g_e}{m_Z^2} \left[f_4^\gamma \left((k_2^\nu g^{\mu\sigma} + k_1^\sigma g^{\mu\nu}) q^2 - q^\mu (k_1^\sigma q^\nu + k_2^\nu q^\sigma) \right) \right. \\ & \left. + f_5^\gamma \left(q^\mu q_\beta \epsilon^{\nu\sigma\alpha\beta} + q^2 \epsilon^{\mu\nu\sigma\alpha} \right) (k_1 - k_2)_\alpha \right] \end{aligned}$$

$$\begin{aligned}
& +h_1^Z \left(k_2^\mu q^\nu k_2^\sigma + k_1^\mu k_1^\nu q^\sigma + (k_1^2 - k_2^2) (q^\nu g^{\mu\sigma} - q^\sigma g^{\mu\nu}) \right. \\
& \left. - k_2^\sigma g^{\mu\nu} q \cdot k_2 - k_1^\nu g^{\mu\sigma} q \cdot k_1 \right) \\
& \left. - h_3^Z \left(k_1^\nu k_{1\beta} \epsilon^{\mu\sigma\alpha\beta} + k_{2\beta} k_2^\sigma \epsilon^{\mu\nu\alpha\beta} + (k_2^2 - k_1^2) \epsilon^{\mu\nu\sigma\alpha} \right) q_\alpha \right], \quad (3.1.2)
\end{aligned}$$

$$\begin{aligned}
\Gamma_{ZZZ}^{\mu\nu\sigma}(q, k_1, k_2) = & \frac{g_e}{m_Z^2} \left[f_4^Z \left(-q^\mu q^\nu k_1^\sigma - k_2^\mu q^\nu k_2^\sigma - k_2^\mu k_1^\nu k_1^\sigma - k_1^\mu k_2^\nu k_2^\sigma \right. \right. \\
& - \left(q^\mu k_2^\nu + k_1^\mu k_1^\nu \right) q^\sigma + g^{\mu\nu} \left(q^2 k_1^\sigma + k_1^2 q^\sigma \right) \\
& + g^{\mu\sigma} \left(q^2 k_2^\nu + k_2^2 q^\nu \right) + g^{\nu\sigma} \left(k_2^2 k_1^\mu + k_1^2 k_2^\mu \right) \\
& \left. - f_5^Z \left(\epsilon^{\mu\nu\alpha\beta} (k_1 - q)_\alpha k_{2\beta} k_2^\sigma + \epsilon^{\mu\nu\sigma\alpha} \left((k_1^2 - k_2^2) q_\alpha \right. \right. \right. \\
& \left. \left. + (k_2^2 - q^2) k_{1\alpha} + (q^2 - k_1^2) k_{2\alpha} \right) \right. \\
& \left. \left. + k_{1\beta} k_1^\nu (k_2 - q)_\alpha \epsilon^{\mu\sigma\alpha\beta} + q_\beta q^\mu (k_2 - k_1)_\alpha \epsilon^{\nu\sigma\alpha\beta} \right) \right], \quad (3.1.3)
\end{aligned}$$

$$\begin{aligned}
\Gamma_{\gamma\gamma Z}^{\mu\nu\sigma}(q, k_1, k_2) = & \frac{g_e}{m_Z^2} \left[h_1^\gamma \left(q^\mu q^\nu k_1^\sigma + q^\sigma k_1^\mu k_1^\nu - g^{\mu\nu} \left(q^2 k_1^\sigma + k_1^2 q^\sigma \right) \right. \right. \\
& \left. \left. + g^{\mu\sigma} \left(k_1^2 q^\nu - q \cdot k_1 k_1^\nu \right) + g^{\nu\sigma} \left(q^2 k_1^\mu - q \cdot k_1 q^\mu \right) \right) \right. \\
& \left. - h_3^\gamma \left(k_{1\beta} k_1^\nu q_\alpha \epsilon^{\mu\sigma\alpha\beta} + q^\mu k_{1\alpha} q_\beta \epsilon^{\nu\sigma\alpha\beta} \right. \right. \\
& \left. \left. + \left(q^2 k_{1\alpha} - k_1^2 q_\alpha \right) \epsilon^{\mu\nu\sigma\alpha} \right) \right]. \quad (3.1.4)
\end{aligned}$$

The notations for momentum and Lorentz indices are shown in Fig. 3.1. We are interested in possible trilinear gauge boson vertices appearing in the processes $e^+e^- \rightarrow ZZ$ and $e^+e^- \rightarrow Z\gamma$ with final state gauge bosons being on-shell. For the process $e^+e^- \rightarrow ZZ$, the vertices γ^*ZZ and Z^*ZZ appear with on-shell conditions $k_1^2 = k_2^2 = m_Z^2$. The terms proportional to k_1^ν and k_2^σ in Eqs. (3.1.2) and (3.1.3) vanish due to the transversity of the polarization states. Thus, in the on-shell case, the vertices for $e^+e^- \rightarrow ZZ$ reduce to

$$\Gamma_{V^*ZZ}^{\mu\nu\sigma}(q, k_1, k_2) = -\frac{g_e}{m_Z^2} \left(q^2 - M_V^2 \right) \left[f_4^V \left(q^\sigma g^{\mu\nu} + q^\nu g^{\mu\sigma} \right) - f_5^V \epsilon^{\mu\nu\sigma\alpha} (k_1 - k_2)_\alpha \right]. \quad (3.1.5)$$

For the process $e^+e^- \rightarrow Z\gamma$ the vertices γZ^*Z and $\gamma^* \gamma Z$ appear with corresponding on-shell and polarization transversity conditions. Putting these conditions in Eqs. (3.1.2) and (3.1.4) and some relabelling of momenta etc. in Eq. (3.1.2) the relevant vertices $Z^* \gamma Z$ and $\gamma^* \gamma Z$

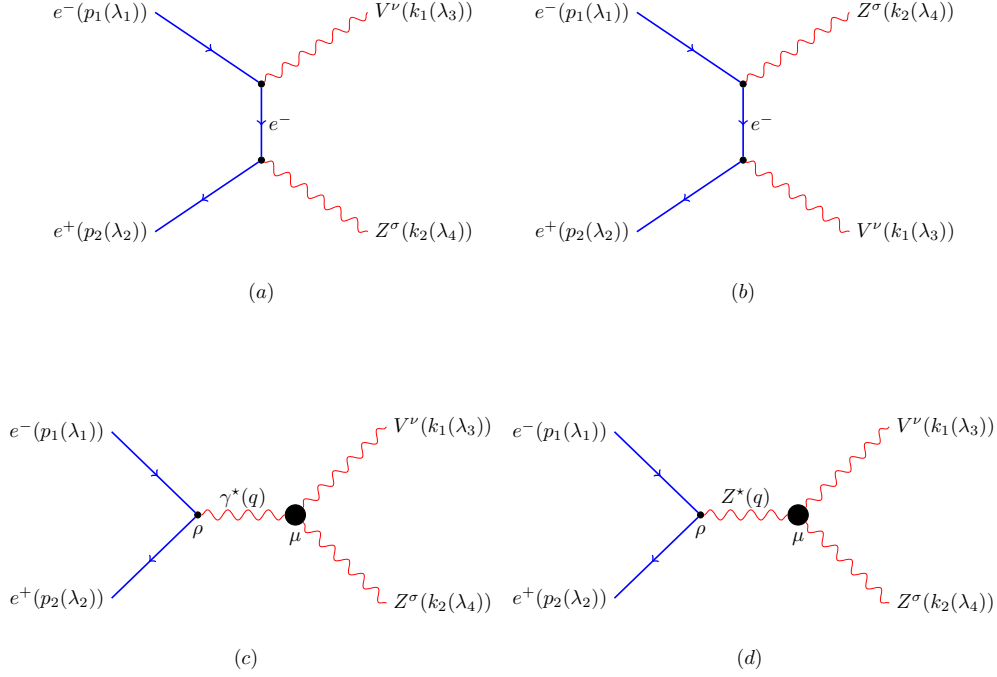


Figure 3.2. Feynman diagrams for the production of ZZ or $Z\gamma$ at e^+e^- collider.

can be represented together by,

$$\Gamma_{V^*\gamma Z}^{\mu\nu\sigma}(q, k_1, k_2) = \frac{ge}{m_Z^2} (q^2 - M_V^2) \left[h_1^V (k_1^\mu g^{\nu\sigma} - k_1^\sigma g^{\mu\nu}) - h_3^V \epsilon^{\mu\nu\sigma\alpha} k_{1\alpha} \right]. \quad (3.1.6)$$

The off-shell V^* is the propagator in our processes and couples to the massless electron current, as shown in Fig. 3.2(c), (d). After above-mentioned reduction of the vertices, there were some terms proportional to q^μ that yield zero upon contraction with the electron current, hence they are dropped from the above expressions. We note that although h^Z and f^γ appear together in the off-shell vertex of γZZ in Eq. (3.1.2), they decouple after choosing separate processes; the f^V appear only in $e^+e^- \rightarrow ZZ$, while the h^V appear only in $e^+e^- \rightarrow Z\gamma$. This decoupling simplifies our analysis as we can study two processes independent of each other when we perform a global fit to the parameters in Section 3.2.

3.1.1 Helicity formalism and polarizations of Z

We use tree level SM interactions along-with anomalous couplings shown in Eq. (3.1.1) for our analysis. The Feynman diagrams for these processes are given in the Fig. 3.2 where the

anomalous vertices are shown with shaded blobs. We compute the processes

$$e^-(p_1, \lambda_1) + e^+(p_2, \lambda_2) \rightarrow V^v(k_1, \lambda_3) + Z^\sigma(k_2, \lambda_4), \quad (3.1.7)$$

in SM as well as in aTGC as is given in Fig. 3.2. The helicity amplitude for this process in tree level in the SM is given by,

$$\begin{aligned} \mathcal{M}_{SM}^{ZV}(\lambda_1, \lambda_2, \lambda_3, \lambda_4) &= \bar{v}(p_2, \lambda_2) \left[\left(\frac{-ig_Z}{2} \gamma^\sigma (C_L P_L + C_R P_R) \right) \frac{l_1}{t} \left(\Gamma_{e^+e^-V}^v \right) \right. \\ &\quad \left. + \left(\Gamma_{e^+e^-V}^v \right) \frac{l_2}{u} \left(\frac{-ig_Z}{2} \gamma^\sigma (C_L P_L + C_R P_R) \right) \right] u(p_1, \lambda_1) \epsilon_\sigma^*(k_2, \lambda_4) \epsilon_\nu^*(k_1, \lambda_3), \end{aligned} \quad (3.1.8)$$

while the aTGC amplitudes with Z and γ mediator are given by,

$$\begin{aligned} \mathcal{M}_{Z(TGC)}^{ZV}(\lambda_1, \lambda_2, \lambda_3, \lambda_4) &= \bar{v}(p_2, \lambda_2) \left(\frac{-ig_Z}{2} \gamma^\rho (C_L P_L + C_R P_R) \right) u(p_1, \lambda_1) \left(\frac{-g_{\rho\mu} + \frac{q_\rho q_\mu}{m_Z^2}}{q^2 - m_Z^2} \right) \times \\ &\quad \left(\Gamma_{Z^*ZV}^{\mu\sigma\nu}(q, k_2, k_1) \right) \epsilon_\sigma^*(k_2, \lambda_4) \epsilon_\nu^*(k_1, \lambda_3) \quad \text{and} \\ \mathcal{M}_{\gamma(TGC)}^{ZV}(\lambda_1, \lambda_2, \lambda_3, \lambda_4) &= \bar{v}(p_2, \lambda_2) \left(ig_e \gamma^\rho \right) u(p_1, \lambda_1) \left(\frac{-g_{\rho\mu}}{q^2} \right) \times \\ &\quad \left(\Gamma_{\gamma^*ZV}^{\mu\sigma\nu}(q, k_2, k_1) \right) \epsilon_\sigma^*(k_2, \lambda_4) \epsilon_\nu^*(k_1, \lambda_3). \end{aligned} \quad (3.1.9)$$

The momentum p_i , k_i ($i = 1, 2$) and the helicities λ_i in Eqs. (3.1.8) and (3.1.9) are shown in the Feynman diagrams in Fig. 3.2. Various symbols used in the above equations are given by,

$$\begin{aligned} P_L &= \frac{1 - \gamma_5}{2}, \quad P_R = \frac{1 + \gamma_5}{2}, \quad l_1 = p_1 - k_1, \quad l_2 = p_1 - k_2, \\ t &= (p_1 - k_1)^2, \quad u = (p_1 - k_2)^2 \quad \text{with } \not{q} = \gamma^\mu a_\mu. \end{aligned} \quad (3.1.10)$$

The vertex for e^+e^-V is

$$\Gamma_{e^+e^-V}^v = ig_e \gamma^v, \quad \Gamma_{e^+e^-Z}^v = \frac{-ig_Z}{2} \gamma^v (C_L P_L + C_R P_R) \quad (3.1.11)$$

and the anomalous vertex $\Gamma_{\gamma^*ZV}^{\mu\sigma\nu}(q, k_2, k_1)$, $\Gamma_{Z^*ZV}^{\mu\sigma\nu}(q, k_2, k_1)$ are taken from the on-shell vertex in Eqs. (3.1.5) and (3.1.6). The transverse and longitudinal polarization vector for Z are

chosen to be

$$\begin{aligned}\epsilon^\mu(k, \pm) &= \frac{1}{\sqrt{2}} \{0, \mp \cos \theta, -i, \pm \cos \theta\}, \\ \epsilon^\mu(k, 0) &= \frac{1}{m_Z} \{|\vec{k}|, k_0 \sin \theta, 0, k_0 \cos \theta\}\end{aligned}\quad (3.1.12)$$

with θ being the polar angle of Z made with the e^- direction which is taken along the positive z -direction. For the photon, the transverse polarizations are same as for the Z with no longitudinal polarization. The kinematics for both processes are given in appendix B.1.

The total helicity amplitude including SM and aTGC will be

$$\begin{aligned}\mathcal{M}_{tot}^{ZV}(\lambda_{e^-}, \lambda_{e^+}, \lambda_\gamma, \lambda_Z) &= \mathcal{M}_{SM}^{ZV}(\lambda_{e^-}, \lambda_{e^+}, \lambda_\gamma, \lambda_Z) + \mathcal{M}_{Z(TGC)}^{ZV}(\lambda_{e^-}, \lambda_{e^+}, \lambda_\gamma, \lambda_Z) \\ &\quad + \mathcal{M}_{\gamma(TGC)}^{ZV}(\lambda_{e^-}, \lambda_{e^+}, \lambda_\gamma, \lambda_Z),\end{aligned}\quad (3.1.13)$$

denoting

$$\lambda_1 = \lambda_{e^-}, \lambda_2 = \lambda_{e^+}, \lambda_3 = \lambda_\gamma, \lambda_4 = \lambda_Z. \quad (3.1.14)$$

The helicity amplitudes for the anomalous part together with SM contributions for both ZZ and $Z\gamma$ processes are given in appendix B.1.

To calculate the polarization observables we calculate the production density matrix in Eq. (2.1.2) as,

$$\rho(\lambda_Z, \lambda'_Z) = \frac{1}{S} \frac{\beta}{64\pi^2 \hat{s}} \int_{d\Omega} d\Omega \frac{1}{2 \times 2} \sum_{\lambda_{e^-}, \lambda_{e^+}, \lambda_\gamma} \left(\mathcal{M}_{tot}^{ZV}(\lambda_{e^-}, \lambda_{e^+}, \lambda_\gamma, \lambda'_Z) \right)^\dagger \mathcal{M}_{tot}^{ZV}(\lambda_{e^-}, \lambda_{e^+}, \lambda_\gamma, \lambda_Z). \quad (3.1.15)$$

The $1/S$ factor is the final state symmetry factor which is $1/2$ for ZZ process and 1 for $Z\gamma$ process. The helicities of e , γ and Z can take values $\lambda_e, \lambda_\gamma \in \{-1, 1\}$ and $\lambda_Z \in \{-1, 0, 1\}$. The density matrix given above is used to calculate all the polarization observables and the total cross section in both processes using the technique discussed in chapter 2 which are given in appendix B.2.

3.1.2 Parametric dependence of observables

The dependences of the observables on the anomalous couplings for the ZZ and $Z\gamma$ processes are given in Tables 3.2 and 3.3, respectively. In the SM, the helicity amplitudes are real, thus the production density matrix elements in Eq. (2.1.2) are all real. This implies A_y , A_{xy} and A_{yz} are all zero in the SM: see Eq. (2.1.32). The asymmetries A_z and A_{xz} are also zero for

Table 3.2. Dependence of the polarization observables on the anomalous coupling in ZZ final state.

Observables	Linear terms	Quadratic terms
σ	f_5^Z, f_5^γ	$(f_4^\gamma)^2, (f_5^\gamma)^2, (f_4^Z)^2, (f_5^Z)^2, f_4^\gamma f_4^Z, f_5^\gamma f_5^Z$
$\sigma \times A_x$	f_5^γ, f_5^Z	–
$\sigma \times A_y$	f_4^γ, f_4^Z	–
$\sigma \times A_{xy}$	f_4^Z, f_4^γ	$f_4^Z f_5^\gamma, f_4^\gamma f_5^Z, f_4^\gamma f_5^\gamma, f_4^Z f_5^Z$
$\sigma \times A_{x^2-y^2}$	f_5^Z, f_5^γ	$(f_4^\gamma)^2, (f_5^\gamma)^2, (f_4^Z)^2, (f_5^Z)^2, f_4^\gamma f_4^Z, f_5^\gamma f_5^Z$
$\sigma \times A_{zz}$	f_5^Z, f_5^γ	$(f_4^\gamma)^2, (f_5^\gamma)^2, (f_4^Z)^2, (f_5^Z)^2, f_4^\gamma f_4^Z, f_5^\gamma f_5^Z$

Table 3.3. Dependence of the polarization observables on the anomalous coupling in Z γ final state.

Observables	Linear terms	Quadratic terms
σ	h_3^Z, h_3^γ	$(h_1^\gamma)^2, (h_3^\gamma)^2, (h_1^Z)^2, (h_3^Z)^2, h_1^\gamma h_1^Z, h_3^\gamma h_3^Z$
$\sigma \times A_x$	h_3^Z, h_3^γ	$(h_1^\gamma)^2, (h_3^\gamma)^2, (h_1^Z)^2, (h_3^Z)^2, h_1^\gamma h_1^Z, h_3^\gamma h_3^Z$
$\sigma \times A_y$	h_1^γ, h_1^Z	–
$\sigma \times A_{xy}$	h_1^γ, h_1^Z	–
$\sigma \times A_{x^2-y^2}$	h_3^γ, h_3^Z	–
$\sigma \times A_{zz}$	h_3^Z, h_3^γ	$(h_1^\gamma)^2, (h_3^\gamma)^2, (h_1^Z)^2, (h_3^Z)^2, h_1^\gamma h_1^Z, h_3^\gamma h_3^Z$

the SM couplings due to the forward-backward symmetry of the Z boson in the c.m. frame, owing to the presence of both t - and u -channel diagrams and unpolarized initial beams. After including anomalous couplings, A_y and A_{xy} receive a non-zero contribution, while A_z , A_{xz} and A_{yz} remain zero for the unpolarized initial beams.

From the list of non-vanishing asymmetries, only A_y and A_{xy} are CP -odd, while the others are CP -even. All the CP -odd observables are linearly dependent upon the CP -odd couplings, like f_4^V and h_1^V , while all the CP -even observables have only quadratic dependence on the CP -odd couplings. In the SM, the Z boson's couplings respect CP symmetry; thus A_y and A_{xy} vanish. Hence, any significant deviation of A_y and A_{xy} from zero at the collider will indicate a clear sign of CP -violating new physics interactions. Observables that have only a linear dependence on the anomalous couplings yield a *single interval limits* on these couplings. On the other hand, any quadratic appearance (like $(f_5^V)^2$ in σ) may yield more than one interval of the couplings, while putting limits. For the case of ZZ process, A_x and A_y do not have any quadratic dependence; hence they yield the cleanest limits on the CP -even and -odd parameters, respectively. Similarly, for the Z γ process, we have A_y , A_{xy} , and $A_{x^2-y^2}$, which

have only a linear dependence and provide clean limits. These clean limits, however, may not be the strongest limits as we will see in the following sections.

3.1.3 Sensitivity of observables to anomalous couplings

Sensitivity of an observable \mathcal{O} dependent on parameter \vec{f} is defined as

$$\mathcal{S}(\mathcal{O}(\vec{f})) = \frac{|\mathcal{O}(\vec{f}) - \mathcal{O}(\vec{f}=0)|}{\delta\mathcal{O}}, \quad (3.1.16)$$

where $\delta\mathcal{O} = \sqrt{(\delta\mathcal{O}_{stat.})^2 + (\delta\mathcal{O}_{sys.})^2}$ is the estimated error in \mathcal{O} . If the observable is an asymmetry, $A = (N^+ - N^-)/(N^+ + N^-)$, the error is given by,

$$\delta A = \sqrt{\frac{1-A^2}{\mathcal{L}\sigma} + \epsilon_A^2}, \quad (3.1.17)$$

where $N^+ + N^- = N_T = \mathcal{L}\sigma$, \mathcal{L} being the integrated luminosity of the collider. The error in the cross section σ will be given by,

$$\delta\sigma = \sqrt{\frac{\sigma}{\mathcal{L}} + (\epsilon\sigma)^2}. \quad (3.1.18)$$

Here ϵ_A and ϵ are the systematic fractional errors in A and σ , respectively, while remaining one are statistical errors.

3.1.3.a One-parameter sensitivity

For numerical calculations, we choose ILC running at c.m. energy $\sqrt{s} = 500$ GeV and integrated luminosity $\mathcal{L} = 100 \text{ fb}^{-1}$. We use $\epsilon_A = \epsilon = 0$ for most of our analysis. However, we do discuss the impact of systematic errors on our results. With this choice the sensitivity of all the polarization asymmetries of Z boson discussed in chapter 2, and the cross section have been calculated varying one parameter at a time. These sensitivities are shown in Figs. 3.3 and 3.4 for the ZZ and $Z\gamma$ processes, respectively, for each observable. In the $e^+e^- \rightarrow Z\gamma$ process we have taken a cut-off on the polar angle, $10^\circ \leq \theta_\gamma \leq 170^\circ$ to keep away from the beam pipe. For these limits, the analytical expressions shown in B.2 are used.

We see that in the ZZ process, the tightest constraint on f_4^γ at 1σ level comes from the asymmetry A_y owing to its linear and strong dependence on the coupling. For f_5^γ , both A_x and the cross section σ_{ZZ} , give comparable limits at 1σ but σ_{ZZ} gives a tighter limit at higher values of sensitivity. This is because the quadratic term in σ_{ZZ} comes with a higher power

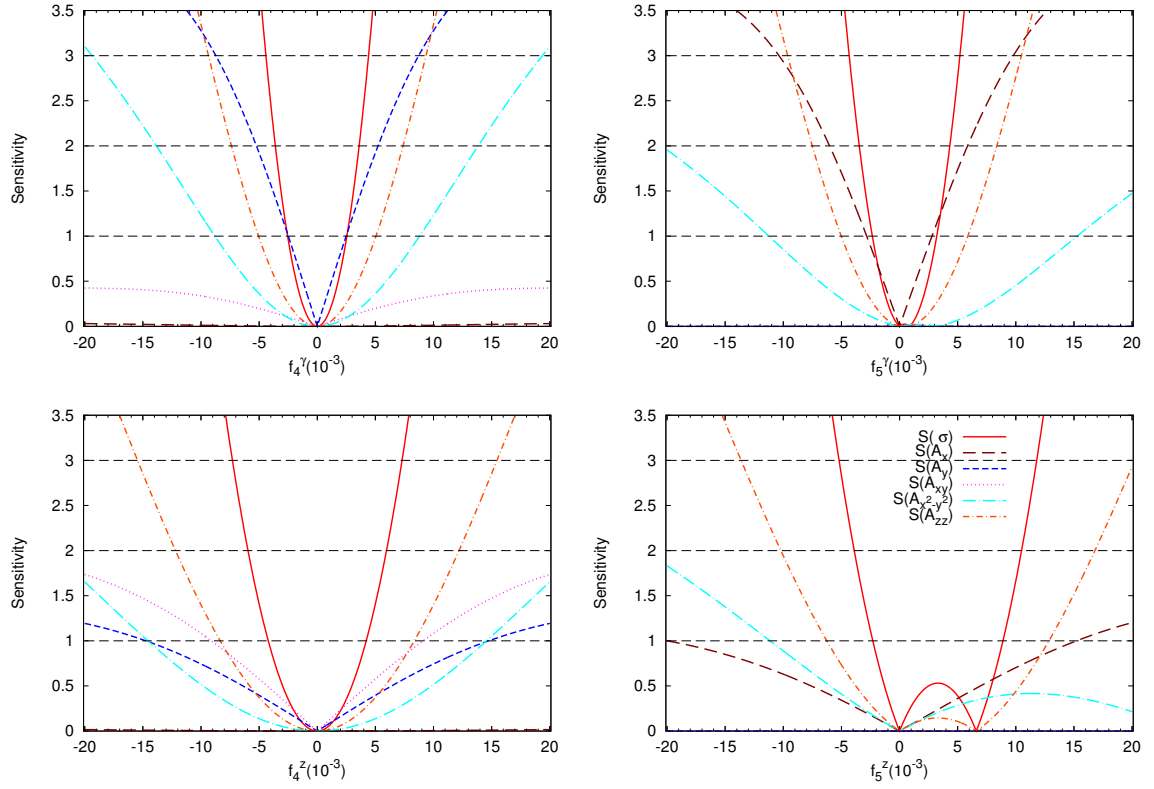


Figure 3.3. Sensitivity of the cross section and asymmetries to anomalous couplings for the process $e^+e^- \rightarrow ZZ$ with $\sqrt{s} = 500$ GeV and $\mathcal{L} = 100$ fb $^{-1}$.

of energy/momenta and hence a larger sensitivity. Similarly, the strongest limit on f_4^Z and f_5^Z as well comes from σ_{ZZ} . Though the cross section gives the tightest constrain on most of the coupling in ZZ process, our polarization asymmetries also provide comparable limits. Another noticeable fact is that σ_{ZZ} has a linear as well as quadratic dependence on f_5^Z and the sensitivity curve is symmetric about a point larger than zero. Thus, when we do a parameter estimation exercise, we will always have a bias toward a positive value of f_5^Z . The same is the case with the coupling f_5^γ , but the strength of the linear term is small and the sensitivity plot with σ_{ZZ} looks almost symmetric about $f_5^\gamma = 0$.

In the $Z\gamma$ process, the tightest constraint on h_1^γ comes from A_{xy} , on h_3^γ it comes from $\sigma_{Z\gamma}$, on it h_1^Z comes from A_y , and on h_3^Z it comes from A_x . The cross section $\sigma_{Z\gamma}$ and A_{zz} has a linear as well as quadratic dependence on h_3^γ , and $\sigma_{Z\gamma}$ and they give two intervals at 1σ level. Other observables can help resolve the degeneracy when we use more than one observables at a time. Still, the cross section prefers a negative value of h_3^γ , and it will be seen again in the multi-variate analysis. The coupling h_3^Z also has a quadratic appearance in the cross section, and it yields a bias toward negative values of h_3^Z .

The tightest limits on the anomalous couplings (at 1σ level), obtained using one observable at a time and varying one coupling at a time, are listed in Table 3.4 along with the

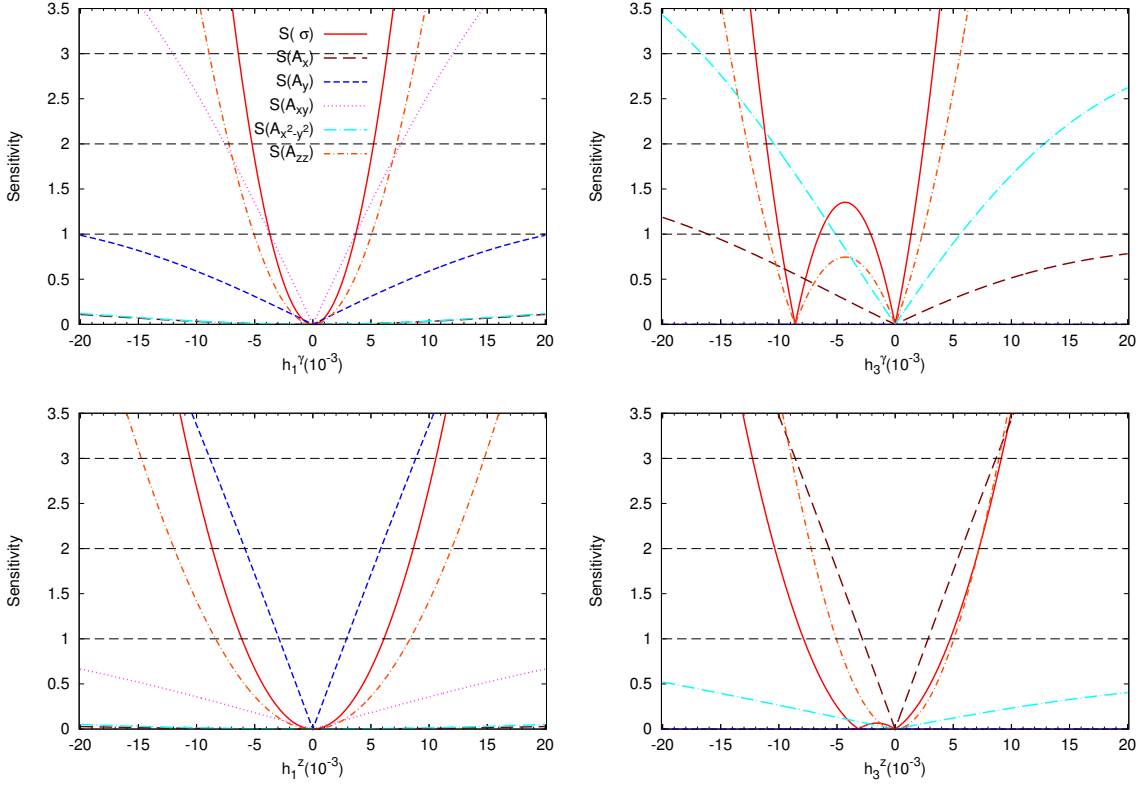


Figure 3.4. Sensitivity of the cross section and asymmetries to anomalous couplings for the process $e^+e^- \rightarrow Z\gamma$ with $\sqrt{s} = 500$ GeV, $\mathcal{L} = 100$ fb $^{-1}$, and $10^\circ \leq \theta_\gamma \leq 170^\circ$.

corresponding observables. A comparison between Tables 3.1 and 3.4 shows that an e^+e^- collider running at 500 GeV and 100 fb $^{-1}$ provides better limits on the anomalous coupling (f_i^V) in the ZZ process than the 7 TeV LHC at 5 fb $^{-1}$. For the $Z\gamma$ process the experimental limits are available from 8 TeV LHC with 19.6 fb $^{-1}$ luminosity (Table 3.1) and they are comparable to the single observable limits shown in Table 3.4. These limits can be further improved if we use all the observables in a χ^2 kind of analysis.

We can further see that the sensitivity curves for CP -odd observables, A_y and A_{xy} , has no or a very mild dependence on the CP -even couplings. The mild dependence comes through the cross section σ , sitting in the denominator of the asymmetries. We see that CP -even observables provide a tight constraint on CP -even couplings and CP -odd observables provide a tight constraint on the CP -odd couplings. Thus, not only can we study the two processes independently, it is possible to study the CP -even and CP -odd couplings almost independent of each other. To this end, we shall perform a two-parameter sensitivity analysis in the next subsection.

A note on the systematic error is in order. The sensitivity of an observable is inversely proportional to the size of its estimated error, Eq. (3.1.16). Including the systematic error will increase the size of the estimated error and hence decrease the sensitivity. For example,

Table 3.4. List of tightest limits on anomalous couplings at 1σ level and the corresponding observable obtained for $\sqrt{s} = 500$ GeV and $\mathcal{L} = 100$ fb $^{-1}$.

ZZ process			Z γ process		
Coupling	Limits	Comes from	Coupling	Limits	Comes from
$ f_4^\gamma $	$\leq 2.4 \times 10^{-3}$	A_y	$ h_1^\gamma $	$\leq 3.6 \times 10^{-3}$	A_{xy}, σ
$ f_4^Z $	$\leq 4.2 \times 10^{-3}$	σ	$ h_1^Z $	$\leq 2.9 \times 10^{-3}$	A_y
f_5^γ	$\in [-2.3, 2.7] \times 10^{-3}$	A_x, σ	h_3^γ	$\in [-2.1, 1.3] \times 10^{-3}$ or $\in [-9.9, -6.5] \times 10^{-3}$	σ
f_5^Z	$\in [-2.3, 8.8] \times 10^{-3}$	σ	$ h_3^Z $	$\leq 2.8 \times 10^{-3}$	A_x

including $\epsilon_A = 1\%$ to $\mathcal{L} = 100$ fb $^{-1}$ increases δA by a factor of 1.3 and dilutes the sensitivity by the same factor. This modifies the best limit on $|f_4^\gamma|$, coming from A_y , to 2.97×10^{-3} (dilution by a factor of 1.3); see Table 3.4. For the cross section, adding $\epsilon = 2\%$ systematic error increases $\delta\sigma$ by a factor of 1.5. The best limit on $|f_4^Z|$, coming from the cross section, changes to 5.35×10^{-3} , dilution by a factor of 1.2. Since the inclusion of the above systematic errors modifies the limits on the couplings only by 20% to 30%, we shall restrict ourselves to the statistical error for simplicity for rest of the analysis.

3.1.3.b Two-parameter sensitivity

We vary two couplings at a time, for each observable, and plot the $\mathcal{S} = 1$ (or $\Delta\chi^2 = 1$) contours in the corresponding parameter plane. These contours are shown in Fig. 3.5 and Fig. 3.6 for ZZ and Z γ processes, respectively. Asterisk (\star) marks in the middle of these plots denote the SM value, i.e., the (0,0) point. Each panel corresponds to two couplings that are varied and all others are kept at zero. The shapes of the contours, for a given observable, are a reflection of its dependence on the couplings as shown in Tables 3.2 and 3.3. For example, let us look at the middle-top panel of Fig. 3.5, i.e. the $(f_4^\gamma - f_5^\gamma)$ plane. The contours corresponding to the cross section (solid/red) and A_{zz} (short-dash-dotted/orange) are circular in shape due to their quadratic dependence on these two couplings with the same sign. The small linear dependence on f_5^γ makes these circles move toward a small positive value, as already observed in the one-parameter analysis above. The A_y contour (short-dash/blue) depends only on f_4^γ in the numerator and a mild dependence on f_5^γ enters through the cross section, sitting in the denominator of the asymmetries. The role of two couplings are exchanged for the A_x contour (big-dash/black). The A_{xy} contour (dotted/magenta) is hyperbolic in shape, indicating a dependence on the product $f_4^\gamma f_5^\gamma$, while a small shift toward positive f_5^γ value indicates a linear dependence on it. Similarly the symmetry about $f_4^\gamma = 0$ indicates no linear

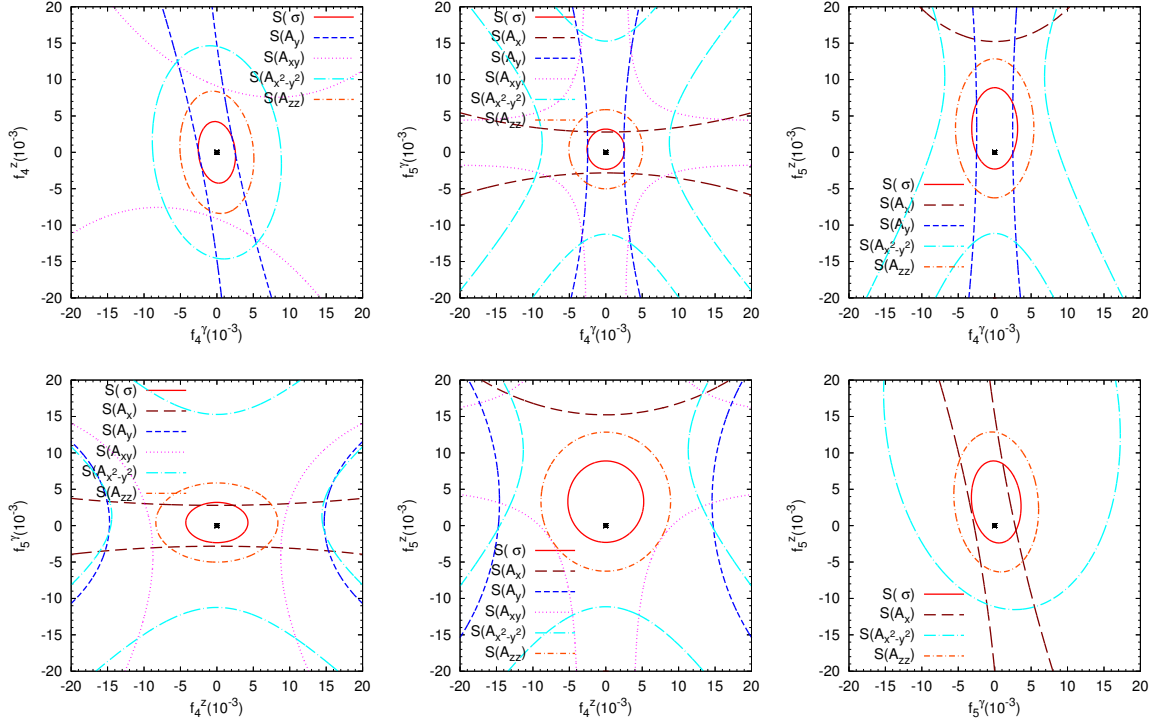


Figure 3.5. 1σ sensitivity contours ($\Delta\chi^2 = 1$) for cross section and asymmetries obtained by varying two parameters at a time and keeping the others at zero for the ZZ process at $\sqrt{s} = 500$ GeV and $\mathcal{L} = 100 \text{ fb}^{-1}$.

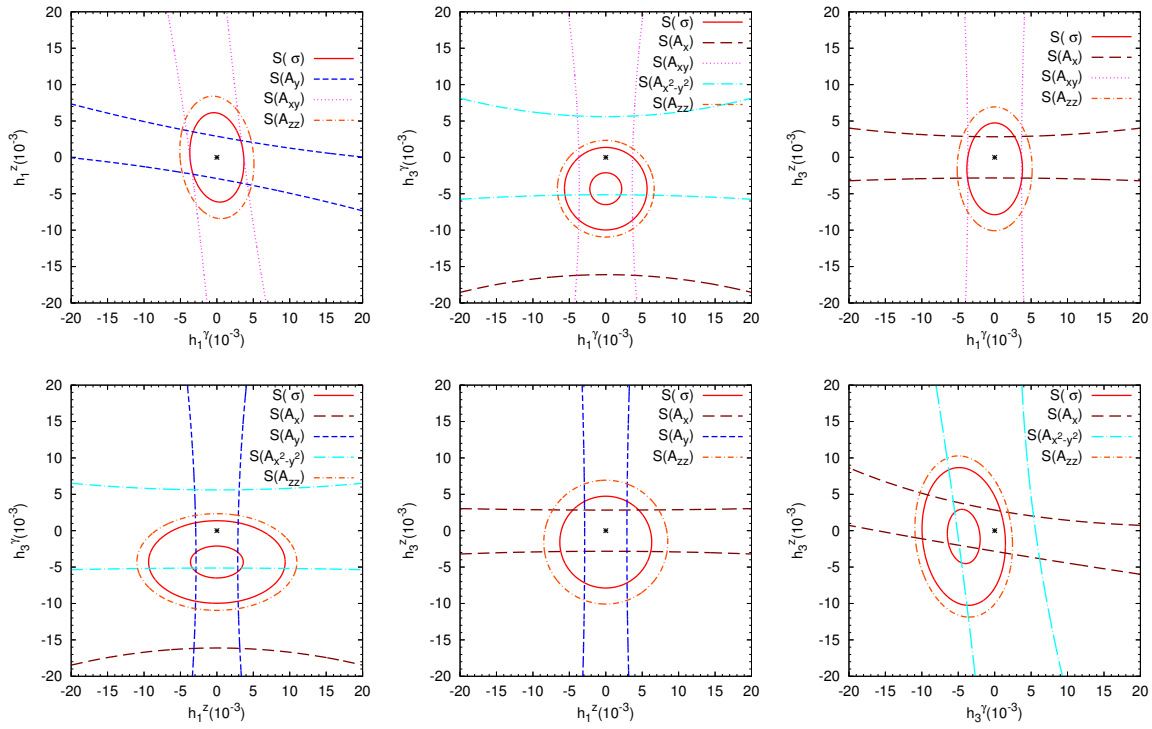


Figure 3.6. 1σ sensitivity contours ($\Delta\chi^2 = 1$) for cross section and asymmetries obtained by varying two parameters at a time and keeping the others at zero for the $Z\gamma$ process at $\sqrt{s} = 500$ GeV, $\mathcal{L} = 100 \text{ fb}^{-1}$, and $10^\circ \leq \theta_\gamma \leq 170^\circ$.

dependence on it for A_{xy} . All these observations can be confirmed by looking at Table 3.2 and the expressions in B.2. Finally, the shape of the $A_{x^2-y^2}$ contour (big-dash-dotted/cyan) indicates a quadratic dependence on two couplings with opposite sign. Similarly, all other panels can be read. Note that taking any one of the coupling to zero in these panels gives us the 1σ limit on the other couplings as found in the one-parameter analysis above.

In the contours for the $Z\gamma$ process, Fig. 3.6, one new kind of shape appears: the annular ring corresponding to $\sigma_{Z\gamma}$ in middle-top, left-bottom, and right-bottom panels. This shape corresponds to a largely linear dependence of the cross section on h_3^γ along with the quadratic dependence. By putting the other couplings to zero in above-mentioned panels, one obtains two disjoint intervals for h_3^γ at 1σ level as found before in the one-parameter analysis. The plane containing two CP -odd couplings, i.e. the left-top panel, has two sets of slanted contours corresponding to A_γ (short-dash/blue) and A_{xy} (dotted/magenta), the CP -odd observables. These observables depend upon both the couplings linearly and hence the slanted (almost) parallel lines. The rest of the panels can be read in the same way.

Till here, we have used only one observable at a time for finding the limits. A combination of all the observables would provide a much tighter limit on the couplings than provided by any one of them alone. Also, the shape, the position, and the orientation of the allowed region would change if the other two parameters were set to some value other than zero. A more comprehensive analysis requires varying all the parameters and using all the observables to find the parameter region of low χ^2 or high likelihood. The likelihood mapping of the parameter space is performed using the MCMC method in the next section.

3.2 Likelihood mapping of parameter space

In this section we perform a mock analysis of parameter estimation of anomalous coupling using *pseudo data* generated by MadGraph5. We choose two benchmark points for coupling parameters as follows:

$$\begin{aligned} \text{SM} & : f_{4,5}^V = 0.000, h_{1,3}^V = 0.000 \text{ and} \\ \text{aTGC} & : f_{4,5}^V = 0.005, h_{1,3}^V = 0.005 . \end{aligned} \quad (3.2.1)$$

For each of these benchmark points we generate events in MadGraph5 for *pseudo data* corresponding to ILC running at 500 GeV and integrated luminosity of $\mathcal{L} = 100 \text{ fb}^{-1}$. The

likelihood of a given point \vec{f} in the parameter space is defined by,

$$\mathcal{L}(\vec{f}) = \prod_i \exp \left[- \frac{(\mathcal{O}_i(\vec{f}) - \mathcal{O}_i(\vec{f}_0))^2}{2(\delta\mathcal{O}_i(\vec{f}_0))^2} \right], \quad (3.2.2)$$

where \vec{f}_0 defines the benchmark point. The product runs over the list of observables we have: the cross section and five non-zero asymmetries. We use the MCMC method to map the likelihood of the parameter space for each of the benchmark point and for both processes. The one-dimensional marginalized distributions and the two-dimensional contours on the anomalous couplings are drawn from the Markov chains using the GetDist package [205, 206].

3.2.1 MCMC analysis for $e^+e^- \rightarrow ZZ$

Here we look at the process $e^+e^- \rightarrow ZZ$ followed by the decays $Z \rightarrow l^+l^-$ and $Z \rightarrow q\bar{q}$, with $l^- = e^-, \mu^-$ in the

MadGraph5 simulations. The total cross section for this whole process would be

$$\sigma = \sigma(e^+e^- \rightarrow ZZ) \times 2 \text{Br}(Z \rightarrow l^+l^-) \text{Br}(Z \rightarrow q\bar{q}). \quad (3.2.3)$$

The theoretical values of $\sigma(e^+e^- \rightarrow ZZ)$ and all the asymmetries are obtained using expressions given in Appendix B and shown in the second column of Tables 3.5 and 3.6 for benchmark points SM and aTGC, respectively. The MadGraph5 simulated values for these observables are given in the third column of the two tables mentioned for two benchmark points. Using these simulated values as *pseudo data* we perform the likelihood mapping of the parameter space and obtain the posterior distributions for parameters and the observables. The last two columns of Tables 3.5 and 3.6 show the 68 % and 95 % Bayesian confidence interval (BCI) of the observables used. One naively expects 68 % BCI to roughly has the same size as the 1σ error in the *pseudo data*. However, we note that the 68 % BCI for all the asymmetries is much narrower than expected, for both benchmark points. This can be understood from the fact that the cross section provides the strongest limit on any parameter, as noticed in the earlier section, thus limiting the range of values for the asymmetries. However, this must allow 68 % BCI of the cross section to match the expectation. This indeed happens for the aTGC case (Table 3.6), but for the SM case, even the cross section is narrowly constrained compared to a naive expectation. The reason for this can be found in

the dependence of the cross section on the parameters. For most of the parameter space, the cross section is larger than the SM prediction, and only for a small range of parameter space, it can be smaller. This was already pointed out while discussing multi-valued sensitivity

Table 3.5. List of observables shown for the process $e^+e^- \rightarrow ZZ$ for the benchmark point SM with $\sqrt{s} = 500$ GeV: theoretical values (column 2), MadGraph5 simulated value for $\mathcal{L} = 100$ fb $^{-1}$ (column 3), 68 % (column 4) and 95 % (column 5) Bayesian confidence intervals (BCI).

Observables	Theoretical (SM)	MadGraph (SM, prior)	68 % BCI (posterior)	95 % BCI (posterior)
σ	38.096 fb	38.16 ± 0.62 fb	$38.61^{+0.31}_{-0.53}$ fb	$38.61^{+0.83}_{-0.74}$ fb
A_x	0.00099	0.0023 ± 0.0161	-0.0021 ± 0.0087	$-0.0021^{+0.016}_{-0.017}$
A_y	0	-0.0016 ± 0.0161	-0.0005 ± 0.0090	$-0.0005^{+0.017}_{-0.017}$
A_{xy}	0	0.0004 ± 0.0161	0.0001 ± 0.0036	$0.0001^{+0.0071}_{-0.0071}$
$A_{x^2-y^2}$	-0.02005	-0.0189 ± 0.0161	$-0.0166^{+0.0032}_{-0.0018}$	$-0.0166^{+0.0043}_{-0.0052}$
A_{zz}	0.17262	0.1745 ± 0.0159	$0.1691^{+0.0035}_{-0.0022}$	$0.1691^{+0.0051}_{-0.0056}$

Table 3.6. List of observables shown for the process $e^+e^- \rightarrow ZZ$ for the benchmark point aTGC with $\sqrt{s} = 500$ GeV. The rest of the details are the same as in Table 3.5.

Observables	Theoretical (aTGC)	MadGraph (aTGC, prior)	68 % BCI (posterior)	95 % BCI (posterior)
σ	43.307 fb	43.33 ± 0.6582 fb	43.40 ± 0.66 fb	43.40 ± 1.3 fb
A_x	-0.02954	-0.0308 ± 0.0151	$-0.0240^{+0.0087}_{-0.013}$	$-0.0240^{+0.021}_{-0.020}$
A_y	0.03424	0.0308 ± 0.0151	$0.0230^{+0.013}_{-0.0085}$	$0.0230^{+0.020}_{-0.022}$
A_{xy}	0.00574	0.0056 ± 0.0152	$0.0041^{+0.0076}_{-0.0063}$	$0.0041^{+0.015}_{-0.015}$
$A_{x^2-y^2}$	-0.00941	-0.0119 ± 0.0152	$-0.0116^{+0.0071}_{-0.0032}$	$-0.0116^{+0.0093}_{-0.012}$
A_{zz}	0.14057	0.1382 ± 0.0150	0.1401 ± 0.0035	$0.1401^{+0.0069}_{-0.0067}$

in Fig. 3.3. We found the lowest possible value of the cross section to be 37.77 fb, obtained for $f_4^{\gamma,Z} \approx 0$, $f_5^\gamma \sim 2 \times 10^{-4}$, and $f_5^Z \sim 3.2 \times 10^{-3}$. Thus, for most of the parameter space the anomalous couplings cannot emulate the negative statistical fluctuations in the cross section making the likelihood function, effectively, a one-sided Gaussian function. This forces the mean of posterior distribution to a higher value. We also note that the upper bound of the 68 % BCI for cross section (38.92 fb) is comparable to the expected 1σ upper bound (38.78 fb). Thus we have an overall narrowing of the range of the posterior distribution of the cross section values. This, in turns, leads to a narrow range of parameters allowed and hence narrow ranges for the asymmetries in the case of SM benchmark point. For the aTGC benchmark point, it is possible to emulate the negative fluctuations in cross section by varying the parameters, thus the corresponding posterior distributions compare with the expected 1σ fluctuations. The narrow ranges for the posterior distribution for all the asymmetries are due

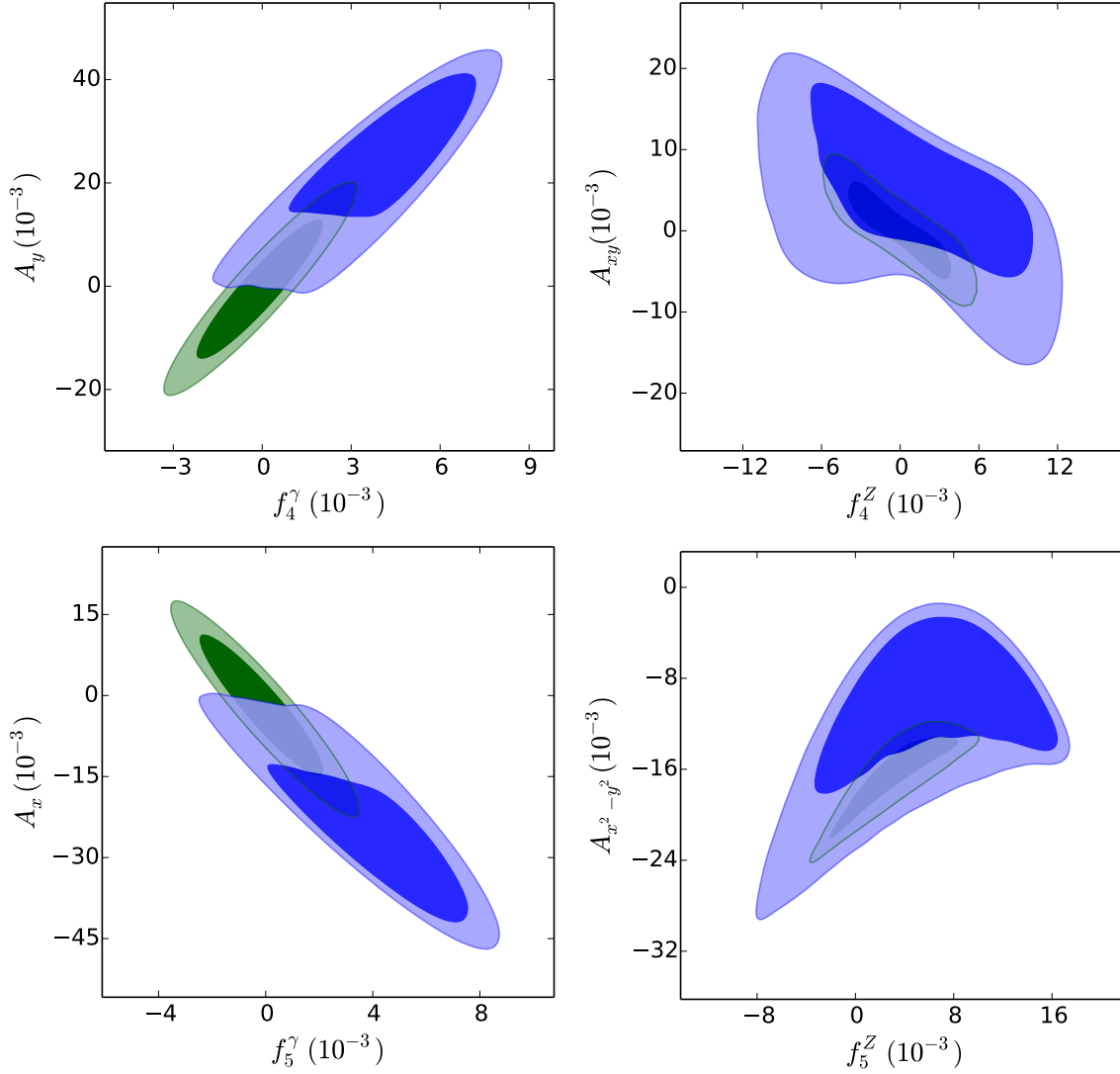


Figure 3.7. Two-dimensional marginalized contours showing most correlated observable for each parameter of the process $e^+e^- \rightarrow ZZ$. The upper transparent layer (*blue*) contours correspond to aTGC, while the lower layer (*green*) contours correspond to SM. The darker shade shows 68 % contours, while the lighter shade is for 95 % contours.

to the tighter constraints on the parameters coming from the cross section and correlation between the observables.

We are using a total of six observables, five asymmetries and one cross section for our analysis of two benchmark points; however, we have only four free parameters. This invariably leads to some correlations between the observables apart from the expected correlations between parameters and observables. Figure 3.7 shows the most prominently correlated observable for each of the parameters. The CP nature of observables is reflected in the parameter it is strongly correlated with. We see that A_y and A_{xy} are linearly dependent upon both f_4^γ and f_4^Z ; however, A_y is more sensitive to f_4^γ as shown in Fig. 3.3 as well. Similarly, for the other asymmetries and parameters, one can see a correlation which is consistent with the sensitivity plots in Fig. 3.3. The strong (and negative) correlation between A_{zz} and σ

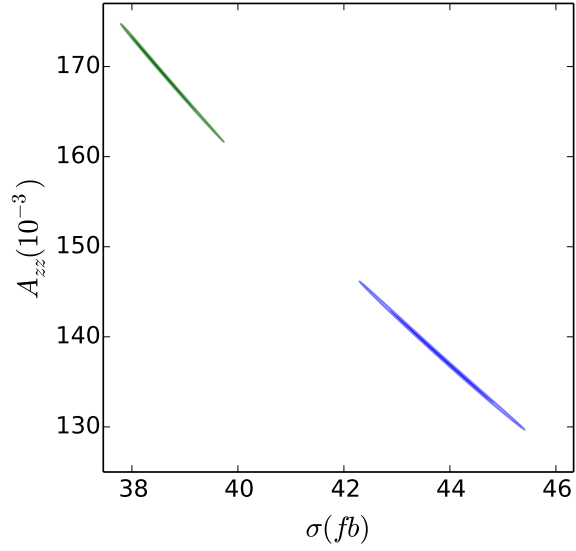


Figure 3.8. Two-dimensional marginalized contours showing correlation between A_{ZZ} and σ in the ZZ process. The rest of the details are the same as in Fig. 3.7.

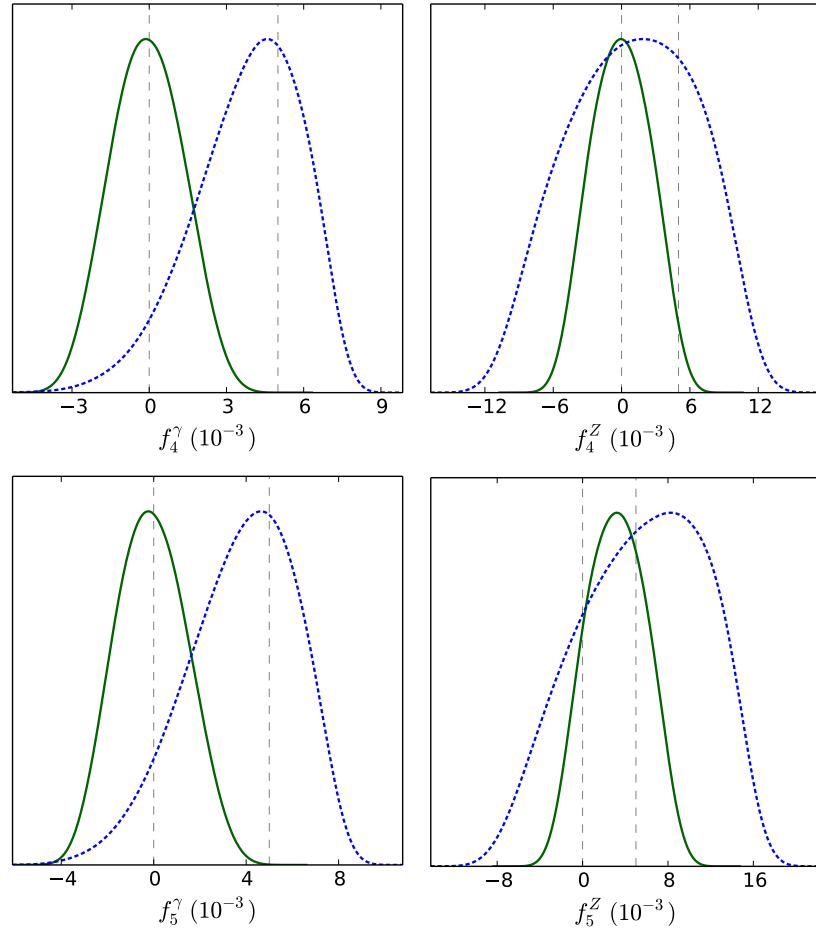


Figure 3.9. One-dimensional marginalized posterior distribution for the parameters of the process $e^+e^- \rightarrow ZZ$. Solid (green) lines are for SM and dashed (blue) lines are for aTGC hypothesis. The values of the parameters for the benchmark points are shown by vertical lines for reference.

shown in Fig. 3.8 indicates that any one of them is sufficient for the analysis, in principle. However, in practice, the cross section puts a much stronger limit than A_{ZZ} , which explains

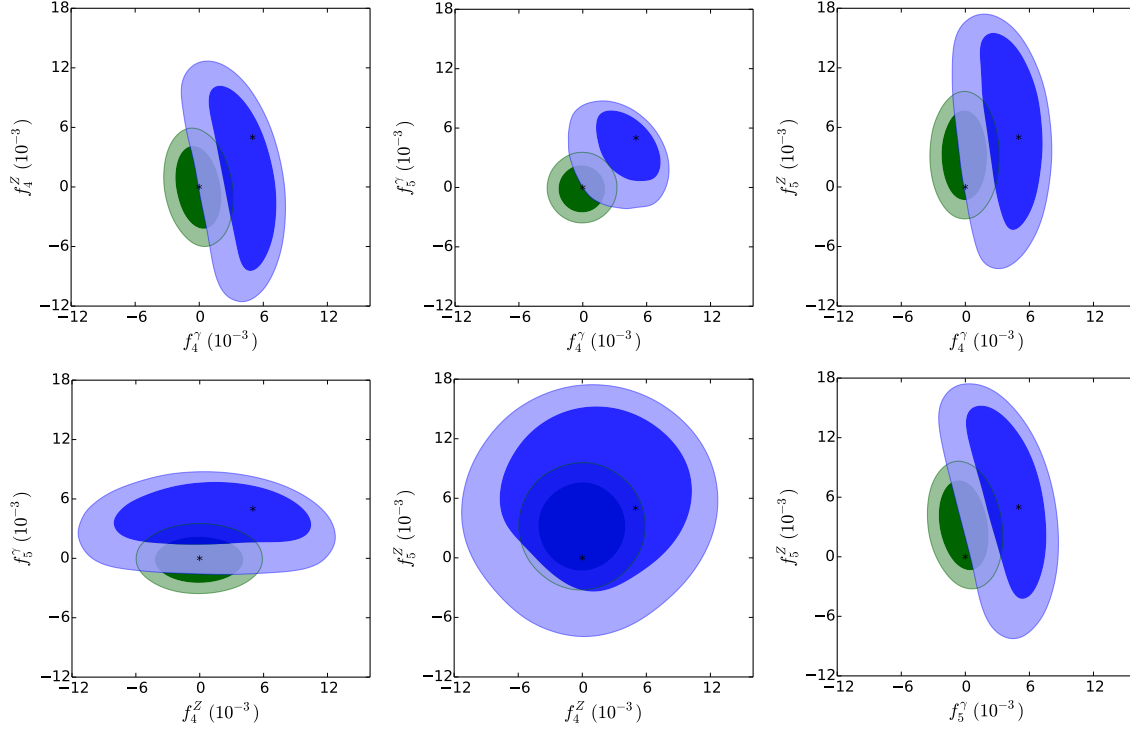


Figure 3.10. Two-dimensional marginalized contours showing correlations between parameters of the process $e^+e^- \rightarrow ZZ$. The other details are the same as in Fig. 3.7.

Table 3.7. The list of best-fit points, posterior 68 % and 95 % BCI for the parameters for the process $e^+e^- \rightarrow ZZ$ for both SM and aTGC benchmark points.

f_i^V	SM Benchmark			aTGC Benchmark		
	68 % BCI	95 % BCI	Best-fit	68 % BCI	95 % BCI	Best-fit
f_4^γ	-0.0001 ± 0.0014	$-0.0001^{+0.0027}_{-0.0027}$	-0.0002	$0.0038^{+0.0026}_{-0.0016}$	$0.0038^{+0.0037}_{-0.0042}$	0.0044
f_4^Z	0.0000 ± 0.0026	$0.0000^{+0.0049}_{-0.0049}$	-0.0002	$0.0010^{+0.0065}_{-0.0055}$	$0.0010^{+0.0098}_{-0.011}$	0.0050
f_5^γ	-0.0001 ± 0.0015	$-0.0001^{+0.0030}_{-0.0029}$	-0.0002	$0.0038^{+0.0029}_{-0.0019}$	$0.0038^{+0.0042}_{-0.0047}$	0.0057
f_5^Z	0.0032 ± 0.0028	$0.0032^{+0.0053}_{-0.0053}$	0.0000	$0.0057^{+0.0074}_{-0.0051}$	$0.0057^{+0.010}_{-0.011}$	0.0037

the much narrower BCI for it as compared to the 1σ expectation.

Finally, we come to the discussion of the parameter estimation. The marginalized one-dimensional posterior distributions for the parameters of ZZ production process are shown in Fig. 3.9, while the corresponding BCI along with best-fit points are listed in Table 3.7 for both benchmark points. The vertical lines near zero correspond to the true value of parameters for SM and the other vertical lines correspond to aTGC. The best-fit points are very close to the true values except for f_5^Z in the aTGC benchmark point due to the multi-valuedness of the cross section. The 95 % BCI of the parameters for two benchmark points overlap, and it appears as if they cannot be resolved. To see the resolution better, we plot two-dimensional posteriors in Fig. 3.10, with the benchmark points shown with an asterisk. Again we see that the 95 % contours do overlap as these contours are obtained after marginalizing over

non-shown parameters in each panel. Any higher-dimensional representation is not possible on paper, but we have checked three-dimensional scatter plot of points on the Markov chains and conclude that the shape of the *good likelihood* region is ellipsoidal for the SM point with the true value at its centre. The corresponding three-dimensional shape for the aTGC point is like a part of an ellipsoidal shell. Thus in full four-dimension, there will not be any overlap (see Section 3.2.3) and we can distinguish the two chosen benchmark points as it is quite obvious from the corresponding cross sections. However, left to only the cross section we would have the entire ellipsoidal shell as possible range of parameters for the aTGC case. The presence of asymmetries in our analysis helps narrow down to a part of the ellipsoid and hence aids the parameter estimation for the ZZ production process.

3.2.2 MCMC analysis for $e^+e^- \rightarrow Z\gamma$

Next we look at the process $e^+e^- \rightarrow Z\gamma$ and $Z \rightarrow l^+l^-$ with $l^- = e^-, \mu^-$ in the MadGraph5 simulations. The total cross section for this whole process is given by,

$$\sigma = \sigma(e^-e^+ \rightarrow Z\gamma) \times Br(Z \rightarrow l^+l^-). \quad (3.2.4)$$

The theoretical values of the cross section and asymmetries (using expression in B.2) are given in the second column of Tables 3.8 and 3.9 for SM and aTGC points, respectively. The tables contain the MadGraph5 simulated data for $\mathcal{L} = 100 \text{ fb}^{-1}$ along with 68 % and 95 % BCI for the observables obtained from the MCMC analysis. For the SM point, Table 3.8, we notice that the 68 % BCI for all the observables are narrower than the 1σ range of the *psuedo data* from MadGraph5. This is again related to the correlations between observables and the fact that the cross section has a lower bound of about 111 fb obtained for $h_3^\gamma \sim -4.2 \times 10^{-3}$ with other parameters close to zero. This lower bound of the cross section leads to narrowing of 68 % BCI for σ and hence for other asymmetries too, as observed in the ZZ production process. The 68 % BCI for $A_{x^2-y^2}$ and A_{zz} are particularly narrow. For A_{zz} , this is related to the strong correlation between $(\sigma - A_{zz})$, while for $A_{x^2-y^2}$ the slower dependence on h_3^γ along with strong dependence of σ on h_3^γ is the cause of a narrow 68 % BCI.

For the aTGC point, there is enough room for the negative fluctuation in the cross section, and hence no narrowing of the 68 % BCI is observed for it; see Table 3.9. The 68 % BCIs for A_x and A_y are comparable to the corresponding 1σ intervals, while the 68 % BCIs for other three asymmetries are certainly narrower than 1σ intervals. This narrowing, as discussed earlier, is due to the parametric dependence of the observables and their correlations. Each

Table 3.8. List of observables shown for the process $e^+e^- \rightarrow Z\gamma$ for the SM point with $\sqrt{s} = 500$ GeV and $\mathcal{L} = 100 \text{ fb}^{-1}$. The rest of the details are the same as in Table 3.5.

Observables	Theoretical (SM)	MadGraph (SM, prior)	68 % BCI (posterior)	95 % BCI (posterior)
σ	112.40 fb	112.6 ± 1.06 fb	$112.64^{+0.64}_{-0.91}$ fb	$112.6^{+1.5}_{-1.4}$ pb
A_x	0.00480	0.0043 ± 0.0094	0.0041 ± 0.0088	$0.0041^{+0.017}_{-0.018}$
A_y	0	-0.0011 ± 0.0094	-0.0009 ± 0.0088	-0.0009 ± 0.017
A_{xy}	0	0.0003 ± 0.0094	0.0001 ± 0.0065	0.0001 ± 0.012
$A_{x^2-y^2}$	0.00527	0.0056 ± 0.0094	$-0.0001^{+0.0064}_{-0.0034}$	$-0.0001^{+0.0079}_{-0.0096}$
A_{zz}	0.17819	0.1781 ± 0.0092	$0.1771^{+0.0043}_{-0.0031}$	$0.1771^{+0.0066}_{-0.0070}$

Table 3.9. List of observables shown for the process $e^+e^- \rightarrow Z\gamma$ for the aTGC point with $\sqrt{s} = 500$ GeV and $\mathcal{L} = 100 \text{ fb}^{-1}$. The rest of the details are the same as in Table 3.5.

Observables	Theoretical (aTGC)	MadGraph (aTGC, prior)	68 % BCI (posterior)	95 % BCI (posterior)
σ	122.0 fb	122.4 ± 1.11 fb	122.3 ± 1.0 fb	122.3 ± 2.0 fb
A_x	0.02404	0.0252 ± 0.0090	0.0263 ± 0.0093	0.0263 ± 0.018
A_y	-0.01775	-0.0165 ± 0.0090	-0.0172 ± 0.0092	-0.0172 ± 0.018
A_{xy}	-0.01350	-0.0104 ± 0.0090	$-0.0109^{+0.0069}_{-0.011}$	$-0.0109^{+0.017}_{-0.015}$
$A_{x^2-y^2}$	0.01440	0.0133 ± 0.0090	$0.0121^{+0.0055}_{-0.0010}$	$0.0121^{+0.0068}_{-0.012}$
A_{zz}	0.13612	0.1361 ± 0.0089	0.1351 ± 0.0041	$0.1351^{+0.0080}_{-0.0079}$

Table 3.10. The list of best-fit points, posterior 68 % and 95 % BCI for the parameters for the process $e^+e^- \rightarrow Z\gamma$ for both benchmark points.

h_i^V	SM Benchmark			aTGC Benchmark		
	68 % BCI	95 % BCI	Best-fit	68 % BCI	95 % BCI	Best-fit
h_1^γ	-0.0001 ± 0.0026	$-0.0001^{+0.0048}_{-0.0047}$	-0.0002	$0.0039^{+0.0047}_{-0.0031}$	$0.0039^{+0.0068}_{-0.0075}$	0.0040
h_1^Z	0.0003 ± 0.0028	$0.0003^{+0.0054}_{-0.0054}$	0.0001	0.0050 ± 0.0033	$0.0050^{+0.0064}_{-0.0063}$	0.0047
h_3^γ	$-0.0030^{+0.0036}_{-0.0020}$	$-0.0030^{+0.0045}_{-0.0054}$	0.0002	$0.00348^{+0.0036}_{-0.00086}$	$0.00348^{+0.0047}_{-0.0076}$	0.0056
h_3^Z	0.0004 ± 0.0028	$0.0004^{+0.0053}_{-0.0055}$	-0.0002	$0.0062^{+0.0030}_{-0.0035}$	$0.0062^{+0.0070}_{-0.0062}$	0.0052

of the parameters has a strong correlation with one of the asymmetries, as shown in Fig. 3.11. The narrow contours indicate that if one can improve the errors on the asymmetries, it will improve the parameter extraction. The steeper is the slope of the narrow contour the larger will be its improvement. We note that A_x and A_y have a steep dependence on the corresponding parameters. Thus even small variations in the parameters lead to large variations in the asymmetries. For A_{xy} and $A_{x^2-y^2}$ the parametric dependence is weaker, leading to their smaller variation with the parameters and hence narrower 68 % BCI.

For the parameter extraction, we look at their one-dimensional marginalized posterior distribution function, shown in Fig. 3.12 for the two benchmark points. The best-fit points along with 68 % and 95 % BCI are listed in Table 3.10. The best-fit points are very close to

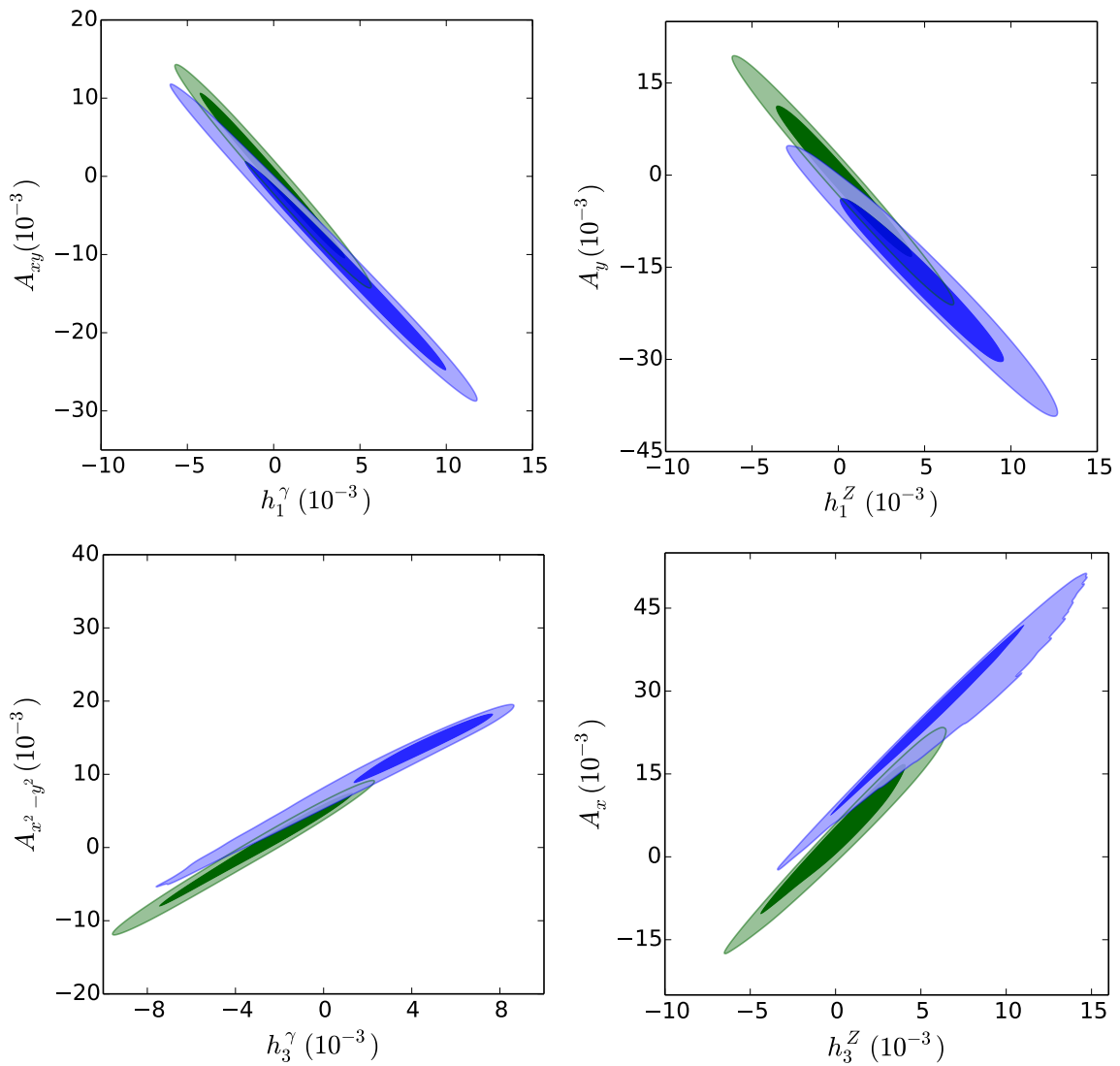


Figure 3.11. Two-dimensional marginalized contours showing most correlated observables for each parameter of the process $e^+e^- \rightarrow Z\gamma$ for two benchmark points. The rest of the details are the same as in Fig. 3.7.

the true values of the parameters, and so are the means of the BCI for all parameters except h_3^γ . For it, there is a downward movement in the value owing to the multi-valuedness of the cross section. Also, we note that the 95 % BCI for the two benchmark points largely overlap, making them seemingly un-distinguishable at the level of one-dimensional BCIs. To highlight the difference between two benchmark points, we look at two-dimensional BC contours as shown in Fig. 3.13. The 68 % BC contours (dark shades) can be roughly compared with the contours of Fig. 3.6. The difference is that Fig. 3.13 has all four parameters varying and all six observables are used simultaneously. The 95 % BC contours for the two benchmark points overlap despite the fact that the cross section can distinguish them very clearly. In full four-dimensional parameter space, the two contours do not overlap, and in the next section, we try to establish this.

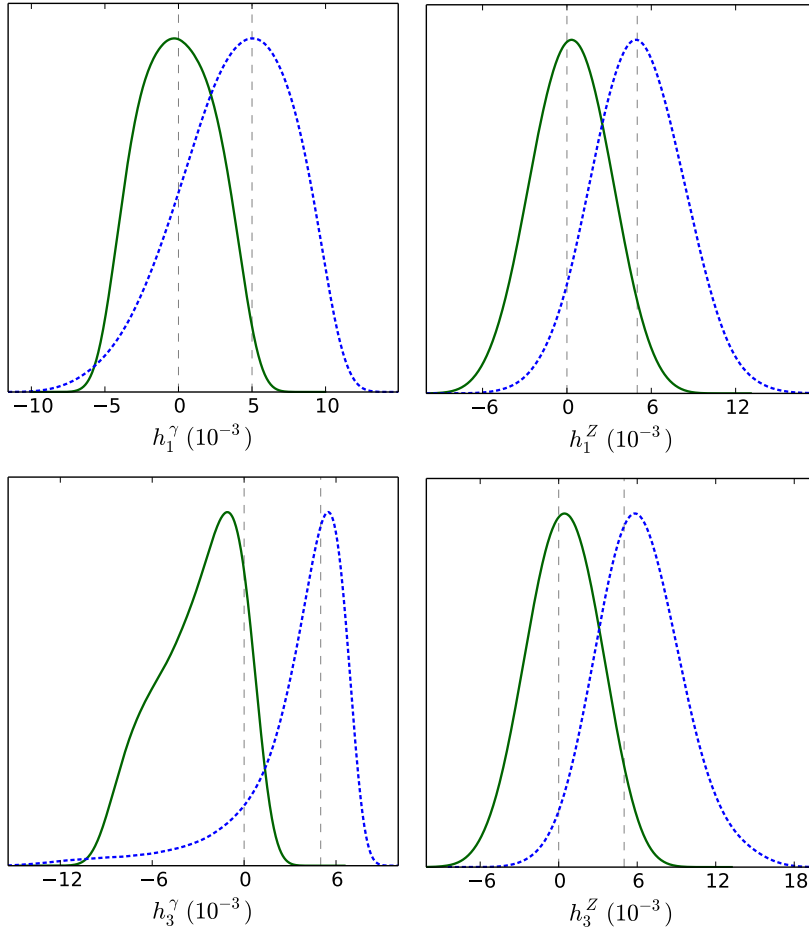


Figure 3.12. Posterior one-dimensional marginalized distributions for parameters of the process $e^+e^- \rightarrow Z\gamma$ for SM (green/solid) and aTGC (blue/dashed) points. Vertical lines denote the values of the benchmark points.

3.2.3 Separability of benchmark aTGCs

To depict the separability of the two benchmark points pictorially, we vary all four parameters for a chosen process as a linear function of one parameter, t , as

$$\vec{f}(t) = (1-t) \vec{f}_{\text{SM}} + t \vec{f}_{\text{aTGC}}, \quad (3.2.5)$$

such that $\vec{f}(0) = \vec{f}_{\text{SM}}$ is the coupling for the SM benchmark point and $\vec{f}(1) = \vec{f}_{\text{aTGC}}$ is the coupling for the aTGC point. In Fig. 3.14 we show the normalized likelihood for the point $\vec{f}(t)$ assuming the SM *pseudo data*, $\mathcal{L}(\vec{f}(t)|\text{SM})$, in solid/green line and assuming the aTGC *pseudo data*, $\mathcal{L}(\vec{f}(t)|\text{aTGC})$, in dashed/blue line. The left panel is for the ZZ production process and the right panel is for the $Z\gamma$ process. The horizontal lines correspond to the normalized likelihood being $e^{-\frac{1}{2}}$, while the full vertical lines correspond to the maximum value, which is normalized to 1. It is clearly visible that the two benchmark points are quite well separated in terms of the likelihood ratios. We have $\mathcal{L}(\vec{f}_{\text{aTGC}}|\text{SM}) \sim 8.8 \times 10^{-19}$

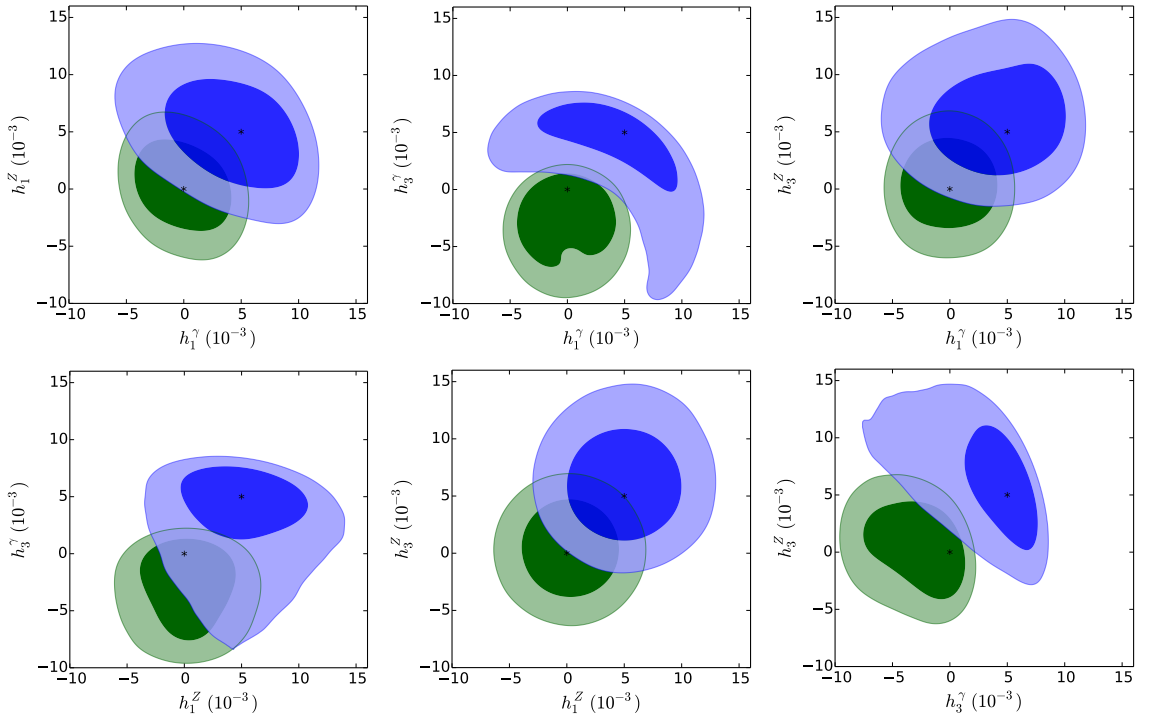


Figure 3.13. Two-dimensional contours for all pairs of the parameters in the process $e^+e^- \rightarrow Z\gamma$. The Upper transparent layers (*blue*) are for aTGC and the lower layers (*green*) for the SM showing the 68 % BC (*dark shades*) and 95 % BC (*light shades*) contours.

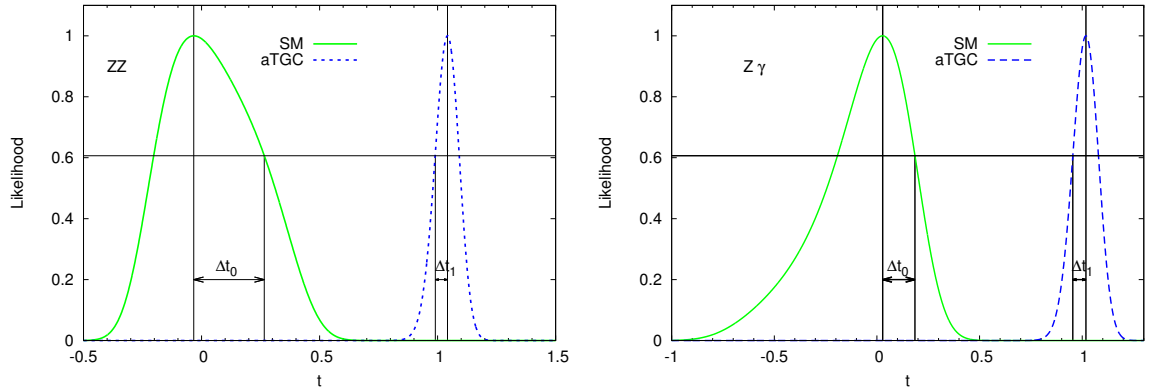


Figure 3.14. Likelihood ratio for the separability of benchmark points for ZZ (left) and $Z\gamma$ (right) final state: SM *pseudo data* are in solid (*green*) and aTGC *pseudo data* are in dotted (*blue*) lines.

for the ZZ process, and it means that the relative likelihood for the SM *pseudo data* being generated by the aTGC parameter value is 8.8×10^{-19} , i.e. negligibly small. Comparing the likelihood ratio to $e^{-n^2/2}$ we can say that the data is $n\sigma$ away from the model point. In this case, SM *pseudo data* is 9.1σ away from the aTGC point for the ZZ process. Similarly we have $\mathcal{L}(\vec{f}_{\text{SM}}|\text{aTGC}) \sim 1.7 \times 10^{-17}$, i.e. the aTGC *pseudo data* is 8.8σ away from the SM point for the ZZ process. For the $Z\gamma$ process we have $\mathcal{L}(\vec{f}_{\text{aTGC}}|\text{SM}) \sim 1.7 \times 10^{-24}$ (10.5σ) and $\mathcal{L}(\vec{f}_{\text{SM}}|\text{aTGC}) \sim 1.8 \times 10^{-25}$ (10.7σ). In all cases, the two benchmark points are well separable as clearly seen in Fig. 3.14.

3.3 Summary

Among all the polarization asymmetries, three of them, A_y , A_{xy} , and A_{yz} , are CP -odd and can be used to measure CP -Odd couplings in the production process. On the other hand, A_z , A_{xz} , and A_{yz} are P -odd observables, while A_x , $A_{x^2-y^2}$, and A_{zz} are CP - and P -even. The anomalous trilinear gauge couplings in the neutral sector, Eq. (3.1.1), are studied here using these asymmetries along with the cross section. The one and two parameter sensitivity of these asymmetries, together with cross section, are explored, and the one-parameter limits using one observable are listed in Table 3.4 for an unpolarized e^+e^- collider. For finding the best and simultaneous limits on the anomalous couplings, we performed a likelihood mapping using the MCMC method and the obtained limits are listed in Tables 3.7 and 3.10 for ZZ and $Z\gamma$ processes, respectively. The observables are calculated up to the quadratic in dimension-6 form factors. In practice, one should consider the effect of dimension-8 contribution at linear order. However, we choose to work with only dimension-6 in couplings with a partial contribution up to quadratic so as to compare the results with the current LHC constraints on dimension-6 parameters. With appropriate polarized initial beams, the anomalous couplings can be further constrained, which will be discussed in the next chapter.

4 The role of beam polarizations along with Z boson polarizations to probe aTGC in $e^+e^- \rightarrow ZZ/Z\gamma$

Contents

4.1	Beam polarizations and polarization observables.	68
4.2	Effect of beam polarization on the sensitivity	71
4.3	Average likelihood and best choice of beam polarization	74
4.4	Results with beam polarizations combined with their opposite values	79
4.5	Summary	83

The contents in this chapter are based on the published article in Ref. [99].

The future ILC [195–197] will be a precision testing machine [207] which will have the possibility of polarized initial beams. Two types of polarization, namely longitudinal and transverse, for both initial beams (e^- and e^+) will play an important role in precise measurement of various parameters, like the coupling among gauge bosons, Higgs coupling to the top quark, and Higgs coupling to the gauge boson. Beam polarization has the ability to enhance the relevant signal to background ratio and hence the sensitivity of observables [207–211]. It can also be used to separate CP -violating couplings from a CP -conserving one [83, 85, 93, 94, 101, 207, 212–216] if CP -violation is present in Nature. These potentials of the beam polarizations have been explored, for example, to study τ polarization [213], top quark polarization [217] and its anomalous couplings [218], littlest Higgs model [219], WWV couplings [208, 209, 220], Higgs couplings to gauge bosons [221–224].

In this chapter, we study the effect of beam polarizations (longitudinal only) on neutral aTGC using the polarization observables of Z in $e^+e^- \rightarrow ZZ/Z\gamma$ processes (as studied in the previous chapter, chapter 3). The neutral aTGC has been studied earlier with unpolarized beam in Refs. [84, 87–90, 96, 97, 104, 105] as well as with polarized beams in Refs. [82, 83, 85, 86, 91–93, 95, 100, 101]. Some of these studies have used a fixed beam polarizations to enhance the sensitivity of observables, while others have used two different sets of beam polarizations (opposite choices) to construct the observables. We see the implication in both the approaches.

4.1 Beam polarizations and polarization observables

The spin density matrix of a spin-1/2 particle, as introduced in Eq. (2.1.14), is given by,

$$\rho_{1/2} = \frac{1}{2} (\mathbb{I}_{2 \times 2} + \vec{p} \cdot \vec{\sigma}), \quad (4.1.1)$$

with σ_i being the Pauli spin matrices. After expansion, the above equation takes the form

$$\rho_{1/2} = \frac{1}{2} \begin{bmatrix} 1 + p_z & p_x - ip_y \\ p_x + ip_y & 1 - p_z \end{bmatrix}. \quad (4.1.2)$$

Thus the polarization density matrices for e^- and e^+ beams, in terms of longitudinal and transverse polarizations, are given by,

$$P_{e^-}(\lambda_{e^-}, \lambda'_{e^-}) = \frac{1}{2} \begin{bmatrix} (1 + \eta_3) & \eta_T \\ \eta_T & (1 - \eta_3) \end{bmatrix} \quad \text{and} \quad (4.1.3)$$

$$P_{e^+}(\lambda_{e^+}, \lambda'_{e^+}) = \frac{1}{2} \begin{bmatrix} (1 + \xi_3) & \xi_T e^{-i\delta} \\ \xi_T e^{i\delta} & (1 - \xi_3) \end{bmatrix}, \quad (4.1.4)$$

where η_3 and η_T (ξ_3 and ξ_T) are longitudinal and transverse polarization of e^- (e^+) with δ being the azimuthal angle between two transverse polarizations. The positive x -axis is taken along the transverse polarization of e^- and positive z -axis along its momentum.

The density matrix for the production of Z boson in the above process (Fig. 4.1) would

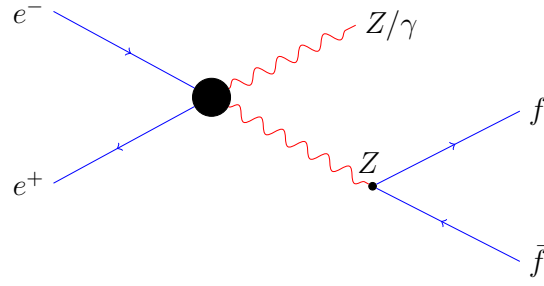


Figure 4.1. Feynman diagram for production of Z boson and its decay to a pair of fermions.

be

$$\rho(\lambda_Z, \lambda'_Z) = \sum_{\lambda_{e^-}, \lambda'_{e^-}, \lambda_{e^+}, \lambda'_{e^+}} \mathcal{M}^\dagger(\lambda'_{e^-}, \lambda'_{e^+}, \lambda'_Z) \times \mathcal{M}(\lambda_{e^-}, \lambda_{e^+}, \lambda_Z) \times P_{e^-}(\lambda_{e^-}, \lambda'_{e^-}) \times P_{e^+}(\lambda_{e^+}, \lambda'_{e^+}). \quad (4.1.5)$$

We note that the different helicities can take the following values:

$$\lambda_Z, \lambda'_Z \in \{-1, 0, 1\} \text{ and } \lambda_{e^\pm}, \lambda'_{e^\pm} \in \{-1, 1\}. \quad (4.1.6)$$

For the present work, we restrict ourselves only to the longitudinal beam polarizations, i.e. $\eta_T = 0 = \xi_T$. With the chosen beam polarizations, we construct the complete set of eight polarization observables for the Z boson along with the total cross section in the processes $e^+e^- \rightarrow ZZ/Z\gamma$. Among the 8 polarization asymmetries of Z boson in the given processes, the asymmetries A_z, A_{xz}, A_{yz} are zero in the SM (as has been seen in chapter 3) even with polarized beam owing to the forward-backward symmetry of produced Z. To make these asymmetries non-zero we redefine the polarization observables $\mathcal{O} \in \{p_z, T_{xz}, T_{yz}\}$ (corresponding to A_z, A_{xz}, A_{yz}) as

$$\mathcal{O} \rightarrow \tilde{\mathcal{O}} = \frac{1}{\sigma_Z} \left[\int_0^{c_{\theta_0}} \text{Comb}(\mathcal{O}, \rho(\lambda, \lambda')) dc_{\theta_Z} - \int_{-c_{\theta_0}}^0 \text{Comb}(\mathcal{O}, \rho(\lambda, \lambda')) dc_{\theta_Z} \right], \quad (4.1.7)$$

where c_{θ_0} is the beam pipe cut and $\text{Comb}(\mathcal{O}, \sigma(\lambda, \lambda'))$ is the combination of production density matrix corresponding the polarization observable \mathcal{O} (given in Eq. (2.1.32)). For example, with $\mathcal{O} = p_z$ one has

$$\text{Comb}(P_z, \rho(\lambda, \lambda')) = \rho(+1, +1) - \rho(-1, -1)$$

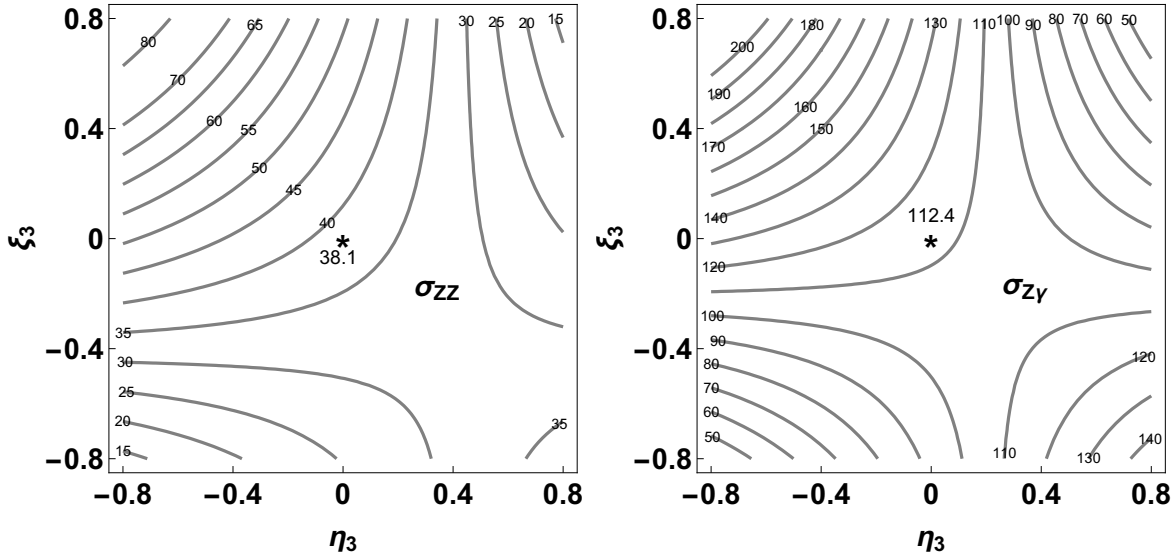


Figure 4.2. The SM cross section (in fb) for the process $e^+e^- \rightarrow ZZ/Z\gamma$ as a function of longitudinal beam polarizations η_3 (for e^-) and ξ_3 (for e^+) at $\sqrt{s} = 500$ GeV.

and the corresponding modified polarization is given by,

$$\tilde{p}_z = \frac{1}{\sigma_Z} \left[\int_0^{c_{\theta_0}} [\rho(+1, +1) - \rho(-1, -1)] dc_{\theta_Z} - \int_{-c_{\theta_0}}^0 [\rho(+1, +1) - \rho(-1, -1)] dc_{\theta_Z} \right]. \quad (4.1.8)$$

The asymmetries \tilde{A}_z corresponding to the modified polarization \tilde{P}_z is given by,

$$\tilde{A}_z \equiv \frac{1}{\sigma} \left(\sigma(c_{\theta_Z} \times c_{\theta_f} > 0) - \sigma(c_{\theta_Z} \times c_{\theta_f} < 0) \right). \quad (4.1.9)$$

Similarly A_{xz} and A_{yz} related to T_{xz} and T_{yz} are modified as,

$$\begin{aligned} \tilde{A}_{xz} &\equiv \frac{1}{\sigma} \left(\sigma(c_{\theta_Z} \times c_{\theta_f} c_{\phi_f} > 0) - \sigma(c_{\theta_Z} \times c_{\theta_f} c_{\phi_f} < 0) \right), \\ \tilde{A}_{yz} &\equiv \frac{1}{\sigma} \left(\sigma(c_{\theta_Z} \times c_{\theta_f} s_{\phi_f} > 0) - \sigma(c_{\theta_Z} \times c_{\theta_f} s_{\phi_f} < 0) \right). \end{aligned} \quad (4.1.10)$$

Redefining these asymmetries increases the total number of the non-vanishing observables to put simultaneous limit on the anomalous coupling and we expect limits tighter than reported earlier in chapter 3.

The total cross section (or the total number of events) of a process plays an important role in determining the sensitivity and the limits on the anomalous couplings. A tighter limit on the anomalous couplings can be obtained if the cross section can be enhanced. Beam polarization can enhance the cross section, and hence it is important to see how it depends on beam polarization. Fig. 4.2 shows the dependence of the cross sections σ_{ZZ} and $\sigma_{Z\gamma}$ on the longitudinal beam polarizations η_3 and ξ_3 at $\sqrt{s} = 500$ GeV. The asterisk mark on the

middle of the plots represents the unpolarized case. We notice that the cross section in the two processes are larger for a negative value of η_3 and a positive value of ξ_3 . The sensitivity on the cross section is expected to be high in the left-top corner of the $\eta_3 - \xi_3$ plane. This would convince us to set beam polarizations at the left-top corner for analysis. But the cross section is not the only observable; the asymmetries have different behaviour on beam polarizations. For example, A_x peaks at the right-bottom corner, i.e. we have an opposite behaviour compared to cross section, while A_z has a similar dependence as the cross section on the beam polarizations in both the processes. Processes involving W^\pm are also expected to have a higher cross section at the left-top corner of $\eta_3 - \xi_3$ plane as W couple to the left chiral electron. Anomalous couplings are expected to change the dependence of all the observables, including the cross section, on the beam polarizations. To explore this, we study the effect of beam polarizations on the sensitivity of cross section and other observables to anomalous couplings in the next section.

4.2 Effect of beam polarization on the sensitivity

The sensitivity of an observables \mathcal{O} depending on anomalous couplings \vec{f} given in Eq. (3.1.16) with a given beam polarizations η_3 and ξ_3 will now be given by,

$$\mathcal{S}(\mathcal{O}(\vec{f}, \eta_3, \xi_3)) = \frac{|\mathcal{O}(\vec{f}, \eta_3, \xi_3) - \mathcal{O}(\vec{0}, \eta_3, \xi_3)|}{|\delta\mathcal{O}(\eta_3, \xi_3)|}, \quad (4.2.1)$$

where $\delta\mathcal{O} = \sqrt{(\delta\mathcal{O}_{stat.})^2 + (\delta\mathcal{O}_{sys.})^2}$ is the estimated error in \mathcal{O} . The estimated error to cross section would be

$$\delta\sigma(\eta_3, \xi_3) = \sqrt{\frac{\sigma(\eta_3, \xi_3)}{\mathcal{L}} + \epsilon_\sigma^2 \sigma(\eta_3, \xi_3)^2}, \quad (4.2.2)$$

whereas the estimated error to the asymmetries would be

$$\delta A(\eta_3, \xi_3) = \sqrt{\frac{1 - A(\eta_3, \xi_3)^2}{\mathcal{L}\sigma(\eta_3, \xi_3)} + \epsilon_A^2}. \quad (4.2.3)$$

Here \mathcal{L} is the integrated luminosity, ϵ_σ and ϵ_A are the systematic fractional error in cross section and asymmetries, respectively. In these analyses we take $\mathcal{L} = 100 \text{ fb}^{-1}$, $\epsilon_\sigma = 0.02$ and $\epsilon_A = 0.01$ as a benchmark. We study the sensitivity of all the observables to the aTGC for some benchmark values and see the effect of beam polarization on them. Choosing a

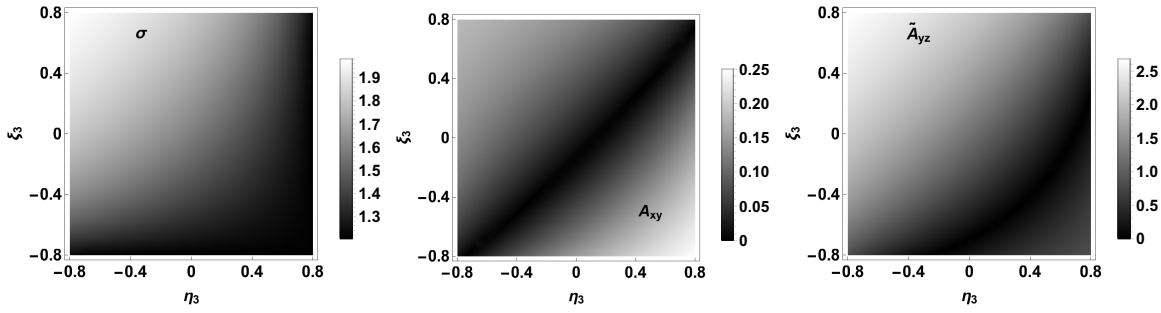


Figure 4.3. Effect of beam polarizations on sensitivity of cross section σ , A_{xy} and \tilde{A}_{yz} in the process $e^+e^- \rightarrow ZZ$ for anomalous couplings $\vec{f} = \{+3, +3, +3, +3\} \times 10^{-3}$ at $\sqrt{s} = 500$ GeV and $\mathcal{L} = 100 \text{ fb}^{-1}$.

benchmark value for the anomalous couplings to be

$$\vec{f} = \{f_4^\gamma, f_4^Z, f_5^\gamma, f_5^Z\} = \{+3, +3, +3, +3\} \times 10^{-3},$$

we show the sensitivities for σ , A_{xy} and \tilde{A}_{yz} in Fig. 4.3 as a function of beam polarizations. The sensitivities for the cross section and \tilde{A}_{yz} peak at the left-top corner of the plots. For A_{xy} sensitivity peak at the right-bottom corner, it is not much smaller in the left-top corner either. The sensitivities of all other asymmetries (not shown here) except \tilde{A}_z peaks at the left-top corner although the exact dependence on the beam polarization may differ. Thus, the combined sensitivity of all the observables is high on the left-top corner of the polarization plane making $(\eta_3, \xi_3) = (-0.8, +0.8)$ the best choice for the chosen benchmark coupling. This best choice, however, strongly depends upon the values of the anomalous couplings. We note that the best choice of the beam polarization is mainly decided by the behaviour of the cross section because most of the asymmetries also have similar dependences on the beam polarizations. This, however, does not mean that the cross section provides the best sensitivity or limits. For example, in Fig. 4.3 we can see that \tilde{A}_{yz} has a better sensitivity than the cross section. For the $Z\gamma$ process with the benchmark point

$$\vec{h} = \{h_1^\gamma, h_1^Z, h_3^\gamma, h_3^Z\} = \{+3, +3, +3, +3\} \times 10^{-3}$$

one obtains similar conclusions: the sensitivities of all observables peak at left-top corner of $\eta_3 - \xi_3$ plane (not shown) except for \tilde{A}_z .

For a complete analysis we need to use all the observables simultaneously. To this end we define a likelihood function considering the set of all the observables depending on the

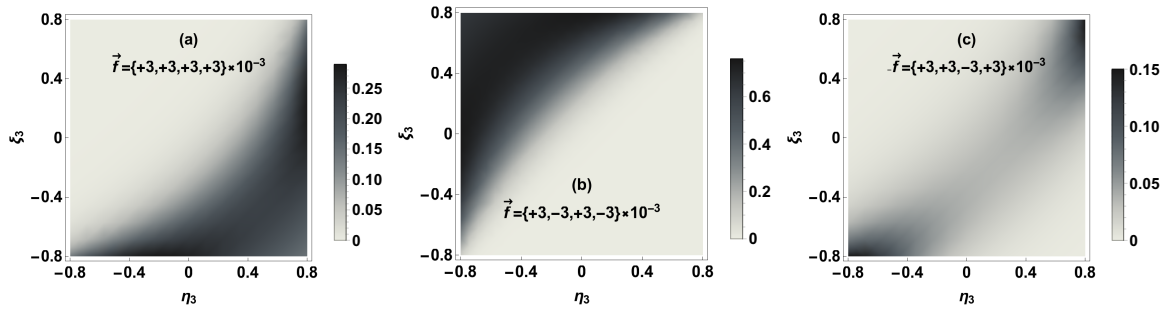


Figure 4.4. Likelihood $L(\{\mathcal{O}\}, \vec{f}; \eta_3, \xi_3)$ for three different benchmark anomalous couplings at $\sqrt{s} = 500$ GeV and $\mathcal{L} = 100$ fb $^{-1}$ in ZZ process.

anomalous coupling \vec{f} as,

$$L(\{\mathcal{O}\}, \vec{f}; \eta_3, \xi_3) = \exp \left[-\frac{1}{2} \sum_i \mathcal{S}(\mathcal{O}_i(\vec{f}, \eta_3, \xi_3))^2 \right], \quad (4.2.4)$$

i runs over the set of observables in a process. Maximum sensitivity of observables requires the likelihood to be minimum. The likelihood defined here is proportional to the p -value and hence the best choice of beam polarizations comes from the *minimum* likelihood or maximum distinguishability.

The beam polarization dependence of the likelihood for the ZZ process at the above chosen anomalous couplings is given in Fig. 4.4(a). The minimum of the likelihood falls in the left-top corner of the $\eta_3 - \xi_3$ plane as expected as most of the observables has higher sensitivity at this corner. For different anomalous couplings, the minimum likelihood changes its position in the $\eta_3 - \xi_3$ plane. We have checked the likelihood for 16 different corners of

$$\vec{f}_{\pm\pm\pm\pm} = \{\pm 3, \pm 3, \pm 3, \pm 3\} \times 10^{-3}$$

and they have different dependences on η_3, ξ_3 . Here we present the likelihood for three different choices of the anomalous couplings in Fig. 4.4. In Fig. 4.4(b), the minimum of the likelihood falls in the right-bottom corner where most of the observables have higher sensitivity. In Fig. 4.4(c) low likelihood falls in both diagonal corners in the $\eta_3 - \xi_3$ plane. This is because some of the observables prefer the left-top corner, while others prefer the right-bottom corner of the polarization plane for higher sensitivity. We have a similar behaviour for the likelihood in the Z γ process.

4.3 Average likelihood and best choice of beam polarization

In the previous section, we observed that, as the anomalous couplings change, the minimum likelihood region changes accordingly and hence the best choice of beam polarizations. So the best choice for the beam polarizations depends on the new physics in the process. If one knows the new physics one could tune the beam polarizations to have the best sensitivity for the analysis. But in order to have a suitable choice of beam polarizations irrespective of the possible new physics one needs to minimize the likelihood averaged over all the anomalous couplings. The likelihood function averaged over a volume in parameter space $V_{\vec{f}}$ would be defined as,

$$L(V_{\vec{f}}, \{\mathcal{O}\}; \eta_3, \xi_3) = \int_{V_{\vec{f}}} L(\{\mathcal{O}\}, \vec{f}; \eta_3, \xi_3) d\vec{f}. \quad (4.3.1)$$

This quantity is nothing but the *weighted volume* of the parameter space that is statistically consistent with the SM. The size of this weighted volume determines the limits on the parameters. The beam polarizations with the minimum averaged likelihood (or minimum weighted volume) is expected to be the average best choice for any new physics in the process. For numerical analysis, we choose the volume to be a hypercube in the 4 dimensional parameter space with sides equal to 2×0.05 (much larger than the available limits on them) in both the processes. The contribution to the average likelihood from the region outside this volume is negligible.

The average likelihood $L(V_{\vec{f}}, \{\mathcal{O}\}; \eta_3, \xi_3)$ in the ZZ process as a function of beam polarization is shown in Fig. 4.5 on log-scale. The dot on the middle of the the plot represents the unpolarized case and the cross mark at $P_{ZZ} = (+0.16, -0.16)$ represents the minimum averaged likelihood point, i.e., the best choice of beam polarizations. The unpolarized point, the best point and the points within two central contour in Fig. 4.5 have the same order of average likelihood and expected to give similar limits on anomalous couplings. The polarization point from darker contours corresponds to larger values of average likelihood, and it is expected to give relatively looser limits on anomalous couplings. To explore this, we estimate simultaneous limits using Markov-Chain–Monte-Carlo (MCMC) method at P_{ZZ} , unpolarized beam, and few other benchmark choices of beam polarizations. The limits thus obtained on the anomalous couplings for the ZZ process are listed in Table 4.1. We note that the limits for the best choice of polarizations (P_{ZZ}) are best but comparable to other nearby

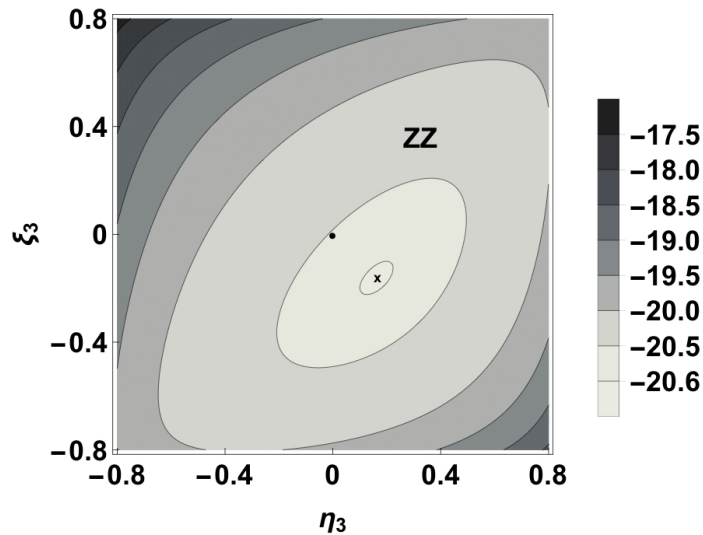


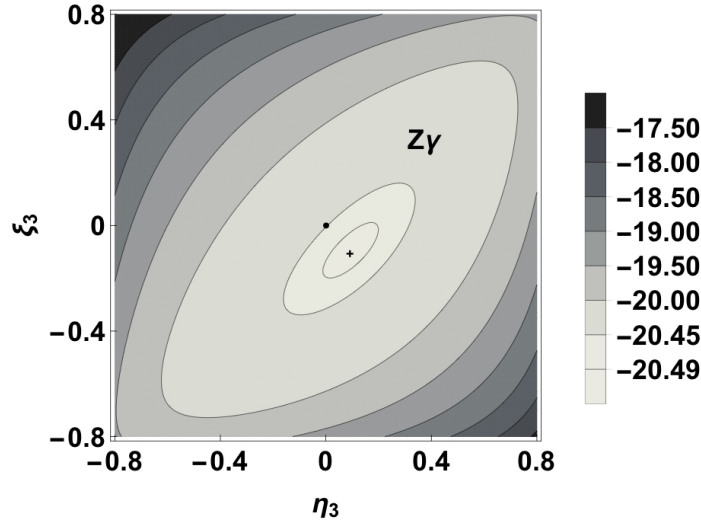
Figure 4.5. The log of average likelihood, $\log[L(V_{\tilde{f}^{\pm}}, \{\mathcal{O}\}; \eta_3, \xi_3)]$ as a function of beam polarization is shown for the ZZ process at $\sqrt{s} = 500$ GeV and $\mathcal{L} = 100$ fb $^{-1}$. The dot at the centre is the (0,0) point, while cross mark at $P_{ZZ} = (+0.16, -0.16)$ is the minimum likelihood point and hence the best choice of beam polarizations for ZZ process.

benchmark beam polarization including the unpolarized beams. This is due to the fact that the average likelihood is comparable for these cases. Further, the limits for $(+0.4, -0.4)$ and $(-0.4, +0.4)$ are increasingly bad, as these points correspond to the third and fourth contours, i.e., we have an increasingly larger average likelihood. The point $(-0.8, +0.8)$ has the largest average likelihood and the corresponding limits are the worst in Table 4.1. We also note that the limits for the unpolarized case in Table 4.1 are better than the ones reported in Ref. [98], when adjusted for the systematic errors. This improvement here is due to the inclusion of three new non-vanishing asymmetries \tilde{A}_z , \tilde{A}_{xz} and \tilde{A}_{yz} . Of these, \tilde{A}_{xz} has a linear dependence on $f_5^{\gamma,Z}$ with larger sensitivity to f_5^Z leading to about 30 % improvement in the limit. Similarly, the CP -odd asymmetry \tilde{A}_{yz} has a linear dependence on $f_4^{\gamma,Z}$ with larger sensitivity to f_4^Z and this again leads to about 30 % improvement in the corresponding limit. The asymmetry \tilde{A}_z has a quadratic dependence on all four parameters and has too poor sensitivity for all of them to be useful.

We do a similar analysis for the $Z\gamma$ process. The average likelihood $L(V_{\tilde{h}}, \{\mathcal{O}\}; \eta_3, \xi_3)$ is shown in Fig. 4.6 on log-scale. Here also the dot on the middle of the plot is for unpolarized case while the plus mark at $P_{Z\gamma} = (+0.09, -0.10)$ is for the minimum averaged likelihood and hence the best choice of beam polarizations. The corresponding simultaneous limits on the anomalous couplings h_i are presented in Table 4.2. Again we notice that the limits obtained for the best choice of the beam polarizations $P_{Z\gamma}$ are tighter than any other point on the polarization plane, yet comparable to the nearby polarization points within the two central

Table 4.1. List of simultaneous limits on the anomalous couplings obtained for $\sqrt{s} = 500$ GeV and $\mathcal{L} = 100 \text{ fb}^{-1}$ for different η_3 and ξ_3 from MCMC in ZZ process.

Beam polarizations	Limits on couplings (10^{-3})								Comments
	f_4^γ		f_4^Z		f_5^γ		f_5^Z		
(η_3, ξ_3)	68 %	95 %	68 %	95 %	68 %	95 %	68 %	95 %	
-0.80, +0.80	+7.3 -9.3	+13.0 -12.0	+15.0 -14.0	+18.0 -19.0	± 7.3	± 13.0	± 11.0	+19.0 -18.0	
-0.40, +0.40	± 3.1	+5.8 -5.7	± 4.4	+8.2 -8.4	± 3.3	+6.3 -6.2	+4.5 -5.2	+9.3 -8.5	
0.00, 0.00	± 1.7	± 3.3	± 2.5	± 4.8	± 1.9	+3.7 -3.6	+2.3 -2.7	+5.1 -4.6	Unpolarized point
+0.09, -0.10	± 1.7	± 3.2	± 2.4	+4.7 -4.6	± 1.8	+3.5 -3.4	+2.2 -2.6	+4.9 -4.5	$P_{Z\gamma}$, best for $Z\gamma$
+0.12, -0.12	± 1.6	± 3.1	± 2.4	± 4.7	± 1.8	+3.5 -3.4	+2.2 -2.6	+5.0 -4.5	P_{best} , combined best
+0.16, -0.16	± 1.6	± 3.1	± 2.4	± 4.7	± 1.8	+3.5 -3.4	+2.3 -2.7	+5.1 -4.5	P_{ZZ} , best for ZZ
+0.40, -0.40	± 1.9	± 3.7	± 3.2	+6.1 -6.2	± 2.1	+4.0 -4.1	+3.1 -3.7	+6.7 -6.0	
+0.80, -0.80	+5.3 -6.2	+9.8 -9.3	+9.7 -12.0	+18.0 -17.0	± 5.4	+9.5 -9.9	± 9.9	+17.0 -18.0	


Figure 4.6. Same as Fig. 4.5 but for the $Z\gamma$ process. The plus mark at $P_{Z\gamma} = (+0.09, -0.10)$ is the lowest likelihood point and hence the best choice of beam polarizations for $Z\gamma$ process.

contours in Fig. 4.6, including the unpolarized point. This again is due to the comparable values of the averaged likelihood of the two central contours containing $P_{Z\gamma}$ and the unpolarized point. The limits at the points $(+0.4, -0.4)$ and $(-0.4, +0.4)$ are worse as they fall in the fourth and fifth contour containing much larger likelihood values. Like the ZZ case the point $(-0.8, +0.8)$ has the largest average likelihood and the corresponding limits are the worst. The simultaneous limits for the unpolarized case (also the $P_{Z\gamma}$) turns out to be much better than the ones reported in Ref. [98] for $h_{1,3}^\gamma$ due to the inclusions of new asymmetries in the present analysis. The CP -odd asymmetry $\tilde{A}_{\gamma Z}$ has linear dependence on $h_1^{\gamma,Z}$ with a large sensitivity towards h_1^γ leading to an improvement in the corresponding limit by a factor of two compare to earlier report when adjusted for systematic errors. The limit on h_3^γ improves

Table 4.2. List of simultaneous limits on the anomalous couplings obtained for $\sqrt{s} = 500$ GeV and $\mathcal{L} = 100 \text{ fb}^{-1}$ for different η_3 and ξ_3 from MCMC in $Z\gamma$ process.

Beam polarizations	Limits on couplings (10^{-3})								Comments
	h_1^γ		h_1^Z		h_3^γ		h_3^Z		
(η_3, ξ_3)	68 %	95 %	68 %	95 %	68 %	95 %	68 %	95 %	
-0.80, +0.80	+7.7 -9.3	± 13.0	± 11.0	+18.0 -19.0	± 7.5	± 13.0	± 11.0	± 19.0	
-0.40, +0.40	± 3.9	+7.4 -7.5	± 6.5	± 12.0	+4.4 -3.7	+7.1 -8.0	± 6.6	+13.0 -12.0	
0.00, 0.00	± 1.6	± 3.1	± 3.7	+7.1 -7.0	+1.6 -1.4	+2.8 -3.0	± 3.6	± 7.1	Unpolarized point
+0.09, -0.10	± 1.5	± 2.9	± 3.6	± 7.0	+1.4 -1.3	+2.6 -2.8	± 3.6	+7.0 -7.1	$P_{Z\gamma}$, best for $Z\gamma$
+0.12, -0.12	± 1.5	± 2.9	± 3.7	± 7.1	± 1.4	+2.6 -2.8	± 3.6	± 7.1	P_{best} , combined best
+0.16, -0.16	± 1.5	± 3.0	± 3.7	+7.2 -7.3	+1.5 -1.3	+2.6 -2.8	± 3.7	+7.1 -7.3	P_{ZZ} , best for ZZ
+0.40, -0.40	± 2.4	± 4.6	± 5.2	± 10.0	+2.5 -2.2	+4.3 -4.7	± 5.2	± 10.0	
+0.80, -0.80	± 5.8	+10.0 -9.9	+11.0 -13.0	+19.0 -18.0	+5.8 -7.2	+10.0 -9.7	+13.0 -15.0	+19.0 -18.0	

by a factor of 3 owing to the asymmetry \tilde{A}_{xz} . The limits on $h_{1,3}^Z$ remain comparable.

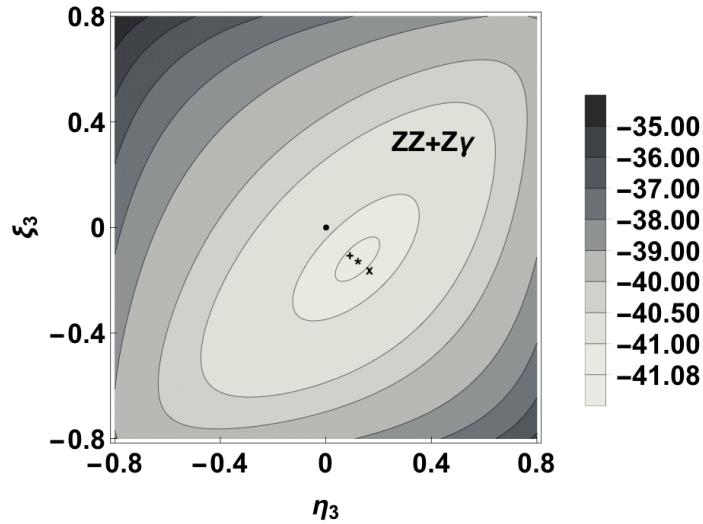


Figure 4.7. The log of average likelihood, $\log[L(V_{\vec{f}, \vec{h}}, \{\mathcal{O}\}; \eta_3, \xi_3)]$, is shown considering both the processes ZZ and $Z\gamma$ at $\sqrt{s} = 500$ GeV, $\mathcal{L} = 100 \text{ fb}^{-1}$. The asterisk mark at $P_{best} = (+0.12, -0.12)$ is the combined best choice for beam polarizations while the other points are for ZZ (cross mark) and $Z\gamma$ (plus mark).

The combined analysis of the processes ZZ and $Z\gamma$ is expected to change the best choice of beam polarizations and limits accordingly. For the average likelihood for these two processes the volume, in which one should average, will change to $V_{\vec{f}|\vec{h}} \rightarrow V_{\vec{F}}$, where $\vec{F} = \{\vec{f}, \vec{h}\}$ and observables from both processes should be added to the likelihood defined in Eq. 4.2.4. The combined averaged likelihood showing dependence on the beam polarizations for the two processes considered here is shown in Fig. 4.7. The dot on the middle of the plot is for the unpolarized case and asterisk mark at $P_{best} = (+0.12, -0.12)$ is the combined best choice

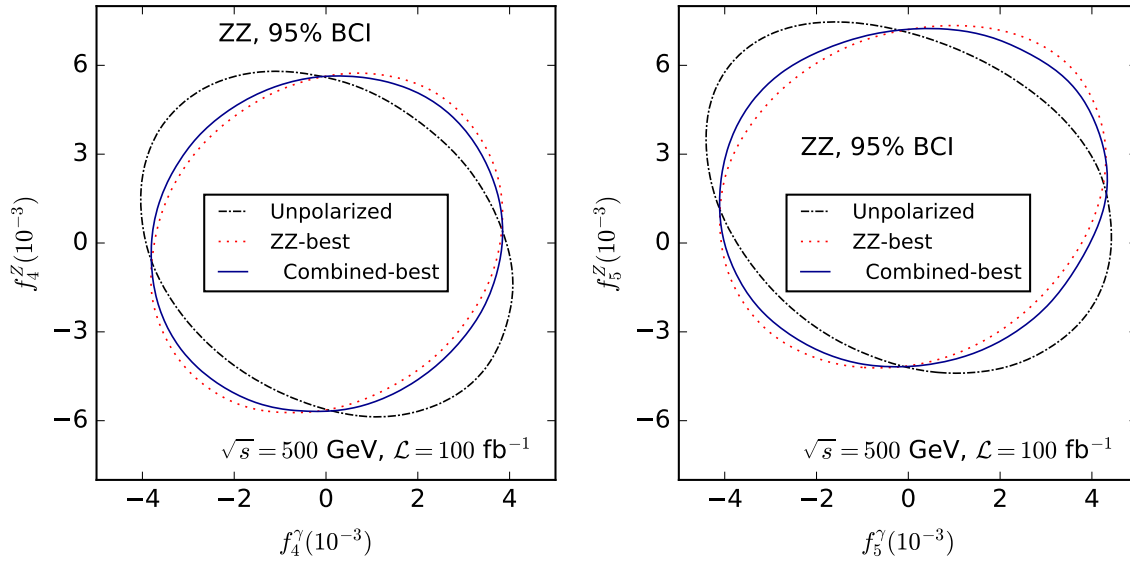


Figure 4.8. Two dimensional marginalised contours at 95 % confidence level (C.L.) from MCMC in ZZ production in f_4^γ - f_4^Z and f_5^γ - f_5^Z planes for unpolarized case, best choice for ZZ process and combined best choice of beam polarization including both processes.

of beam polarizations. Other points are due to P_{ZZ} and $P_{Z\gamma}$. The combined best choice point sits in between P_{ZZ} and $P_{Z\gamma}$. The limits, presented in Table 4.1 and 4.2, at the combined best choice of the beam polarizations are slightly weaker than the limit at the best choice points but comparable in both processes as expected. Thus the combined best choice can be a good benchmark beam polarizations for the process ZZ and $Z\gamma$ to study at ILC.

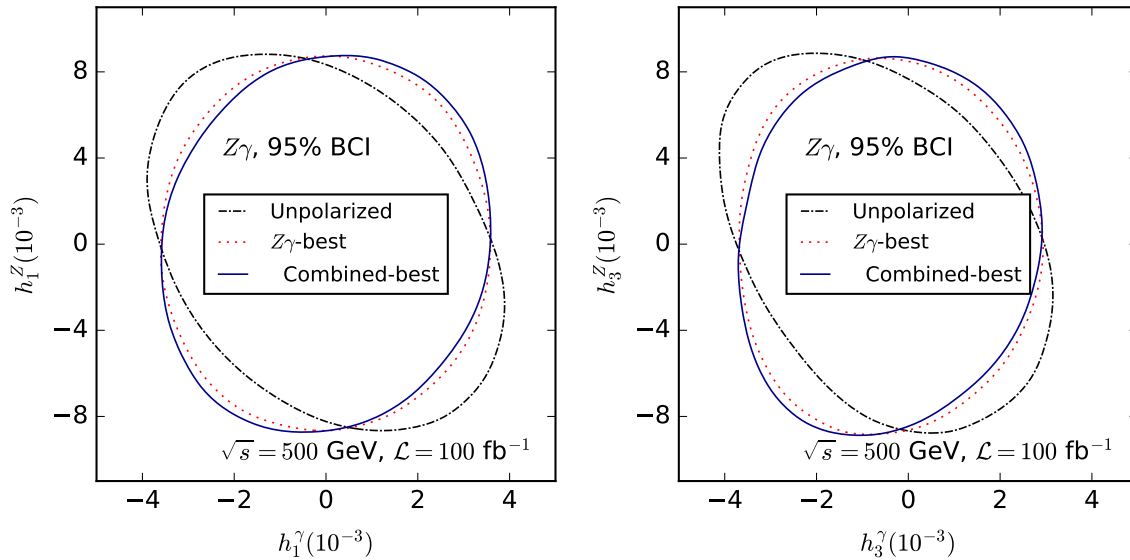


Figure 4.9. Two dimensional marginalised contours at 95 % C.L. from MCMC in $Z\gamma$ production in h_1^γ - h_1^Z and h_3^γ - h_3^Z planes for unpolarized case, best choice for $Z\gamma$ process and combined best choice of beam polarization including both processes.

The best choice of beam polarizations, obtained here, depends on the size of the estimated error of the observables and hence on the systematics ϵ_σ and ϵ_A . Numerical analysis shows

that the best choice points, for both processes separately and combined, move away from the unpolarized point along the cross diagonal axis towards the right-bottom corner on the $\eta_3 - \xi_3$ plane when ϵ_σ or ϵ_A or both are increased. For example, if we double ϵ_σ and ϵ_A both, i.e. we take $\epsilon_\sigma = 0.04$ and $\epsilon_A = 0.02$, the best choice points P_{ZZ} , $P_{Z\gamma}$ and P_{best} become $(+0.20, -0.20)$, $(+0.13, -0.12)$ and $(+0.17, -0.16)$, respectively. On the other hand, the best choice points move towards the unpolarized point as the systematics are decreased. For example, when the systematics are reduced by 1/2, i.e. for $\epsilon_\sigma = 0.01$ and $\epsilon_A = 0.005$, the best choice points for ZZ , $Z\gamma$ and for combined process move to $(+0.15, -0.15)$, $(+0.08, -0.08)$ and $(+0.11, -0.11)$, respectively. However, the best choice points do not move further closer to the unpolarized point when the size of systematics becomes smaller than the statistical one.

Similar analysis as presented in Fig. 4.7 can be done by combining many processes, as one should do, to choose a suitable beam polarizations at ILC. For many processes with different couplings, the volume in which one should do the average will change to $V_{\vec{f}/\vec{h}} = V_{\vec{F}}$, where \vec{F} would be the set of all couplings for all the processes considered. The set of observables $\{\mathcal{O}\}$ would include all the relevant observables from all the processes combined in the expression for the likelihood.

The best choice of beam polarization in both processes not only gives tighter constraints on the anomalous couplings but also changes the correlation among the couplings. In Figs. 4.8 and 4.9, we show correlations among the anomalous couplings in both processes in marginalised contours at 95 % BCI from MCMC for the unpolarized case as well as three best choices of beam polarizations. The correlations got reduced in the best choices of beam polarization apart from tightening the limits on them.

4.4 Results with beam polarizations combined with their opposite values

The above analyses of obtaining best choice of beam polarization and the limits on the couplings is done using a fixed choice of beam polarizations. However, an e^+e^- machine will run with longitudinal beam polarizations switching between (η_3, ξ_3) and $(-\eta_3, -\xi_3)$ [207]. For integrated luminosity of 100 fb^{-1} , one will have half the luminosity (50 fb^{-1}) available for each polarization configuration. We combine the beam polarization $(+\eta_3, +\xi_3)$ and its

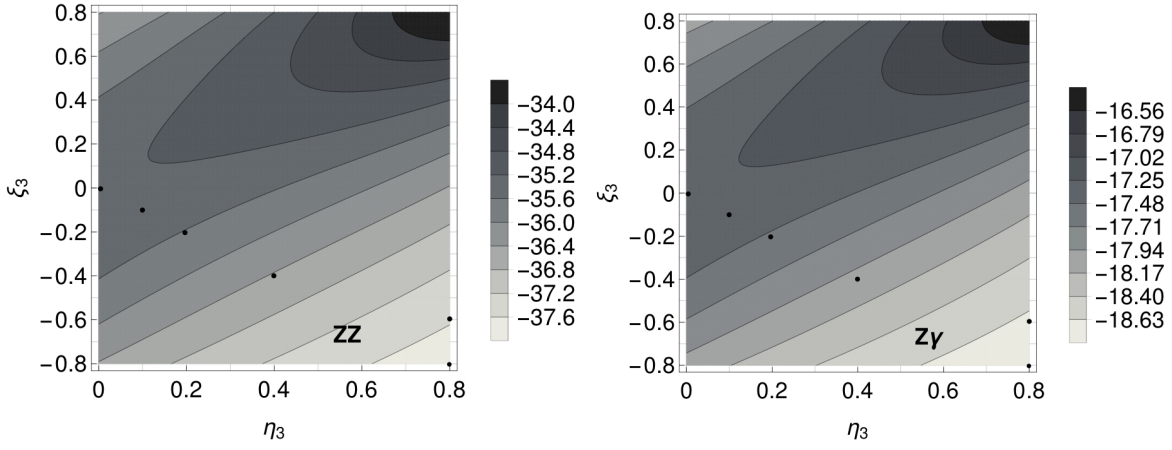


Figure 4.10. The log of average likelihood, $\log[L(V_{\tilde{f}}, \{\mathcal{O}\}; \eta_3, \xi_3)]$ as a function of beam polarization ($\pm\eta_3, \pm\xi_3$) is shown for the ZZ (left-panel) and $Z\gamma$ (right-panel) process for $\sqrt{s} = 500$ GeV and $\mathcal{L} = 100 \text{ fb}^{-1}$. The dots (\bullet) on the plots are the choice of polarizations for obtaining simultaneous limits given in Table 4.3 and Figs. 4.11 & 4.12.

opposite ($-\eta_3, -\xi_3$) at the level of χ^2 as,

$$\chi_{tot}^2(\pm\eta_3, \pm\xi_3) = \sum_i^N \left(\chi^2[obs_i(+\eta_3, +\xi_3)] + \chi^2[obs_i(-\eta_3, -\xi_3)] \right), \quad (4.4.1)$$

where $N = 9$ is the total number of observables.

Table 4.3. List of simultaneous limits at 95 % C.L. on the anomalous couplings (10^{-3}) obtained for $\sqrt{s} = 500$ GeV and $\mathcal{L} = 100 \text{ fb}^{-1}$ for different beam polarization ($\pm\eta_3, \pm\xi_3$) from MCMC in ZZ and $Z\gamma$ processes.

f^V, h^V	(0.0, 0.0)	($\pm 0.1, \mp 0.1$)	($\pm 0.2, \mp 0.2$)	($\pm 0.4, \mp 0.4$)	($\pm 0.8, \mp 0.6$)	($\pm 0.8, \mp 0.8$)
f_4^γ	+3.3 -3.3	+3.0 -3.0	+2.9 -2.9	+2.6 -2.6	+2.1 -2.1	+2.0 -2.0
f_4^Z	+4.8 -4.8	+4.4 -4.4	+4.3 -4.3	+4.0 -3.9	+3.6 -3.6	+3.4 -3.4
f_5^γ	+3.7 -3.6	+3.3 -3.3	+3.1 -3.2	+2.6 -2.8	+2.1 -2.3	+2.0 -2.1
f_5^Z	+5.1 -4.6	+6.0 -2.8	+5.8 -2.8	+5.3 -2.6	+4.7 -2.5	+4.4 -2.4
h_1^γ	+3.1 -3.1	+2.7 -2.7	+2.6 -2.5	+2.3 -2.3	+2.0 -2.0	+1.9 -1.9
h_1^Z	+7.0 -7.0	+6.1 -6.0	+5.5 -5.6	+4.4 -4.4	+3.4 -3.5	+3.3 -3.2
h_3^γ	+2.6 -2.8	+2.0 -2.9	+2.0 -2.7	+1.8 -2.4	+1.7 -2.0	+1.6 -1.9
h_3^Z	+7.0 -7.1	+6.0 -5.8	+5.4 -5.2	+4.2 -4.1	+3.2 -3.1	+3.0 -2.9

We calculate the *weighted-volume* in Eq. (4.3.1) using the total χ^2 given in Eq. (4.4.1) for both ZZ and $Z\gamma$ production processes and they are shown in Fig. 4.10 as a function of beam polarization ($\pm\eta_3, \pm\xi_3$). The *weighted-volume* or the averaged likelihood decreases along the $\pm\eta_3 = \mp\xi_3$ line and the beam polarization ($\pm 0.8, \mp 0.8$) poses the minimum values

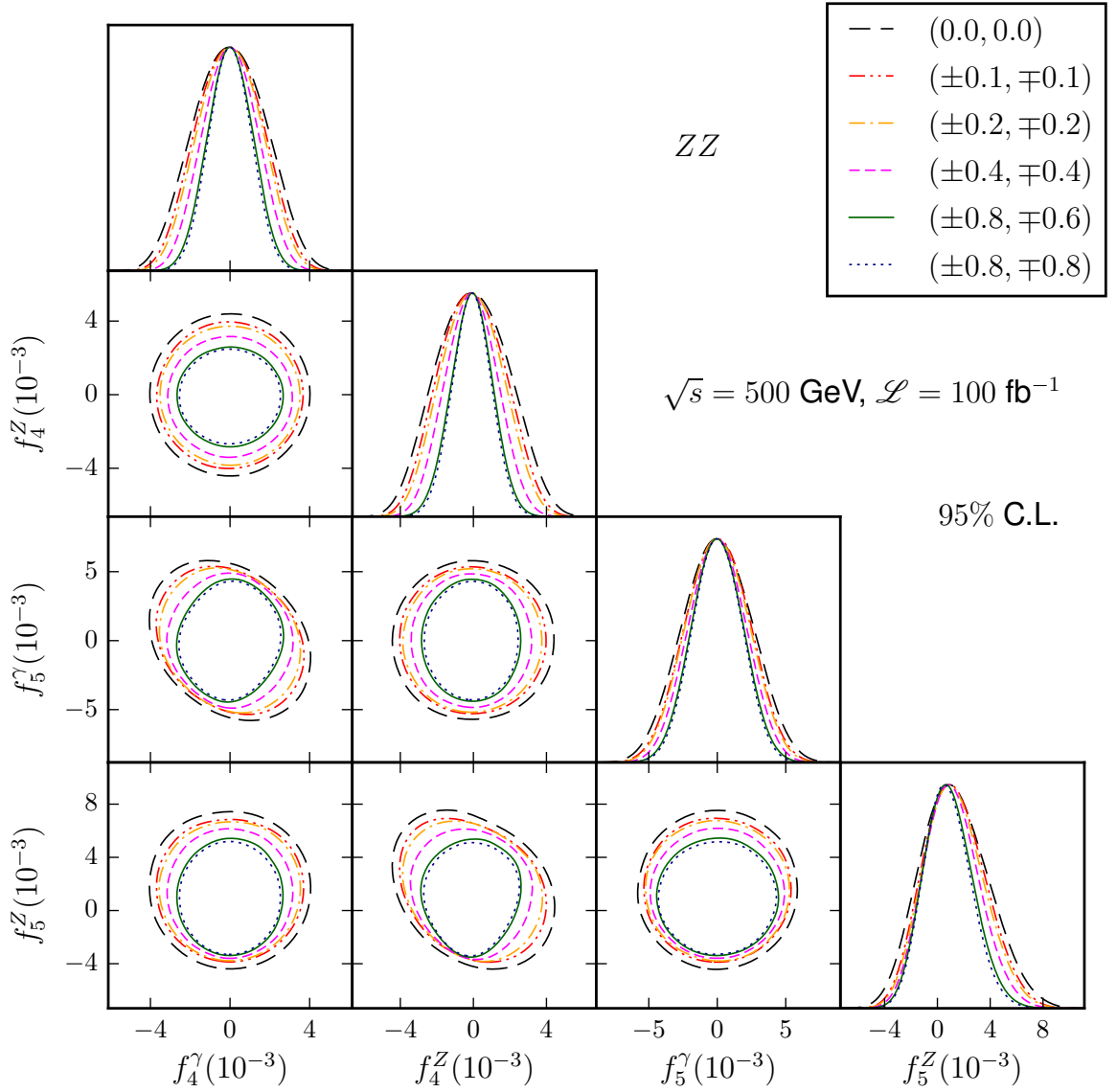


Figure 4.11. All the one dimensional marginalised projections and two dimensional marginalised contours at 95 % C.L. in triangular array from MCMC in ZZ production for $\sqrt{s} = 500$ GeV and $\mathcal{L} = 100 \text{ fb}^{-1}$ for different beam polarizations $(\pm\eta_3, \pm\xi_3)$.

for both ZZ and $Z\gamma$ processes and their combined one. There are constant lines for a constant values of the *weighted-volume* implying that each beam polarization points on a given line will provide similar limit on the couplings. Though, the point $(\pm 0.8, \mp 0.8)$ is the best choice for beam polarization, the point $(\pm 0.8, \mp 0.6)$ is the best within the limitation for positron polarization, i.e., $|\xi_3| < 0.6$.

We estimate simultaneous limits on the couplings in both processes using MCMC with the combined χ^2 given in Eq. (4.4.1) for a set of beam polarizations $(0, 0)$, $(\pm 0.1, \mp 0.1)$, $(\pm 0.2, \mp 0.2)$, $(\pm 0.4, \mp 0.4)$, $(\pm 0.8, \mp 0.6)$, and $(\pm 0.8, \mp 0.8)$. The simultaneous limits at 95 % BCI on the anomalous couplings are shown in Table 4.3 for both processes. It can be seen that the limits with beam polarization combined with the opposite values given in Table 4.3

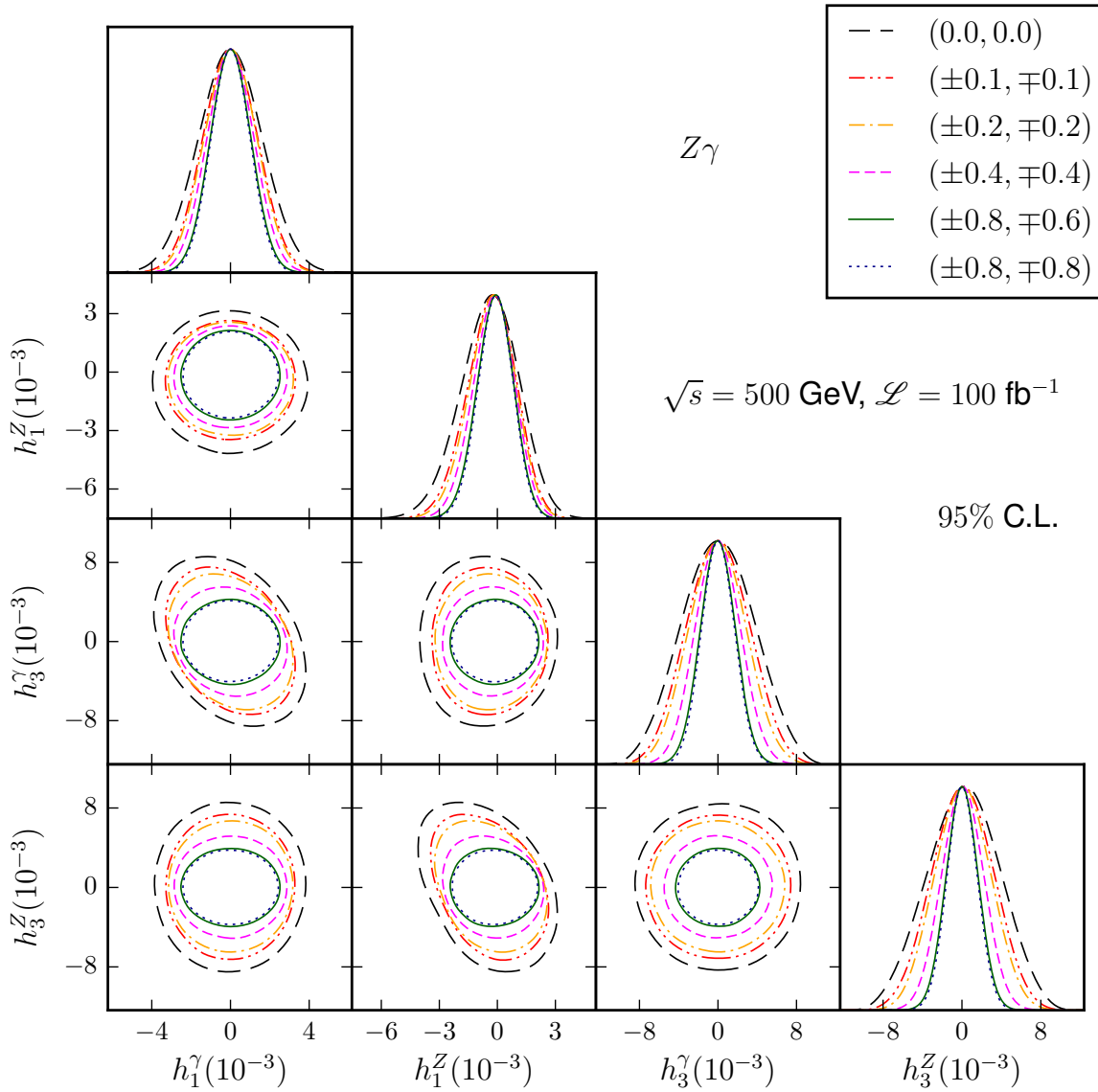


Figure 4.12. All the one dimensional marginalised projections and two dimensional marginalised contours at 95 % C.L. in triangular array from MCMC in $Z\gamma$ production for $\sqrt{s} = 500$ GeV and $\mathcal{L} = 100 \text{ fb}^{-1}$ for different beam polarizations $(\pm\eta_3, \pm\xi_3)$.

are better than the limits with fixed beam polarization given in Tables 4.1 & 4.2 with the same luminosity of 100 fb^{-1} . The one dimensional marginalised projections and two dimensional marginalised contours at 95 % BC in triangular array from MCMC obtained for the same set of beam polarizations as in Table 4.3 are shown in Fig. 4.11 and Fig. 4.12 for ZZ and $Z\gamma$ processes, respectively. We observe that as the amplitude of beam polarizations are increased, the correlations reduce ($f_4^\gamma - f_5^\gamma$, $f_4^Z - f_5^Z$ in Fig. 4.11 and $h_1^\gamma - h_3^\gamma$, $h_1^Z - h_3^Z$ in Fig. 4.12) along with the limits getting tighter.

4.5 Summary

To summarize, we studied the effects of beam polarization on polarization asymmetries and corresponding sensitivities towards anomalous couplings in this chapter. Using the *minimum averaged* likelihood, we found the best choice of the beam polarization for the two processes for fixed beam polarization as well as when opposite beam polarization are combined together. Here, the list of observables includes the cross section along with eight polarization asymmetries for the Z boson. Simultaneous limits on anomalous couplings were obtained using the MCMC method for a set of benchmark beam polarizations for both fixed choices and combined with flipped choices. The simultaneous limits for a fixed choice of beam polarizations are presented in Tables 4.1 and 4.2, while for choice for polarizations combined with opposite values are presented in Table 4.3. The limits obtained for the unpolarized case are better than the ones reported in chapter 3. This is because the present analysis includes three new observables \tilde{A}_z , \tilde{A}_{xz} and \tilde{A}_{yz} . These new asymmetries yield better limits on $f_{4,5}^Z$ and $h_{1,3}^\gamma$, while we have comparable (yet better) limits on $f_{4,5}^\gamma$ and $h_{1,3}^Z$. In the fixed beam polarization case, the best choices of beam polarizations are somewhere closer to the unpolarized point. In the combined case, however, the best choices of beam polarization appear to be as maximum as can be, and that is same for two processes separately as well as combinedly.

5 The probe of aTGC in ZZ production at the LHC and the role of Z boson polarizations

Contents

5.1 The signal and background.	87
5.2 Probe of the anomalous couplings	91
5.2.1 Effect of aTGC in kinematic distributions	91
5.2.2 Sensitivity of observables to the couplings	94
5.2.3 Simultaneous limits on the aTGC	95
5.2.4 Role of the polarization asymmetries in parameter extraction	96
5.3 Summary	98

The contents in this chapter are based on the published article in Ref. [106].

In the previous two chapters, we studied the neutral aTGC at a future linear collider, the ILC. It is natural to see the implication of the aTGC using the polarization observables at the current collider LHC, which already have collected enough data to put stringent limits on the aTGC. In this chapter, we see the prospects of aTGC in ZZ production in 4-lepton final state at the LHC. The neutral aTGC appearing in the ZZ production at dimension-6 are given by the subset

$$\mathcal{L}_{ZZV} = \frac{e}{m_Z^2} \left[- \left[f_4^\gamma (\partial_\mu F^{\mu\beta}) + f_4^Z (\partial_\mu Z^{\mu\beta}) \right] Z_\alpha (\partial^\alpha Z_\beta) + \left[f_5^\gamma (\partial^\sigma F_{\sigma\mu}) + f_5^Z (\partial^\sigma Z_{\sigma\mu}) \right] \tilde{Z}^{\mu\beta} Z_\beta \right] \quad (5.0.1)$$

of the full Lagrangian given in Eq. (3.1.1) containing only four parameters f_4^V and f_5^V . There has been a lot of study of these neutral aTGC for a hadron collider [82, 84, 87–90, 102, 103] with different techniques. These neutral aTGCs have also been searched at the LHC in different processes [141–147] including the ZZ production [141, 146] using cross section in suitable kinematical cuts. The stringent limits on these aTGC has been obtained in ZZ production itself at the LHC [146]. The tightest limits at 95 % C.L. for $\sqrt{s} = 13$ TeV and $\mathcal{L} = 35.9 \text{ fb}^{-1}$ are

$$\begin{aligned} -0.0012 < f_4^Z < 0.0010, & \quad -0.0010 < f_5^Z < 0.0013, \\ -0.0012 < f_4^\gamma < 0.0013, & \quad -0.0012 < f_5^\gamma < 0.0013, \end{aligned} \quad (5.0.2)$$

obtained by varying one parameter at a time and using only the cross section as observable. We note that these ranges of couplings do not violate unitarity bound up to an energy scale of 10 TeV. Whereas a size as large as $\mathcal{O}(\pm 0.1)$ of the couplings can be allowed if the unitarity violation is assumed to take place at the energy scale of 3 TeV, a typical energy range explored by the current 13 TeV LHC. Our strategy, here, is to see the significance of the polarization observables on top of the cross section in probing the aTGC.

The leading order (LO) result of the ZZ pair production cross section is way below the result measured at the LHC [146, 147]. However, the existing next-to-next-to-leading order (NNLO) [225, 226] results are comparable with the measured values at CMS [146] and ATLAS [147]. We, however, obtain the cross section at next-to-leading order (NLO) in the SM and in aTGC using MADGRAPH5_aMC@NLO [190] and have used the SM k -factor to match to the NNLO value. The details of these calculations are described in section 5.1.

The LHC being a symmetric collider, most of the polarization of Z in ZZ pair production are either zero or close to zero except the polarization T_{xz} , $T_{xx} - T_{yy}$, and T_{zz} . For better significance, we used the tilde asymmetry \widetilde{A}_{xz} corresponding to T_{xz} as given in Eq. (4.1.10) with c_{θ_Z} being measured in the Lab frame. To get the momentum direction of Z boson, one needs a reference axis (z -axis), but we can not assign a direction at the LHC because it is a symmetric collider. So we consider the direction of the boost of the $4l$ final state to be the proxy for reference z -axis. In $q\bar{q}$ fusion, the quark is supposed to have larger momentum than the anti-quark at the LHC, thus above proxy statistically stands for the direction of the quark and c_{θ_Z} is measured w.r.t. the boost.

5.1 The signal and background

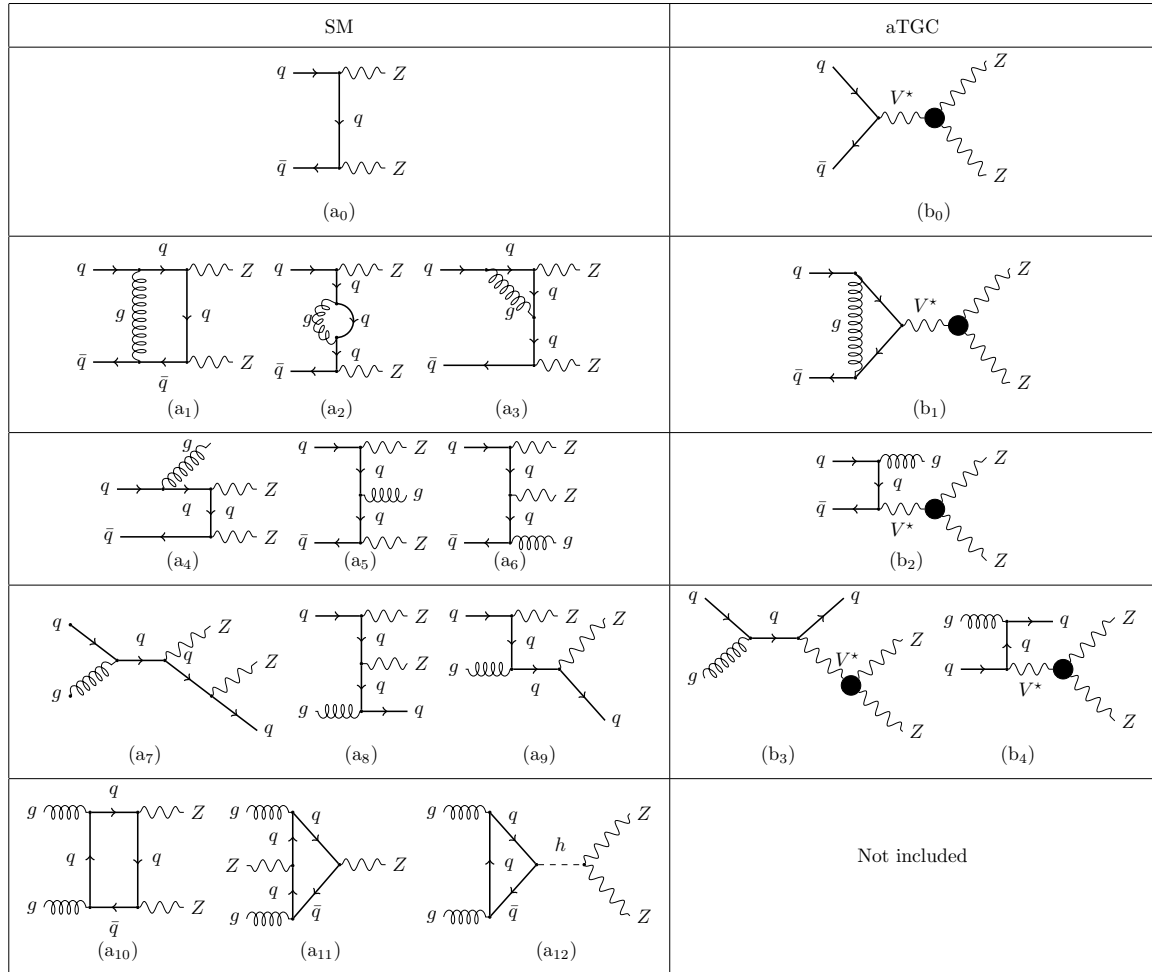


Figure 5.1. Representative Feynman diagrams for ZZ pair production at the LHC in the SM ($q\bar{q}$ and gg initiated) as well as in aTGC ($q\bar{q}$ initiated) at tree level together with NLO in QCD.

We are interested in studying anomalous triple gauge boson couplings in ZZ pair production at the LHC. The tree level standard model contribution to this process comes from the representative diagram (a₀) in Fig. 5.1, while the tree level aTGC contribution is shown in the diagram (b₀). Needless to say, the tree level cross section in the SM is way below the measured cross section at the LHC, because QCD corrections are very high in this process. In the SM, at NLO ($\mathcal{O}(\alpha_s)$), virtual contributions come from the representative diagrams (a₁–a₃) and real contributions come from (a₄–a₉) in the $q\bar{q}$ initiated sub-process. The gg initiated sub-process appears at 1-loop level, the diagrams (a₁₀–a₁₂), and contributes at $\mathcal{O}(\alpha_s^2)$. The LO, NLO and NNLO results from theoretical calculation available in literature [225,226] and our estimate in MATRIX [226–234] for ZZ production cross section at $\sqrt{s} = 13$ TeV for a pp collider are listed in Table 5.1. The recent experimental measurement from CMS [146] and ATLAS [147] are also shown for comparison. The cross section at NLO receives as much as

Table 5.1. The theoretical estimates and experimental measurements of the ZZ production cross section at $\sqrt{s} = 13$ TeV at the LHC. The uncertainties in the theoretical estimates come from scale variation.

Obtained at	σ_{LO} [pb]	σ_{NLO} [pb]	σ_{NNLO} [pb]
MATRIX	$9.833^{+5.2\%}_{-6.2\%}$	$14.08^{+2.9\%}_{-2.4\%}$	$16.48^{+3.0\%}_{-2.4\%}$
Heinrich <i>et al.</i> [225]	$9.890^{+4.9\%}_{-6.1\%}$	$14.51^{+3.0\%}_{-2.4\%}$	$16.92^{+3.2\%}_{-2.6\%}$
Cascioli <i>et al.</i> [226]	$9.887^{+4.9\%}_{-6.1\%}$	$14.51^{+3.0\%}_{-2.4\%}$	$16.91^{+3.2\%}_{-2.4\%}$
CMS [146]	$17.2 \pm 0.5(\text{stat.}) \pm 0.7(\text{syst.}) \pm 0.4(\text{lumi.})$		
ATLAS [147]	$17.3 \pm 0.6(\text{stat.}) \pm 0.5(\text{syst.}) \pm 0.6(\text{lumi.})$		

$\sim 46\%$ correction over LO and further the NNLO cross section receives $\sim 16\%$ correction over the NLO result. At NNLO the $q\bar{q}$ sub-process receives 10% correction [226] over NLO and the gg initiated $\mathcal{O}(\alpha_s^3)$ sub-process receives 70% correction [235] over its $\mathcal{O}(\alpha_s^2)$ result. The higher order corrections to the cross section vary w.r.t. $\sqrt{\hat{s}}$ or m_{ZZ} as shown in Fig. 5.2 with only $q\bar{q}$ initiated processes in the *left-panel* and $q\bar{q} + gg$ initiated processes in the *right-panel* obtained at MATRIX [226–234]. The lower panels display the respective bin-by-bin ratios to the NLO central predictions. The NLO to LO ratio does not appear to be constant over the range of m_{ZZ} . Thus a simple k -factor with LO events can not be used as proxy for NLO events. We use results obtained at MADGRAPH5_aMC@NLO including NLO QCD corrections for our analysis. The LO and NLO results obtained in MADGRAPH5_aMC@NLO v2.6.2 with PDF (parton-distribution-function) sets NNPDF23 are

$$\begin{aligned}
\sigma_{\mathcal{O}(\alpha_s^0)}^{q\bar{q}\rightarrow ZZ} &= 9.341^{+4.3\%}_{-5.3\%} \text{ pb}, \\
\sigma_{\mathcal{O}(\alpha_s)}^{q\bar{q}\rightarrow ZZ} &= 13.65^{+3.2\%}_{-3.6\%} \text{ pb}, \\
\sigma_{\mathcal{O}(\alpha_s^2)}^{gg\rightarrow ZZ} &= 1.142^{+24.5\%}_{-18.7\%} \text{ pb}, \\
\sigma_{\text{mixed}_1}^{q\bar{q}+gg\rightarrow ZZ} &= \sigma_{\mathcal{O}(\alpha_s)}^{q\bar{q}\rightarrow ZZ} + \sigma_{\mathcal{O}(\alpha_s^2)}^{gg\rightarrow ZZ} \\
&= 14.79^{+4.8\%}_{-4.7\%} \text{ pb}.
\end{aligned} \tag{5.1.1}$$

The errors in the subscript and superscript on the cross section are the uncertainty from scale variation. The total cross section combining the $q\bar{q}$ sub-process at $\mathcal{O}(\alpha_s^2)$ with gg at $\mathcal{O}(\alpha_s^3)$ is given by,

$$\sigma_{\text{mixed}_2}^{q\bar{q}+gg\rightarrow ZZ} = \underbrace{\sigma_{\mathcal{O}(\alpha_s)}^{q\bar{q}\rightarrow ZZ} \times 1.1}_{\mathcal{O}(\alpha_s^2)} + \underbrace{\sigma_{\mathcal{O}(\alpha_s^2)}^{gg\rightarrow ZZ} \times 1.7}_{\mathcal{O}(\alpha_s^3)}$$

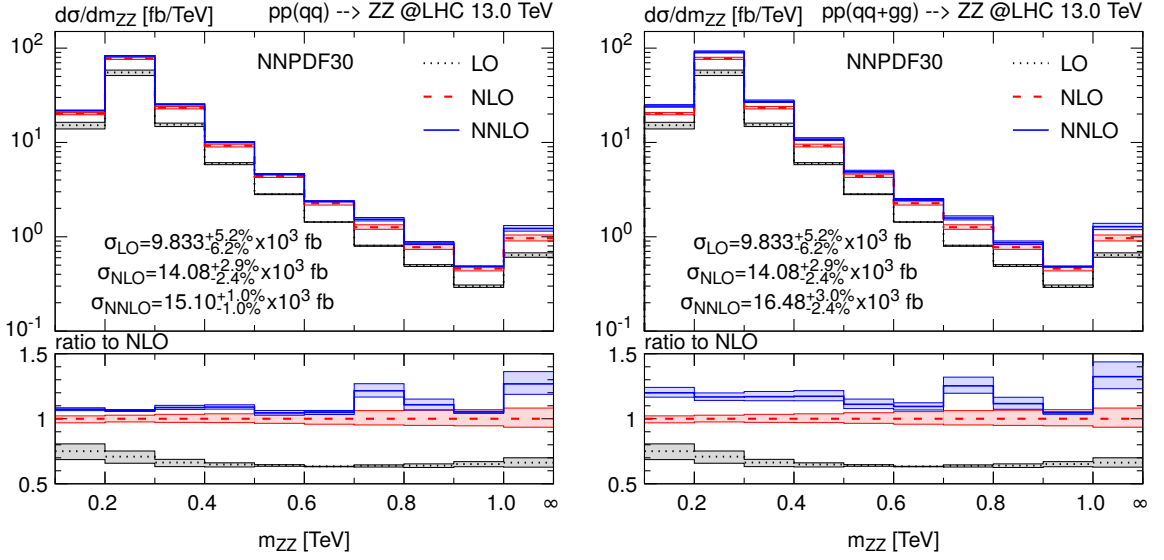


Figure 5.2. The differential distributions of m_{ZZ} in the ZZ production at the LHC at $\sqrt{s} = 13$ TeV in LO, NLO and NNLO obtained using MATRIX. In the *left-panel* $q\bar{q}$ initiated results are shown, while in the *right-panel* $q\bar{q} + gg$ initiated results are shown.

$$= 16.96^{+5.6%}_{-5.3%} \text{ pb.} \quad (5.1.2)$$

The MadGraph5 results are below the MATRIX results due the difference in PDF sets. The aTGC has also a substantial NLO QCD correction and they come from the diagram (b₂) at 1 loop level and from (b₂–b₄) as the real radiative process. The aTGC effect is not included in the gg process where the aTGC may come from a similar diagram with $h \rightarrow ZZ$ in Fig. 5.1(a₁₂) but h replaced with a Z . As an example of NLO QCD correction of aTGC in this process, we obtain cross section at $\sqrt{s} = 13$ TeV with all couplings $f_i^V = 0.001$. The cross section for only aTGC part, $(\sigma^{\text{aTGC}} - \sigma^{\text{SM}})$ at LO and NLO are 71.82 fb (0.77 %) and 99.94 fb (0.73 %), respectively. Thus NLO result comes with a substantial amount (~ 39 %) of QCD correction over LO at this given aTGC point.

The signal consists of $4l$ ($2e2\mu/4e/4\mu$) final state which includes ZZ , $Z\gamma^*$, and $\gamma^*\gamma^*$ processes. The signal events are generated in MADGRAPH5_aMC@NLO with PDF sets NNPDF23 in the SM as well as in the aTGC as $pp \rightarrow VV \rightarrow 2e2\mu$ ($V = Z/\gamma^*$) at NLO in QCD in $q\bar{q}$, qg as well as in 1-loop gg initiated process with the following basic cuts (in accordance with Ref. [146]),

- $p_T^l > 10$ GeV, hardest $p_T^l > 20$ GeV, and second hardest $p_T^l > 12$ GeV,
- $|\eta_e| < 2.5$, $|\eta_\mu| < 2.4$,
- $\Delta R(e, \mu) > 0.05$, $\Delta R(l^+, l^-) > 0.02$.

To select the ZZ final state from the above generated signal we further put a constraint on invariant mass of same flavoured oppositely charged leptons pair with

- $60 \text{ GeV} < m_{l+l^-} < 120 \text{ GeV}$.

The $2e2\mu$ cross section up to a factor of two is used as the proxy for the $4l$ cross section for the ease of event generation and related handling.

The background event consisting $t\bar{t}Z$ and WWZ with leptonic decay are generated at LO in `MADGRAPH5_aMC@NLO` with `NNPDF23` with the same sets of cuts as applied to the signal, and their cross section is matched to NLO in QCD with a k -factor of 1.4¹. This k -factor estimation was done at the production level. We have estimated the total cross section of the signal in the SM to be

$$\begin{aligned}
 \sigma(pp \rightarrow ZZ \rightarrow 4l)_{\mathcal{O}(\alpha_s)}^{q\bar{q}} &= 28.39 \text{ fb}, \\
 \sigma(pp \rightarrow ZZ \rightarrow 4l)_{\mathcal{O}(\alpha_s^2)}^{gg} &= 1.452 \text{ fb}, \\
 \sigma(pp \rightarrow ZZ \rightarrow 4l)_{mixed_1}^{q\bar{q}+gg} &= 29.85 \text{ fb}, \\
 \sigma(pp \rightarrow ZZ \rightarrow 4l)_{mixed_2}^{q\bar{q}+gg} &= 33.70 \text{ fb}.
 \end{aligned} \tag{5.1.3}$$

The background cross section at NLO is estimated to be

$$\sigma(pp \rightarrow t\bar{t}Z + WWZ \rightarrow 4l + \cancel{E}_T)_{NLO} = 0.020 \text{ fb}. \tag{5.1.4}$$

The values of various parameters used for the generation of signal and background are

- $m_Z = 91.1876 \text{ GeV}$, $M_H = 125.0 \text{ GeV}$,
- $G_F = 1.16639 \times 10^{-5} \text{ GeV}^{-2}$, $\alpha_{EM} = 1/132.507$,
 $\alpha_s = 0.118$,
- $\Gamma_Z = 2.441404 \text{ GeV}$, $\Gamma_H = 6.382339 \text{ MeV}$.

The renormalization and factorization scale is set to $\sum M_i^T/2$, M_i^T are the transverse mass of all final state particles.

In our analysis, the total cross section in the SM including the aTGC is taken as²

$$\sigma_{\text{Tot}} = \sigma_{mixed_2}^{\text{SM}} + (\sigma_{\text{NLO}}^{\text{aTGC}} - \sigma_{\text{NLO}}^{\text{SM}}), \tag{5.1.5}$$

¹This k -factor for the backgrounds along with the NLO to NNLO k -factor for the signal is of-course an approximation as they really depend on kinematic and angular distributions.

² $mixed_1 \approx q\bar{q}(\mathcal{O}(\alpha_s)) + gg(\mathcal{O}(\alpha_s^2))$, $mixed_2 \approx q\bar{q}(\mathcal{O}(\alpha_s^2)) + gg(\mathcal{O}(\alpha_s^3))$

the SM is considered at order $mixed_2$, whereas the aTGC contribution along with its interference with the SM are considered at NLO in QCD (as the NNLO contribution is not known with aTGC).

We will use polarization asymmetries as described in the previous section in our analysis. Assuming that the NNLO effect cancels away because of the ratio of two cross section, we will use the asymmetries as

$$A_i = \frac{\Delta\sigma_i^{mixed_1}}{\sigma^{mixed_1}}. \quad (5.1.6)$$

We use total cross section at $mixed_2$ order and asymmetries at $mixed_1$ order to put constrain on the anomalous couplings. We note that the Z boson momentum is required to be reconstructed to obtain its polarization asymmetries, which require the right pairing of two oppositely charged leptons coming from a same Z boson in $4e/4\mu$ channel. The right pairing of leptons for the Z boson in the same flavoured channel is possible with $\sim 95.5\%$ for $m_{4l} > 300$ GeV and $\sim 99\%$ for $m_{4l} > 700$ GeV for both SM and aTGC by requiring a smaller value of $|m_Z - m_{l+l-}|$. This small miss pairing is neglected as it allows to use the $2e2\mu$ channel as a proxy for the full $4l$ final state with good enough accuracy.

5.2 Probe of the anomalous couplings

The observables in this process, we have, are the cross section and the polarization asymmetries. We use these observables in a suitable kinematical cut region for m_{4l} and ΔR (signal region) to study the sensitivity on aTGC and obtain limits on them.

5.2.1 Effect of aTGC in kinematic distributions

The effect of aTGC on the observables varies with energy scale. We study the effect of aTGC on various observables in their distribution and determine the signal region. In Fig. 5.3 we show four lepton invariant mass (m_{4l}) or centre-of-mass energy ($\sqrt{\hat{s}}$) distribution (*left-panel*) and ΔR distribution of $\mu^+\mu^-$ pair (*right-panel*) at $\sqrt{s} = 13$ TeV for the SM along with background $t\bar{t}Z + WWZ$ and some benchmark aTGC points for events normalized to luminosity 300 fb^{-1} using MADANALYSIS5 [236]. The gg contribution is at its LO ($\mathcal{O}(\alpha_s^2)$), while all other contributions are shown at NLO ($\mathcal{O}(\alpha_s)$). The $q\bar{q} \rightarrow ZZ, Z\gamma$ contribution is shown in *green band*, $gg \rightarrow ZZ, Z\gamma$ is in *blue band* and the background $t\bar{t}Z + WWZ$ con-

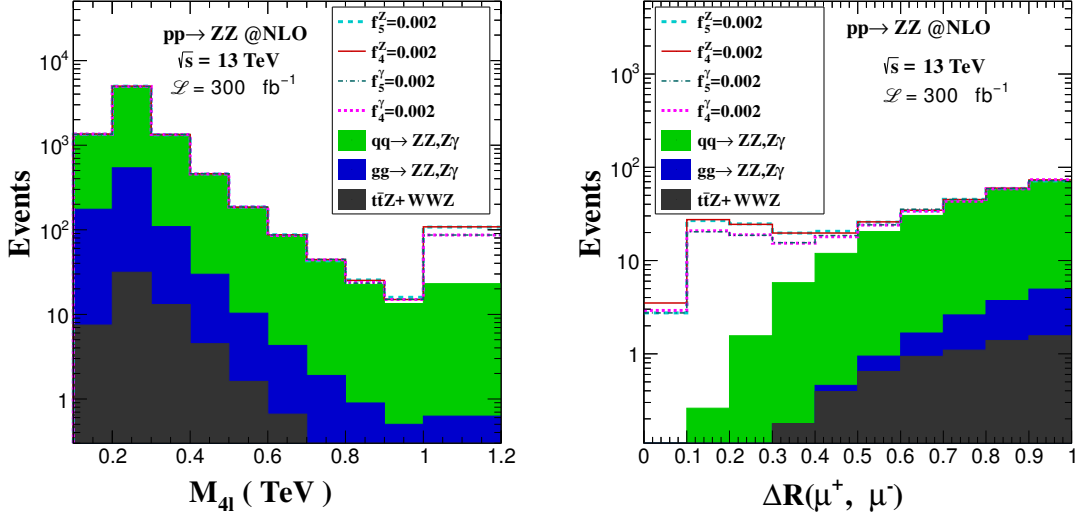


Figure 5.3. The differential distributions of m_{4l} (left-panel) and $\Delta R(\mu^+, \mu^-)$ (right-panel) in the ZZ production at the LHC at $\sqrt{s} = 13$ TeV and $\mathcal{L} = 300$ fb $^{-1}$ at NLO in QCD. The *light-shaded* region with maximum heights (green shaded), the *dark-shaded* region (blue shaded) and the *light-shaded* region with smallest heights (grey shaded) correspond to $q\bar{q}$ SM contribution, gg SM contributions and the background, respectively. The aTGC contributions are shown with different line types (colours).

tribution is shown in *grey band*. The aTGC contribution for various choices are shown in *dashed/cyan* ($f_5^Z = 0.002$), *solid/red* ($f_4^Z = 0.002$), *dashed-dotted/dark-green* ($f_5^\gamma = 0.002$) and *small-dashed/magenta* ($f_4^\gamma = 0.002$). For the m_{4l} distribution in left, all events above 1 TeV are added in the last bin. All the aTGC benchmark i.e., $f_i^V = 0.002$ are not visibly different than the SM $q\bar{q}$ contribution upto $\sqrt{\hat{s}} = 0.8$ TeV and there are significant excess of events in the last bin, i.e., above $\sqrt{\hat{s}} = 1$ TeV. This is due to momentum dependence [98] of the interaction vertex that leads to increasing contribution at higher momentum transfer. In the distribution of $\Delta R(\mu^+, \mu^-)$ in the *right-panel*, the effect of aTGC is higher for lower ΔR (below 0.5). In the ZZ process, the Z bosons are highly boosted for larger $\sqrt{\hat{s}}$ and their decay products are collimated leading to a smaller ΔR separation between the decay leptons. To see this kinematic effect, we plot events in $m_{4l} - \Delta R$ plane in Fig. 5.4 (left-panel). Here, we choose a minimum ΔR between e pair and μ pair event by event. We note that additional events coming from aTGC contributions have higher m_{4l} and lower ΔR between leptons. For $\Delta R < 0.2$ most of the events contribute to the $m_{4l} > 1$ TeV bin and they are dominantly coming from aTGC, Fig. 5.4 (right-panel). Thus we can choose $m_{4l} > 1$ TeV to be the signal region.

In this analysis, the set of observables consist of the cross section and polarization asymmetries \widetilde{A}_{xz} , $A_{x^2-y^2}$, and A_{zz} . The signal region for the cross section σ is chosen to be $m_{4l} > 1$ TeV as we have discussed in the previous section. In case of asymmetries, we choose the

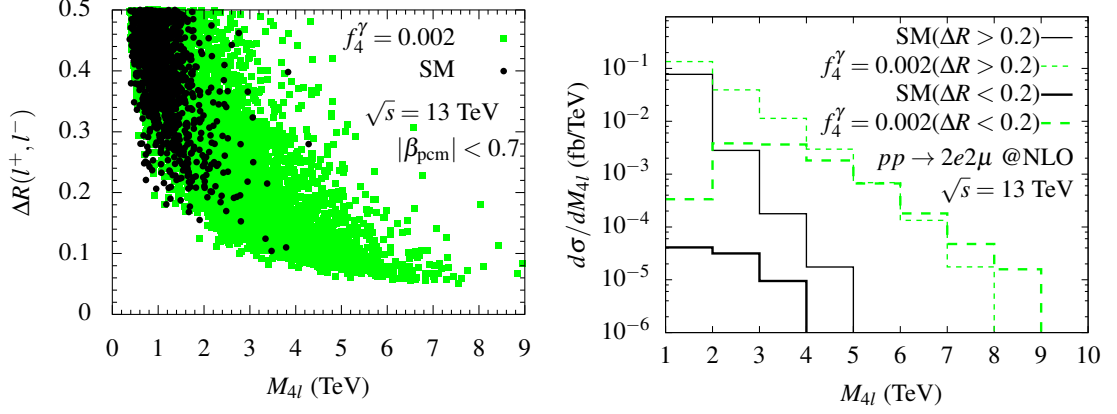


Figure 5.4. m_{4l} vs ΔR scattered plot (left) and m_{4l} distribution for $\Delta R(l^+, l^-) \geq 0.2$ (right) in ZZ production at the LHC at $\sqrt{s} = 13$ TeV for the SM and for aTGC with $f_4^\gamma = 0.002$.

signal region as $m_{4l} > 0.3$ TeV for \widetilde{A}_{xz} and $m_{4l} > 0.7$ TeV for $A_{x^2-y^2}$ and A_{zz} as the effect of aTGC is found to be best in these region corresponding to these asymmetries. The expression for the cross section and the polarization asymmetries as a function of couplings are obtained by numerical fitting the data generated by MADGRAPH5_aMC@NLO. The events are generated for different set of values of the couplings $f_i^V = (f_4^\gamma, f_4^Z, f_5^\gamma, f_5^Z)$ and then various cross sections, i.e., the total cross section and the numerator of the asymmetries, \mathcal{O} , are fitted as

$$\mathcal{O} = \mathcal{O}_0 + f_i^V \times \mathcal{O}_i + f_i^V \times f_j^V \times \mathcal{O}_{ij}, \quad (5.2.1)$$

in general, where \mathcal{O}_0 is the value of corresponding cross sections in the SM. The observables, considered here, are all CP -even in nature which leads to the modification of Eq. (5.2.1) as

$$\mathcal{O} = \mathcal{O}_0 + f_5^V \times \mathcal{O}_5^V + f_4^\gamma f_4^Z \times \mathcal{O}_4^{\gamma,Z} + f_5^\gamma f_5^Z \times \mathcal{O}_5^{\gamma,Z} + (f_i^V)^2 \times \mathcal{O}_i^{VV}, \quad (5.2.2)$$

as the f_4^V are CP -odd, while f_5^V are CP -even couplings reducing the unknown from 15 to 9 to be solved. The numerical expressions of the cross section and the asymmetries as a function of the couplings are given in appendix C.1. The observables are obtained up to $\mathcal{O}(\Lambda^{-4})$, i.e., quadratic in dimension-6. In practice, one should consider the effect of dimension-8 contribution at linear order. However, we choose to work with only dimension-6 in couplings with a contribution up to quadratic so as to compare the results with the current LHC constraints on dimension-6 parameters [146]. A note on keeping terms up to quadratic in couplings, and not terminating at linear order, is presented in appendix C.2.

5.2.2 Sensitivity of observables to the couplings

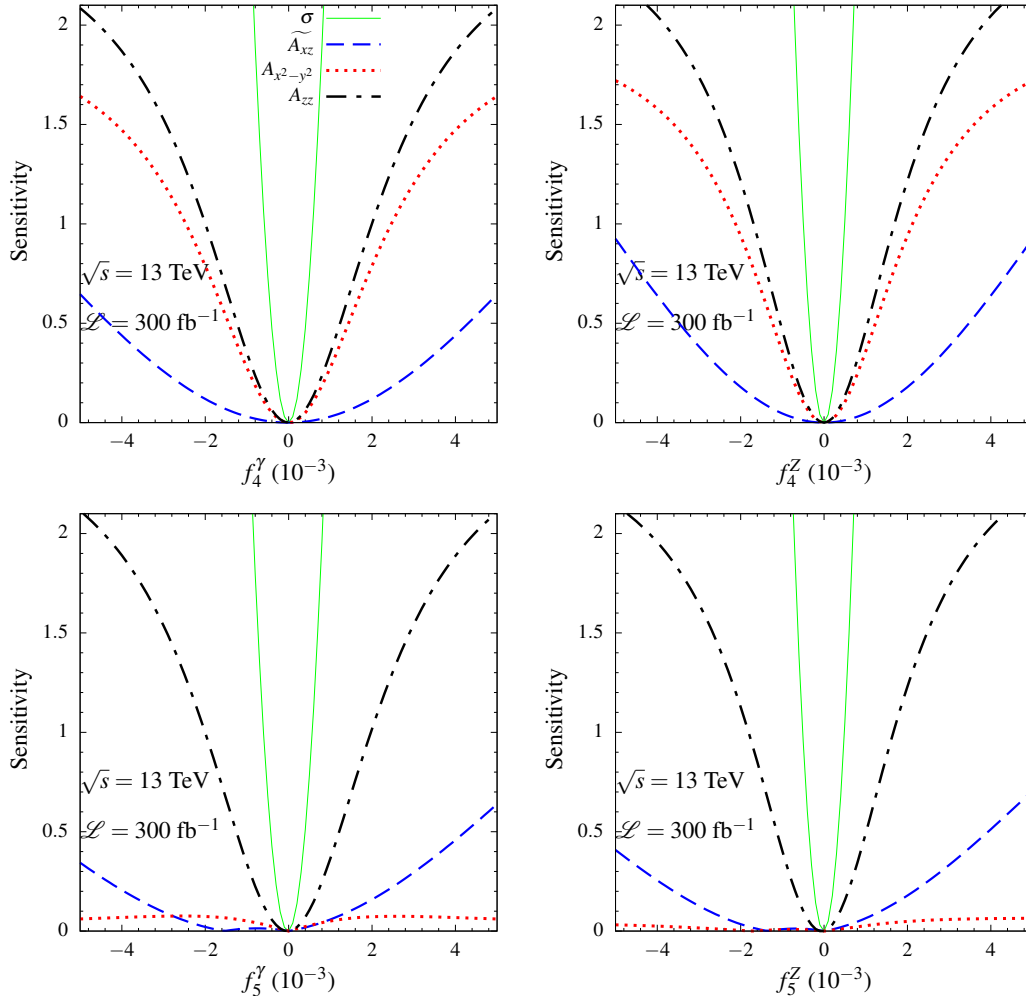


Figure 5.5. The sensitivity of the cross section and the polarization observables to the anomalous couplings at $\sqrt{s} = 13$ TeV and $\mathcal{L} = 300$ fb $^{-1}$ in ZZ production at the LHC.

We studied the sensitivities (see Eq. (3.1.16) for definition) of all the observables to the couplings and show them in Fig. 5.5 for $\mathcal{L} = 300$ fb $^{-1}$. We consider systematic uncertainties of $\epsilon_{\sigma} = 5$ % [146] and $\epsilon_A = 2$ % as a benchmark. We find asymmetries to be less sensitive than the cross section to the couplings and thus cross section wins in putting limits on the couplings. The sensitivity curves of all the couplings in each observable are symmetric about zero as f_4^V (being CP -odd) does not appear in linear in any observables, and also the linear contribution from f_5^V are negligibly small compared to their quadratic contribution (see appendix C.1). For example, the coefficient of f_5^V are ~ 1 in $\sigma(m_{A_I} > 1$ TeV) (Eq. (C.1.3)), while the coefficient of $(f_5^V)^2$ are $\sim 5 \times 10^4$. Thus even at $f_5^V = 10^{-3}$ the quadratic contribution is 50 times stronger than the linear one. Although the asymmetries are not strongly sensitive to the couplings as the cross section, they are useful in the measurement of the anomalous couplings, which will be discussed in the next section.

Table 5.2. One parameter limits (10^{-3}) at 95 % C.L. on anomalous couplings in ZZ production at the LHC at $\sqrt{s} = 13$ TeV for various luminosities.

param / \mathcal{L}	35.9 fb $^{-1}$	150 fb $^{-1}$	300 fb $^{-1}$	1000 fb $^{-1}$
f_4^γ	+1.22 -1.20	+0.85 -0.85	+0.72 -0.72	+0.55 -0.55
f_5^γ	+1.21 -1.23	+0.84 -0.87	+0.71 -0.74	+0.54 -0.57
f_4^Z	+1.04 -1.03	+0.73 -0.72	+0.62 -0.61	+0.47 -0.47
f_5^Z	+1.03 -1.05	+0.72 -0.74	+0.61 -0.63	+0.46 -0.49

It is noteworthy to mention that the sensitivity of $A_{x^2-y^2}$ are flat and negligible for CP -even couplings f_5^V , while they vary significantly for CP -odd couplings f_4^V . Thus the asymmetry $A_{x^2-y^2}$, although a CP -even observables, is able to distinguish between CP -odd and CP -even interactions in the ZZ production at the LHC.

We use the total χ^2 as (Eq. (3.1.16))

$$\chi^2(f_i) = \sum_j [\mathcal{S} \mathcal{O}_j(f_i)]^2 \quad (5.2.3)$$

to obtain the single parameter limits on the couplings by varying one parameter at a time and keeping all other to their SM values. The single parameter limits thus obtained on all the anomalous couplings at 95 % C.L. for four benchmark luminosities $\mathcal{L} = 35.9$ fb $^{-1}$, 150 fb $^{-1}$, 300 fb $^{-1}$ and 1000 fb $^{-1}$ are presented in Table 5.2. The limit at $\mathcal{L} = 35.9$ fb $^{-1}$ given in the first column of Table 5.2 are comparable to the tightest limit available at the LHC by CMS [225] given in Eq. (5.0.2).

5.2.3 Simultaneous limits on the aTGC

Table 5.3. Simultaneous limits (10^{-3}) at 95 % C.L. on anomalous couplings in ZZ production at the LHC at $\sqrt{s} = 13$ TeV for various luminosities from MCMC.

param / \mathcal{L}	35.9 fb $^{-1}$	150 fb $^{-1}$	300 fb $^{-1}$	1000 fb $^{-1}$
f_4^γ	+1.17 -1.15	+0.81 -0.81	+0.67 -0.68	+0.52 -0.52
f_5^γ	+1.50 -1.13	+0.78 -0.83	+0.66 -0.68	+0.51 -0.53
f_4^Z	+0.95 -0.96	+0.67 -0.67	+0.58 -0.58	+0.45 -0.44
f_5^Z	+0.95 -0.98	+0.68 -0.69	+0.57 -0.57	+0.43 -0.45

A likelihood-based analysis using the total χ^2 with the MCMC method is done by varying all the parameters simultaneously to extract simultaneous limits on all the anomalous

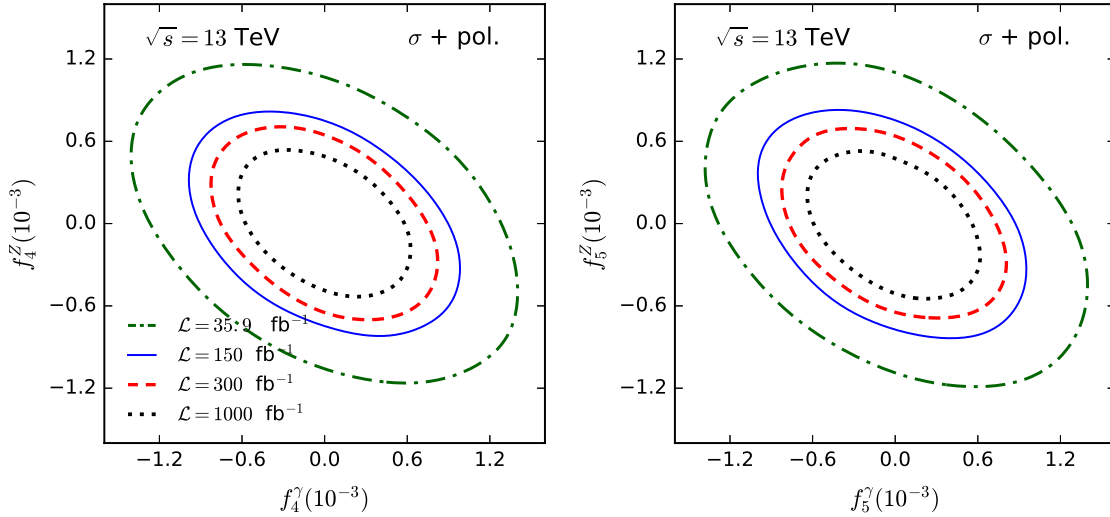


Figure 5.6. Two dimensional marginalised contours at 95 % BCI from MCMC using the cross section σ along with polarization asymmetries (pol.) at $\sqrt{s} = 13$ TeV for various luminosities in ZZ production at the LHC.

couplings for the four benchmark luminosities chosen. The two dimensional marginalised contours at 95 % C.L. in the $f_4^\gamma - f_4^Z$ and $f_5^\gamma - f_5^Z$ planes are shown in Fig. 5.6 for the four benchmark luminosities chosen, using the cross section together with the polarization asymmetries, i.e. using ($\sigma + \text{pol.}$). The outer most contours are for $\mathcal{L} = 35.9 \text{ fb}^{-1}$ and the inner most contours are for $\mathcal{L} = 1000 \text{ fb}^{-1}$. The corresponding simultaneous limits on the aTGC couplings for four benchmark luminosities are presented in Table 5.3. The simultaneous limits are usually less tight than the one-dimensional limits, but find the opposite in some case, which can be seen comparing Table 5.3 with Table 5.2. The reason for this is the following. The cross section, the dominant observable, has a very little linear dependence, while it has a large quadratic dependence on the couplings (see Eq. (C.1.3)). As a result, when one obtains the limit on one parameter in the multi-parameter analysis, a slight deviation on any other parameter from zero (SM point) tightens the limit on the former coupling.

5.2.4 Role of the polarization asymmetries in parameter extraction

The inclusion of polarization asymmetries with the cross section has no significant effect in constraining the anomalous couplings. The asymmetries may still be useful in extracting parameters if excess events were found at the LHC. To explore this, we do a toy analysis of parameter extraction using the data for all aTGC couplings $f_i^V = 0.002$ (well above current limit) and use the MCMC method to extract back these parameters. We deliberately choose the benchmark couplings with large values so as to emulate a situation where a deviation from the SM is observed. In Fig. 5.7, we show two-dimensional marginalized contours for

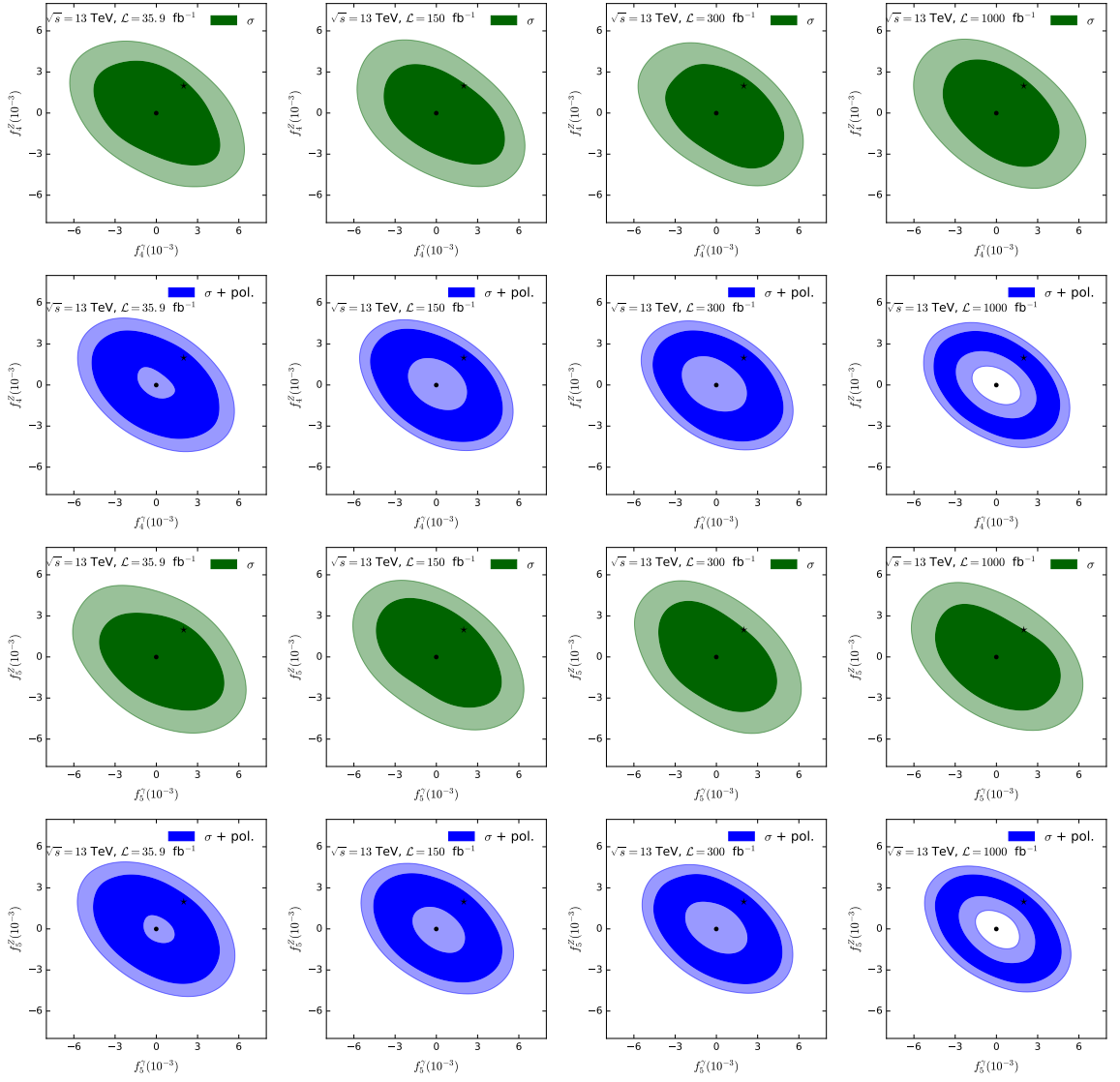


Figure 5.7. Comparison of σ vs $(\sigma + \text{pol.})$ in two dimensional marginalised contours from MCMC for aTGC benchmark $f_i^V = 0.002$ in f_4^V - f_4^Z panel and f_5^V - f_5^Z panel at $\sqrt{s} = 13$ TeV for various luminosities in ZZ production at the LHC.

the four benchmark luminosities for the benchmark aTGC couplings in f_4^V - f_4^Z and f_5^V - f_5^Z planes for the set of observables σ and $(\sigma + \text{pol.})$ for comparison. The *darker-shaded* regions are for 68 % C.L., while *lighter-shaded* regions are for 95 % C.L. The dot (.) and the star (★) mark in the plot are for the SM (0,0) and aTGC benchmark (0.002,0.002) points, respectively. We note that the SM point is inside the 68 % C.L. contours even at a high luminosity of $\mathcal{L} = 1000 \text{ fb}^{-1}$ if we use only cross section as observable, see row-1 and 3 of Fig. 5.7. The distinction between the SM and the aTGC get improved when polarization asymmetries are included, i.e., the SM point is outside the 95 % C.L. contour for luminosity of much less than $\mathcal{L} = 1000 \text{ fb}^{-1}$, see row-2 and 4 of the figure. As the luminosity increases, from the left column to the right, the contours for $(\sigma + \text{pol.})$ shrink around the star (★) mark maintaining the shape of a ring giving better exclusion of the SM from aTGC benchmark.

Polarization asymmetries are thus useful in the measurement of the anomalous couplings if excess events are found at the LHC.

5.3 Summary

In summary, we studied anomalous triple gauge boson couplings in the neutral sector in ZZ pair production at the LHC and investigated the role of Z boson polarizations in this chapter. The QCD corrections in this process are very high and can not be ignored. We obtained the cross section and the asymmetries at higher order in QCD. The aTGC contributes more in the higher $\sqrt{\hat{s}}$ region as they are momentum dependent. The major background $t\bar{t}Z + WWZ$ are negligibly small, and they vanish in the signal regions. Although the asymmetries are not as sensitive as the cross section to the couplings, the asymmetry $A_{x^2-y^2}$ is able to distinguish between CP -even and CP -odd couplings. We estimated the one parameter as well as simultaneous limits on the couplings using all the observables based on the total χ^2 for luminosities 35.9 fb^{-1} , 150 fb^{-1} , 300 fb^{-1} and 1000 fb^{-1} . Our one parameter limits are comparable to the best available limits obtained at the LHC [146]. The asymmetries are instrumental in extracting the parameters should a deviation from the SM is observed at the LHC. We performed a toy analysis of parameter extraction with a benchmark aTGC coupling point with $f_i^V = 0.002$ and found that the polarizations observables along with the cross section can exclude the SM from the aTGC point better than the cross section can do alone. In this work, the observables for the aTGC are obtained at $\mathcal{O}(\alpha_s)$, while they are obtained in the next order in the SM. The NNLO result in aTGC, when available, is expected to improve the limits on the couplings.

6 The probe of aTGC in $e^+e^- \rightarrow W^+W^-$ and the role of W boson polarizations along with beam polarizations

Contents

6.1	Observables and effect of beam polarizations	103
6.2	Probe of the anomalous couplings	105
6.2.1	Sensitivity of observables on anomalous couplings and their binning	107
6.2.2	Effect of beam polarizations to the limits on aTGC	111
6.2.3	On the choice of beam polarizations	119
6.3	Summary	121

The contents in this chapter are based on the published article and preprints in Refs. [118,177].

The non-abelian gauge symmetry $SU(2) \times U(1)$ of the Standard Model allows the WWV ($V = \gamma, Z$) couplings after the electroweak symmetry breaking by the Higgs field. To test the SM WWV couplings, one has to hypothesize BSM couplings and make sure they do not appear at all, or they are severely constrained. There are two approaches to study BSM WWV couplings; one is effective operator, approach another is effective form factor approach, as discussed in section 1.3. In the EFT approach, the dimension-6 operators contributing to

WWV couplings are [61, 62]

$$\begin{aligned}
 \mathcal{O}_{WWW} &= \text{Tr}[W_{\mu\nu}W^{\nu\rho}W_\rho^\mu], \\
 \mathcal{O}_W &= (\mathcal{D}_\mu\Phi)^\dagger W^{\mu\nu}(\mathcal{D}_\nu\Phi), \\
 \mathcal{O}_B &= (\mathcal{D}_\mu\Phi)^\dagger B^{\mu\nu}(\mathcal{D}_\nu\Phi), \\
 \mathcal{O}_{\widetilde{WWW}} &= \text{Tr}[\widetilde{W}_{\mu\nu}W^{\nu\rho}W_\rho^\mu], \\
 \mathcal{O}_{\widetilde{W}} &= (\mathcal{D}_\mu\Phi)^\dagger \widetilde{W}^{\mu\nu}(\mathcal{D}_\nu\Phi),
 \end{aligned} \tag{6.0.1}$$

which respect the SM gauge symmetry. Among these operators, \mathcal{O}_{WWW} , \mathcal{O}_W and \mathcal{O}_B are CP -even, while $\mathcal{O}_{\widetilde{WWW}}$ and $\mathcal{O}_{\widetilde{W}}$ are CP -odd. These effective operators, after EWSB, also provides ZZV , HZV couplings which can be examined in various processes, e.g. ZV production, WZ production, HV production processes. The couplings in these processes may contain some other effective operator as well.

In the form factor approach, the most general Lagrangian for the WWV couplings is given by [64],

$$\begin{aligned}
 \mathcal{L}_{WWV} &= ig_{WWV}(g_1^V(W_{\mu\nu}^+W^{-\mu} - W^{+\mu}W_{\mu\nu}^-)V^\nu + ig_4^V W_\mu^+ W_\nu^- (\partial^\mu V^\nu + \partial^\nu V^\mu) \\
 &\quad - ig_5^V \epsilon^{\mu\nu\rho\sigma} (W_\mu^+ \partial_\rho W_\nu^- - \partial_\rho W_\mu^+ W_\nu^-) V_\sigma + \frac{\lambda^V}{m_W^2} W_\mu^{+\nu} W_\nu^{-\rho} V_\rho^\mu \\
 &\quad + \left. \frac{\widetilde{\lambda}^V}{m_W^2} W_\mu^{+\nu} W_\nu^{-\rho} \widetilde{V}_\rho^\mu + \kappa^V W_\mu^+ W_\nu^- V^{\mu\nu} + \widetilde{\kappa}^V W_\mu^+ W_\nu^- \widetilde{V}^{\mu\nu} \right).
 \end{aligned} \tag{6.0.2}$$

Here $W_{\mu\nu}^\pm = \partial_\mu W_\nu^\pm - \partial_\nu W_\mu^\pm$, $V_{\mu\nu} = \partial_\mu V_\nu - \partial_\nu V_\mu$, $\widetilde{V}^{\mu\nu} = 1/2\epsilon^{\mu\nu\rho\sigma} V_{\rho\sigma}$, and the overall coupling constants are defined as $g_{WW\gamma} = -g \sin\theta_W$ and $g_{WWZ} = -g \cos\theta_W$, θ_W being the weak mixing angle. In the SM $g_1^V = 1$, $\kappa^V = 1$ and other couplings are zero. The anomalous part in g_1^V , κ^V would be $\Delta g_1^V = g_1^V - 1$, $\Delta\kappa^V = \kappa^V - 1$, respectively. The couplings g_1^V , κ^V and λ^V are CP -even (both C and P -even), while g_4^V (odd in C , even in P), $\widetilde{\kappa}^V$ and $\widetilde{\lambda}^V$ (even in C , odd in P) are CP -odd. On the other hand g_5^V is both C and P -odd making it CP -even. We note that the coupling ($c_i^{\mathcal{L}}$) of the Lagrangian in Eq. (6.0.2) are related to the couplings of the operators in Eq. (6.0.1) through the relations given in Eq. (1.3.13) when $SU(2) \times U(1)$ gauge invariance is assumed.

For convenience, we label the anomalous couplings of the three scenarios as follows: The couplings of the operators in Eq. (6.0.1), the couplings of effective vertices in \mathcal{L}_{WWV} in Eq. (6.0.2) and the vertex couplings translated from the operators in Eq. (1.3.13) are labelled

as $c_i^{\mathcal{O}}$, $c_i^{\mathcal{L}}$, and $c_i^{\mathcal{L}^g}$, respectively. The couplings in the three scenarios are thus,

$$c_i^{\mathcal{O}} = \{c_{WWW}, c_W, c_B, c_{\widetilde{WW}}, c_{\widetilde{W}}\}, \quad (6.0.3)$$

$$c_i^{\mathcal{L}} = \{\Delta g_1^V, g_4^V, g_5^V, \lambda^V, \widetilde{\lambda}^V, \Delta \kappa^V, \widetilde{\kappa}^V\}, \quad V = \gamma, Z, \quad (6.0.4)$$

$$c_i^{\mathcal{L}^g} = \{\lambda^V, \widetilde{\lambda}^V, \Delta \kappa^\gamma, \widetilde{\kappa}^\gamma, \Delta g_1^Z, \Delta \kappa^Z, \widetilde{\kappa}^Z\}. \quad (6.0.5)$$

In the theoretical side, these anomalous gauge boson self couplings may be obtained from some high scale new physics such as MSSM [76–78], extra dimension [79,80], Georgi-Machacek model [81], etc. by integrating out the heavy degrees of freedom. Some of these couplings can also be obtained at loop level within the SM [237,238].

There has been a lot of studies to probe the anomalous WWZ/γ couplings in the effective operators method as well as in the effective vertex factor approach subjected to $SU(2) \times U(1)$ invariance for various colliders: for e^+e^- linear collider [64,107–118], for Large Hadron electron collider (LHeC) [119–121], $e-\gamma$ collider [122] and for LHC [102,114,115,123–132]. Some CP -odd WWV couplings have been studied in Refs. [117,131]. Direct measurement of these charged aTGC have been performed at the LEP [149–152], Tevatron [153,154], LHC [143,155–169] and Tevatron-LHC [170]. The tightest one parameter limit obtained on the anomalous couplings from experiments are given in Table 6.1. The tightest limits on operator couplings ($c_i^{\mathcal{O}}$) are obtained in Ref. [167] for CP -even ones and in Ref. [157] for CP -odd ones. These limits translated to $c_i^{\mathcal{L}^g}$ using Eq. (1.3.13) are also given in Table 6.1. The tightest limits on the couplings g_4^Z and g_5^Z are obtained in Ref. [150,151] considering the Lagrangian in Eq. (6.0.2).

The W^+W^- production is one of the important processes to be studied at the ILC [195–197] for precision test [207] as well as for BSM physics. This process has been studied earlier for SM phenomenology as well as for various BSM physics with and without beam polarization [64,208,209,219,220,239]. Here we intend to study WWV anomalous couplings in $e^+e^- \rightarrow W^+W^-$ at $\sqrt{s} = 500$ GeV and integrated luminosity of $\mathcal{L} = 100 \text{ fb}^{-1}$ using the cross section, forward-backward asymmetry and 8 polarizations asymmetries of W^- for a set of choices of longitudinally polarized e^+ and e^- beams in the channel $W^- \rightarrow l^- \bar{\nu}_l$ ($l = e, \mu$)¹ and $W^+ \rightarrow \text{hadrons}$. The polarization of Z and W are being used widely recently for various BSM studies [180–186] along with studies with anomalous gauge boson couplings [98,99,106,149]. Recently the polarizations of W/Z has been measured in WZ production at the

¹For simplicity we do not include tau decay mode as the tau decays to neutrino within the beam pipe giving extra missing momenta affecting the reconstruction of the events.

Table 6.1. The list of tightest limits obtained on the anomalous couplings of dimension-6 operators in Eq. (6.0.1) and effective vertices in Eq. (6.0.2) in $SU(2) \times U(1)$ gauge (except g_4^Z and g_5^Z) at 95% C.L. from experiments.

$c_i^{\mathcal{O}}$	Limits (TeV $^{-2}$)	Remark
$\frac{c_{WWW}}{\Lambda^2}$	[-1.58, +1.59]	CMS $\sqrt{s} = 13$ TeV, $\mathcal{L} = 35.9$ fb $^{-1}$, $SU(2) \times U(1)$ [167]
$\frac{c_W}{\Lambda^2}$	[-2.00, +2.65]	CMS [167]
$\frac{c_B}{\Lambda^2}$	[-8.78, +8.54]	CMS [167]
$\frac{c_{\widetilde{WWW}}}{\Lambda^2}$	[-11, +11]	ATLAS $\sqrt{s} = 7(8)$ TeV, $\mathcal{L} = 4.7(20.2)$ fb $^{-1}$ [157]
$\frac{c_{\widetilde{W}}}{\Lambda^2}$	[-580, 580]	ATLAS [157]
$c_i^{\mathcal{L}_g}$	Limits ($\times 10^{-2}$)	Remark
λ^V	[-0.65, +0.66]	CMS [167]
$\Delta\kappa^\gamma$	[-4.4, +6.3]	CMS $\sqrt{s} = 8$ TeV, $\mathcal{L} = 19$ fb $^{-1}$, $SU(2) \times U(1)$ [156]
Δg_1^Z	[-0.61, +0.74]	CMS [167]
$\Delta\kappa^Z$	[-0.79, +0.82]	CMS [167]
$\widetilde{\lambda}^V$	[-4.7, +4.6]	ATLAS [157]
$\widetilde{\kappa}^Z$	[-14, -1]	DELPHI (LEP2), $\sqrt{s} = 189-209$ GeV, $\mathcal{L} = 520$ pb $^{-1}$ [151]
$c_i^{\mathcal{L}}$	Limits ($\times 10^{-2}$)	Remark
g_4^Z	[-59, -20]	DELPHI [151]
g_5^Z	[-16, +9.0]	OPAL (LEP), $\sqrt{s} = 183-209$ GeV, $\mathcal{L} = 680$ pb $^{-1}$ [150]

LHC [240]. Besides the final state polarizations, the initial state beam polarizations at the ILC can be used to enhance the relevant signal to background ratio [207–211]. It also has the ability to distinguish between CP -even and CP -odd couplings [83, 85, 93, 94, 101, 207, 212–216]. We note that an e^+e^- machine will run with longitudinal beam polarizations switching between (η_3, ξ_3) and $(-\eta_3, -\xi_3)$ [207], where $\eta_3(\xi_3)$ is the longitudinal polarization of e^- (e^+). For integrated luminosity of 100 fb $^{-1}$, one will have half the luminosity available for each polarization configurations. The most common observables, the cross section for example, studied in literature with beam polarizations are the total cross section

$$\sigma_T(\eta_3, \xi_3) = \sigma(+\eta_3, +\xi_3) + \sigma(-\eta_3, -\xi_3) \quad (6.0.6)$$

and the difference

$$\sigma_A(\eta_3, \xi_3) = \sigma(+\eta_3, +\xi_3) - \sigma(-\eta_3, -\xi_3). \quad (6.0.7)$$

We find that combining the two opposite beam polarizations at the level of χ^2 rather than

combining them as in Eq. (6.0.6) & (6.0.7), we can constrain the anomalous couplings better in this analysis, see Sect. 6.2.2 for explanation.

We note that there exist 64 polarization correlations [64] apart from 8 + 8 polarizations for W^+ and W^- . The measurement of these correlations require identification of light quark flavours in the above channel, which is not possible, hence we are not including polarization correlations in our analysis. In the case of both the W s decaying leptonically, there are two missing neutrinos and reconstruction of polarization observables suffers combinatorial ambiguity. Here we aim to work with a set of observables that can be reconstructed uniquely and test their ability to probe the anomalous couplings including partial contribution up to $\mathcal{O}(\Lambda^{-4})^2$.

6.1 Observables and effect of beam polarizations

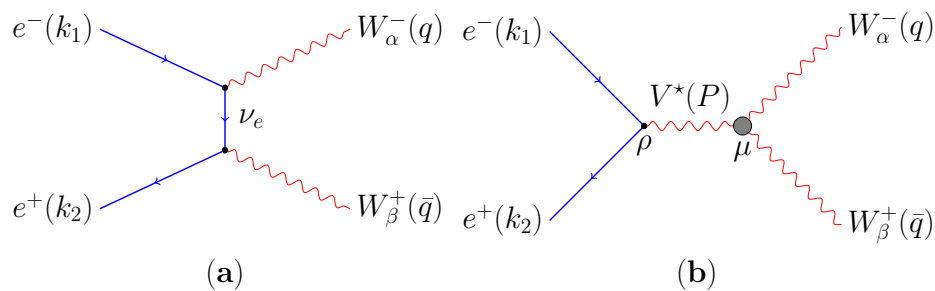


Figure 6.1. Feynman diagrams of $e^+e^- \rightarrow W^+W^-$, (a) t -channel and (b) s -channel with anomalous W^+W^-V ($V = \gamma, Z$) vertex contribution shown by the shaded blob.

We study W^+W^- production at ILC running at $\sqrt{s} = 500$ GeV and integrated luminosity $\mathcal{L} = 100 \text{ fb}^{-1}$ using longitudinal polarization of e^- and e^+ beams giving 50 fb^{-1} to each choice of beam polarization. The Feynman diagrams for the process are shown in Fig. 6.1 where Fig. 6.1(a) corresponds to the ν_e mediated t -channel diagram and the Fig. 6.1(b) corresponds to the V (Z/γ) mediated s -channel diagram containing the aTGC contributions represented by the shaded blob. The decay mode is chosen to be

$$W^+ \rightarrow q_u \bar{q}_d, \quad W^- \rightarrow l^- \bar{\nu}_l, \quad l = e, \mu, \quad (6.1.1)$$

where q_u and q_d are up-type and down-type quarks, respectively. We use complete set of eight spin-1 observables of W^- boson (see chapter 2) along with the production rate. Owing

²We calculate cross section up to $\mathcal{O}(\Lambda^{-4})$, i.e., quadratic in dimension-6 (as linear approximation is not valid, e.g., see appendix C.2) and linear in dimension-8 couplings choosing dimension-8 couplings to be zero to compare our result with current LHC constraints on dimension-6 parameters [157, 167].

to the t -channel process (Fig. 6.1a) and absence of a u -channel process, like in ZV productions in chapters 3 & 4, the W^\pm produced are not forward-backward symmetric. We include the forward-backward asymmetry of the W^- , defined as

$$A_{fb} = \frac{1}{\sigma_{W^+W^-}} \left[\int_0^1 \frac{d\sigma_{W^+W^-}}{d\cos\theta_{W^-}} - \int_{-1}^0 \frac{d\sigma_{W^+W^-}}{d\cos\theta_{W^-}} \right], \quad (6.1.2)$$

to the set of observables making a total of ten observables including the cross section as well. Here θ_{W^-} is the production angle of the W^- w.r.t. the e^- beam direction and $\sigma_{W^+W^-}$ is the production cross section. The asymmetries of the W^- can be measured in a real collider from the final state lepton l^- . One has to calculate the asymmetries in the rest frame of W^- which require the missing $\bar{\nu}_l$ momenta to be reconstructed. At an e^+e^- collider, as studied here, reconstructing the missing $\bar{\nu}_l$ is possible because only one missing particle is involved and no PDFs are involved, i.e., initial momenta are known. But for a collider where PDFs are involved, reconstructing the actual missing momenta may not be possible.

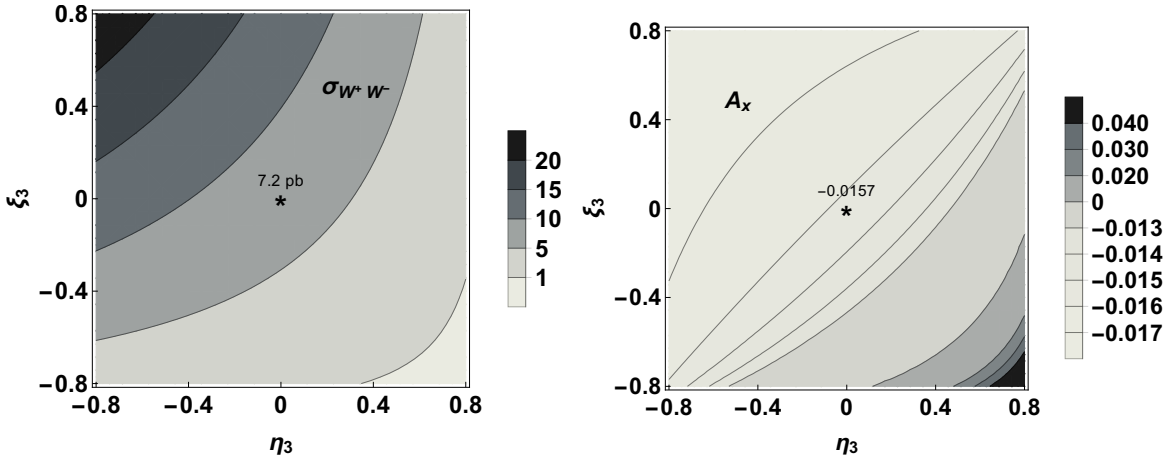


Figure 6.2. The production cross section $\sigma_{W^+W^-}$ in pb (*left-panel*) and the polarization asymmetry A_x (*right-panel*) in the SM as a function of longitudinal beam polarizations η_3 (for e^-) and ξ_3 (for e^+) at $\sqrt{s} = 500$ GeV. The asterisks mark represent the unpolarized points and the number near it correspond to the SM values for corresponding observables with unpolarized beams.

We explore the dependence of the cross section and asymmetries on the longitudinal polarization η_3 of e^- and ξ_3 of e^+ . In Fig. 6.2 we show the production cross section $\sigma_{W^+W^-}$ and A_x as a function of beam polarization as an example. The cross section decreases along $\eta_3 = -\xi_3$ path from 20 pb on the left-top corner to 7.2 pb at the unpolarized point and further to 1 pb in the right-bottom corner. This is due to the fact that the W^\pm couples to left chiral e^- i.e., it requires e^- to be negatively polarized and e^+ to be positively polarized for the higher cross section. The variation of A_{fb} (not shown) with beam polarization is the same as the cross section but very slow above the line $\eta_3 = \xi_3$. From this, we can expect that a positive

η_3 and a negative ξ_3 will reduce the SM contributions to observables increasing the S/\sqrt{B} ratio ($S = \text{signal}$, $B = \text{background}$). Some other asymmetries, like A_x , have opposite dependence on the beam polarizations compared to the cross section, their modulus get reduce for negative η_3 and positive ξ_3 .

6.2 Probe of the anomalous couplings

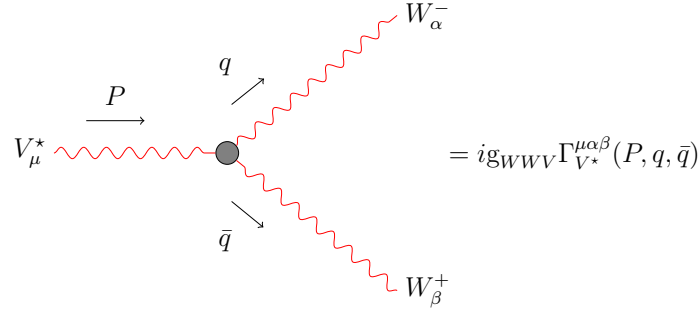


Figure 6.3. The WWV vertex showing anomalous contribution represented the shaded blob on top of SM. The momentum P is incoming to the vertex, while q and \bar{q} are outgoing from the vertex.

The W^+W^-V vertex (Fig. 6.3) for the Lagrangian in Eq. (6.0.2) for on-shell W s would be $ig_{WWV}\Gamma_V^{\mu\alpha\beta}$ [64, 107] and it is given by,

$$\begin{aligned} \Gamma_V^{\mu\alpha\beta} = & f_1^V (q - \bar{q})^\mu g^{\alpha\beta} - \frac{f_2^V}{m_W^2} (q - \bar{q})^\mu P^\alpha P^\beta + f_3^V (P^\alpha g^{\mu\beta} - P^\beta g^{\mu\alpha}) + i f_4^V (P^\alpha g^{\mu\beta} + P^\beta g^{\mu\alpha}) \\ & + i f_5^V \epsilon^{\mu\alpha\beta\rho} (q - \bar{q})_\rho - f_6^V \epsilon^{\mu\alpha\beta\rho} P_\rho + \frac{\widetilde{f}_7^V}{m_W^2} (\bar{q}^\alpha \epsilon^{\mu\beta\rho\sigma} + q^\beta \epsilon^{\mu\alpha\rho\sigma}) q_\rho \bar{q}_\sigma, \end{aligned} \quad (6.2.1)$$

where P, q, \bar{q} are the four-momenta of V, W^-, W^+ , respectively. The momentum conventions are shown in Fig. 6.3. The form factors f_i s have been obtained from the Lagrangian in Eq. (6.0.2) using FeynRules [204] to be

$$\begin{aligned} f_1^V &= g_1^V + \frac{s}{2m_W^2} \lambda^V, \quad f_2^V = \lambda^V, \quad f_3^V = g_1^V + \kappa^V + \lambda^V, \\ f_4^V &= g_4^V, \quad f_5^V = g_5^V, \quad f_6^V = \widetilde{\kappa}^V + \left(1 - \frac{s}{2m_W^2}\right) \widetilde{\lambda}^V, \quad \widetilde{f}_7^V = \widetilde{\lambda}^V. \end{aligned} \quad (6.2.2)$$

We use the vertex factors in Eq. (6.2.1) for the analytical calculation of our observables and cross validate them numerically with MadGraph5 [190] implementation of Eq. (6.0.2). As an example, we present two observables $\sigma_{W^+W^-}$ and A_{zz} for the SM ($c_i^{\mathcal{L}} = 0.0$) and for a

Table 6.2. The dependence of observables (numerators) on the form factor couplings in the form of $c_i^{\mathcal{L}}$ (linear), $(c_i^{\mathcal{L}})^2$ (quadratic) and $c_i^{\mathcal{L}}c_j^{\mathcal{L}}$, $i \neq j$ (interference) in the process $e^+e^- \rightarrow W^+W^-$. Here, $V \in \{\gamma, Z\}$. The “✓” (*checkmark*) represents the presence and “—” (*big-dash*) corresponds to absence.

Parameters	σ	$\sigma \times A_x$	$\sigma \times A_y$	$\sigma \times A_z$	$\sigma \times A_{xy}$	$\sigma \times A_{xz}$	$\sigma \times A_{yz}$	$\sigma \times A_{x^2-y^2}$	$\sigma \times A_{zz}$	$\sigma \times A_{fb}$
Δg_1^V	✓	✓	—	✓	—	✓	—	✓	✓	✓
g_4^V	—	—	✓	—	✓	—	✓	—	—	—
g_5^V	✓	✓	—	✓	—	✓	—	✓	✓	✓
λ^V	✓	✓	—	✓	—	✓	—	✓	✓	✓
$\widetilde{\lambda}^V$	—	—	✓	—	✓	—	✓	—	—	—
$\Delta \kappa^V$	✓	✓	—	✓	—	✓	—	✓	✓	✓
$\widetilde{\kappa}^V$	—	—	✓	—	✓	—	✓	—	—	—
$(\Delta g_1^V)^2$	✓	✓	—	—	—	—	—	✓	✓	—
$(g_4^V)^2$	✓	—	—	—	—	—	—	✓	✓	—
$(g_5^V)^2$	✓	—	—	—	—	—	—	✓	✓	—
$(\lambda^V)^2$	✓	✓	—	—	—	—	—	✓	✓	—
$(\widetilde{\lambda}^V)^2$	✓	✓	—	—	—	—	—	✓	✓	—
$(\Delta \kappa^V)^2$	✓	✓	—	—	—	—	—	✓	✓	—
$(\widetilde{\kappa}^V)^2$	✓	✓	—	—	—	—	—	✓	✓	—
$\Delta g_1^V g_4^V$	—	—	—	—	—	—	✓	—	—	—
$\Delta g_1^V g_5^V$	—	—	—	✓	—	—	—	—	—	✓
$\Delta g_1^V \lambda^V$	✓	✓	—	—	—	—	—	✓	✓	—
$\Delta g_1^V \widetilde{\lambda}^V$	—	—	✓	—	✓	—	—	—	—	—
$\Delta g_1^V \Delta \kappa^V$	✓	✓	—	—	—	—	—	✓	✓	—
$\Delta g_1^V \widetilde{\kappa}^V$	—	—	✓	—	✓	—	—	—	—	—
$g_4^V g_5^V$	—	—	—	—	✓	—	—	—	—	—
$g_4^V \lambda^V$	—	—	—	—	—	—	✓	—	—	—
$g_4^V \widetilde{\lambda}^V$	—	—	—	✓	—	✓	—	—	—	✓
$g_4^V \Delta \kappa^V$	—	—	—	—	—	—	✓	—	—	—
$g_4^V \widetilde{\kappa}^V$	—	—	—	✓	—	✓	—	—	—	✓
$g_5^V \lambda^V$	—	—	—	✓	—	✓	—	—	—	✓
$g_5^V \widetilde{\lambda}^V$	—	—	—	—	—	—	✓	—	—	—
$g_5^V \Delta \kappa^V$	—	—	—	✓	—	✓	—	—	—	✓
$g_5^V \widetilde{\kappa}^V$	—	—	—	—	—	—	✓	—	—	—
$\lambda^V \widetilde{\lambda}^V$	—	—	✓	—	✓	—	—	—	—	—
$\lambda^V \Delta \kappa^V$	✓	✓	—	—	—	—	—	✓	✓	—
$\lambda^V \widetilde{\kappa}^V$	—	—	✓	—	✓	—	—	—	—	—
$\widetilde{\lambda}^V \Delta \kappa^V$	—	—	✓	—	✓	—	—	—	—	—
$\widetilde{\lambda}^V \widetilde{\kappa}^V$	✓	✓	—	—	—	—	—	✓	✓	—
$\Delta \kappa^V \widetilde{\kappa}^V$	—	—	✓	—	✓	—	—	—	—	—

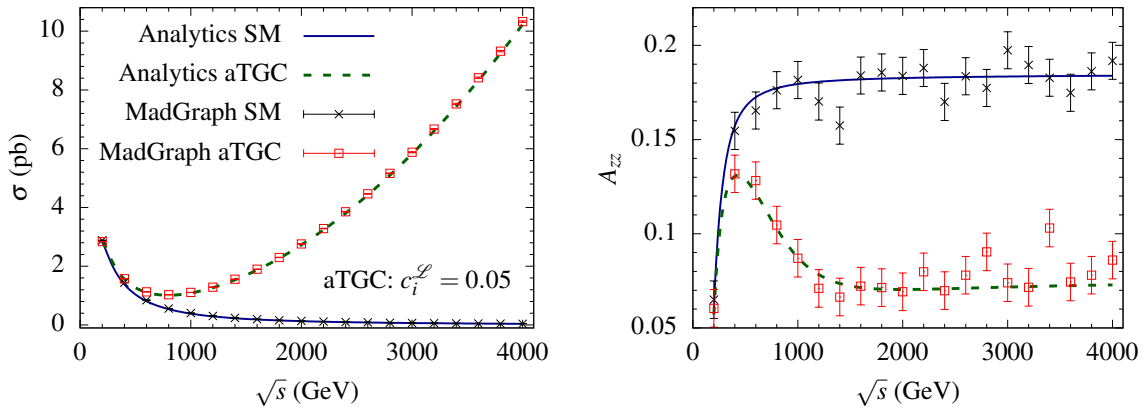


Figure 6.4. The cross section σ including the decays in pb (*left-panel*) and the asymmetry A_{zz} (*right-panel*) in the SM and aTGC with all anomalous couplings ($c_i^{\mathcal{L}}$) at 0.05 as a function of \sqrt{s} for the SM analytic (*solid/blue*) and aTGC analytic (*dashed/green*) with unpolarized beams. The *crossed* (black) points and *boxed* (red) points with errorbars correspond to results from MadGraph5. The errorbars are given for number of events of 10^4 .

chosen couplings point $c_i^{\mathcal{L}} = 0.05$, in Fig. 6.4. The agreement between the analytical and the numerical calculations over a range of \sqrt{s} indicates the validity of relations in Eq. (6.2.2), specially the s dependence of f_1^V and f_6^V .

Analytical expressions of all the observables have been obtained and their dependence on the anomalous couplings $c_i^{\mathcal{L}}$ are given in Table 6.2. The CP -even couplings in CP -even observables σ , A_x , A_z , A_{xz} , $A_{x^2-y^2}$, and A_{zz} appear in linear as well as in quadratic form but do not appear in the CP -odd observables A_y , A_{xy} , and A_{yz} . On the other hand, CP -odd couplings appears linearly in CP -odd observables and quadratically in CP -even observables. Thus the CP -even couplings may have a double patch in their confidence intervals leading to asymmetric limits which will be discussed in subsection 6.2.1. The CP -odd couplings, however, will have a single patch in their confidence intervals and will acquire symmetric limits.

6.2.1 Sensitivity of observables on anomalous couplings and their binning

We studied the sensitivities (see Eq. (4.2.1) for definition) of all 10 observables to all the 14 couplings of the Lagrangian in Eq. (6.0.2). We take $\mathcal{L} = 50 \text{ fb}^{-1}$ of integrated luminosity for each of the opposite beam polarizations and systematic uncertainties of $\epsilon_\sigma = 2 \%$ for the cross section and $\epsilon_A = 1 \%$ for the asymmetries as a benchmark scenario for the present analyses. The sensitivities of all observables on g_4^Z and $\Delta\kappa^\gamma$ are shown in Fig. 6.5 as representative. Being a CP -odd coupling (either only linear or only quadratic terms present in the observ-

ables), g_4^Z has a single patch in the confidence interval, while the $\Delta\kappa^\gamma$ being a CP -even (linear as well as quadratic terms present in the observables) has two patches in the sensitivity curve, as noted earlier. The CP -odd observable A_y provides the tightest one parameter limit on g_4^Z . The tightest 1σ limit on $\Delta\kappa^\gamma$ is obtained using A_{fb} , while at 2σ level, a combination of A_{fb} and A_x provide the tightest limit.

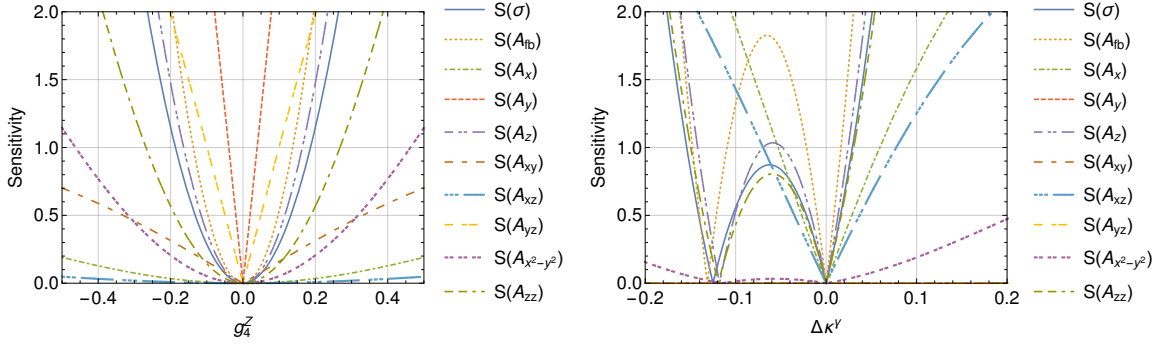


Figure 6.5. The one parameter sensitivities of the cross section σ , A_{fb} and 8 polarization asymmetries (A_i) on g_4^Z (left-panel) and on $\Delta\kappa^\gamma$ (right-panel) for $\sqrt{s} = 500$ GeV, $\mathcal{L} = 100$ fb $^{-1}$ with unpolarized beams.

Here, we have a total of 14 different anomalous couplings to be measured, while we only have 10 observables. A certain combination of large couplings may mimic the SM within the statistical errors. To avoid these we need more number of observables to be included in the analysis. We achieve this by dividing $\cos\theta_{W^-}$ into eight bins and calculate the cross section and polarization asymmetries in all of them. In Fig. 6.6 the cross section and the polarization asymmetries A_z , A_x , and A_y are shown as a function of $\cos\theta_{W^-}$ for the SM and some aTGC couplings for both polarized and unpolarized beams. The sensitivities for unpolarized SM cases are shown in *dotted* (blue) lines; SM with polarization of $(\eta_3, \xi_3) = (+0.6, -0.6)$ are shown in *dashed* (black) lines. The *solid* (red) lines correspond to unpolarized aTGC values, while *dashed-dotted* (green) lines represent polarized aTGC values of observables. For the cross section (*left-top-panel*), we take Δg_1^γ to be 0.1 and all other couplings to zero for both polarized and unpolarized beams. We see that the fractional deviation from the SM value is larger in the most backward bin ($\cos\theta_{W^-} \in (-1.0, -0.75)$) and gradually reduces in the forward direction. The deviation is even larger in case of beam polarization. The sensitivity of the cross section on Δg_1^γ is thus expected to be high in the most backward bin. For the asymmetries A_z (*right-top-panel*), A_{xz} (*left-bottom-panel*) and A_y (*right-bottom-panel*), the aTGC are assumed to be $\Delta\kappa^Z = 0.05$, $\lambda^Z = 0.05$ and $g_4^Z = 0.05$, respectively, while others are kept at zero. The changes in the asymmetries due to aTGC are larger in the backward bins for both polarized and unpolarized beams. We note that the asymmetries may not have the

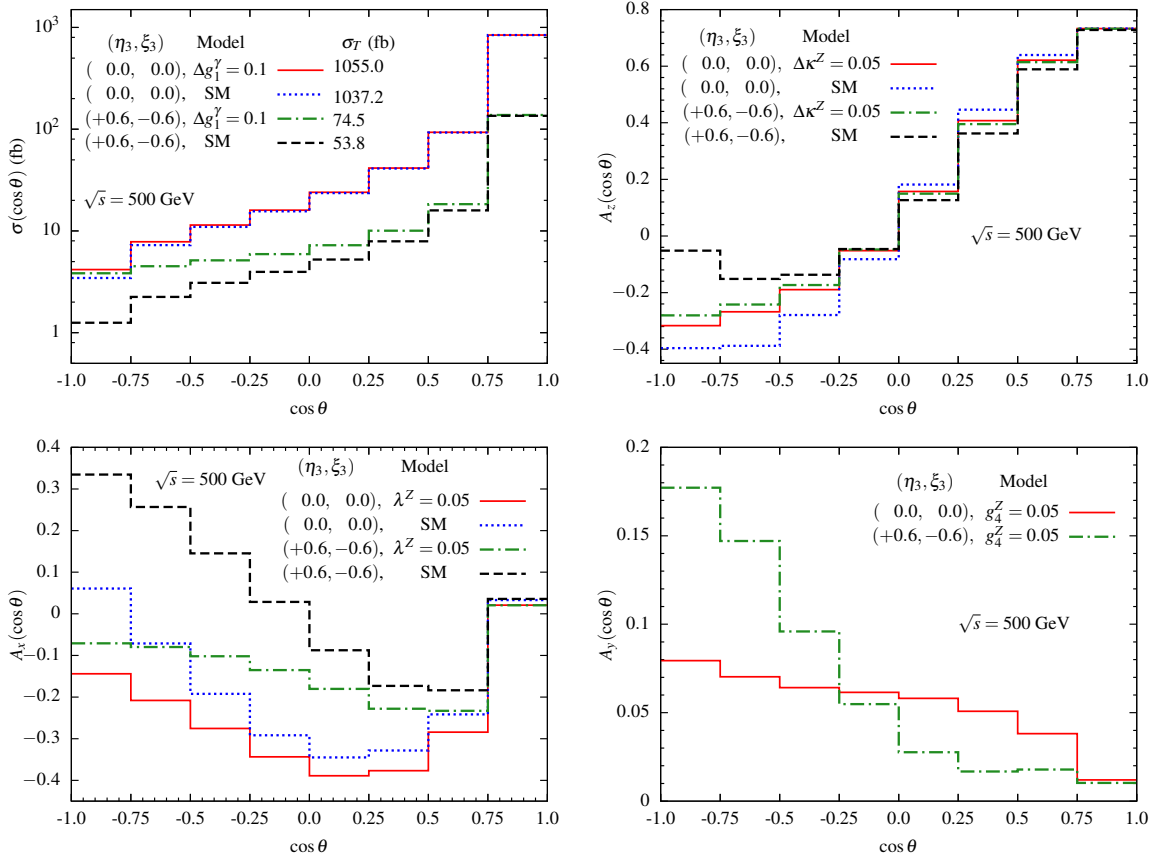


Figure 6.6. The cross section σ (left-top), A_z (right-top), A_x (left-bottom) and A_y (right-bottom) as a function of $\cos\theta$ of W^- in 8 bin for $\sqrt{s} = 500$ GeV. The *dotted* (blue) lines correspond to the SM unpolarized values, *solid* (red) lines correspond to the unpolarized aTGC values, *dashed* (black) lines represent the polarized SM values, and *dashed-dotted* (green) lines represent polarized aTGC values of observables. For aTGC, only one anomalous coupling has been assumed non-zero and others kept at zero in each *panel*.

highest sensitivity in the most backward bin, but in some other bins. We consider the cross section and eight polarization asymmetries in all 8 bins, i.e., we have 72 observables in our analysis.

One parameter sensitivity of the set of 9 observables in all 8 bins to all the couplings have been studied. We show sensitivity of A_y on g_4^Z and of A_z on $\Delta\kappa^\gamma$ in the 8 bin in Fig. 6.7 as representative. The tightest limits based on sensitivity (coming from one bin) is roughly twice as tight as compared to the unbin case in Fig. 6.5. Thus we expect simultaneous limits on all the couplings to be tighter when using binned observables. We perform a set of MCMC analyses with a different set of observables for different kinematical cuts with unpolarized beams to understand their roles in providing limits on the anomalous couplings. These analyses are listed in Table 6.3. The corresponding 14-dimensional rectangular volume³ made

³This volume of limit is the the volume of a 14-dimensional rectangular box bounding by the 95% BCI projection of simultaneous limits in each coupling, which can be a measure of goodness of the benchmark beam polarization. We computed the cross section and other asymmetries keeping term up to quadratic in couplings. In this case, even a single observable can give a finite volume of limit and constrain all 14 couplings, which

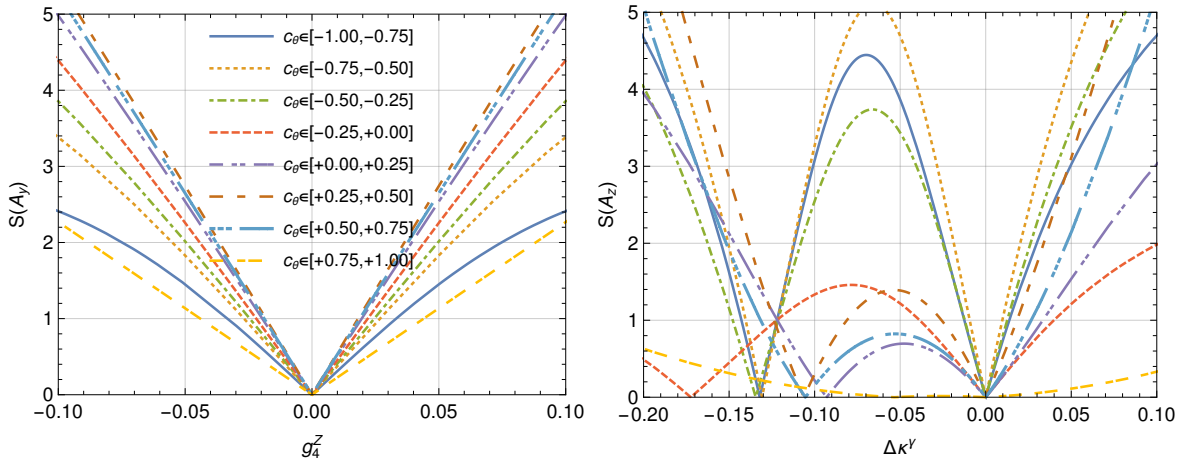


Figure 6.7. The one parameter sensitivities of A_x on g_4^Z (left-panel) and of A_z on $\Delta\kappa^\gamma$ (right-panel) in 8 bins at $\sqrt{s} = 500$ GeV, $\mathcal{L} = 100$ fb $^{-1}$ with $c_\theta = \cos\theta_{W^-}$ with unpolarized beams.

Table 6.3. The list of analyses performed in the present work and set of observables used with different kinematical cuts to obtain simultaneous limits on the anomalous couplings at $\sqrt{s} = 500$ GeV, $\mathcal{L} = 100$ fb $^{-1}$ with unpolarized beams. The rectangular volumes of couplings at 95% BCI are shown in the last column for each analyses (see text for details).

Analysis name	Set of observables	Kinematical cut on $\cos\theta_{W^-}$	Volume of Limits
σ -ubinned	σ	$\cos\theta_{W^-} \in [-1.0, 1.0]$	4.4×10^{-11}
Unbinned	σ, A_{fb}, A_i	$\cos\theta_{W^-} \in [-1.0, 1.0]$	3.1×10^{-12}
σ -binned	σ	$\cos\theta_{W^-} \in [\frac{m-5}{4}, \frac{m-4}{4}], m = 1, 2, \dots, 8$	3.7×10^{-12}
Pol.-binned	A_i	"	1.6×10^{-15}
Binned	σ, A_i	"	5.2×10^{-17}

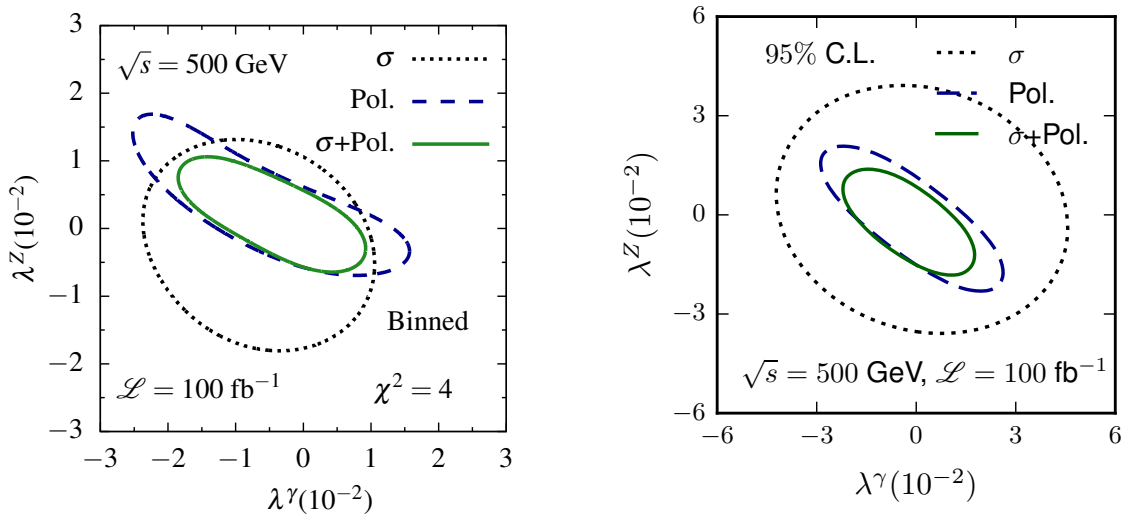


Figure 6.8. The $\chi^2 = 4$ contours in the left-panel and 95 % C.L. contours from simultaneous analysis in the right-panel in the λ^γ - λ^Z plane using the binned cross sections (σ) alone in dotted (black) lines, just binned polarizations asymmetries (Pol.) in dashed (blue) lines and the bin cross section together with binned polarization asymmetries ($\sigma + \text{Pol.}$) in solid (green) lines for $\sqrt{s} = 500$ GeV, $\mathcal{L} = 100$ fb $^{-1}$.

would not be possible if only terms linear in couplings were present.

out of 95% Bayesian confidence interval on the anomalous couplings are also listed in Table 6.3 in the last column. The simplest analysis would be to consider only the cross section in the full $\cos\theta_{W^-}$ domain and perform MCMC analysis which is named as σ -ubinned. The typical 95% limits on the parameters range from $\sim \pm 0.04$ to ± 0.25 giving the volume of limits to be 4.4×10^{-11} . As we have polarizations asymmetries, the straight forward analysis would be to consider all the observables for the full domain of $\cos\theta_{W^-}$. This analysis is named Unbinned where limits on anomalous couplings get constrained better reducing the volume of limits by a factor of 10 compared to the σ -ubinned. To see how binning improve the limits, we performed an analysis named σ -binned using only the cross section in 8 bins. We see that the analysis σ -binned is better than the analysis σ -unbinned and comparable to the analysis Unbinned. To see the strength of the polarization asymmetries, we performed an analysis named Pol.-binned using just the polarization asymmetries in 8 bins. We see that this analysis is much better than the analysis σ -binned. The most natural and complete analysis would be to consider all the observables after binning. The analysis is named as Binned which has limits much better than any analyses. The comparison between the analyses σ -binned, Pol.-binned and Binned is shown in Fig. 6.8 in the panel λ^γ - λ^Z in two-parameter (*left-panel*) as well as in multi-parameter (*right-panel*) analysis using MCMC as representative. The *right-panel* reflects the Table 6.3. The behaviours are same even in the two parameter analysis (*left-panel*) by keeping all other parameter to zero, i.e., the bounded region for $\chi^2 = 4$ is smaller in Pol.-binned (Pol.) than σ -binned (σ) and smallest for Binned (σ +Pol.).

We also calculate one parameter limits on all the couplings at 95 % C.L. considering all the binned observables with unpolarized beams in the effective vertex formalism as well as in the effective operator approach and list them in the last column of Tables 6.4 & 6.5, respectively for comparison. In the next subsection, we study the effect of beam polarizations on the limits of the anomalous couplings.

6.2.2 Effect of beam polarizations to the limits on aTGC

A suitable choice of beam polarizations can enhance the signal to background ratio tightening the constraints on the aTGC. Below we discuss the comparison between various combinations of beam polarizations to better constrain the aTGC. After that, we see the effect of beam polarizations in constraining the aTGC for both fixed choices and best combined choices.

6.2.2.a Combining beam polarization with it's opposite values

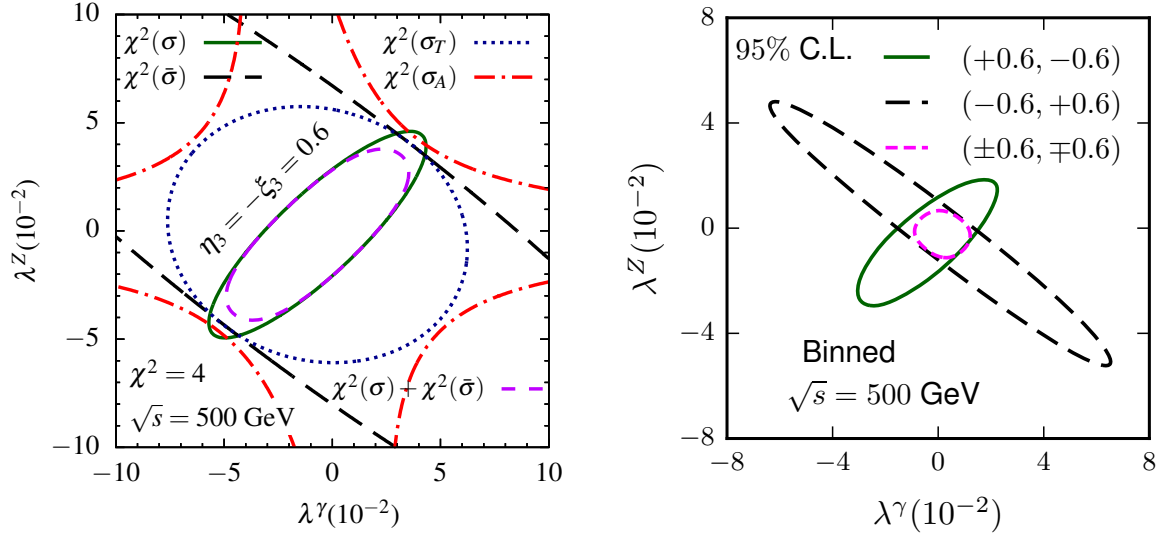


Figure 6.9. The $\chi^2 = 4$ contours of the unbinned cross sections $\sigma = \sigma(+\eta_3, +\xi_3)$ in solid/green lines, $\bar{\sigma} = \sigma(-\eta_3, -\xi_3)$ in big-dashed/black lines, $\sigma_T = \sigma(+\eta_3, +\xi_3) + \sigma(-\eta_3, -\xi_3)$ in dotted/blue line, $\sigma_A = \sigma(+\eta_3, +\xi_3) - \sigma(-\eta_3, -\xi_3)$ in dash-dotted/red line and the combined χ^2 of σ and $\bar{\sigma}$ in dashed/magenta lines for polarization $(\eta_3, \xi_3) = (+0.6, -0.6)$ on $\lambda^\gamma - \lambda^Z$ plane are shown in the left-panel. The 95 % C.L. contours from simultaneous analysis in $\lambda^\gamma - \lambda^Z$ plane for the beam polarization $(+0.6, -0.6)$, $(-0.6, +0.6)$ and their combined one $(\pm 0.6, \mp 0.6)$ are shown in the right-panel using all the binned observables, i.e., in Binned case. The analyses are done for $\sqrt{s} = 500$ GeV and $\mathcal{L} = 50 \text{ fb}^{-1}$ luminosity to each beam polarization set.

To reduce the systematic errors in an analysis due to luminosity, the beam polarizations are flipped between two opposite choices frequently giving half the total luminosity to both the polarization choices in an e^+e^- collider. One can, in principle, use the observables, e.g., the total cross section (σ_T) or their difference (σ_A) as in Eqs. (6.0.6) & (6.0.7), respectively or for the two opposite polarization choices (σ & $\bar{\sigma}$) separately for a suitable analysis. In this work, we do not combine the beam polarization $(+\eta_3, +\xi_3)$ and it's opposite $(-\eta_3, -\xi_3)$ at the level of observables, rather we combine them at the level of χ^2 (as we did in chapter 4, see Eq. (4.4.1)) given by,

$$\chi_{tot}^2(\pm\eta_3, \pm\xi_3) = \sum_{bin} \sum_N \left(\chi^2[\mathcal{O}_N(+\eta_3, +\xi_3)] + \chi^2[\mathcal{O}_N(-\eta_3, -\xi_3)] \right), \quad (6.2.3)$$

where N runs over all the observables. This is because the later combination constrains the couplings better than any combinations and of-course the individuals. To depict this, we present the $\chi^2 = 4$ contours of the unbinned cross sections in Fig. 6.9 (left-panel) for beam polarization $(+0.6, -0.6)$ (σ) and $(-0.6, +0.6)$ ($\bar{\sigma}$) and the combinations σ_T and σ_A along with the combined χ^2 in the $\lambda^\gamma - \lambda^Z$ plane for $\mathcal{L} = 50 \text{ fb}^{-1}$ luminosity to each polar-

ization choice as representative. A systematic error of 2% is used as a benchmark in the cross section. The nature of the contours can be explain as follows: In the WW production, the aTGC contributions appear only in the s -channel (see Fig. 6.1), where initial state e^+e^- couples through γ/Z boson and both left and right chiral electrons contribute almost equally. The t -channel diagram, however, is pure background and receives contribution only from left chiral electrons. As a result the $\bar{\sigma}$ (*big-dashed/black*) contains more background than σ (*solid/green*) leading to a weaker limit on the couplings. Further, inclusion of $\bar{\sigma}$ into σ_T (*dotted/blue*) and σ_A (*dashed-dotted/red*) reduces the signal to background ratio and hence they are less sensitive to the couplings. The total χ^2 for the combined beam polarizations shown in *dashed* (magenta) is, of course, the best to constrain the couplings. This behaviour is reverified with the simultaneous analysis using the binned cross sections and polarization asymmetries (72 observables in the Binned case) and shown in Fig. 6.9 (*right-panel*) in the same $\lambda^\gamma-\lambda^Z$ plane showing the 95 % C.L. contours for beam polarizations (+0.6, -0.6), (-0.6, +0.6), and their combinations ($\pm 0.6, \mp 0.6$). Thus we choose to combine the opposite beam polarization choices at the level of χ^2 rather than combining them at the level of observables.

6.2.2.b Case of fixed beam polarizations

Although, we will have data for two opposite choice of beam polarizations, we first investigate how the fixed beam polarizations of various amplitudes affect the limits. We estimate simultaneous limits on all the 14 (independent) anomalous couplings $c_i^{\mathcal{L}}$ using MCMC method in the Binned case for five different set of fixed choices of beam polarizations (η_3, ξ_3) namely (-0.8, +0.8), (-0.4, +0.4), (0.0, +0.0), (+0.4, -0.4) and (+0.8, -0.8). We choose the cross-diagonal choices as they provide optimal result for the cross section. The cross section depending on beam polarizations can be expressed as,

$$\begin{aligned}\sigma(\eta_3, \xi_3) &= (1 + \eta_3)(1 - \xi_3)\frac{1}{4}\sigma_R + (1 - \eta_3)(1 + \xi_3)\frac{1}{4}\sigma_L \\ &= (1 - \eta_3\xi_3)\frac{1}{4}(\sigma_R + \sigma_L) + (\eta_3 - \xi_3)\frac{1}{4}(\sigma_R - \sigma_L),\end{aligned}\quad (6.2.4)$$

where σ_R denotes the e_R annihilation cross section, while σ_L is that for e_L annihilation cross section. Thus, the $\eta_3 = -\xi_3$ polarizations will give optimal result for the cross section. The 95 % BCI limits on the couplings $c_i^{\mathcal{L}}$ are shown in Fig. 6.10 for the above choices of beam polarizations. We observe that the limits on anomalous couplings are tightest for the beam

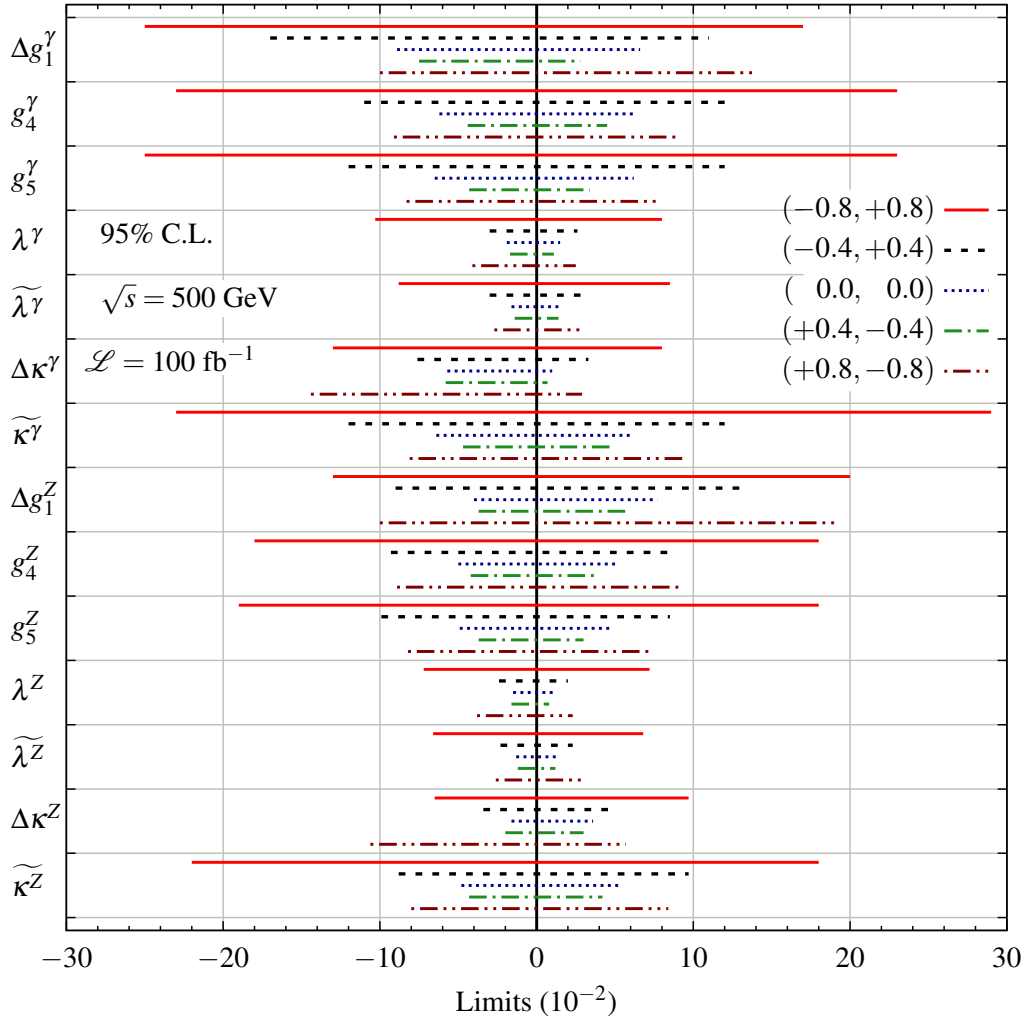


Figure 6.10. The 95 % BCI limits on the anomalous couplings $c_i^{\mathcal{L}}$ for a set of fixed choices of beam polarizations for $\sqrt{s} = 500$ GeV, $\mathcal{L} = 100 \text{ fb}^{-1}$ using the binned observables.

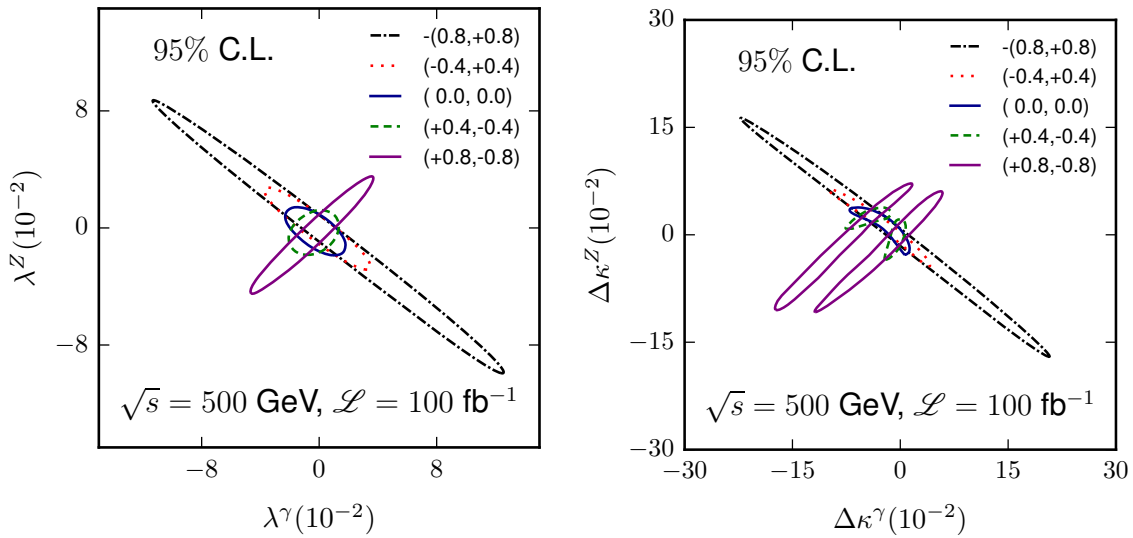


Figure 6.11. The 95 % C.L. contours from simultaneous analysis in $\lambda^\gamma - \lambda^Z$ plane (*left-panel*) and $\lambda^\gamma - \lambda^Z$ plane (*right-panel*) for a set of fixed choices of beam polarizations for $\sqrt{s} = 500$ GeV, $\mathcal{L} = 100 \text{ fb}^{-1}$ using the binned observables.

polarization $(+0.4, -0.4)$. We estimate simultaneous limits on the couplings on several other polarization points along $\eta_3 = -\xi_3$ direction and find the $(+0.4, -0.4)$ polarization to be the best to provide tightest limits. The correlations among the parameters are also studied in this case. In Fig. 6.11, we show the 95 % C.L. contours from simultaneous analysis in $\lambda^\gamma - \lambda^Z$ plane (*left-panel*) and $\Delta\kappa^\gamma - \Delta\kappa^Z$ plane (*right-panel*) for the set of fixed choices of beam polarizations. We see that, $(-0.8, +0.8)$ and $(+0.8, -0.8)$ polarizations give orthogonal contours with maximal correlation and anti-correlation, respectively in both planes much like seen in Fig. 6.9. In the $\Delta\kappa^\gamma - \Delta\kappa^Z$ plane, we see an interesting case: An elliptical contour for beam polarization of $(-0.8, +0.8)$ (*dotted/black*) breaks into two disconnected regions for $(+0.4, -0.4)$ (*solid/green*) and then these disconnected regions grow in size for $(+0.8, -0.8)$ (*dashed/purple*). The contours for beam polarization $(+0.4, -0.4)$ are tighter and less correlated. The results and conclusions differs when two opposite choice of beam polarizations are considered, which are discussed below.

6.2.2.c Case of beam polarization combined with their flipped values

Here, we perform MCMC analysis to estimated simultaneous limits on the couplings of both form factors and effective operators for beam polarizations combined with their opposite values. We perform the analysis for beam polarizations of (η_3, ξ_3) to be $(0, 0)$, $(+0.2, -0.2)$, $(+0.4, -0.4)$, $(+0.6, -0.6)$, $(+0.8, -0.6)$, $(+0.8, -0.8)$ combined with their opposite values using the χ^2 given in Eq. (6.2.3). The 95 % BCI simultaneous limits for the chosen set of beam polarizations combined according to Eq. (6.2.3) are shown in Table 6.4 for effective vertex formalism ($c_i^{\mathcal{L}}$) and in Table 6.5 for effective operator approach ($c_i^{\mathcal{O}}$). The corresponding translated limits to the vertex factor couplings $c_i^{\mathcal{L}^g}$ are also shown in the Table 6.5. While presenting limits, the following notations are used:

$$\begin{matrix} high \\ low \end{matrix} \equiv [low, high]$$

with *low* being lower limit and *high* being upper limit. A pictorial visualization of the limits shown in Table 6.4 & and 6.5 is given in Fig. 6.12 for the easy comparisons. The limits on the couplings get tighter as the amplitude of beam polarizations are increased along $\eta_3 = -\xi_3$ path and become tightest at the extreme beam polarization $(\pm 0.8, \mp 0.8)$. However, the choice $(\pm 0.8, \mp 0.6)$ is best to put constraints on the couplings within the technological reach [241, 242].

To show the effect of beam polarizations, the marginalised 1D projections for the cou-

Table 6.4. List of posterior 95 % BCI of anomalous couplings $c_i^{\mathcal{L}}$ (10^{-2}) of the Lagrangian in Eq. (6.0.2) at $\sqrt{s} = 500$ GeV, $\mathcal{L} = 100$ fb $^{-1}$ for a chosen set of longitudinal beam polarizations η_3 and ξ_3 from MCMC in Binned case. The limits for the best choice of beam polarization within technological reach, i.e., $(\pm 0.8, \mp 0.6)$ are marked in **bold**. The pictorial visualisation for these 95 % BCI of $c_i^{\mathcal{L}}$ is shown in Fig. 6.12 in the *left-panel*. The one parameter (1P) limits (10^{-2}) at 95 % BCI with unpolarized beams are given in the last column for comparison. The notations used here are $_{low}^{high} \equiv [low, high]$ with *low* being lower limit and *high* being upper limit.

param	(0,0)	($\pm 0.2, \mp 0.2$)	($\pm 0.4, \mp 0.4$)	($\pm 0.6, \mp 0.6$)	($\pm 0.8, \mp 0.6$)	($\pm 0.8, \mp 0.8$)	1P(0,0)
Δg_1^γ	+5.5 -8.5	+3.3 -7.4	+2.7 -6.0	+2.1 -2.7	+1.7 -2.3	+1.6 -2.0	+1.3 -1.4
g_4^γ	+5.8 -6.0	+5.3 -5.4	+4.0 -4.0	+3.0 -3.0	+2.5 -2.5	+2.2 -2.2	+1.9 -1.9
g_5^γ	+6.1 -6.1	+5.1 -5.2	+2.6 -3.1	+1.4 -2.0	+1.1 -1.6	+1.0 -1.4	+1.9 -2.0
λ^γ	+1.4 -1.8	+1.2 -1.6	+1.2 -1.2	+1.0 -0.68	+0.89 -0.61	+0.81 -0.57	+0.77 -1.1
$\tilde{\lambda}^\gamma$	+1.6 -1.6	+1.4 -1.4	+1.1 -1.1	+0.88 -0.88	+0.82 -0.82	+0.77 -0.78	+1.0 -1.0
Δk^γ	+0.91 -5.7	+0.32 -4.4	+0.46 -4.3	+0.28 -0.69	+0.27 -0.55	+0.25 -0.48	+0.33 -0.34
\tilde{k}^γ	+6.1 -6.0	+5.2 -5.2	+4.0 -3.9	+2.9 -3.0	+2.6 -2.6	+2.3 -2.3	+2.3 -2.4
Δg_1^Z	+7.2 -3.7	+5.6 -2.8	+4.5 -2.6	+2.1 -2.0	+1.8 -1.7	+1.6 -1.5	+1.3 -1.3
g_4^Z	+4.8 -4.7	+4.3 -4.3	+3.3 -3.3	+2.5 -2.5	+2.2 -2.2	+2.0 -2.0	+1.4 -1.4
g_5^Z	+4.7 -4.8	+4.0 -4.1	+2.1 -2.3	+1.3 -1.5	+1.0 -1.3	+0.86 -1.2	+1.2 -1.3
λ^Z	+1.1 -1.5	+1.0 -1.3	+0.80 -1.1	+0.49 -0.94	+0.47 -0.83	+0.44 -0.76	+0.56 -0.57
$\tilde{\lambda}^Z$	+1.3 -1.3	+1.1 -1.1	+0.90 -0.90	+0.77 -0.77	+0.73 -0.73	+0.68 -0.68	+0.57 -0.56
Δk^Z	+3.6 -1.5	+3.2 -0.49	+3.1 -0.44	+0.56 -0.38	+0.43 -0.35	+0.36 -0.32	+0.43 -0.48
\tilde{k}^Z	+4.7 -5.0	+4.2 -4.2	+3.3 -3.3	+2.5 -2.5	+2.2 -2.2	+2.1 -2.0	+1.5 -1.5

Table 6.5. The list of posterior 95 % BCI of anomalous couplings c_i^ϕ (TeV^{-2}) of effective operators in Eq. (6.0.1) and their translated limits on the couplings $c_i^{\mathcal{L}_{i^s}}$ (10^{-2}) for $\sqrt{s} = 500$ GeV, $\mathcal{L} = 100 \text{ fb}^{-1}$ in Binned case for a chosen set of longitudinal beam polarizations η_3 and ξ_3 from MCMC. The pictorial visualisations for these 95 % BCI of c_i^ϕ and $c_i^{\mathcal{L}_{i^s}}$ are shown in Fig. 6.12 in *right-top* and *right-bottom* panel, respectively. Rest details are same as in Table 6.4.

param	(0,0)	($\pm 0.2, \mp 0.2$)	($\pm 0.4, \mp 0.4$)	($\pm 0.6, \mp 0.6$)	($\pm 0.8, \mp 0.8$)	$1P(0,0)$	
$\frac{c_{WW}}{\Lambda^2}$	+1.3 -1.9	+1.2 -1.4	+1.2 -1.1	+1.1 -0.96	+1.1 -1.0	+1.0 -0.94	+0.84 -0.97
$\frac{c_W}{\Lambda^2}$	+5.0 -1.4	+4.6 -1.1	+0.83 -0.86	+0.58 -0.72	+0.60 -0.73	+0.55 -0.63	+0.55 -0.58
$\frac{c_B}{\Lambda^2}$	+2.7 -23.7	+1.9 -20.2	+0.98 -1.3	+0.62 -0.75	+0.56 -0.64	+0.47 -0.53	+1.2 -1.3
$\frac{c_{WW}}{\Lambda^2}$	+1.4 -1.4	+1.1 -1.1	+0.97 -0.97	+0.94 -0.93	+0.91 -0.90	+0.87 -0.87	+0.97 -0.98
$\frac{c_{\bar{W}}}{\Lambda^2}$	+2.1 -12.0	+9.8 -10.0	+6.6 -6.7	+4.2 -4.1	+3.2 -3.2	+2.6 -2.6	+10.1 -9.9
λ^V	+0.52 -0.79	+0.50 -0.58	+0.49 -0.46	+0.46 -0.40	+0.45 -0.41	+0.42 -0.39	+0.35 -0.40
$\widetilde{\lambda}^V$	+0.60 -0.60	+0.44 -0.45	+0.40 -0.40	+0.39 -0.38	+0.37 -0.37	+0.36 -0.36	+0.40 -0.41
Δk^γ	+0.52 -6.4	+0.44 -5.1	+0.28 -0.38	+0.24 -0.32	+0.25 -0.32	+0.23 -0.28	+0.56 -0.61
\widetilde{k}^γ	+3.9 -3.9	+3.2 -3.2	+2.1 -2.1	+1.3 -1.3	+1.0 -1.0	+0.84 -0.84	+3.2 -3.2
Δg_1^Z	+2.1 -0.59	+1.9 -0.45	+0.34 -0.36	+0.24 -0.30	+0.25 -0.30	+0.23 -0.26	+0.23 -0.24
Δk^Z	+3.6 -0.73	+3.2 -0.45	+0.34 -0.33	+0.21 -0.24	+0.21 -0.24	+0.19 -0.20	+0.30 -0.30
\widetilde{k}^Z	+1.1 -1.1	+0.92 -0.91	+0.62 -0.61	+0.38 -0.38	+0.29 -0.30	+0.24 -0.24	+0.92 -0.93

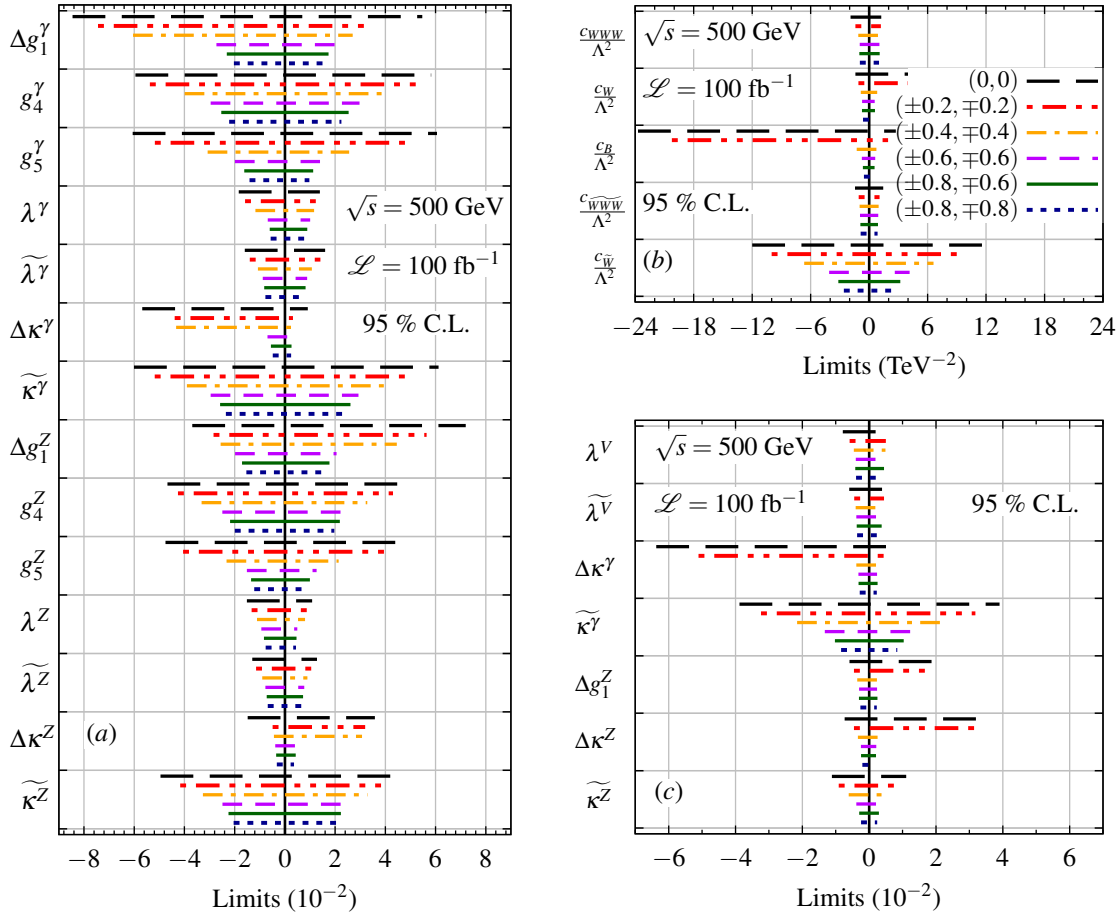


Figure 6.12. The pictorial visualisation of 95 % BCI limits (a) : on the anomalous couplings $c_i^{\mathcal{L}}$ in the left-panel, (b) : on $c_i^{\mathcal{O}}$ in the right-top-panel and (c) : on $c_i^{\mathcal{L}g}$ in the right-bottom-panel for $\sqrt{s} = 500$ GeV, $\mathcal{L} = 100 \text{ fb}^{-1}$ using the binned observables. The numerical values of the limits can be read of in Tables 6.4 & 6.5.

plings λ^γ , Δg_1^Z and $\Delta \kappa^Z$ as well as 2D projections at 95 % C.L. on $\lambda^\gamma - \lambda^Z$, $\Delta g_1^Z - \widetilde{\kappa}^Z$ and $\Delta \kappa^\gamma - \Delta \kappa^Z$ planes are shown in Fig. 6.13 for form factors ($c_i^{\mathcal{L}}$) as representative. We observe that as the amplitude of beam polarizations are increased from (0, 0) to $(\pm 0.8, \mp 0.8)$, the contours get smaller centred around the SM values in the 2D projections which are reflected in the 1D projections as well. In the $\Delta \kappa^\gamma - \Delta \kappa^Z$ plane, the contour gets divided into two parts at $(\pm 0.4, \mp 0.4)$ and then become one single contour later centred around the SM values. In the case of effective operators ($c_i^{\mathcal{O}}$), all the 1D and 2D (95 % C.L.) projections after marginalization are shown in Fig. 6.14. In this case the couplings c_W and c_B has two patches up-to beam polarization $(\pm 0.2, \mp 0.2)$ and become one single patch starting at beam polarization $(\pm 0.3, \mp 0.3)$ centred around the SM values. As the amplitude of beam polarizations are increased along the $\eta_3 = -\xi_3$ line, the measurement of the anomalous couplings gets improved. The set of beam polarizations chosen here are mostly along the $\eta_3 = -\xi_3$ line, but some choices off to the line might provide the same results. A discussion on the choice of beam polarization is

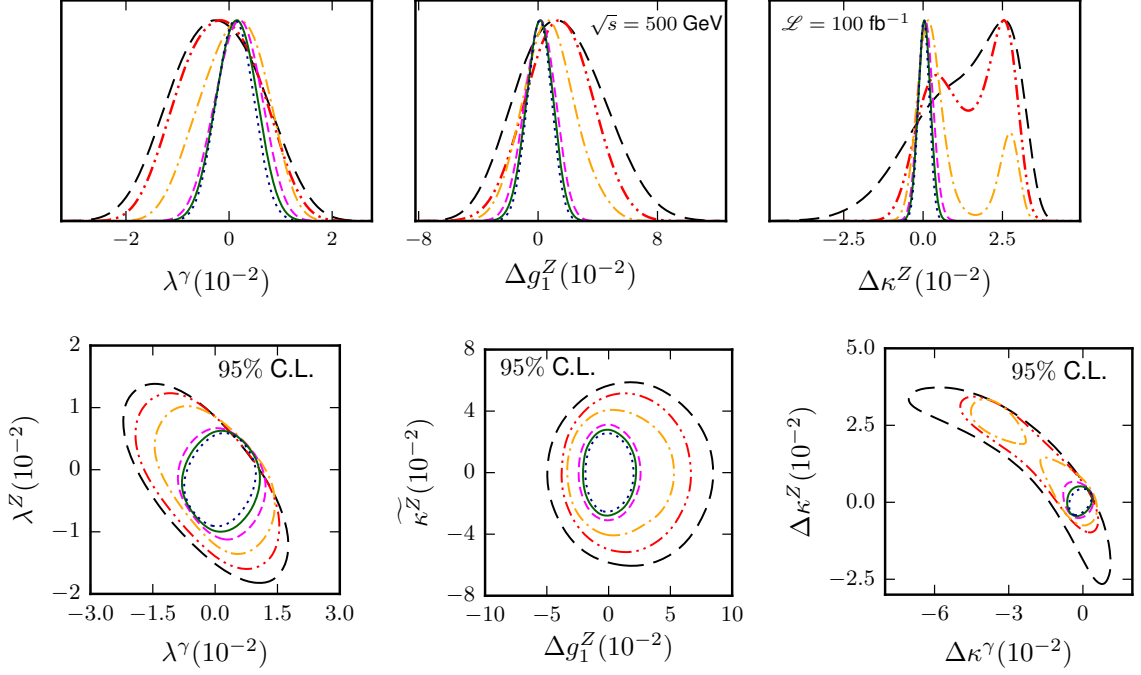


Figure 6.13. The marginalised 1D projections for the couplings λ^γ , Δg_1^Z and $\Delta \kappa^Z$ in the *top-panel* and 2D projection at 95 % C.L. on λ^γ - λ^Z , Δg_1^Z - $\tilde{\kappa}^Z$ and $\Delta \kappa^\gamma$ - $\Delta \kappa^Z$ planes in *bottom-panel* from MCMC for a set of choice of beam polarizations are shown for $\sqrt{s} = 500$ GeV, $\mathcal{L} = 100$ fb $^{-1}$ using the binned observables in the effective vertex formalism. The legend labels are same as in Figs. 6.12 & 6.14.

given in the next subsection.

6.2.3 On the choice of beam polarizations

In the previous subsection, we found that the beam polarization choice $(\pm\eta_3, \pm\xi_3) = (\pm 0.8, \pm 0.6)$ is the best choice of beam polarizations to provide simultaneous limits on the anomalous couplings obtained by MCMC analysis. Here, we discuss the average likelihood or the weighted volume of the parameter space defined as [99],

$$L(V_{\vec{f}}; \eta_3, \xi_3) = \int_{V_{\vec{f}}} \exp\left[-\frac{1}{2}\chi_{tot}^2(\vec{f}, \eta_3, \xi_3)\right] d\vec{f} \quad (6.2.5)$$

to cross-examine the beam polarization choices made in the previous section, as we did in section 4.3 for ZV production. Here \vec{f} is the couplings vector and $V_{\vec{f}}$ is the volume of parameter space over which the average is done; $L(V_{\vec{f}}; \eta_3, \xi_3)$ corresponds to the volume of the parameter space that is statistically consistent with the SM. One naively expects the limits to be tightest when $L(V_{\vec{f}}; \eta_3, \xi_3)$ is minimum. We calculate the above quantity as a function of $(\pm\eta_3, \pm\xi_3)$ for Binned case in the effective vertex formalism given in Lagrangian in Eq. (6.0.2) and present it in Fig. 6.15. As the opposite beam polarizations are combined,

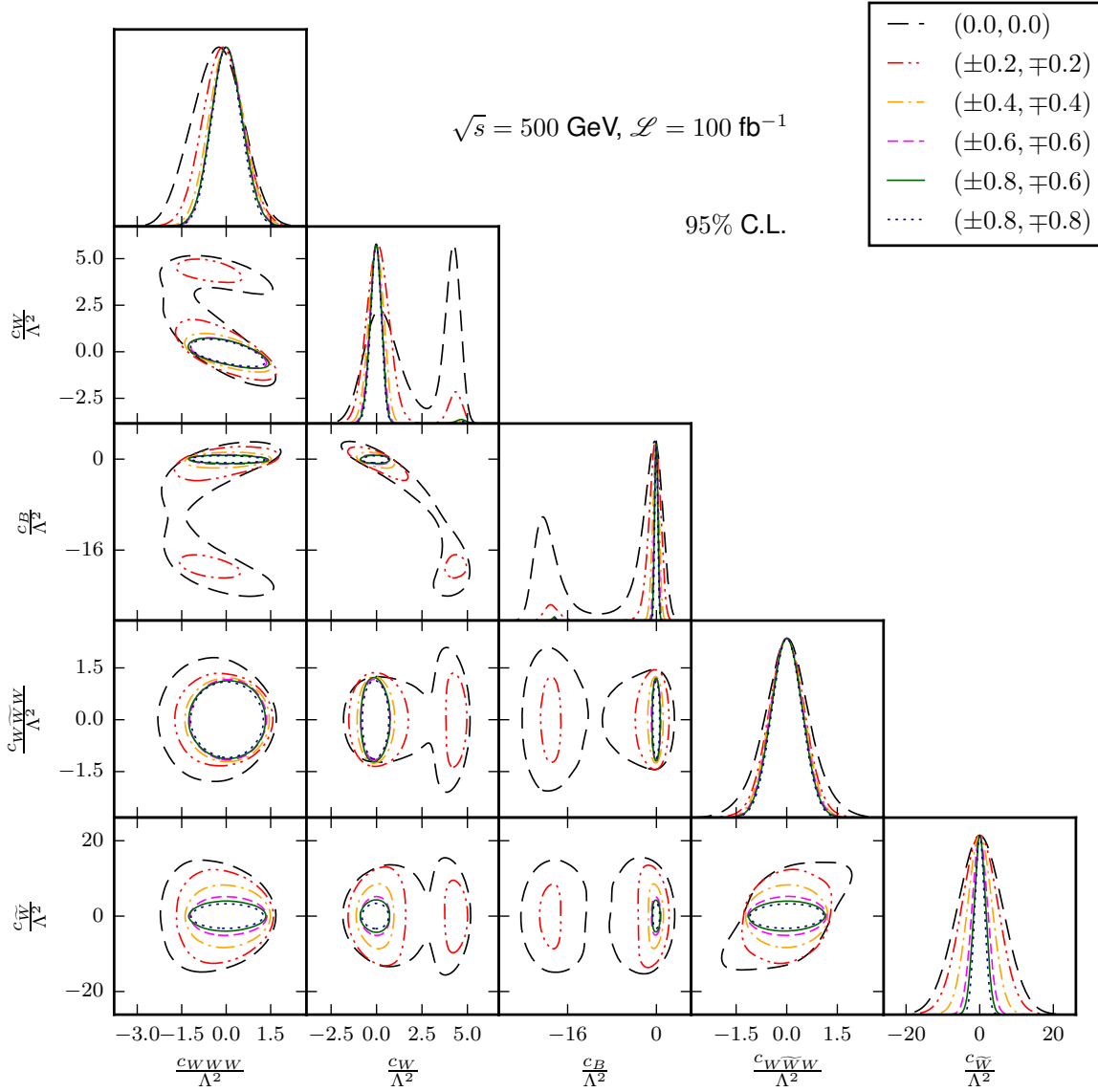


Figure 6.14. All the marginalised 1D projections and 2D projections at 95 % C.L. from MCMC in triangular array for the effective operators (TeV^{-2}) for a set of choice of beam polarizations for $\sqrt{s} = 500 \text{ GeV}, \mathcal{L} = 100 \text{ fb}^{-1}$ using the binned observables.

only the half-portion are shown in the η_3 - ξ_3 plane. The dot (\bullet) points along the $\eta_3 = -\xi_3$ are the chosen choices of beam polarizations for the MCMC analysis. We see that the average likelihood decreases along $\eta_3 = -\xi_3$ line while it increases along $\eta_3 = \xi_3$ line. The constant lines or contours of average likelihood in the figure imply that any beam polarizations along the lines/contours will provide the similar shape of 1D and 2D projections of couplings and their limits. For example, the point $(\pm 0.8, \mp 0.6)$ is equivalent to the point $(\pm 0.7, \mp 0.7)$ as well as $(\pm 0.6, \pm 0.8)$ roughly in providing simultaneous limits which are verified from the limits obtained by MCMC analysis. It is clear that the polarization $(\pm 0.8, \mp 0.6)$ is indeed the best choice to provide simultaneous limits on the anomalous couplings within the achievable range.

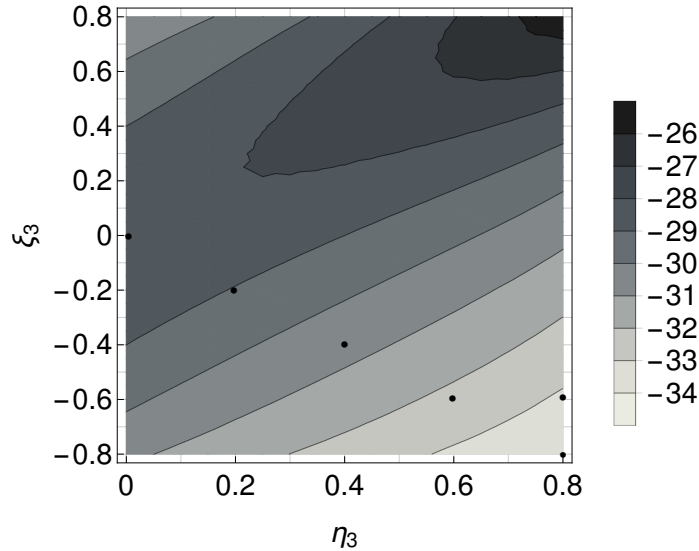


Figure 6.15. The averaged likelihood $L_{Av} = L(V_f; \eta_3, \xi_3)$ in log scale as a function of $(\pm\eta_3, \pm\xi_3)$ in the effective vertex formalism for $\sqrt{s} = 500$ GeV, $\mathcal{L} = 100$ fb $^{-1}$.

6.3 Summary

In summary, here, we studied the anomalous triple gauge boson couplings in $e^+e^- \rightarrow W^+W^-$ with longitudinally polarized beams using W boson polarization observables together with the total cross section and the forward-backward asymmetry for $\sqrt{s} = 500$ GeV and luminosity of $\mathcal{L} = 100$ fb $^{-1}$. We estimated simultaneous limits on all the couplings for several chosen set of beam polarizations in both effective vertex formalism and effective operator approach. The limits on the couplings are tighter when $SU(2) \times U(1)$ symmetry is assumed. We showed the consistency between the best choice of beam polarizations and minimum likelihood averaged over the anomalous couplings. The extreme beam polarization $(\pm 0.8, \mp 0.8)$ appears to be the best to provide the tightest constraint on the anomalous couplings in both approaches at the ILC (same as obtained for $e^+e^- \rightarrow ZV$ in Chapter 4). Our one parameter limits with unpolarized beams and simultaneous limits for best polarization choice are much better than the one parameter limits available from experiment, see Table 6.5.

7 The probe of aTGC in $W^\pm Z$

productions at the LHC and the role of Z/W boson polarizations

Contents

7.1	Signal cross sections and their sensitivity to anomalous couplings	124
7.2	The asymmetries	130
7.3	Probe of the anomalous couplings	134
7.3.1	Limits on the couplings	136
7.3.2	The role of asymmetries in parameter extraction	139
7.4	Summary	141

The contents in this chapter are based on the published article in Ref. [178].

In the previous chapter, the polarization asymmetries are shown to give promising results in probing the aTGC in the charge sector in a future e^+e^- collider. In this chapter, we want to probe the aTGC in the charge sector at the current hadron collider LHC in the $W^\pm Z$ production processes in $3l + \cancel{E}_T$ channel. The anomalous couplings appearing in the $W^\pm Z$ production at the LHC are

$$\begin{aligned}
 \mathcal{L}_{WWZ} = & ig_{WWZ} \left[(1 + \Delta g_1^Z) (W_{\mu\nu}^+ W^{-\mu} - W^{+\mu} W_{\mu\nu}^-) Z^\nu + \frac{\lambda^Z}{m_W^2} W_\mu^{+\nu} W_\nu^{-\rho} Z_\rho^\mu \right. \\
 & \left. + \frac{\tilde{\lambda}^Z}{m_W^2} W_\mu^{+\nu} W_\nu^{-\rho} \tilde{Z}_\rho^\mu + (1 + \Delta k^Z) W_\mu^+ W_\nu^- Z^{\mu\nu} + \tilde{\kappa}^Z W_\mu^+ W_\nu^- \tilde{Z}^{\mu\nu} \right] \quad (7.0.1)
 \end{aligned}$$

containing half (7) the couplings of the full WWV Lagrangian in Eq. (6.0.2). There has been

a lot of studies of these aTGC at the LHC [102, 114, 115, 123–132] in different perspective. Direct measurement of these aTGC at the LHC [143, 155–169] are also available in different processes using the cross sections with various kinematical cuts. Our aim, here, is to study these WWZ anomalous couplings in ZW^\pm production at the LHC at $\sqrt{s} = 13$ TeV using the cross section, forward backward asymmetry and polarizations asymmetries of Z and W^\pm in the $3l + \cancel{E}_T$ channel. In addition to the vertex form factor in Eq. (7.0.1), we will also probe the effective dimension-6 operators given in Eq. (6.0.2) independently. Similar to the study in the previous chapter, we see the modification of the form factors in Eq. (7.0.1) subjected to $SU(2) \times U(1)$ gauge invariance through relations given in Eq. (1.3.13). The polarizations of W^\pm/Z has been estimated earlier in the same process ZW^\pm production that we are looking at [243–245] and also has been measured recently at the LHC [240] in the SM.

The $W^\pm Z$ process in $3l + \cancel{E}_T$ channel has got quite a bit of attention recently for having excess at the LHC [169]. This has been looked as an anomaly and has been addressed in terms of two BSM scalar [246]. This final state is also important for various BSM searches, including supersymmetry and dark matter.

7.1 Signal cross sections and their sensitivity to anomalous couplings

The process of interest is the ZW^\pm production in the $3l + \cancel{E}_T$ channel at the LHC. The representative Feynman diagrams at Born level are displayed in Fig. 7.1 containing doubly-resonant processes (*upper-row*) as well as singly-resonant processes (*lower-row*). The presence of anomalous WWZ couplings is shown by the shaded blob. While this may contain the $WW\gamma$ couplings due to the off-shell γ , this has been cut out by Z selection cuts, described later. The leading order result (148.4 fb estimated by MATRIX in Ref. [247]) for the $3l + \cancel{E}_T$ cross section at the LHC is way below the measured cross section at the LHC (258 fb measured by CMS [248]). Higher-order corrections are thus necessary to add to the tree level result. The NLO corrections in QCD appear in the vertices connected to the quarks (see, Fig. 7.1) with either QCD loops or QCD radiations from the quarks. The SM cross sections of ZW^\pm production in the $e^+e^-\mu^\pm$ channel obtained by MATRIX and MADGRAPH5_aMC@NLO v2.6.4 (mg5_aMC) for $\sqrt{s} = 13$ TeV for the CMS fiducial phase-phase region are presented in the Table 7.1. The CMS fiducial phase-phase region [248] is given

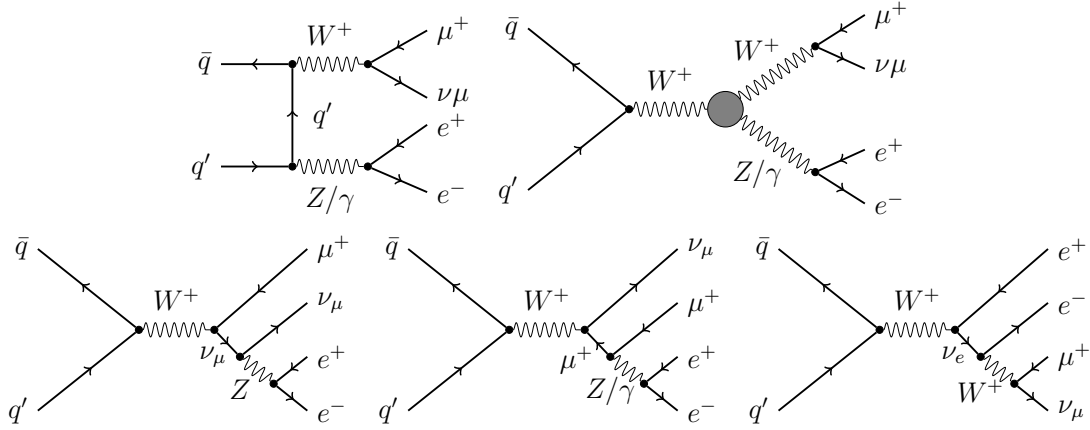


Figure 7.1. Sample of Born level Feynman diagrams for ZW^+ production in the $e^+e^-\mu^+\nu_\mu$ channel at the LHC. The diagrams for ZW^- can be obtained by charge conjugation. The shaded blob represents the presence of anomalous WWV couplings on top of SM.

by,

$$p_T(l_{Z,1}) > 20 \text{ GeV}, \quad p_T(l_{Z,2}) > 10 \text{ GeV}, \quad p_T(l_W) > 20 \text{ GeV},$$

$$|\eta_l| < 2.5, \quad 60 \text{ GeV} < m_{l^+l^-} < 120 \text{ GeV}, \quad m_{l^+l^-} > 4 \text{ GeV}. \quad (7.1.1)$$

We use the values of the SM input parameters same as used in Ref. [247] (default in MATRIX). A fixed renormalization (μ_R) and factorization (μ_F) scale of $\mu_R = \mu_F = \mu_0 = \frac{1}{2}(m_Z + m_W)$ is used and the uncertainties are estimated by varying the μ_R and μ_F in the range of $0.5\mu_0 \leq \mu_R, \mu_F \leq 2\mu_0$ and shown in Table 7.1. We use the NNPDF3.0 sets of parton distribution functions (PDFs) with $\alpha_s(m_Z)$ for our calculations. The combined result for all leptonic

Table 7.1. The theoretical estimates and experimental measurements of the cross sections of ZW^\pm productions in the $e^+e^-\mu^\pm\nu_\mu/\bar{\nu}_\mu$ channel at $\sqrt{s} = 13 \text{ TeV}$ at the LHC for CMS fiducial phase-space. The uncertainties in the theoretical estimates are due to scale variation.

Process	Obtained at	σ_{LO} (fb)	σ_{NLO} (fb)	σ_{NNLO} (fb)
$pp \rightarrow e^+e^-\mu^+\nu_\mu$	MATRIX	$22.08^{+5.2\%}_{-6.2\%}$	$43.95^{+5.4\%}_{-4.3\%}$	$48.55^{+2.2\%}_{-2.0\%}$
	mg5_aMC	$22.02^{+6.1\%}_{-7.2\%}$	$43.63^{+6.6\%}_{-6.6\%}$	—
$pp \rightarrow e^+e^-\mu^-\bar{\nu}_\mu$	MATRIX	$14.45^{+5.6\%}_{-6.7\%}$	$30.04^{+5.6\%}_{-4.5\%}$	$33.39^{+2.3\%}_{-2.1\%}$
	mg5_aMC	$14.38^{+6.4\%}_{-7.6\%}$	$29.85^{+6.8\%}_{-6.8\%}$	—
$pp \rightarrow 3l + \cancel{E}_T$	MATRIX [247]	$148.4^{+5.4\%}_{-6.4\%}$	$301.4^{+5.1\%}_{-4.4\%}$	$334.3^{+2.3\%}_{-2.1\%}$
$pp \rightarrow 3l + \cancel{E}_T$	CMS [248]	$258.0 \pm 8.1\% \text{ (stat)}^{+7.4\%}_{-7.7\%} \text{ (syst)} \pm 3.1 \text{ (lumi)}$		

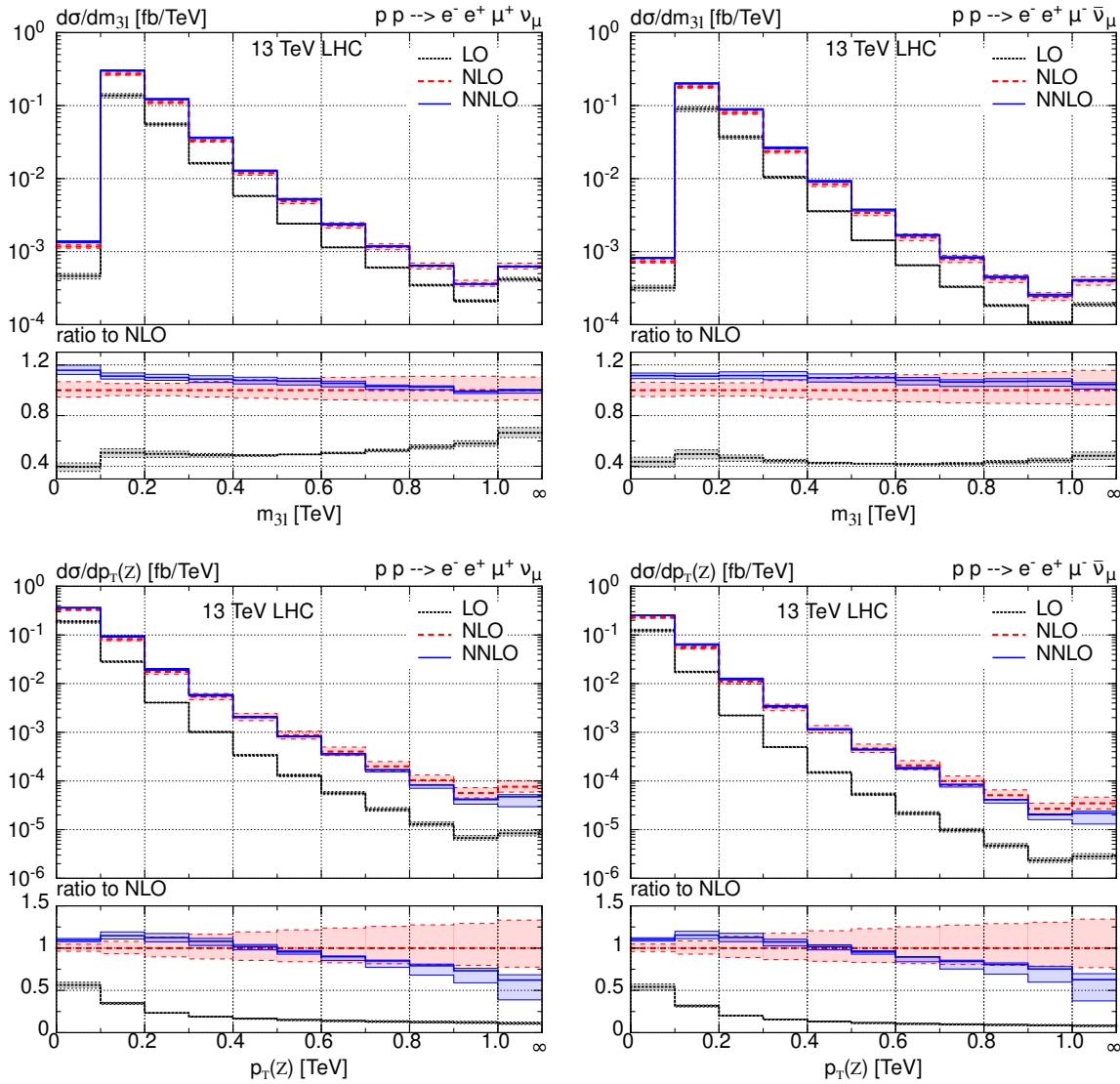


Figure 7.2. The differential distributions of m_{3l} (top-row) and $p_T(Z)$ (bottom-row) in the ZW^+ (left-column) and ZW^- (right-column) production in the $e^+e^-\mu^\pm + \cancel{E}_T$ channel at the LHC for $\sqrt{s} = 13$ TeV at LO, NLO and NNLO obtained using MATRIX [229–234, 247, 249] for CMS fiducial phase-space.

channel given in Ref. [247] and the measured cross section by CMS [248] are also presented in the same table. The uncertainties in the theoretical estimates are due to scale variation. The result obtained by MATRIX and mg5_aMC matches quite well at both LO and NLO level. The NLO corrections have increased the LO cross section by up to 100 %, and the NNLO cross section is further increased by 10 % from the NLO value. It is thus necessary to include QCD corrections to leading order result. The higher order corrections to the cross section vary with kinematical variable like m_{3l} and $p_T(Z)$, as shown in Fig. 7.2 obtained by MATRIX [229–234, 247, 249]. The lower panels display the respective bin-by-bin ratios to the NLO central predictions. The NLO to LO ratio does not appear to be constant over the range of m_{3l} and $p_T(Z)$. Thus a simple k -factor with LO events can not be used as a proxy for NLO

events. We use results from mg5_aMC with NLO QCD corrections for our analysis in the rest of the paper. However, the SM values (Table 7.1) and distributions (Fig. 7.2) at LO and NLO in QCD are kept for completeness.

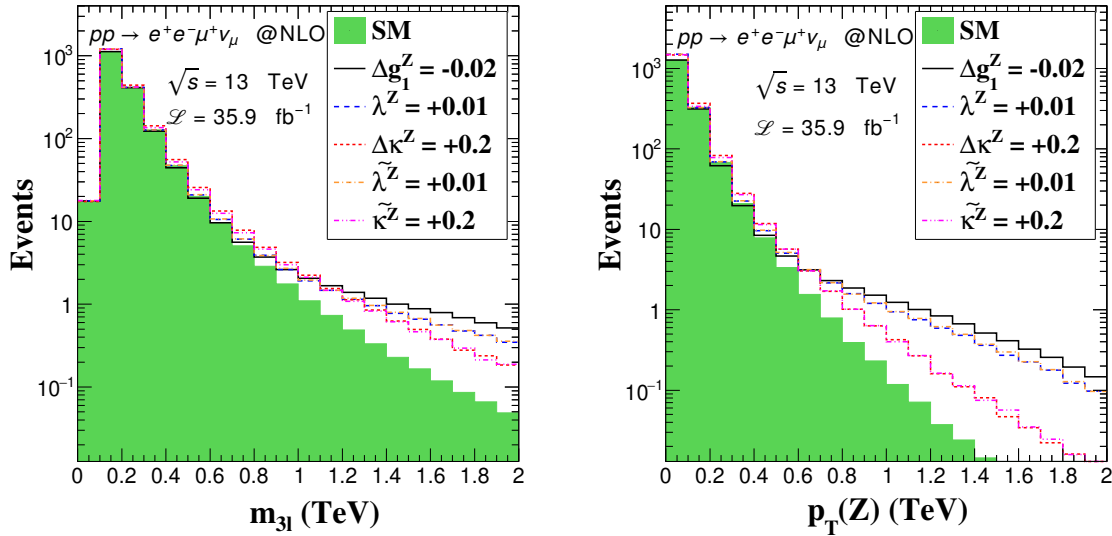


Figure 7.3. The differential distributions of m_{3l} and $p_T(Z)$ in the W^+Z production in the $e^+e^-\mu^+\nu_\mu$ channel at the LHC at $\sqrt{s} = 13$ TeV and $\mathcal{L} = 35.9$ fb $^{-1}$ at NLO in the SM and five benchmark anomalous couplings.

The signal for the $e^+e^-\mu^+$ and $e^+e^-\mu^-$ are generated separately using mg5_aMC at NLO in QCD for SM as well as SM including aTGC. We use the FeynRules [204] to generate QCD NLO UFO model of the Lagrangian in Eq. (7.0.1) for mg5_aMC. These signal are then used as a proxy for the $3l+\cancel{E}_T$ final state upto a factor of four for the four channels. For these, the p_T cut for e^\pm and μ^\pm are kept at the same value, i.e., $p_T(l) > 10$ GeV. We use a threshold for the tripleton invariant mass (m_{3l}) of 100 GeV to select the doubly resonant contribution of tripleton final state. We will see later that lower cuts of m_{3l} higher than 100 GeV are required for best sensitivity to the anomalous couplings. The event selection cuts for this analysis are thus,

$$p_T(l) > 10 \text{ GeV}, \quad |\eta_l| < 2.5, \quad 60 \text{ GeV} < m_{l^+l^-} < 120 \text{ GeV}, \quad m_{l^+l^-} > 4 \text{ GeV}, \quad m_{3l} > 100 \text{ GeV}. \quad (7.1.2)$$

We explore the effect of aTGC in the distributions of m_{3l} and $p_T(Z)$ in both ZW^+ and ZW^- production and show them in Fig. 7.3. The distribution of m_{3l} in the *left-panel* and $p_T(Z)$ in the *right-panel* in the $e^+e^-\mu^+\nu_\mu$ channel are shown for SM (filled/green) and five anomalous benchmark couplings of $\Delta g_1^Z = -0.02$ (solid/black), $\lambda^Z = +0.01$ (dashed/blue), $\Delta \kappa^Z = +0.2$ (dotted/red), $\tilde{\lambda}^Z = +0.01$ (dash-dotted/orange) and $\tilde{\kappa}^Z = +0.2$ (dashed-dotted/magenta) with events normalised to an integrated luminosity of $\mathcal{L} = 35.9$ fb $^{-1}$. For each

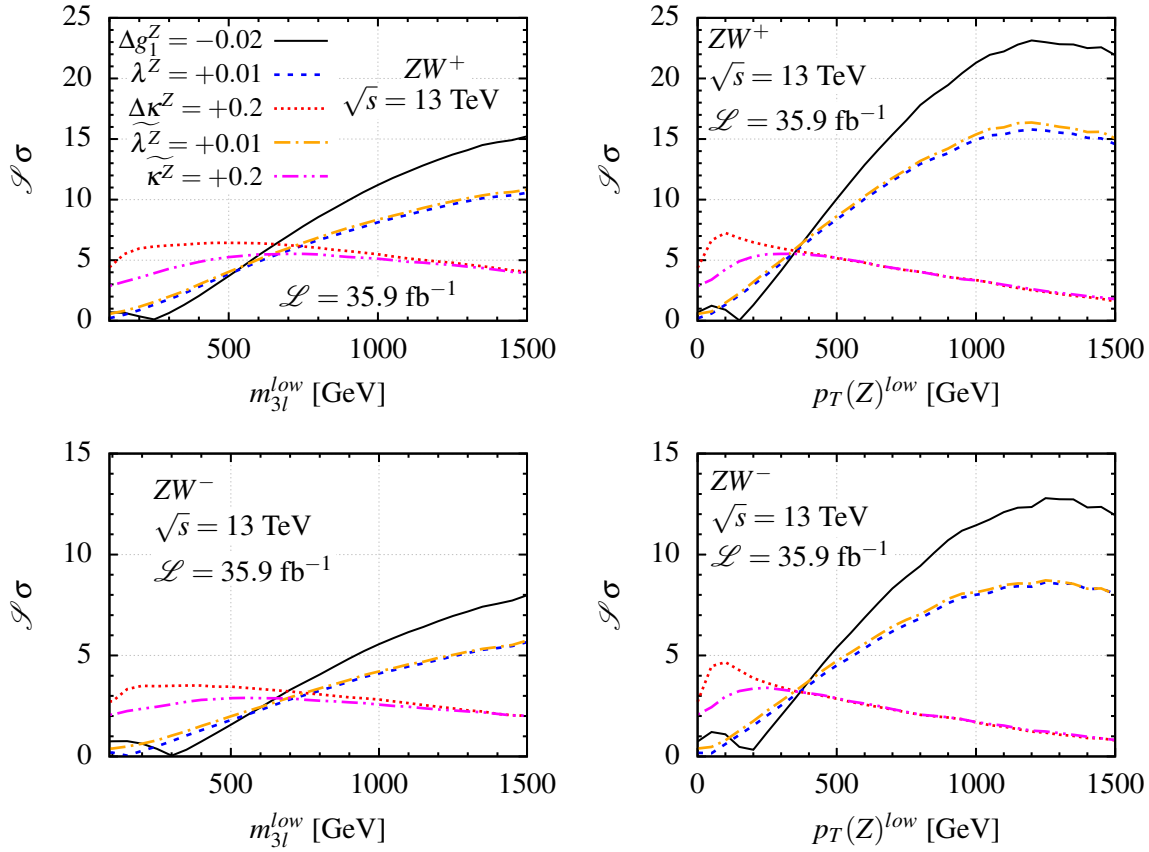


Figure 7.4. The sensitivity of cross sections to the five benchmark aTGC as a function of the lower cut on m_{3l} and $p_T(Z)$ in the ZW^\pm production at the LHC at $\sqrt{s} = 13$ TeV and $\mathcal{L} = 35.9$ fb $^{-1}$.

of the benchmark couplings, only one of the couplings get non-zero value at a time while others remain zero. More benchmark scenarios with more than one parameters getting non-zero values at a time are considered for the comparison of reconstructed neutrino solutions in section 7.2. The higher m_{3l} and higher $p_T(Z)$ seems to have higher sensitivity to the anomalous couplings which is due to higher momentum transfer at higher energies, for example see Ref. [118]. We studied the sensitivities (see Eq. (3.1.16)) of the cross sections to the anomalous couplings by varying lower cuts on m_{3l} and $p_T(Z)$ for the above mentioned five benchmark scenarios. The sensitivity of the cross sections, ignoring the systematic uncertainty, for the five benchmark cases (as used in Fig. 7.3) are shown in Fig. 7.4 for ZW^+ in the upper-row and for ZW^- in the lower-row as a function of lower cut of m_{3l} (left-column) and $p_T(Z)$ (right-column) for luminosity of $\mathcal{L} = 35.9$ fb $^{-1}$. It is clear that the sensitivities increase as the cut increases for both m_{3l} and $p_T(Z)$ for couplings Δg_1^Z , λ^Z and $\widetilde{\lambda}^Z$, while they decrease just after ~ 150 GeV of cuts for the couplings $\Delta \kappa^Z$ and $\widetilde{\kappa}^Z$. This can also be seen in Fig. 7.3 where $\Delta \kappa^Z$ and $\widetilde{\kappa}^Z$ contribute more than other three couplings for $m_{3l} < 0.8$ TeV and $p_T(Z) < 0.6$ TeV. Taking hints from Fig. 7.4, we identify four bins in m_{3l} - $p_T(Z)$ plane to

Table 7.2. The sensitivity of the cross sections on the five benchmark aTGC in the four bins (see Eq. (7.1.3)) of m_{3l} and $p_T(Z)$ in the ZW^\pm productions at the LHC at $\sqrt{s} = 13$ TeV and $\mathcal{L} = 35.9$ fb $^{-1}$.

aTGC	ZW^+				ZW^-			
	Bin_{11}	Bin_{12}	Bin_{21}	Bin_{22}	Bin_{11}	Bin_{12}	Bin_{21}	Bin_{22}
$\Delta g_1^Z = -0.02$	1.17	1.14	7.52	44.5	0.32	2.10	3.95	23.19
$\lambda^Z = 0.01$	3.08	5.37	6.08	26.2	1.58	2.63	3.32	13.68
$\Delta \kappa^Z = 0.2$	8.52	0.50	3.28	4.87	5.01	0.15	1.64	2.40
$\widetilde{\lambda}^Z = 0.01$	3.20	5.56	6.18	27.2	1.70	2.69	3.37	13.83
$\widetilde{\kappa}^Z = 0.2$	6.50	0.60	3.15	4.89	3.86	0.22	1.65	2.36

maximize the sensitivity of all the couplings. These four bins are given by,

$$\begin{aligned}
 Bin_{11} & : 400 \text{ GeV} < m_{3l} < 1500 \text{ GeV}, 200 \text{ GeV} < p_T(Z) < 1200 \text{ GeV}, \\
 Bin_{12} & : 400 \text{ GeV} < m_{3l} < 1500 \text{ GeV}, p_T(Z) > 1200 \text{ GeV}, \\
 Bin_{21} & : m_{3l} > 1500 \text{ GeV}, 200 \text{ GeV} < p_T(Z) < 1200 \text{ GeV}, \\
 Bin_{22} & : m_{3l} > 1500 \text{ GeV}, p_T(Z) > 1200 \text{ GeV}.
 \end{aligned} \tag{7.1.3}$$

The sensitivities of the cross sections to the benchmark anomalous couplings are calculated in the said four bins for luminosity of $\mathcal{L} = 35.9$ fb $^{-1}$ and they are shown in Table 7.2 in both ZW^+ and ZW^- productions. As expected, we see that Bin_{22} has the higher sensitivity to couplings Δg_1^Z , λ^Z and $\widetilde{\lambda}^Z$, while Bin_{11} has higher, but comparable sensitivity to couplings $\Delta \kappa^Z$ and $\widetilde{\kappa}^Z$. The simultaneous cuts on both the variable have increased the sensitivity by a significant amount as compared to the individual cuts. For example, the Fig. 7.4 shows that cross section in ZW^+ has a maximum sensitivity of 15 and 22 on $\Delta g_1^Z = -0.02$ for individual m_{3l} and $p_T(Z)$ lower cuts, respectively. While imposing a simultaneous lower cuts on both the variable, the same sensitivity increases to 44.5 (in Bin_{22}).

At the LHC, the other contributions to the $3l + \cancel{E}_T$ channel come from the production of ZZ , $Z\gamma$, $Z + j$, $t\bar{t}$, Wt , $WW + j$, $t\bar{t} + V$, tZ , VVV as has been studied by CMS [169, 248] and ATLAS [240, 250]. The total non- WZ contributions listed above is about 40 % of the WZ contributions [248]. We include these extra contributions to the cross sections while estimating limits on the anomalous couplings in Sect. 7.3.

7.2 The asymmetries

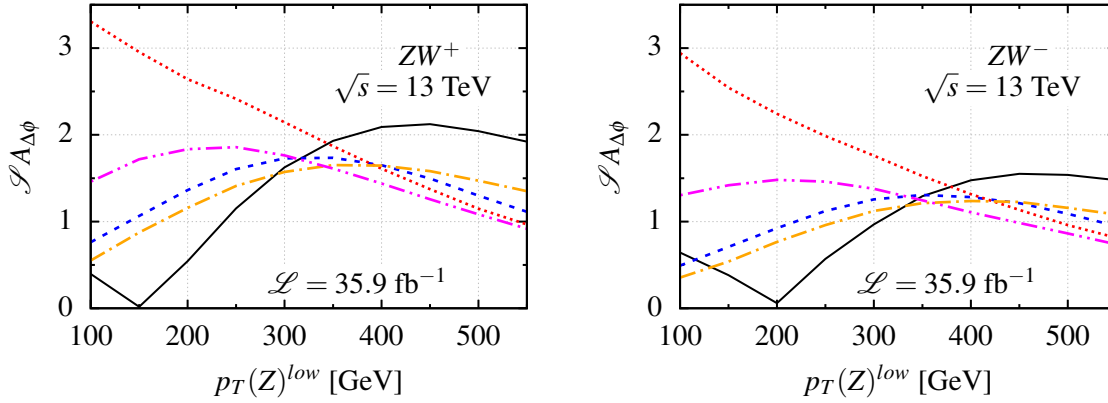


Figure 7.5. The sensitivity of the asymmetry $A_{\Delta\phi}$ on the five benchmark aTGC as a function of the lower cut on $p_T(Z)$ in the ZW^\pm productions at the LHC at $\sqrt{s} = 13$ TeV and $\mathcal{L} = 35.9$ fb $^{-1}$. The legend labels are same as in Fig. 7.4.

We use the polarization asymmetries of Z and W in each W^+Z and W^-Z processes, i.e., $4 \times 8 = 32$ polarization asymmetries along with the cross sections in four bins. Beside these, the Z and the W^\pm boson produced in the ZW^\pm production are not forward backward symmetric owing to only a t -channel diagram and not having an u -channel diagram (see Fig. 7.1). These provide an extra observable, the forward-backward asymmetry defined as,

$$A_{fb}^V = \frac{\sigma(\cos\theta_V > 0) - \sigma(\cos\theta_V < 0)}{\sigma(\cos\theta_V > 0) + \sigma(\cos\theta_V < 0)}, \quad (7.2.1)$$

θ_V is the production angle of the V w.r.t. the colliding quark-direction. One more angular variable sensitive to aTGC is the angular separation of the lepton l_W from W^\pm and the Z in the transverse plane, i.e.,

$$\Delta\phi(l_W, Z) = \cos^{-1} \left(\frac{\vec{p}_T(l_W) \cdot \vec{p}_T(Z)}{p_T(l_W) p_T(Z)} \right). \quad (7.2.2)$$

One can construct an asymmetry based on the $\Delta\phi$ as,

$$A_{\Delta\phi} = \frac{\sigma(\cos(\Delta\phi(l_W, Z)) > 0) - \sigma(\cos(\Delta\phi(l_W, Z)) < 0)}{\sigma(\cos(\Delta\phi(l_W, Z)) > 0) + \sigma(\cos(\Delta\phi(l_W, Z)) < 0)}. \quad (7.2.3)$$

The sensitivities of $A_{\Delta\phi}$ to the five benchmark aTGC are shown in Fig. 7.5 as a function of lower cuts on $p_T(Z)$ in both ZW^\pm for luminosity of $\mathcal{L} = 35.9$ fb $^{-1}$. A choice of $p_T(Z)^{low} = 300$ GeV appears to be an optimal choice for sensitivity for all the couplings. The m_{3l} cut, however, reduces the sensitivities to all the aTGC.

To construct the asymmetries, we need to set a reference frame and assign the leptons to the correct mother spin-1 particle. For the present process with missing neutrino, we face a set of challenges in constructing the asymmetries. These are discussed below.

Selecting Z candidate leptons The Z boson momentum is required to be reconstructed to obtain all the asymmetries which require the right pairing of the Z boson leptons l_Z^+ and l_Z^- . Although the opposite flavour channels $e^+e^-\mu^\pm/\mu^+\mu^-e^\pm$ are safe, the same flavour channels $e^+e^-e^\pm/\mu^+\mu^-\mu^\pm$ suffer ambiguity to select the right Z boson candidate leptons. The right pairing of leptons for the Z boson in the same flavoured channel is possible with $\geq 96.5\%$ accuracy for $m_{3l} > 100$ GeV and $\geq 99.8\%$ accuracy for $m_{3l} > 550$ GeV in both SM and benchmark aTGC by requiring a smaller value of $|m_Z - m_{l+l^-}|$. This small miss pairing is neglected to use the $2e\mu\nu_\mu$ channel as a proxy for a $3l + \cancel{E}_T$ final state with good enough accuracy.

The reconstruction of neutrino momentum The other major issue is to obtain the asymmetries related to W^\pm bosons, which require to reconstruct their momenta. As the neutrino from W^\pm goes missing, reconstruction of W^\pm boson momenta is possible with a two-fold ambiguity using the transverse missing energy p_T/\cancel{E}_T and the on-shell W mass (m_W) constrain. The two solutions for the longitudinal momentum of the missing neutrino are given by,

$$p_z(\nu)_\pm = \frac{-\beta p_z(l_W) \pm E(l_W)\sqrt{D}}{p_T^2(l_W)} \quad (7.2.4)$$

with

$$D = \beta^2 - p_T^2(\nu)p_T^2(l_W), \quad \beta = m_W^2 + p_x(l_W)p_x(\nu) + p_y(l_W)p_y(\nu). \quad (7.2.5)$$

Because the W is not produced on-shell all the time, among the two solutions of neutrino's longitudinal momenta, one of them will be closer to the true value, and another will be far from the true value. There are no suitable selector or discriminator to select the correct solution from the two solutions. Even if we substitute the Monte-Carlo truth m_W to solve for $p_z(\nu)$ we don't have any discriminator to distinguish between the two solutions $p_z(\nu)_\pm$. The smaller value of $|p_z(\nu)|$ corresponds to the correct solution only for $\approx 65\%$ times on average in ZW^+ and little lower in ZW^- production. One more discriminator which is $||\beta_Z| - |\beta_W||$, the smaller value of this can choose the correct solution a little over the boundary, i.e., $\approx 55\%$. We have tried machine-learning approaches (artificial neural network) to select the correct solutions, but the accuracy was not better than 65%. In some cases, we have $D < 0$ with the

on-shell W , for these cases either one can throw those events (which affects the distribution and statistics) or one can vary the m_W from its central value to have $D > 0$. Here, we follow the later. So, as the best available option, we choose the smaller value of $|p_z(\nu)|$ to be the correct solution to reconstruct the W boson momenta. At this point, it becomes important to explore the effect of reconstruction on asymmetries and their sensitivities to aTGC. To this end, we consider three scenarios:

Abs. True The first thing is to use the Monte-Carlo truth events and estimate the asymmetries in the lab frame. The observables in this scenario are directly related to the dynamics up to a rotation of frame [173, 188, 189].

Reco. True Using the pole mass of W in Eq. (7.2.5) and choosing the solution closer to the Monte-Carlo true value is the best that one can do in reconstruction. The goal of any reconstruction algorithm would be to become as close to this scenario as possible.

Small $|p_z(\nu)|$ This choice is a best available realistic algorithm which we will be using for the analysis.

The values of reconstructed asymmetries and hence polarizations get shifted from **Abs. True** case. In case of **Reco. True**, the shifts are roughly constant, while in case of **Small $|p_z(\nu)|$** , the shifts are not constant over varying lower cut on m_{3l} and $p_T(Z)$ due to the 35 % wrong choice. It is, thus, expected that the reconstructed sensitivities to aTGC remain same in **Reco. True** and change in **Small $|p_z(\nu)|$** case when compared to the **Abs. True** case. In the **Small $|p_z(\nu)|$** reconstruction case, sensitivities of some asymmetries to aTGC are less than that of the **Abs. True** case, while they are higher for some other asymmetries. This is illustrated in Fig. 7.6 (top-row) comparing the sensitivity of some polarization asymmetries, e.g., A_y to $\tilde{\kappa}^Z = +0.2$ in cross (\times) points, A_z to $\Delta g_1^Z = -0.02$ in square (\square) points, and A_{zz} to $\Delta \kappa^Z = +0.2$ in circular (\odot) points for the three scenarios of **Abs. True** (solid/blue line), **Reco. True** (dotted/red) and **Small $|p_z(\nu)|$** (dash-dotted/blue) for varying lower cuts on $p_T(Z)$ and m_{3l} in ZW^+ production with a luminosity of $\mathcal{L} = 100 \text{ fb}^{-1}$. The sensitivities are roughly same for **Abs. True** and **Reco. True** reconstruction in all asymmetries for both $p_T(Z)$ and m_{3l} cuts. In the **Small $|p_z(\nu)|$** reconstruction case, sensitivity is smaller for A_{zz} ; higher for A_y ; and it depends on cut for A_z when compared to the **Abs. True** case. When all the W asymmetries are combined, the total χ^2 is higher in the **Small $|p_z(\nu)|$** case compared to the **Reco. True** case for about 100 chosen benchmark point, see Fig. 7.6 (bottom-panel). Here,

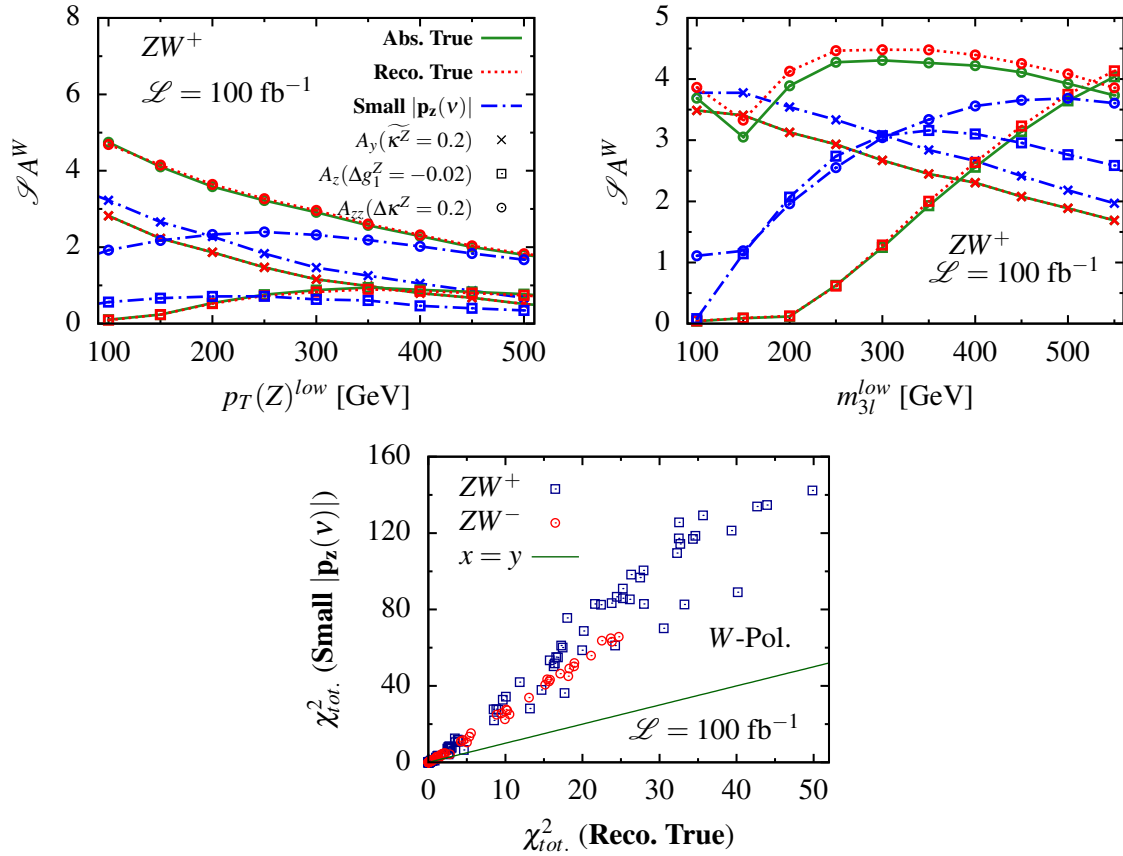


Figure 7.6. The sensitivity of some polarization asymmetries of W^+ (ZW^+) on some benchmark aTGC for three scenarios: with absolute truth (**Abs. True**) information of neutrino in *solid/blue* lines, with the close to true reconstructed solution of neutrino (**Reco. True**) in *dotted/red* lines and with the smaller $|p_z(v)|$ to be the true solution (**Small $|p_z(v)|$**) in *dash-dotted/blue* lines as a function of the lower cut on $p_T(Z)$ (*top-left-panel*) and m_{3l} (*top-right-panel*) at $\sqrt{s} = 13 \text{ TeV}$ and $\mathcal{L} = 100 \text{ fb}^{-1}$. The scatter plot of the total χ^2 for about 100 aTGC points using all the asymmetries of W^\pm for **Reco. True** in x -axis with **Small $|p_z(v)|$** in y -axis is shown in the *bottom-panel*.

a total χ^2 of all the asymmetries of W (A_i^W) for a benchmark point ($\{c_i\}$) is given by,

$$\chi^2(A_i^W)(\{c_i\}) = \sum_j^{N=9} \left(\mathcal{S}A_j^W(\{c_i\}) \right)^2. \quad (7.2.6)$$

The said increment of χ^2 is observed in both W^+Z (\square /blue) and W^-Z (\odot /red) production processes. So even if we are not able to reconstruct the W and hence its polarization observables correctly, realistic effects end up enhancing the overall sensitivity of the observables to the aTGC.

Reference z -axis for polarizations The other challenge to obtain the polarization of V is that one needs a reference axis (z -axis) to get the momentum direction of V , which is not possible at the LHC as it is a symmetric collider. Thus, for the asymmetries related to Z boson, we consider the direction of total visible longitudinal momenta as an unambiguous

choice for positive z -axis. For the case of W , the direction of reconstructed boost is used as a proxy for the positive z -axis. The latter choice is inspired by the fact that in $q'\bar{q}$ fusion the quark is supposed to have larger momentum than the anti-quark at the LHC, thus the above proxy could stand statistically for the direction of the quark direction.

List of observables The set of observables used in this analysis are,

σ_i : The cross sections in four bins (4),

A_{pol}^Z : Eight polarization asymmetries of Z (8),

A_{fb}^Z : Forward backward asymmetry of Z (1),

$A_{\Delta\phi}$: Azimuthal asymmetry (1),

A_{pol}^W : Eight polarization asymmetries of reconstructed W (8),

A_{fb}^W : Forward backward asymmetry of reconstructed W ¹ (1),

which make a total of $N(\mathcal{O}) = (4 + 8 + 1 + 1 + 8 + 1) \times 2 = 46$ observables including both processes. All the asymmetry from Z side and all the asymmetries from W side are termed as A_i^Z and A_i^W , respectively for latter uses. The total χ^2 for all observables would be the quadratic sum of sensitivities (Eq. (3.1.16)) given by,

$$\chi_{tot}^2(c_i) = \sum_j^{N=46} (\mathcal{S} \mathcal{O}_j(c_i))^2. \quad (7.2.7)$$

We use these set of observables in some chosen kinematical region to obtain limits on aTGC in the next section.

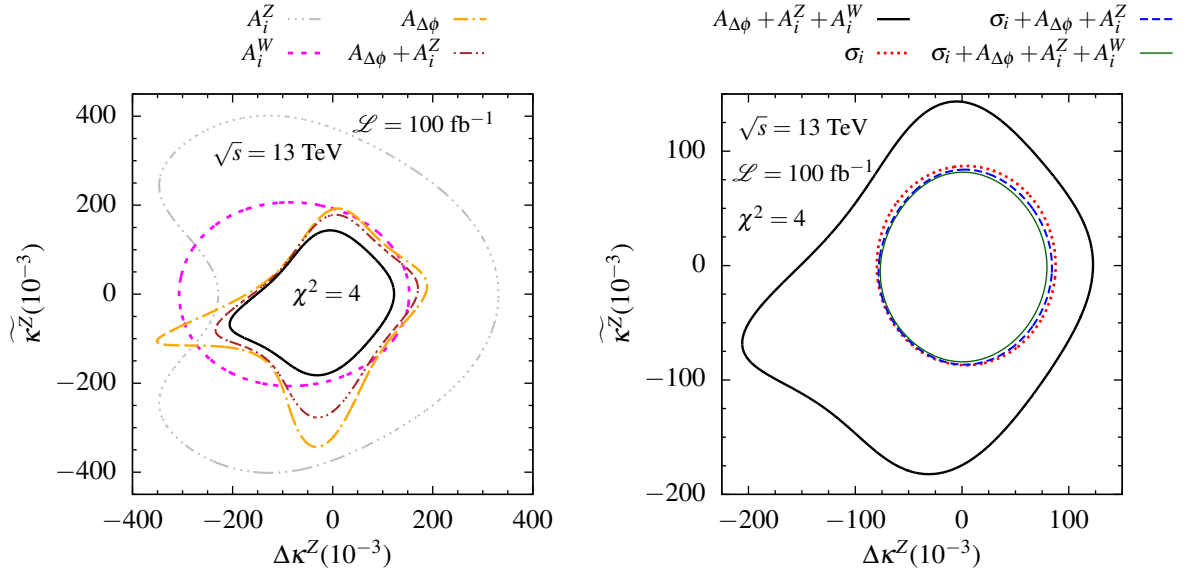
7.3 Probe of the anomalous couplings

We studied the sensitivities of all the ($N(\mathcal{O}) = 46$) observables for varying lower cuts on m_{3l} and $p_T(Z)$ separately as well as simultaneously (grid scan in the step of 50 GeV in each direction) for the chosen benchmark anomalous couplings. The maximum sensitivities are observed for simultaneous lower cuts on m_{3l} and $p_T(Z)$ given in Table 7.3 for all the asymmetries in both ZW^\pm processes. Some of these cuts can be realised from Fig. 7.5 & 7.6.

¹We note that the forward backward asymmetry of Z and W are ideally the same in the CM frame. However, since we measure the Z and W $\cos\theta$ w.r.t. different quantity, i.e., visible p_z for Z and reconstructed boost for W , they are practically different and we use them as two independent observables.

Table 7.3. The list of optimized lower cuts (opt. cut) on $(m_{3l}, p_T(Z))$ for various asymmetries to maximize the sensitivity to the anomalous couplings.

\mathcal{O}	Z in ZW^+	Z in ZW^-	W^\pm in ZW^\pm
A_x	(200, 100)	(100, 150)	(250, 0)
A_y	(150, 100)	(100, 100)	''
A_z	(550, 50)	(100, 250)	''
A_{xy}	(150, 100)	(150, 100)	''
A_{xz}	(150, 0)	(200, 50)	''
A_{yz}	(100, 50)	(100, 0)	''
$A_{x^2-y^2}$	(400, 150)	(300, 100)	''
A_{zz}	(550, 0)	(300, 400)	''
A_{fb}	(300, 0)	(550, 0)	''
	ZW^+		ZW^-
$A_{\Delta\phi}$	(100, 300)		(100, 300)

**Figure 7.7.** The $\chi^2 = 4$ contours are shown in the $\Delta\kappa^Z - \tilde{\kappa}^Z$ plane with different asymmetries and their combinations in the *left-panel*, various combinations of the cross sections and asymmetries in the *right-panel* for $\sqrt{s} = 13$ TeV and $\mathcal{L} = 100$ fb $^{-1}$. The contour for $A_{\Delta\phi} + A_i^Z + A_i^W$ (thick-solid/black line) is repeated in both panel for comparison.

The SM values of the asymmetries of Z and W and their corresponding polarizations for the selection cuts (sel. cut in Eq. (7.1.2)) and for the optimized cuts (opt. cut in Table 7.3) are listed in Table E.1 in appendix E.1 for completeness. We use the cross sections in the four bins and all asymmetries with the optimized cuts to obtain limits on the anomalous couplings for both effective vertices and effective operators. We use the semi-analytical ex-

pressions for the observables fitted with the simulated data from mg5_aMC. The details of the fitting procedures are described in appendix E.2. The uncertainty on the cross sections and asymmetries are taken as $\epsilon_\sigma = 20\%$ and $\epsilon_A = 2\%$, respectively consistent with the analysis by CMS [248] and ATLAS [240]. We note that these uncertainties are not considered in the previous sections for qualitative analysis and optimization of cuts.

The sensitivities of all the observables to the aTGC are studied by varying one-parameter, two-parameter and all-parameter at a time in the optimized cut region. We look at the $\chi^2 = 4$ contours in the $\Delta\kappa^Z\text{-}\widetilde{\kappa}^Z$ plane for a luminosity of $\mathcal{L} = 100 \text{ fb}^{-1}$ for various combinations of asymmetries and cross sections and show them in Fig. 7.7. We observe that the Z -asymmetries (A_i^Z) are weaker than the W -asymmetries (A_i^W); A_i^W provides very symmetric limits, while A_i^Z has a sense of directionality. The $A_{\Delta\phi}$ is better than both A_i^Z and A_i^W in most of the directions in $\Delta\kappa^Z\text{-}\widetilde{\kappa}^Z$ plane. After combining A_i^Z , A_i^W and $A_{\Delta\phi}$, we get a tighter contours; but the shape is dictated by $A_{\Delta\phi}$. We see (Fig. 7.7 right-panel) that the cross sections have higher sensitivities compared to the asymmetries to the aTGC. The cross sections dominate constraining the couplings, while the contribution from the asymmetries remain sub-dominant at best. Although the directional constraints provided by the asymmetries get washed away when combined with the cross sections, they are expected to remain prominent to extract non-zero couplings should a deviation from the SM be observed. This possibility is discussed in the subsection 7.3.2.

7.3.1 Limits on the couplings

We extract simultaneous limits on all the anomalous couplings using all the observables using MCMC method. We perform this analysis in two ways: (i) vary effective vertex factors couplings ($c_i^{\mathcal{L}}$) and (ii) vary effective operators couplings ($c_i^{\mathcal{O}}$) and translate them in to effective vertex factors couplings ($c_i^{\mathcal{L}^g}$). The definitions for $c_i^{\mathcal{L}}$, $c_i^{\mathcal{O}}$, and $c_i^{\mathcal{L}^g}$ can be found in Eqs. (6.0.4), (6.0.3), and (6.0.5), respectively. The 95 % BCI (Bayesian confidence interval) obtained on aTGC are listed in Table 7.4 for four choices of integrated luminosities: $\mathcal{L} = 35.9 \text{ fb}^{-1}$, $\mathcal{L} = 100 \text{ fb}^{-1}$, $\mathcal{L} = 300 \text{ fb}^{-1}$ and $\mathcal{L} = 1000 \text{ fb}^{-1}$. The correlation among the parameters are studied (using GetDist [205]) and they are shown in Fig. 7.8 along with 1D projections for effective vertex factors. The limits on the couplings get tighter as the luminosity is increased, as it should be. The shape of the contours are very circular in all two-parameter projections as the cross sections dominate in constraining the aTGC. The same conclusions are drawn when effective operators are varied as independent parameters.

Table 7.4. The list of simultaneous limits from MCMC at 95 % BCI on the effective vertex couplings $c_i^{\mathcal{L}}$ and the effective operator couplings $c_i^{\mathcal{O}}$ along with translated limits on effective vertices $c_i^{\mathcal{L}s}$ for various luminosities. The notations for $c_i^{\mathcal{L}}$, $c_i^{\mathcal{O}}$, and $c_i^{\mathcal{L}s}$ are given in Eqs. (6.0.4), (6.0.3), and (6.0.5), respectively.

$c_i^{\mathcal{L}}$ (10^{-3})	35.9 fb $^{-1}$	100 fb $^{-1}$	300 fb $^{-1}$	1000 fb $^{-1}$
Δg_1^Z	[-4.20, +2.15]	[-3.47, +1.50]	[-2.92, +0.963]	[-2.48, +0.565]
λ^Z	[-2.24, +2.11]	[-1.78, +1.66]	[-1.42, +1.30]	[-1.14, +1.01]
$\Delta \kappa^Z$	[-83.0, +83.5]	[-64.1, +66.6]	[-47.9, +52.8]	[-34.2, +42.1]
$\widetilde{\lambda}^Z$	[-2.19, +2.19]	[-1.74, +1.72]	[-1.38, +1.36]	[-1.09, +1.09]
$\widetilde{\kappa}^Z$	[-88.4, +86.2]	[-70.4, +67.5]	[-54.9, +51.8]	[-43.2, +40.1]
$c_i^{\mathcal{O}}$ (TeV $^{-2}$)				
$\frac{c_{WW}}{\Lambda^2}$	[-0.565, +0.540]	[-0.445, +0.426]	[-0.365, +0.327]	[-0.258, +0.257]
$\frac{c_W}{\Lambda^2}$	[-0.747, +0.504]	[-0.683, +0.397]	[-0.624, +0.274]	[-0.390, +0.196]
$\frac{c_B}{\Lambda^2}$	[-67.1, +67.8]	[-59.2, +60.1]	[-52.6, +47.6]	[-33.3, +30.9]
$\frac{c_{\widetilde{WW}}}{\Lambda^2}$	[-0.514, +0.516]	[-0.430, +0.415]	[-0.342, +0.339]	[-0.244, +0.252]
$\frac{c_{\widetilde{W}}}{\Lambda^2}$	[-68.5, +69.2]	[-60.4, +61.2]	[-52.0, +52.7]	[-32.7, +34.2]
$c_i^{\mathcal{L}s}$ (10^{-3})				
Δg_1^Z	[-3.10, +2.10]	[-2.84, +1.65]	[-2.59, +1.14]	[-1.62, +0.814]
λ^Z	[-2.31, +2.21]	[-1.82, +1.74]	[-1.49, +1.34]	[-1.06, +1.05]
$\Delta \kappa^Z$	[-63.4, +62.1]	[-56.4, +54.6]	[-44.8, +48.3]	[-29.1, +30.6]
$\widetilde{\lambda}^Z$	[-2.10, +2.11]	[-1.76, +1.70]	[-1.40, +1.39]	[-1.00, +1.03]
$\widetilde{\kappa}^Z$	[-64.5, +63.8]	[-57.1, +56.3]	[-49.1, +48.4]	[-31.9, +30.5]

The limits on $c_i^{\mathcal{L}s}$ are tighter compared to the limits on $c_i^{\mathcal{L}}$ (see Table 7.4); the comparison between them are shown in the two-parameter marginalised plane in Fig. 7.9 in Δg_1^Z - κ^Z , λ^Z - $\widetilde{\lambda}^Z$ and κ^Z - $\widetilde{\kappa}^Z$ planes as representative for luminosity $\mathcal{L} = 100$ fb $^{-1}$ (outer contours) and $\mathcal{L} = 1000$ fb $^{-1}$ (inner contours). The limits and the contours are roughly same in λ^Z - $\widetilde{\lambda}^Z$ plane. The contours are more symmetric around the SM for $c_i^{\mathcal{L}s}$ compared to $c_i^{\mathcal{L}}$, e.g., see Δg_1^Z - κ^Z plane. The limits obtained here for luminosity 35.9 fb $^{-1}$ are better than the experimentally observed limits at the LHC given in Table 6.1 except on c_B and hence on $\Delta \kappa^Z$. This is due to the fact that the LHC analysis [167] uses WW production on top of WZ production whereas we only use WZ production process. But our limits on the couplings are better when compared with the WZ production process alone at the LHC [169]. In Fig. 7.10, we present the comparison of limits obtained by the CMS analyses with $ZW + WW$ [167]

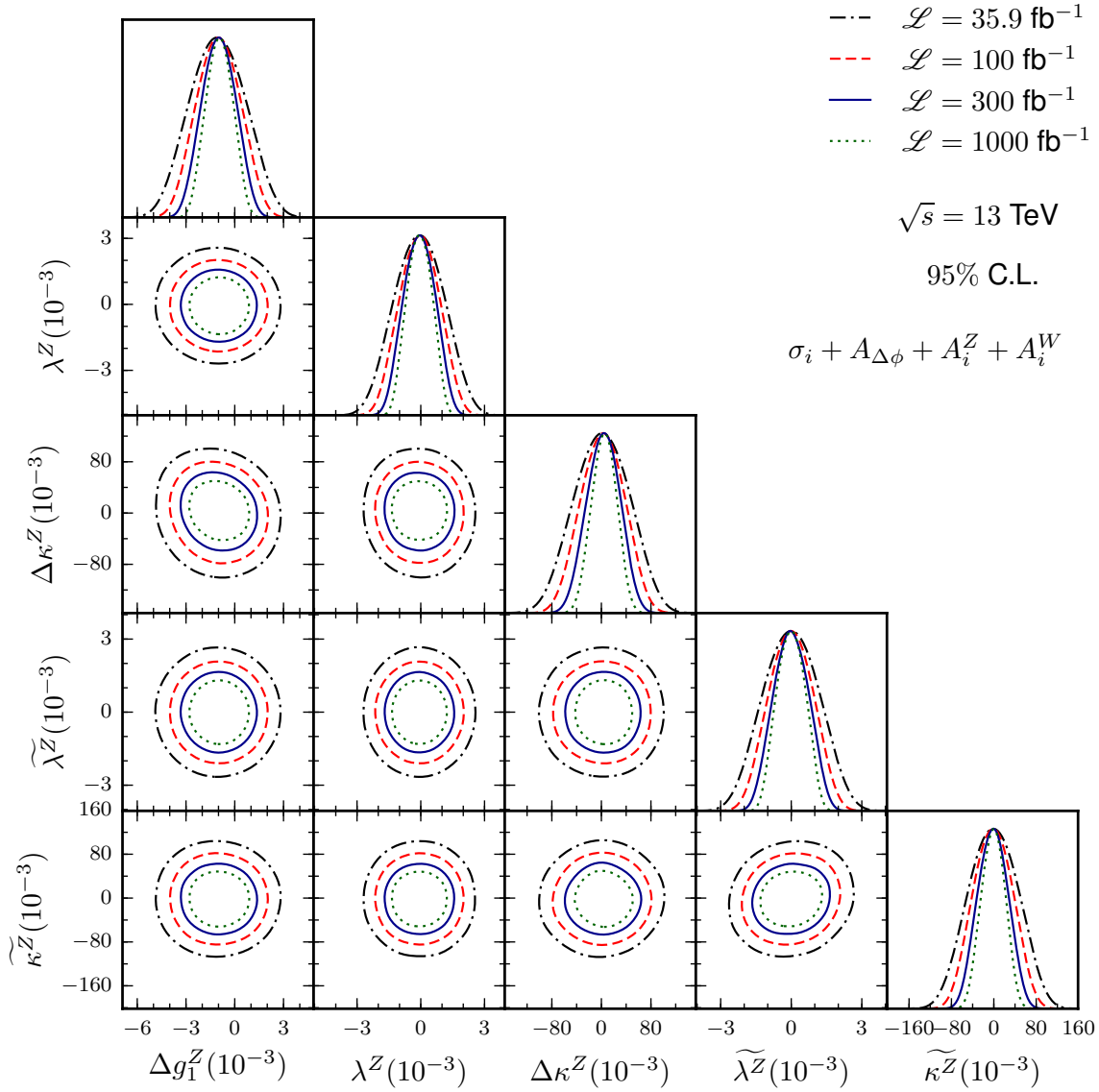


Figure 7.8. All the marginalised 1D projections and 2D projections at 95 % BCI from MCMC in triangular array for the effective vertices ($c_i^{\mathcal{L}}$) for various luminosities at $\sqrt{s} = 13 \text{ TeV}$ using all the observables.

process and ZW [169] with our estimate with two parameter 95 % BCI contours in the $c_{WW}/\Lambda^2 - c_W/\Lambda^2$ plane (*left-panel*) and $c_W/\Lambda^2 - c_B/\Lambda^2$ plane (*right-panel*). The contour in the plane $c_{WW}/\Lambda^2 - c_W/\Lambda^2$ in our estimate (We expect) (*solid/green line*) is tighter compared to both CMS $ZW + WW$ (*dashed/black line*) and CMS ZW analyses (*dotted/blue line*). This is because we use binned cross sections in the analysis. The limit on the couplings c_B/Λ^2 (*right-panel*) on the other hand is tighter, yet comparable, with CMS ZW and weaker than the CMS $ZW + WW$ analysis because the ZW process itself is less sensitive to c_W .

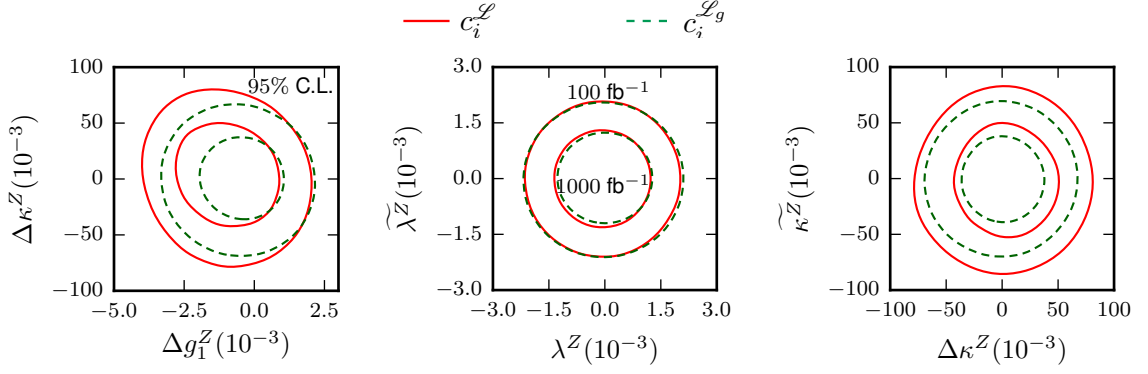


Figure 7.9. The marginalised 2D projections at 95 % BCI from MCMC in the Δg_1^Z - $\Delta \kappa^Z$, λ^Z - $\tilde{\lambda}^Z$, and $\Delta \kappa^Z$ - $\tilde{\kappa}^Z$ planes are shown in *solid/red* when the effective vertex factors ($c_i^{\mathcal{L}}$) are treated independent, while shown in *dashed/green* when the operators are treated independent ($c_i^{\mathcal{L}g}$) for luminosities $\mathcal{L} = 1000 \text{ fb}^{-1}$ (two inner contours) and $\mathcal{L} = 100 \text{ fb}^{-1}$ (two outer contours) at $\sqrt{s} = 13 \text{ TeV}$ using all the observables.

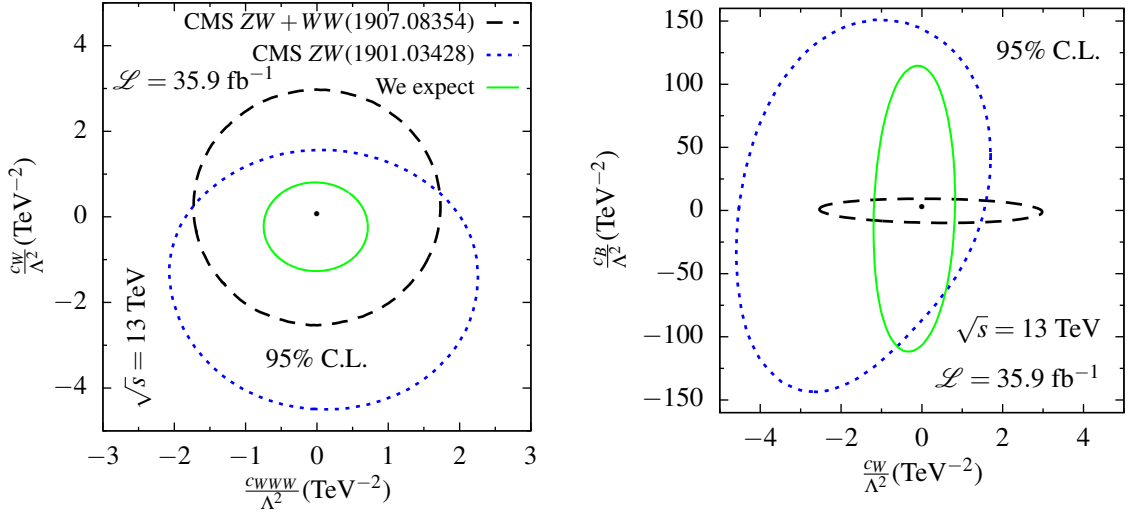


Figure 7.10. The two parameter 95 % C.L. contours in the c_{WW}/Λ^2 - c_W/Λ^2 plane (*left-panel*) and c_W/Λ^2 - c_B/Λ^2 plane (*right-panel*) for our estimate in *solid/green* lines, for CMS ZW + WW in *dashed/black* lines and for CMS ZW in *dotted/blue* lines at $\sqrt{s} = 13 \text{ TeV}$ and $\mathcal{L} = 35.9 \text{ fb}^{-1}$ using all the observables.

7.3.2 The role of asymmetries in parameter extraction

The asymmetries are subdominant in constraining the couplings much like seen in Ref. [106] for $pp \rightarrow ZZ$ case. But the asymmetries help significantly giving directional constraint in the parameter space. To see this, we perform a toy analysis to extract non zero anomalous couplings with pseudo data generated by the set of anomalous couplings of

$$\text{aTGC-Bench} : \{\Delta g_1^Z, \lambda^Z, \Delta \kappa^Z, \tilde{\lambda}^Z, \tilde{\kappa}^Z\} = \{0.01, 0.01, 0.1, 0.01, 0.1\} \quad (7.3.1)$$

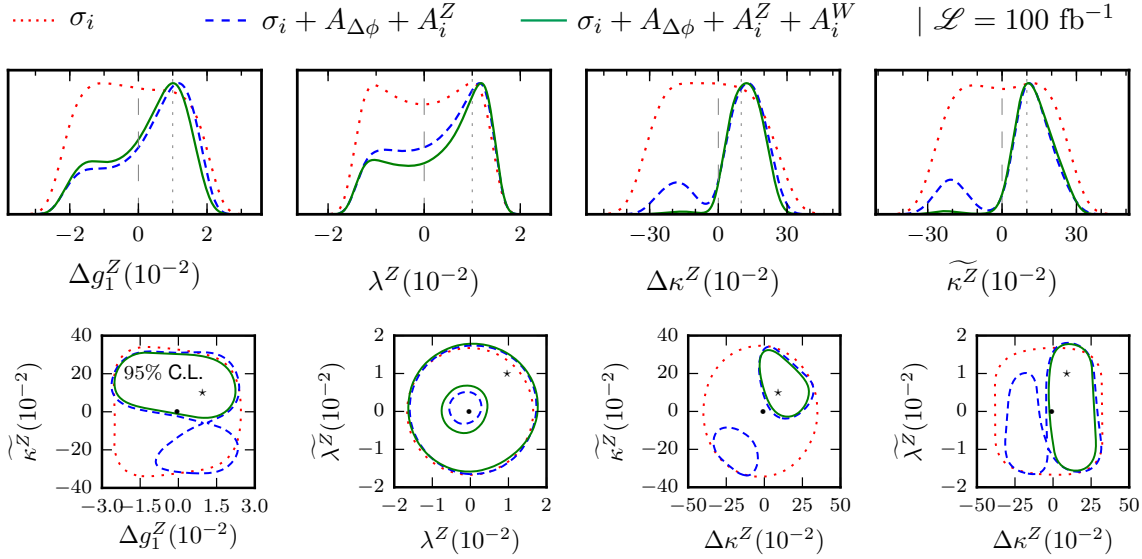


Figure 7.11. The marginalised 1D projections for the couplings Δg_1^Z , λ^Z , $\Delta\kappa^Z$, and $\widetilde{\kappa}^Z$ in *top-panel* and 2D projections at 95 % BCI on $\Delta g_1^Z - \widetilde{\kappa}^Z$, $\lambda^Z - \widetilde{\lambda}^Z$, $\Delta\kappa^Z - \widetilde{\kappa}^Z$, and $\Delta\kappa^Z - \widetilde{\lambda}^Z$ planes in *bottom-panel* from MCMC with observables σ_i (*dotted/red line*), $\sigma_i + A_{\Delta\phi} + A_i^Z$ (*dashed/blue line*) and $\sigma_i + A_{\Delta\phi} + A_i^Z + A_i^W$ (*solid/green line*) for aTGC-Bench couplings $\{\Delta g_1^Z, \lambda^Z, \Delta\kappa^Z, \widetilde{\lambda}^Z, \widetilde{\kappa}^Z\} = \{0.01, 0.01, 0.1, 0.01, 0.1\}$ at $\sqrt{s} = 13 \text{ TeV}$ and $\mathcal{L} = 100 \text{ fb}^{-1}$.

using MCMC method. We choose these benchmark couplings well above the current limits so as to mimic a situation of deviation from the SM is observed, as we have considered for ZZ production in chapter 5. In Fig. 7.11, we show the posterior marginalised 1D projections for the couplings Δg_1^Z , λ^Z , $\Delta\kappa^Z$, and $\widetilde{\kappa}^Z$ in *top-panel* and 2D projections at 95 % BCI on $\Delta g_1^Z - \widetilde{\kappa}^Z$, $\lambda^Z - \widetilde{\lambda}^Z$, $\Delta\kappa^Z - \widetilde{\kappa}^Z$, and $\Delta\kappa^Z - \widetilde{\lambda}^Z$ planes in *bottom-panel*. We extract the limits using σ_i only (*dotted/red line*), using σ_i along with $A_{\Delta\phi} + A_i^Z$ (*dashed/blue line*) and all observables $\sigma_i + A_{\Delta\phi} + A_i^Z + A_i^W$ (*solid/green line*) for integrated luminosity of $\mathcal{L} = 100 \text{ fb}^{-1}$. The *dashed* lines in 1D projections and dot (\bullet) in the 2D contours represent the SM point, while the *dotted* lines in 1D projections and star-mark (\star) in the contours represent the couplings from aTGC-Bench. As the asymmetries $A_{\Delta\phi}$ and asymmetries of Z (A_i^Z) are added on top of the cross sections, the measurement gets better and it further gets better when the asymmetries of W (A_i^W) are added, which can be seen from both 1D projections and 2D contours. The cross sections are blind to the orientation of aTGC-Bench couplings and sensitive only to the magnitude of deviation from the SM. The asymmetries, however, give direction to the measurement, e.g., in $\Delta\kappa^Z - \widetilde{\kappa}^Z$ plane $\sigma_i + A_{\Delta\phi} + A_i^Z$ provide two patches (excluding the SM), and we get one single (true) region when using all the asymmetries along with the cross sections. In the $\lambda^Z - \widetilde{\lambda}^Z$ plane the asymmetries could not provide a direction, however, they shrink the 95 % contours from simply connected patch to an annular region (excluding the SM). For the other couplings the asymmetries favour the regions of the correct solution of

aTGC-Bench couplings. For higher luminosities (not shown here), the contours become tighter, and the $1D$ curves become sharper centred around the aTGC-Bench couplings when using $\sigma_i + A_i$, while σ_i alone remain blind to the aTGC-Bench. Thus the asymmetries help in the measurement of anomalous couplings provided an excess of events of aTGC kind are observed.

We note that the $3l + \cancel{E}_T$ excess in the lower $p_T(Z)$ region at the LHC [169] interpreted by two extra scalar [246] may be fitted by aTGC, which is beyond the scope of this present work.

7.4 Summary

To summarize this chapter, we studied the WWZ anomalous couplings in the ZW^\pm production at the LHC and examined the role of polarization asymmetries together with $\Delta\phi(l_W, Z)$ asymmetry and forward-backward asymmetry on the estimation of limits on the anomalous couplings. We reconstructed the missing neutrino momentum by choosing the small $|p_z(\nu)|$ from the two-fold solutions and estimated the W polarization asymmetries, while the Z polarization asymmetries are kept free from any reconstruction ambiguity. We generated NLO events at mg5_aMC for about 100 sets of anomalous couplings and used them for the numerical fitting of semi-analytic expressions of all the observables as a function of couplings. We estimated simultaneous limits on the anomalous couplings using MCMC method for both effective vertex formalism and effective operator approach for luminosities 35.9 fb^{-1} , 100 fb^{-1} , 300 fb^{-1} and 1000 fb^{-1} . The limits obtained for $\mathcal{L} = 35.9 \text{ fb}^{-1}$ are tighter than the available limits obtained at the LHC (see Table 6.1 & 7.4) except on c_W (and $\Delta\kappa^Z$). The asymmetries are helpful in extracting the values of anomalous couplings if a deviation from the SM is observed at the LHC. We performed a toy analysis of parameter extraction with some benchmark aTGC couplings and observed that the inclusion of asymmetries to the cross sections improves the parameter extraction significantly.

8

Conclusions and outlooks

It is for sure that new physics beyond the SM is needed to address many open questions of the SM. So far, there is no hint of new physics at the LHC. The new physics scale could be standing at very high energy not to be directly observed at the current energy range. These high scale new physics may leave footprints in the present energy through higher dimensional effective operators, which often predict new vertices or modify some of the SM vertices. These new or modified vertices are called anomalous couplings. This thesis deals in probing the anomalous triple gauge boson couplings, i.e., new VVZ ($V = Z/\gamma$) vertices as well as new and modified WWV vertices at various colliders. Precise measurements of these gauge boson self couplings can help us to understand the electroweak symmetry breaking in detail. As the Z boson and W boson has polarized couplings to the electrons and quarks, they are produced polarized in any process. The inclusion of aTGC further modifies the values of the polarizations of the gauge bosons. Thus, the polarizations, along with the cross sections, can be used to probe the aTGC in a collider.

A spin-1 particle has a total of eight polarizations which are three degrees of vector polarizations and five degrees of tensor polarizations, see chapter 2. The polarizations are related to the various combinations of the elements of the production density matrix of the particle. The information for the polarizations is transferred to the angular distributions of the decay products of the particle. So, the polarizations can be measured from the production density matrix as well as from the angular information of their decayed products by constructing some asymmetries in a Monte-Carlo event generator or a real collider. The density matrix method and the method of asymmetry from decay distributions of calculating polarizations of a spin-1 particle are shown to be consistent through the examples of the processes ZZ , $Z\gamma$ and W^+W^- productions at an e^+e^- collider in the SM. These polarization asymmetries, along with the cross sections and other asymmetries, are used to probe the aTGC in the di-boson productions processes (ZZ , $Z\gamma$, and W^+W^-) at an e^+e^- collider as well as (ZZ and $W^\pm Z$) at the LHC.

In the e^+e^- collider (chapters 3, 4 & 6), we calculated the polarization asymmetries from the production density matrix by analytical helicity amplitude method, while we estimated them from the decay angular distributions at the LHC (chapters 5 & 7). Some of the polarization asymmetries are CP -even while some others are CP -odd. The CP -odd nature of the couplings can be identified by the CP -odd polarization asymmetries A_y , A_{xy} , and A_{yz} . A CP -even polarization asymmetry can also identify a CP -odd couplings in a suitable kinematic region, e.g., the CP -even asymmetry $A_{x^2-y^2}$ probes CP -odd couplings in the ZZ production, discussed in chapter 5. Although A_z , A_{xz} , and A_{yz} are zero in ZZ and $Z\gamma$ production (see chapter 3), they can be made non-zero by little modification using the direction of Z , see chapter 4. The spin of the gauge bosons has different orientation for different polar angle orientation in a general two-body reaction. Thus the gauge boson poses different values of polarizations for different polar orientations. We used this information to make bins w.r.t. the polar angle of W and calculated its polarizations in each bin in the WW production process, discussed in chapter 6.

For the aTGC, we restricted ourselves up to the dimension-6 terms for both the form factors (respecting the Lorentz invariance and $U(1)_{EM}$) as well as the effective operators (respecting the SM gauge symmetry). As the effective operators for neutral aTGC appear at dimension-8 onward, we studied the neutral aTGC using the form factor approach (chapters 3, 4, & 5). For the charged aTGC, however, we studied both the form factors as well as effective operators (chapter 6 & 7). We considered the dimension-6 operator up to their quadratic contribution as the linear approximation is not valid, see appendix C.2.

We studied the sensitivity of the polarization asymmetries along with the cross sections to the anomalous couplings and found their one parameter limits. There is a particular polarization asymmetry which is highly correlated to a particular aTGC parameter giving us the best suitable observable for each parameter, e.g., see chapter 3. We estimated the simultaneous limits on the aTGC using the MCMC method for different luminosities. The polarization asymmetries give significant improvement on the constraints of the aTGC at e^+e^- collider, but not at the LHC. However, the polarization asymmetries show directional limits and help to pinpoint non-zero aTGC values at the LHC. To demonstrate this, we performed a toy analysis of parameter extraction with some benchmark aTGC and observed that the inclusion of the asymmetries to the cross sections improves the parameter extraction significantly in both ZZ (chapter 5) and ZW^\pm (chapter 7) productions at the LHC. The limits on the couplings, for the charged aTGC, are tighter when $SU(2) \times U(1)$ symmetry is assumed, see chapter 6 & 7. In the ZW^\pm production process (chapter 7), the $\Delta\phi(l_W, Z)$ asymmetry is used, along with the

forward-backward asymmetry, polarization asymmetries and cross sections. This azimuthal asymmetry is more sensitive to aTGC than the polarization asymmetries. We reconstructed the missing neutrino momenta by choosing small $|p_z(\nu)|$ from the two-fold solutions and estimated the W asymmetries, while the Z asymmetries are free from any such reconstruction ambiguity.

The beam polarization at e^+e^- collider plays a vital role in probing the aTGC. The limits on the aTGC get improved by suitably tuning the beam polarizations. We estimated the best choice of beam polarization based on average likelihood to put the tightest constraints on the anomalous couplings. The best choice of beam polarization changes as the values of the anomalous couplings change. Thus, we estimated the best choice of beam polarizations using the likelihood, averaged over the couplings. The best choices are found to be in the extreme corner ($\pm 0.8, \mp 0.8$ for e^- and e^+) when beam polarizations are combined with their opposite choices for both ZV (chapter 4) and WW (chapter 6) production processes. For fixed beam polarizations, however, the best choices are ($\sim 0.1, \sim -0.1$) and ($0.4, -0.4$) for ZV and WW production, respectively.

The polarization asymmetries of the Z and W have shown promising results in probing the anomalous gauge boson couplings. They provide a large set of observables to obtain simultaneous limits on a large set of anomalous couplings, $ZZ/Z\gamma$ has 4 couplings, and W^+W^- has 14 couplings. In all the analyses, we consider certain simplifying assumptions, such as the absence of initial-state/final-state radiation, hadronization, and detector effects. The limits on the aTGC are expected to get dilute if we consider those realistic effects, but the qualitative features of the observables will remain the same.

In conclusion, we proposed some novel techniques to probe new physics beyond the SM at colliders. Application of these techniques to the data from the LHC and future colliders may reveal the underlying mechanism of the electroweak symmetry breaking and help to discover new physics.

Outlooks

The spins of the gauge bosons in the di-boson production processes are correlated, providing 64 potential correlators, see chapter 2. Their spins could be correlated even if they are produced unpolarized individually, e.g., $t\bar{t}$ production case at the LHC. In our analyses, we did not use the spin-spin correlations of the gauge bosons for simplicity; they would improve the results if used. Apart from the anomalous triple gauge boson couplings, the

polarization observables can be used to study any new physics associated with them. For example, one can study the anomalous quartic gauge boson couplings and Higgs to gauge boson couplings in processes like triple gauge boson production (VVV) [201, 202], vector boson scattering [203], $t\bar{t}Z$ production, VHH production [251], VVH production. The polarization observables are also helpful in probing the FCNC interactions [180], e.g., tqZ couplings. Besides these, polarizations of gauge bosons can help in probing SUSY, extra dimension, and dark matter by looking at their SM backgrounds. The effective operators that we consider for the aTGC may also provide quartic couplings which appear in different processes [201–203, 252]. One can consider all the processes containing the contribution of a given operator and derive a limit on it at a given collider for a complete study.

Appendices

A The Standard Model Feynman rules in the electroweak theory

The Pauli sigma matrices are

$$\sigma_1 = \sigma_x = \begin{pmatrix} 0 & 1 \\ 1 & 0 \end{pmatrix}, \quad \sigma_2 = \sigma_y = \begin{pmatrix} 0 & -i \\ i & 0 \end{pmatrix}, \quad \sigma_3 = \sigma_z = \begin{pmatrix} 1 & 0 \\ 0 & -1 \end{pmatrix}. \quad (\text{A.0.1})$$

The γ matrices in Dirac basis are given by:

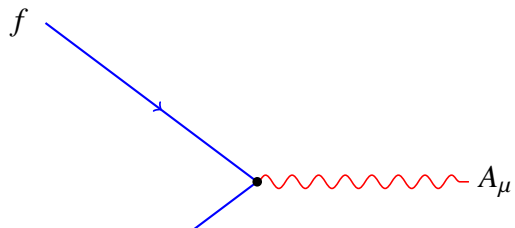
$$\gamma^0 = \begin{pmatrix} \mathbb{I}_{2 \times 2} & 0 \\ 0 & -\mathbb{I}_{2 \times 2} \end{pmatrix}, \quad \gamma^k = \begin{pmatrix} 0 & \sigma_k \\ -\sigma_k & 0 \end{pmatrix}, \quad \gamma_5 = i\gamma^0\gamma^1\gamma^2\gamma^3 = \begin{pmatrix} 0 & \mathbb{I}_{2 \times 2} \\ \mathbb{I}_{2 \times 2} & 0 \end{pmatrix}, \quad k = 1, 2, 3. \quad (\text{A.0.2})$$

The Feynman rules in the electroweak theory, which are used in this thesis, are given below.

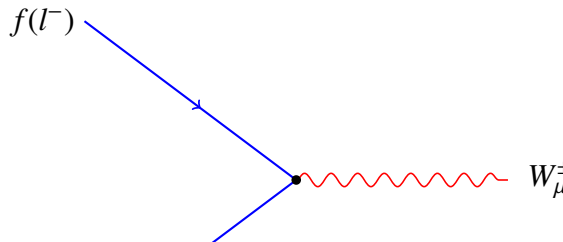
Dirac propagator : $\begin{array}{c} \xrightarrow{p} \\ \text{---} \end{array} = \frac{i}{\not{p} - m + i\epsilon}$

Photon propagator : $\begin{array}{c} \xrightarrow{\gamma(p)} \\ \mu \text{ --- } \nu \end{array} = \frac{-ig_{\mu\nu}}{p^2 + i\epsilon}$

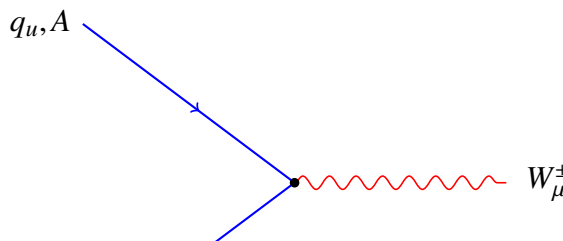
Massive boson propagator : $\begin{array}{c} \xrightarrow{p} \\ \mu \text{ --- } \nu \end{array} = \frac{i(-g_{\mu\nu} + \frac{p_\mu p_\nu}{m^2})}{p^2 - m^2 + i\epsilon}$



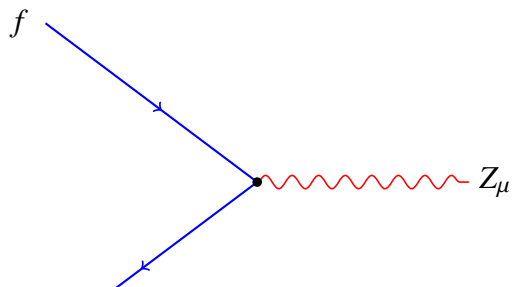
$$= iQ_f e \gamma^\mu$$



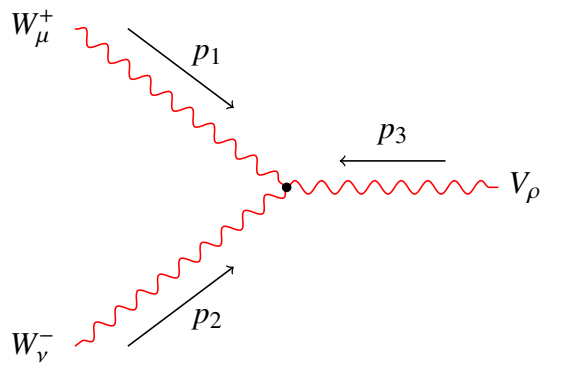
$$= -\frac{ig}{2\sqrt{2}} \gamma^\mu (1 - \gamma_5)$$



$$= -\frac{ig}{2\sqrt{2}} \gamma^\mu (1 - \gamma_5) V_{AB}$$



$$= -\frac{ig}{\cos \theta_W} \gamma^\mu \left(\begin{array}{c} T_3 \frac{1}{2} (1 - \gamma_5) - Q \sin^2 \theta_W \\ \underbrace{C_L \frac{1}{2} (1 - \gamma_5) + C_R \frac{1}{2} (1 + \gamma_5)}_{\equiv (v_f - a_f \gamma_5)} \end{array} \right)$$



$$= -ig_{WWV} \left[g^{\mu\nu} (p_1 - p_2)^\rho + g^{\nu\rho} (p_2 - p_3)^\mu + g^{\rho\mu} (p_3 - p_1)^\nu \right]$$

$g_{WWZ} = -e \cot \theta_W, \quad g_{WW\gamma} = -e$

B Helicity amplitudes and polarization observables in $e^+e^- \rightarrow ZZ/Z\gamma$

B.1 Helicity amplitudes

Vertices in SM are taken as

$$\begin{aligned} e^- e^+ Z^\mu &\Rightarrow -i \frac{g_Z}{2} \gamma^\mu (C_L P_L + C_R P_R), \\ e^- e^+ \gamma^\mu &\Rightarrow i g_e \gamma^\mu, \end{aligned} \quad (\text{B.1.1})$$

where $C_L = -1 + 2 \sin^2 \theta_W$, $C_R = 2 \sin^2 \theta_W$, with $\sin^2 \theta_W = 1 - \left(\frac{m_W}{m_Z}\right)^2$. Here θ_W is the Weinberg mixing angle. The couplings g_e, g_Z are given by,

$$g_e = e = \sqrt{4\pi\alpha_{EM}} \quad \text{and} \quad g_Z = \frac{g_e}{\cos \theta_W \sin \theta_W}. \quad (\text{B.1.2})$$

$P_L = \frac{1-\gamma_5}{2}$, $P_R = \frac{1+\gamma_5}{2}$ are the left and right chiral operators. Here $\sin \theta$ and $\cos \theta$ are written as s_θ and c_θ respectively.

B.1.1 For the process $e^+e^- \rightarrow ZZ$

The four-momentum of the particles in this process are (see Fig. B.1)

$$\begin{aligned} p_1^\mu &= \frac{\sqrt{\hat{s}}}{2} \{1, 0, 0, 1\}, & p_2^\mu &= \frac{\sqrt{\hat{s}}}{2} \{1, 0, 0, -1\} \\ k_1^\mu &= \frac{\sqrt{\hat{s}}}{2} \{1, -\beta \sin \theta, 0, -\beta \cos \theta\}, & k_2^\mu &= \frac{\sqrt{\hat{s}}}{2} \{1, \beta \sin \theta, 0, \beta \cos \theta\}, \end{aligned} \quad (\text{B.1.3})$$

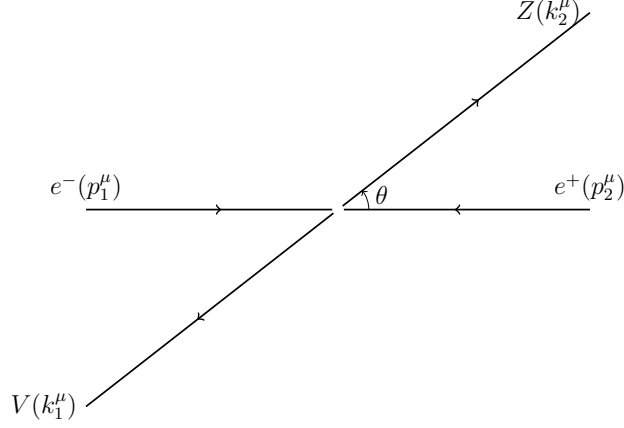


Figure B.1. Schematic diagram for $e^-e^+ \rightarrow ZV$ kinematics.

$\sqrt{\hat{s}}$ being the centre-of-mass energy of the colliding beams. The on-shell condition of Z , $k_1^2 = k_2^2 = m_Z^2$ gives β as

$$\beta = \sqrt{1 - \frac{4m_Z^2}{\hat{s}}}. \quad (\text{B.1.4})$$

We also define $f^Z = f_4^Z + if_5^Z\beta$, $f^\gamma = f_4^\gamma + if_5^\gamma\beta$.

$$\begin{aligned} \mathcal{M}_{\lambda_{e^-}, \lambda_{e^+}, \lambda_{z(1)}, \lambda_{z(2)}} &= \mathcal{M}_{SM} + \mathcal{M}_{aTGC} \\ \mathcal{M}_{+,-,+} &= -\frac{ig_Z^2 C_R^2 (1-\beta^2) c_\theta s_\theta}{1 + 2\beta^2 (1 - 2c_\theta^2) + \beta^4} \end{aligned}$$

$$\mathcal{M}_{+,-,+0} = -\frac{ig_Z^2 C_R^2 \sqrt{1-\beta^2} (1-2c_\theta + \beta^2)(1+c_\theta)}{\sqrt{2}(1 + 2\beta^2 (1 - 2c_\theta^2) + \beta^4)} - \frac{\sqrt{2}(1+c_\theta) g_e \beta (2g_e f^\gamma - C_{RGZ} f^Z)}{(1-\beta^2)^{3/2}}$$

$$\mathcal{M}_{+,-,+,-} = \frac{ig_Z^2 C_R^2 (1+\beta^2)(1+c_\theta)s_\theta}{1 + 2\beta^2 (1 - 2c_\theta^2) + \beta^4}$$

$$\mathcal{M}_{+,-,0,+} = \frac{ig_Z^2 C_R^2 \sqrt{1-\beta^2} (1+2c_\theta + \beta^2)(1-c_\theta)}{\sqrt{2}(1 + 2\beta^2 (1 - 2c_\theta^2) + \beta^4)} + \frac{\sqrt{2}(1-c_\theta) g_e \beta (2g_e f^\gamma - C_{RGZ} f^Z)}{(1-\beta^2)^{3/2}}$$

$$\mathcal{M}_{+,-,0,0} = -\frac{2ig_Z^2 C_R^2 (1-\beta^2) c_\theta s_\theta}{1 + 2\beta^2 (1 - 2c_\theta^2) + \beta^4}$$

$$\begin{aligned} \mathcal{M}_{+,-,0,-} &= -\frac{ig_Z^2 C_R^2 \sqrt{1-\beta^2} (1-2c_\theta + \beta^2)(1+c_\theta)}{\sqrt{2}(1 + 2\beta^2 (1 - 2c_\theta^2) + \beta^4)} \\ &+ \frac{\sqrt{2}(1+c_\theta) g_e \beta (2g_e f^{\gamma*} - C_{RGZ} f^{Z*})}{(1-\beta^2)^{3/2}} \end{aligned}$$

$$\begin{aligned}
\mathcal{M}_{+,-,-,+} &= -\frac{ig_Z^2 C_R^2 (1+\beta^2)(1-c_\theta)s_\theta}{1+2\beta^2(1-2c_\theta^2)+\beta^4} \\
\mathcal{M}_{+,-,-,0} &= \frac{ig_Z^2 C_R^2 \sqrt{1-\beta^2}(1+2c_\theta+\beta^2)(1-c_\theta)}{\sqrt{2}(1+2\beta^2(1-2c_\theta^2)+\beta^4)} - \frac{\sqrt{2}(1-c_\theta)g_e\beta(2g_e f^{\gamma\star} - C_{RgZ}f^{Z\star})}{(1-\beta^2)^{3/2}} \\
\mathcal{M}_{+,-,-,-} &= -\frac{ig_Z^2 C_R^2 (1-\beta^2)c_\theta s_\theta}{1+2\beta^2(1-2c_\theta^2)+\beta^4} \\
\mathcal{M}_{-,+,+,+} &= -\frac{ig_Z^2 C_L^2 (1-\beta^2)c_\theta s_\theta}{1+2\beta^2(1-2c_\theta^2)+\beta^4} \\
\mathcal{M}_{-,+,+,0} &= -\frac{ig_Z^2 C_L^2 \sqrt{1-\beta^2}(1+2c_\theta+\beta^2)(1-c_\theta)}{\sqrt{2}(1+2\beta^2(1-2c_\theta^2)+\beta^4)} + \frac{\sqrt{2}(1-c_\theta)g_e\beta(2g_e f^\gamma - C_{LgZ}f^Z)}{(1-\beta^2)^{3/2}} \\
\mathcal{M}_{-,+,+,-} &= \frac{ig_Z^2 C_L^2 (1+\beta^2)(1-c_\theta)s_\theta}{1+2\beta^2(1-2c_\theta^2)+\beta^4} \\
\mathcal{M}_{-,+,0,+} &= \frac{ig_Z^2 C_L^2 \sqrt{1-\beta^2}(1-2c_\theta+\beta^2)(1+c_\theta)}{\sqrt{2}(1+2\beta^2(1-2c_\theta^2)+\beta^4)} - \frac{\sqrt{2}(1+c_\theta)g_e\beta(2g_e f^\gamma - C_{LgZ}f^Z)}{(1-\beta^2)^{3/2}} \\
\mathcal{M}_{-,+,0,0} &= -\frac{2ig_Z^2 C_L^2 (1-\beta^2)c_\theta s_\theta}{1+2\beta^2(1-2c_\theta^2)+\beta^4} \\
\mathcal{M}_{-,+,0,-} &= -\frac{ig_Z^2 C_L^2 \sqrt{1-\beta^2}(1+2c_\theta+\beta^2)(1-c_\theta)}{\sqrt{2}(1+2\beta^2(1-2c_\theta^2)+\beta^4)} \\
&\quad - \frac{\sqrt{2}(1-c_\theta)g_e\beta(2g_e f^{\gamma\star} - C_{LgZ}f^{Z\star})}{(1-\beta^2)^{3/2}} \\
\mathcal{M}_{-,+,-,+} &= \frac{ig_Z^2 C_L^2 (1+\beta^2)(1+c_\theta)s_\theta}{1+2\beta^2(1-2c_\theta^2)+\beta^4} \\
\mathcal{M}_{-,+,-,0} &= \frac{ig_Z^2 C_L^2 \sqrt{1-\beta^2}(1-2c_\theta+\beta^2)(1+c_\theta)}{\sqrt{2}(1+2\beta^2(1-2c_\theta^2)+\beta^4)} + \frac{\sqrt{2}(1+c_\theta)g_e\beta(2g_e f^{\gamma\star} - C_{LgZ}f^{Z\star})}{(1-\beta^2)^{3/2}} \\
\mathcal{M}_{-,+,-,-} &= -\frac{ig_Z^2 C_L^2 (1-\beta^2)c_\theta s_\theta}{1+2\beta^2(1-2c_\theta^2)+\beta^4}
\end{aligned}$$

B.1.2 For the process $e^+e^- \rightarrow Z\gamma$

The four momentum of the particles in this process are

$$\begin{aligned}
p_1^\mu &= \frac{\sqrt{\hat{s}}}{2} \{1, 0, 0, 1\}, & p_2^\mu &= \frac{\sqrt{\hat{s}}}{2} \{1, 0, 0, -1\} \\
k_1^\mu &= \frac{\sqrt{\hat{s}}}{2} \{\beta, -\beta \sin\theta, 0, -\beta \cos\theta\}, & k_2^\mu &= \frac{\sqrt{\hat{s}}}{2} \{2-\beta, \beta \sin\theta, 0, \beta \cos\theta\}.
\end{aligned} \quad (\text{B.1.6})$$

The four momentum of γ satisfy $k_1^2 = 0$. The onn-shell condition of Z , $k_2^2 = m_Z^2$ provides β as

$$\beta = 1 - \frac{M_Z^2}{\hat{s}}. \quad (\text{B.1.7})$$

We define $h^\gamma = h_1^\gamma + ih_3^\gamma$ and $h^Z = h_1^Z + ih_3^Z$.

$$\begin{aligned} \mathcal{M}_{\lambda_{e^-}, \lambda_{e^+}, \lambda_Z, \lambda_\gamma} &= \mathcal{M}_{SM} + \mathcal{M}_{aTGC} \\ \mathcal{M}_{+, -, +, +} &= \frac{-ig_e g_Z C_R s_\theta (1-\beta)}{\beta(1-c_\theta)} - \frac{g_e (2g_e h^\gamma - C_R g_Z h^Z) s_\theta \beta}{4(1-\beta)} \\ \mathcal{M}_{+, -, +, -} &= \frac{ig_e g_Z C_R s_\theta}{\beta(1-c_\theta)} \\ \mathcal{M}_{+, -, 0, +} &= \frac{i\sqrt{2}g_e g_Z C_R \sqrt{1-\beta}}{\beta} + \frac{(1-c_\theta)g_e (2g_e h^\gamma - C_R g_Z h^Z) \beta}{4\sqrt{2}(1-\beta)^{3/2}} \\ \mathcal{M}_{+, -, 0, -} &= \frac{-i\sqrt{2}g_e g_Z C_R \sqrt{1-\beta}}{\beta} + \frac{(1+c_\theta)g_e (2g_e h^{\gamma*} - C_R g_Z h^{Z*}) \beta}{4\sqrt{2}(1-\beta)^{3/2}} \\ \mathcal{M}_{+, -, -, +} &= \frac{-ig_e g_Z C_R s_\theta}{\beta(1+c_\theta)} \\ \mathcal{M}_{+, -, -, -} &= \frac{ig_e g_Z (1-\beta) s_\theta}{\beta(1+c_\theta)} - \frac{g_e (2g_e h^{\gamma*} - C_R g_Z h^{Z*}) s_\theta \beta}{4(1-\beta)} \\ \mathcal{M}_{-, +, +, +} &= \frac{ig_e g_Z C_L s_\theta (1-\beta)}{\beta(1+c_\theta)} - \frac{g_e (2g_e h^\gamma - C_L g_Z h^Z) s_\theta \beta}{4(1-\beta)} \\ \mathcal{M}_{-, +, +, -} &= \frac{-ig_e g_Z C_L s_\theta}{\beta(1+c_\theta)} \\ \mathcal{M}_{-, +, 0, +} &= \frac{i\sqrt{2}g_e g_Z C_L \sqrt{1-\beta}}{\beta} - \frac{(1+c_\theta)g_e (2g_e h^\gamma - C_L g_Z h^Z) \beta}{4\sqrt{2}(1-\beta)^{3/2}} \\ \mathcal{M}_{-, +, 0, -} &= \frac{-i\sqrt{2}g_e g_Z C_L \sqrt{1-\beta}}{\beta} - \frac{(1-c_\theta)g_e (2g_e h^{\gamma*} - C_L g_Z h^{Z*}) \beta}{4\sqrt{2}(1-\beta)^{3/2}} \\ \mathcal{M}_{-, +, -, +} &= \frac{ig_e g_Z C_L s_\theta}{\beta(1-c_\theta)} \\ \mathcal{M}_{-, +, -, -} &= \frac{-ig_e g_Z C_L (1-\beta) s_\theta}{\beta(1-c_\theta)} - \frac{g_e (2g_e h^{\gamma*} - C_L g_Z h^{Z*}) s_\theta \beta}{4(1-\beta)} \end{aligned} \quad (\text{B.1.8})$$

B.2 Polarization observables

B.2.1 For the process $e^+e^- \rightarrow ZZ$

$$\sigma(e^+e^- \rightarrow ZZ) = \frac{1}{2} \frac{1}{32\pi\beta\hat{s}} \tilde{\sigma}_{ZZ} \quad (\text{B.2.1})$$

$$\begin{aligned}
\tilde{\sigma}_{ZZ} &= \frac{1}{2}g_Z^4(C_L^4 + C_R^4) \left(\frac{(5 - 2\beta^2 + \beta^4) \log\left(\frac{1+\beta}{1-\beta}\right)}{2(\beta + \beta^3)} - 1 \right) \\
&+ g_Z^3 g_e (C_L^3 - C_R^3) f_5^Z \frac{(3 - \beta^2)(2\beta + (1 + \beta^2) \log\left(\frac{1+\beta}{1-\beta}\right))}{2\beta(1 - \beta^2)} \\
&- g_Z^2 g_e^2 (C_L^2 - C_R^2) f_5^\gamma \frac{(3 - \beta^2)(2\beta - (1 + \beta^2) \log\left(\frac{1+\beta}{1-\beta}\right))}{\beta(1 - \beta^2)} \\
&+ 16g_Z^2 g_e^2 (C_L^2 + C_R^2) \frac{\beta^2 ((f_4^Z)^2 + (f_5^Z)^2 \beta^2)}{3(1 - \beta^2)^3} \\
&- 64g_Z g_e^3 (C_L + C_R) \frac{\beta^2 (f_4^\gamma f_4^Z + f_5^\gamma f_5^Z \beta^2)}{3(1 - \beta^2)^3} \\
&+ 128g_e^4 \frac{\beta^2 ((f_4^\gamma)^2 + (f_5^\gamma)^2 \beta^2)}{3(1 - \beta^2)^3} \tag{B.2.2}
\end{aligned}$$

$$\begin{aligned}
\tilde{\sigma}_{ZZ} \times P_x &= g_Z^4 (C_L^4 - C_R^4) \frac{\pi(1 - \beta^2)^{3/2}}{4(1 + \beta^2)} + g_Z^3 g_e (C_L^3 + C_R^3) \frac{f_5^Z \pi \beta^2 (1 + 2\beta^2)}{4(1 - \beta^2)^{3/2}} \\
&- g_Z^2 g_e^2 (C_L^2 + C_R^2) \frac{f_5^\gamma \pi \beta^2 (1 + 2\beta^2)}{2(1 - \beta^2)^{3/2}} \tag{B.2.3}
\end{aligned}$$

$$\begin{aligned}
\tilde{\sigma}_{ZZ} \times P_y &= -g_Z^3 g_e (C_L^3 + C_R^3) \frac{f_4^Z \pi \beta (2 + \beta^2)}{4(1 - \beta^2)^{3/2}} + g_Z^2 g_e^2 (C_L^2 + C_R^2) \frac{f_4^\gamma \pi \beta (2 + \beta^2)}{2(1 - \beta^2)^{3/2}} \tag{B.2.4}
\end{aligned}$$

$$\begin{aligned}
\tilde{\sigma}_{ZZ} \times T_{xy} &= g_Z^3 g_e (C_L^3 - C_R^3) \frac{\sqrt{3}}{8} f_4^Z f_{xy}(\beta) \\
&- g_Z^2 g_e^2 (C_L^2 - C_R^2) \frac{\sqrt{3}}{4} f_4^\gamma f_{xy}(\beta) + g_Z^2 g_e^2 (C_L^2 + C_R^2) \frac{4}{\sqrt{3}} \frac{f_4^Z f_5^Z \beta^3}{(1 - \beta^2)^3} \\
&+ g_Z g_e^3 (C_L + C_R) \frac{8}{\sqrt{3}} \frac{(f_4^Z f_5^\gamma + f_4^\gamma f_5^Z) \beta^3}{(1 - \beta^2)^3} + g_e^4 \frac{32 f_4^\gamma f_5^\gamma \beta^3}{\sqrt{3} (1 - \beta^2)^3}, \\
f_{xy}(\beta) &= \frac{\left(2(\beta + \beta^3) - (1 - \beta^2)^2 \log\left(\frac{1+\beta}{1-\beta}\right)\right)}{\beta^2 (1 - \beta^2)} \tag{B.2.5}
\end{aligned}$$

$$\tilde{\sigma}_{ZZ} \times (T_{xx} - T_{yy}) = g_Z^4 (C_L^4 + C_R^4) \sqrt{\frac{3}{2}} \frac{(1 - \beta^2)(2\beta - (1 + \beta^2) \log\left(\frac{1+\beta}{1-\beta}\right))}{8\beta^3}$$

$$\begin{aligned}
& - \left(g_Z^3 g_e (C_L^3 - C_R^3) f_5^Z + g_Z^2 g_e^2 (C_L^2 - C_R^2) 2f_5^\gamma \right) f_{x^2-y^2}(\beta) \\
& + g_Z^2 g_e^2 (C_L^2 + C_R^2) 2 \sqrt{\frac{2}{3}} \frac{\beta^2 \left((f_4^Z)^2 - (f_5^Z)^2 \beta^2 \right)}{(1-\beta^2)^3} \\
& - g_Z g_e^3 (C_L + C_R) 8 \sqrt{\frac{2}{3}} \frac{\beta^2 \left(f_4^\gamma f_4^Z - f_5^\gamma f_5^Z \beta^2 \right)}{(1-\beta^2)^3} \\
& + g_e^4 16 \sqrt{\frac{2}{3}} \frac{\beta^2 \left((f_4^\gamma)^2 - (f_5^\gamma)^2 \beta^2 \right)}{(1-\beta^2)^3}, \\
f_{x^2-y^2}(\beta) & = \sqrt{\frac{3}{2}} \frac{\left(2(\beta + \beta^3) - (1-\beta^2)^2 \log\left(\frac{1+\beta}{1-\beta}\right) \right)}{4\beta(1-\beta^2)} \tag{B.2.6}
\end{aligned}$$

$$\begin{aligned}
\tilde{\sigma}_{ZZ} \times T_{ZZ} & = g_Z^4 (C_L^4 + C_R^4) \frac{f_{zz}(\beta)}{8\sqrt{6}\beta^3(1+\beta^2)} + g_Z^3 g_e (C_L^3 - C_R^3) f_5^Z \frac{f_{zz}(\beta)}{4\sqrt{6}\beta(1-\beta^2)} \\
& - g_Z^2 g_e^2 (C_L^2 - C_R^2) \frac{f_{zz}(\beta) f_5^\gamma}{2\sqrt{6}\beta(1-\beta^2)} \\
& - g_Z^2 g_e^2 (C_L^2 + C_R^2) \frac{4}{3} \sqrt{\frac{2}{3}} \frac{\beta^2 \left((f_4^Z)^2 + (f_5^Z)^2 \beta^2 \right)}{(1-\beta^2)^3} \\
& + g_Z g_e^3 (C_L + C_R) \frac{16}{3} \sqrt{\frac{2}{3}} \frac{\beta^2 \left(f_4^\gamma f_4^Z + f_5^\gamma f_5^Z \beta^2 \right)}{(1-\beta^2)^3} \\
& - g_e^4 \frac{32}{3} \sqrt{\frac{2}{3}} \frac{\beta^2 \left((f_4^\gamma)^2 + (f_5^\gamma)^2 \beta^2 \right)}{(1-\beta^2)^3}, \\
f_{zz}(\beta) & = \left((3 + \beta^2 + 5\beta^4 - \beta^6) \log\left(\frac{1+\beta}{1-\beta}\right) - 2\beta(3-\beta^2)(1+\beta^2) \right) \tag{B.2.7}
\end{aligned}$$

B.2.2 For the process $e^+e^- \rightarrow Z\gamma$

$$\sigma(e^+e^- \rightarrow Z\gamma) = \frac{1}{32\pi\beta\hat{s}} \tilde{\sigma}_{Z\gamma}, \quad c_\theta \in [-c_{\theta_0}, c_{\theta_0}] \tag{B.2.8}$$

$$\begin{aligned}
\tilde{\sigma}_{Z\gamma} & = -g_e^2 g_Z^2 (C_L^2 + C_R^2) \frac{1}{\beta^2} \left(c_{\theta_0} \beta^2 - 2(2 - 2\beta + \beta^2) \tanh^{-1}(c_{\theta_0}) \right) \\
& + g_e^2 g_Z^2 (C_L^2 - C_R^2) \frac{c_{\theta_0} h_3^Z (2-\beta)}{2(1-\beta)} - g_e^3 g_Z (C_L - C_R) \frac{c_{\theta_0} h_3^\gamma (2-\beta)}{(1-\beta)} \\
& + g_e^2 g_Z^2 (C_L^2 + C_R^2) c_{\theta_0} \left((h_1^Z)^2 + (h_3^Z)^2 \right) h_\sigma(\beta) \\
& - g_e^3 g_Z (C_L + C_R) c_{\theta_0} \left(h_1^\gamma h_1^Z + h_3^\gamma h_3^Z \right) 4h_\sigma(\beta) \\
& + g_e^4 c_{\theta_0} \left((h_1^\gamma)^2 + (h_3^\gamma)^2 \right) 8h_\sigma(\beta), \\
h_\sigma(\beta) & = \frac{\beta^2 (9 - 6\beta - c_{\theta_0}^2 (1 - 2\beta))}{96(1-\beta)^3} \tag{B.2.9}
\end{aligned}$$

$$\begin{aligned}
\tilde{\sigma}_{Z\gamma} \times P_x &= g_e^2 g_Z^2 (C_L^2 - C_R^2) 2 \frac{\sqrt{1-\beta}}{\beta^2} (2-\beta) \sinh^{-1}(c_{\theta_0}) \\
&+ g_e^2 g_Z^2 (C_L^2 + C_R^2) h_3^Z h_x^1(\beta) - g_e^3 g_Z (C_L + C_R) h_3^\gamma 2 h_x^1(\beta) \\
&+ g_e^2 g_Z^2 (C_L^2 - C_R^2) \left((h_1^Z)^2 + (h_3^Z)^2 \right) h_x^2(\beta) - g_e^3 g_Z (C_L - C_R) \left(h_1^\gamma h_1^Z + h_3^\gamma h_3^Z \right) 4 h_x^2(\beta), \\
h_x^1(\beta) &= \frac{(c_{\theta_0} s_{\theta_0} (2-3\beta) - 3(2-\beta) \sinh^{-1}(c_{\theta_0}))}{8(1-\beta)^{3/2}}, \\
h_x^2(\beta) &= \frac{\beta^2 (c_{\theta_0} s_{\theta_0} + \sinh^{-1}(c_{\theta_0}))}{32(1-\beta)^{5/2}}
\end{aligned} \tag{B.2.10}$$

$$\begin{aligned}
\tilde{\sigma}_{Z\gamma} \times P_y &= g_e^2 g_Z^2 (C_L^2 + C_R^2) \frac{h_1^Z (c_{\theta_0} s_{\theta_0} \beta - (4-\beta) \sin^{-1}(c_{\theta_0}))}{8(1-\beta)^{3/2}} \\
&- g_e^3 g_Z (C_L + C_R) \frac{h_1^\gamma (c_{\theta_0} s_{\theta_0} \beta - (4-\beta) \sin^{-1}(c_{\theta_0}))}{4(1-\beta)^{3/2}}
\end{aligned} \tag{B.2.11}$$

$$\tilde{\sigma}_{Z\gamma} \times T_{xy} = g_e^3 g_Z (C_L - C_R) \frac{\sqrt{3}}{2} \frac{h_1^\gamma c_{\theta_0}}{2(1-\beta)} - g_e^2 g_Z^2 (C_L^2 - C_R^2) \frac{\sqrt{3}}{4} \frac{h_1^Z c_{\theta_0}}{4(1-\beta)} \tag{B.2.12}$$

$$\tilde{\sigma}_{Z\gamma} \times (T_{xx} - T_{yy}) = g_e^2 g_Z^2 (C_L^2 + C_R^2) \frac{\sqrt{6} c_{\theta_0} (1-\beta)}{\beta^2} - g_e^3 g_Z (C_L - C_R) \sqrt{\frac{3}{2}} \frac{h_3^\gamma c_{\theta_0}}{(1-\beta)} \tag{B.2.13}$$

$$\begin{aligned}
\tilde{\sigma}_{Z\gamma} \times T_{zz} &= -g_e^2 g_Z^2 (C_L^2 + C_R^2) \frac{1}{\sqrt{6} \beta^2} \left(c_{\theta_0} (6 - 6\beta + \beta^2) - 2(2 - 2\beta + \beta^2) \tanh^{-1}(c_{\theta_0}) \right) \\
&- g_e^2 g_Z^2 (C_L^2 - C_R^2) \frac{c_{\theta_0} h_3^Z (1+\beta)}{2 \sqrt{6} (1-\beta)} + g_e^3 g_Z (C_L - C_R) \frac{c_{\theta_0} h_3^\gamma (1+\beta)}{\sqrt{6} (1-\beta)} \\
&- g_e^2 g_Z^2 (C_L^2 + C_R^2) c_{\theta_0} \left((h_1^Z)^2 + (h_3^Z)^2 \right) h_{zz}(\beta) \\
&+ g_e^3 g_Z (C_L + C_R) c_{\theta_0} \left(h_1^\gamma h_1^Z + h_3^\gamma h_3^Z \right) 4 h_{zz}(\beta) - g_e^4 c_{\theta_0} \left((h_1^\gamma)^2 + (h_3^\gamma)^2 \right) 8 h_{zz}(\beta), \\
h_{zz}(\beta) &= \frac{(c_{\theta_0}^2 (2-\beta) + 3\beta) \beta^2}{48 \sqrt{6} (1-\beta)^3}
\end{aligned} \tag{B.2.14}$$

C Polarization observables of Z boson in ZZ production at the LHC

The production density matrix at the LHC will be

$$\rho(\lambda, \lambda') = \int dx_1 f_1(x_1, Q^2) \int dx_2 f_2(x_2, Q^2) \hat{\rho}(\lambda, \lambda'), \quad (\text{C.0.1})$$

where $\hat{\rho}$ is the parton level density matrix, $f_1(x_1, Q^2)$ and $f_2(x_2, Q^2)$ are the parton distribution functions for two parton from the two colliding protons with energy fraction x_1 and x_2 , respectively. The Q is the scale factor assumed. The observables are calculated using the distribution of the decay products of the Z boson, not from the production density matrix. Events were generated in `MADGRAPH5_aMC@NLO` for a set of couplings values, functional form of the observables were obtained by numerical fitting the data. The observables are listed below.

C.1 Expressions of observables

$$\begin{aligned} \sigma(M_{4l} > 0.3 \text{ TeV}) &= 7.9503 + f_5^\gamma \times 16.886 + f_5^Z \times 4.0609 + f_4^\gamma f_4^Z \times 58561 \\ &+ f_5^\gamma f_5^Z \times 54131 + (f_4^\gamma)^2 \times 58771 + (f_4^Z)^2 \times 81647 \\ &+ (f_5^\gamma)^2 \times 55210 + (f_5^Z)^2 \times 78325 \quad \text{fb} \end{aligned} \quad (\text{C.1.1})$$

$$\begin{aligned} \sigma(M_{4l} > 0.7 \text{ TeV}) &= 0.37616 + f_5^\gamma \times 3.8161 + f_5^Z \times 2.9704 + f_4^\gamma f_4^Z \times 55005 \\ &+ f_5^\gamma f_5^Z \times 52706 + (f_4^\gamma)^2 \times 57982 + (f_4^Z)^2 \times 80035 \\ &+ (f_5^\gamma)^2 \times 57131 + (f_5^Z)^2 \times 78515 \quad \text{fb} \end{aligned} \quad (\text{C.1.2})$$

$$\begin{aligned}
\sigma(M_{4l} > 1 \text{ TeV}) &= 0.096685 + f_5^\gamma \times 1.9492 + f_5^Z \times 1.7106 + f_4^\gamma f_4^Z \times 51788 \\
&+ f_5^\gamma f_5^Z \times 51204 + (f_4^\gamma)^2 \times 54933 + (f_4^Z)^2 \times 75432 \\
&+ (f_5^\gamma)^2 \times 54507 + (f_5^Z)^2 \times 74466 \quad \text{fb}
\end{aligned} \tag{C.1.3}$$

$$\begin{aligned}
A_{xz}^{\text{num.}}(M_{4l} > 0.3 \text{ TeV}) &= -0.77152 + f_5^\gamma \times 6.1912 + f_5^Z \times 7.8270 + f_4^\gamma f_4^Z \times 2869.5 \\
&+ f_5^\gamma f_5^Z \times 396.94 + (f_4^\gamma)^2 \times 1029.7 + (f_4^Z)^2 \times 2298.7 \\
&- (f_5^\gamma)^2 \times 274.02 - (f_5^Z)^2 \times 1495.5 \quad \text{fb}
\end{aligned} \tag{C.1.4}$$

$$\begin{aligned}
A_{x^2-y^2}^{\text{num.}}(M_{4l} > 0.3 \text{ TeV}) &= -0.94583 + f_5^\gamma \times 2.4091 - f_5^Z \times 0.17878 + f_4^\gamma f_4^Z \times 2700.4 \\
&- f_5^\gamma f_5^Z \times 5491.1 + (f_4^\gamma)^2 \times 4298.7 + (f_4^Z)^2 \times 5835.1 \\
&- (f_5^\gamma)^2 \times 6576.7 - (f_5^Z)^2 \times 8467.8 \quad \text{fb}
\end{aligned} \tag{C.1.5}$$

$$\begin{aligned}
A_{x^2-y^2}^{\text{num.}}(M_{4l} > 0.7 \text{ TeV}) &= -0.04295 + f_5^\gamma \times 1.5563 + f_5^Z \times 0.37094 + f_4^\gamma f_4^Z \times 3299.8 \\
&- f_5^\gamma f_5^Z \times 5853.9 + (f_4^\gamma)^2 \times 4241.8 + (f_4^Z)^2 \times 5679.3 \\
&- (f_5^\gamma)^2 \times 6520.1 - (f_5^Z)^2 \times 8559.3 \quad \text{fb}
\end{aligned} \tag{C.1.6}$$

$$\begin{aligned}
A_{zz}^{\text{num.}}(M_{4l} > 0.7 \text{ TeV}) &= 0.048175 - f_5^\gamma \times 0.12125 - f_5^Z \times 1.5339 - f_4^\gamma f_4^Z \times 6449.2 \\
&- f_5^\gamma f_5^Z \times 5860.4 - (f_4^\gamma)^2 \times 6344.7 - (f_4^Z)^2 \times 8907.4 \\
&- (f_5^\gamma)^2 \times 6457.7 - (f_5^Z)^2 \times 8346.8 \quad \text{fb}
\end{aligned} \tag{C.1.7}$$

The asymmetries will be given as,

$$\begin{aligned}
\widetilde{A}_{xz} &= \frac{A_{xz}^{\text{num.}}(M_{4l} > 0.3 \text{ TeV})}{\sigma(M_{4l} > 0.3 \text{ TeV})} \\
A_{x^2-y^2} &= \frac{A_{x^2-y^2}^{\text{num.}}(M_{4l} > 0.7 \text{ TeV})}{\sigma(M_{4l} > 0.7 \text{ TeV})} \\
A_{zz} &= \frac{A_{zz}^{\text{num.}}(M_{4l} > 0.7 \text{ TeV})}{\sigma(M_{4l} > 0.7 \text{ TeV})}
\end{aligned} \tag{C.1.8}$$

C.2 Note on linear approximation

We note that, the linear approximation of considering anomalous couplings will be valid if the quadratic contribution on the cross section will be much smaller than the linear contribution, i.e.,

$$|f_i \times \sigma_i| \gg |f_i^2 \times \sigma_{ii}|, \quad \text{or} \quad |f_i| \ll \frac{\sigma_i}{\sigma_{ii}}, \quad (\text{C.2.1})$$

where σ_i and σ_{ii} are the linear and quadratic coefficient of the coupling f_i in the cross section. Based on $\sigma(M_{4l} > 1 \text{ TeV})$ in Eq. (C.1.3) the linear approximation constrain f_5^V as

$$|f_5^Z| \ll 2.2 \times 10^{-5}, \quad |f_5^Y| \ll 3.5 \times 10^{-5}, \quad (\text{C.2.2})$$

which are much much smaller than the limit (see Eq. (5.0.2)) observed at the LHC [146]. To this end we keep terms upto quadratic in couplings in our analysis.

D The helicity amplitudes in $e^+e^- \rightarrow W^+W^-$ in SM+aTGC

We compute the processes

$$e^-(k_1, \lambda_{e^-}) + e^+(k_2, \lambda_{e^+}) \rightarrow W_\alpha^-(q, \lambda_{W^-}) + W_\beta^+(\bar{q}, \lambda_{W^+}). \quad (\text{D.0.1})$$

The helicity amplitudes for this process in SM in the t-channel (\mathcal{M}_T), SM+aTGC in Z-mediated s-channel (\mathcal{M}_{sZ}) and γ -mediated s-channel ($\mathcal{M}_{s\gamma}$) are given by,

$$i\mathcal{M}_T(\lambda_{e^-}, \lambda_{e^+}, \lambda_{W^-}, \lambda_{W^+}) = i\bar{v}(k_2, \lambda_{e^+}) \left(\frac{-ig_W}{2\sqrt{2}} \gamma^\beta (1 - \gamma_5) \right) \left(\frac{i}{(k_1 - \not{q})} \right) \left(\frac{-ig_W}{2\sqrt{2}} \gamma^\alpha (1 - \gamma_5) \right) u(k_1, \lambda_{e^-}) \epsilon_\beta^*(\bar{q}, \lambda_{W^+}) \epsilon_\alpha(q, \lambda_{W^-}), \quad (\text{D.0.2})$$

$$i\mathcal{M}_{sZ}(\lambda_{e^-}, \lambda_{e^+}, \lambda_{W^-}, \lambda_{W^+}) = i\bar{v}(k_2, \lambda_{e^+}) \left(\frac{-ig_Z}{2} \gamma^\rho (v_e - a_e \gamma_5) \right) u(k_1, \lambda_{e^-}) \left(\frac{-i \left(g_{\rho\mu} - \frac{P_\rho P_\mu}{m_Z^2} \right)}{P^2 - m_Z^2} \right) \left(ig_{WWZ} \Gamma_{Z^*}^{\mu\alpha\beta}(P, q, \bar{q}) \right) \epsilon_\beta^*(\bar{q}, \lambda_{W^+}) \epsilon_\alpha(q, \lambda_{W^-}), \quad (\text{D.0.3})$$

$$i\mathcal{M}_{s\gamma}(\lambda_{e^-}, \lambda_{e^+}, \lambda_{W^-}, \lambda_{W^+}) = i\bar{v}(k_2, \lambda_{e^+}) \left(ig_e \gamma^\rho \right) u(k_1, \lambda_{e^-}) \left(\frac{-ig_{\rho\mu}}{P^2} \right) \left(ig_{WW\gamma} \Gamma_{\gamma^*}^{\mu\alpha\beta}(P, q, \bar{q}) \right) \epsilon_\beta^*(\bar{q}, \lambda_{W^+}) \epsilon_\alpha(q, \lambda_{W^-}). \quad (\text{D.0.4})$$

The total helicity matrix element is thus

$$\begin{aligned} \mathcal{M}_{\text{tot}}(\lambda_{e^-}, \lambda_{e^+}, \lambda_{W^-}, \lambda_{W^+}) &= \mathcal{M}_T(\lambda_{e^-}, \lambda_{e^+}, \lambda_{W^-}, \lambda_{W^+}) + \mathcal{M}_{sZ}(\lambda_{e^-}, \lambda_{e^+}, \lambda_{W^-}, \lambda_{W^+}) \\ &+ \mathcal{M}_{s\gamma}(\lambda_{e^-}, \lambda_{e^+}, \lambda_{W^-}, \lambda_{W^+}) \end{aligned} \quad (\text{D.0.5})$$

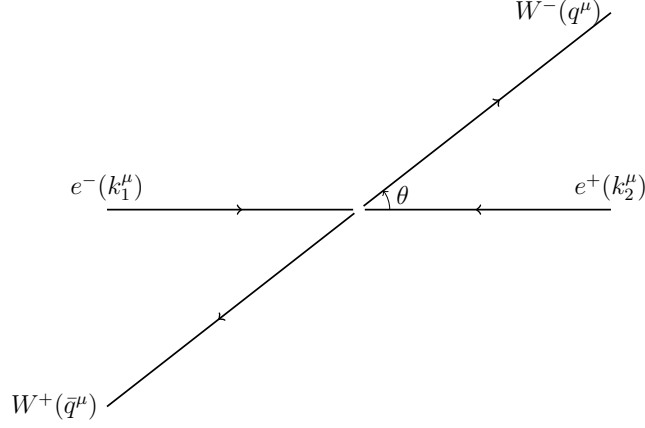


Figure D.1. Schematic diagram for $e^-e^+ \rightarrow W^-W^+$ kinematics.

The WWV vertex factor $\left(ig_{WW\gamma}I_{\gamma^*}^{\mu\alpha\beta}(P, q, \bar{q})\right)$ contains both SM and aTGC contribution and they are given in Eq. (6.2.1) with the relation in Eq. (6.2.2) to the Lagrangian in Eq. (6.0.2). Here, the coupling constants are

$$g_W = \frac{g_e}{s_w}, \quad g_Z = \frac{g_w}{c_w}, \quad c_w = \cos\theta_W = \frac{m_W}{m_Z}, \quad s_w = \sqrt{1 - c_w^2},$$

$$g_{WW\gamma} = -g_e, \quad g_{WWZ} = -g_e \frac{c_w}{s_w}, \quad g_e = e = \sqrt{4\pi\alpha_{EM}}. \quad (\text{D.0.6})$$

The four-momentum of the particles in this process are (see Fig. D.1)

$$k_1^\mu = \frac{\sqrt{\hat{s}}}{2} \{1, 0, 0, 1\}, \quad k_2^\mu = \frac{\sqrt{\hat{s}}}{2} \{1, 0, 0, -1\}$$

$$q^\mu = \frac{\sqrt{\hat{s}}}{2} \{1, -\beta \sin\theta, 0, -\beta \cos\theta\}, \quad \bar{q}^\mu = \frac{\sqrt{\hat{s}}}{2} \{1, \beta \sin\theta, 0, \beta \cos\theta\}, \quad (\text{D.0.7})$$

$\sqrt{\hat{s}}$ being the centre-of-mass energy of the colliding beams. The on-shell condition of W^\pm , $q^2 = \bar{q}^2 = m_W^2$ gives β as

$$\beta = \sqrt{1 - \frac{4m_W^2}{\hat{s}}}. \quad (\text{D.0.8})$$

The polarization vector for the W 's are similar as in Eq. (3.1.12) and they are

$$\epsilon^\mu(q, \pm) = \frac{1}{\sqrt{2}} \{0, \mp \cos\theta, -i, \pm \cos\theta\},$$

$$\epsilon^\mu(q, 0) = \frac{1}{m_W} \{|\vec{q}|, q_0 \sin\theta, 0, q_0 \cos\theta\}. \quad (\text{D.0.9})$$

The density matrix is calculated in the similar way as in given Eq. (3.1.15) with the symmetry

factor $S = 1$ and replacing Z and V with W^- and W^+ respectively.

The non-zero helicity amplitudes in SM including aTGC for this process are given below with the following notations,

$$c_\theta = \cos\theta, \quad s_\theta = \sin\theta.$$

$$\begin{aligned} \mathcal{M}_T(\lambda_{e^-}, \lambda_{e^+}, \lambda_{W^+}, \lambda_{W^-}) &= \mathcal{M}_{SM} + \mathcal{M}_{aTGC} \\ \mathcal{M}_{-,+,-,-} &= \frac{(1+c_\theta)g_W^2 s_\theta}{1-2c_\theta\beta+\beta^2} \\ &= \frac{(1+c_\theta) \left(2g_{WW\gamma}g_e\beta - \frac{\hat{s}g_Z g_{WWZ}(a_f+v_f)\beta}{\hat{s}-m_Z^2} - \frac{g_W^2(1-2c_\theta+2\beta-\beta^2)}{1-2c_\theta\beta+\beta^2} \right)}{\sqrt{2-2\beta^2}} \\ &+ \frac{1}{\sqrt{2}(1-\beta^2)^{3/2}}(1+c_\theta) \left(g_{WW\gamma}g_e \left(if_6^\gamma(1-\beta^2) - \beta(f_3^\gamma - f_3^\gamma\beta^2 - if_4^\gamma(1-\beta^2) - \beta(2if_7^\gamma + f_5^\gamma(1-\beta^2))) \right) - \frac{\frac{1}{2}\hat{s}g_Z g_{WWZ}(a_f+v_f)}{\hat{s}-m_Z^2} \right. \\ &\left. \left(if_6^Z(1-\beta^2) - \beta(f_3^Z - f_3^Z\beta^2 + if_4^Z(1-\beta^2) + \beta(2if_7^Z + f_5^Z(1-\beta^2))) \right) \right) \\ \mathcal{M}_{-,+,-,+} &= -s_\theta \left(g_{WW\gamma}g_e\beta - \frac{\frac{1}{2}\hat{s}g_Z g_{WWZ}(a_f+v_f)\beta}{\hat{s}-m_Z^2} + \frac{g_W^2(c_\theta-\beta)}{1-2c_\theta\beta+\beta^2} \right) \\ &+ s_\theta \left(g_{WW\gamma}g_e(f_1^\gamma\beta - if_6^\gamma) - \frac{\frac{1}{2}\hat{s}g_Z g_{WWZ}(a_f+v_f)(f_1^Z\beta - if_6^Z)}{\hat{s}-m_Z^2} \right) \\ &+ \frac{(1+c_\theta) \left(2g_{WW\gamma}g_e\beta - \frac{\hat{s}g_Z g_{WWZ}(a_f+v_f)\beta}{\hat{s}-m_Z^2} - \frac{g_W^2(1-2c_\theta+2\beta-\beta^2)}{1-2c_\theta\beta+\beta^2} \right)}{\sqrt{2-2\beta^2}} \\ \mathcal{M}_{-,+,0,-} &= \frac{(1+c_\theta)}{\sqrt{2}(1-\beta^2)^{3/2}} \left(g_{WW\gamma}g_e \left(if_6^\gamma(1-\beta^2) + \beta(f_3^\gamma - f_3^\gamma\beta^2 + if_4^\gamma(1-\beta^2) + \beta(2if_7^\gamma + f_5^\gamma(-1+\beta^2))) \right) - \frac{\frac{1}{2}\hat{s}g_Z g_{WWZ}(a_f+v_f)}{\hat{s}-m_Z^2} \right. \\ &\left. \left(if_6^Z(1-\beta^2) + \beta(f_3^Z - f_3^Z\beta^2 + if_4^Z(1-\beta^2) + \beta(2if_7^Z - f_5^Z(1-\beta^2))) \right) \right) \\ &+ \frac{s_\theta \left(g_{WW\gamma}g_e\beta(3-\beta^2) - \frac{\frac{1}{2}\hat{s}g_Z g_{WWZ}(a_f+v_f)\beta(3-\beta^2)}{\hat{s}-m_Z^2} + \frac{g_W^2(2c_\theta-3\beta+\beta^3)}{1-2c_\theta\beta+\beta^2} \right)}{(1-\beta^2)} \end{aligned}$$

$$\begin{aligned}
& + \frac{s_\theta}{(1-\beta^2)^2} \left(g_{WW\gamma} g_e \beta \left(f_1^\gamma - 2f_3^\gamma - 4f_2^\gamma \beta^2 + 2f_3^\gamma \beta^2 - f_1^\gamma \beta^4 \right) \right. \\
& \left. + \frac{\frac{1}{2} \hat{s} g_Z g_{WWZ} (a_f + v_f) \beta \left(2 \left(f_3^Z + 2f_2^Z \beta^2 - f_3^Z \beta^2 \right) - f_1^Z (1 - \beta^4) \right)}{\hat{s} - m_Z^2} \right) \\
\mathcal{M}_{-,+,0,+} & = \frac{(1-c_\theta)}{\left(\hat{s} - m_Z^2 \right) \sqrt{2-2\beta^2} \left(1 - 2c_\theta \beta + \beta^2 \right)} \left(m_Z^2 \left(g_W^2 \left(1 + 2c_\theta - 2\beta - \beta^2 \right) \right. \right. \\
& + 2g_{WW\gamma} g_e \beta \left(1 - 2c_\theta \beta + \beta^2 \right) \left. \right) - \hat{s} \left(g_W^2 \left(1 + 2c_\theta - 2\beta - \beta^2 \right) \right. \\
& + \left. \left. \left(2g_{WW\gamma} g_e - g_Z g_{WWZ} (a_f + v_f) \right) \beta \left(1 - 2c_\theta \beta + \beta^2 \right) \right) \right) \\
& + \frac{(1-c_\theta)}{\sqrt{2} \left(1 - \beta^2 \right)^{3/2}} \left(-g_{WW\gamma} g_e \left(-if_6^\gamma \left(-1 + \beta^2 \right) + \beta \left(f_3^\gamma \left(-1 + \beta^2 \right) \right) \right. \right. \\
& + \left. \left. if_4^\gamma \left(-1 + \beta^2 \right) + \beta \left(2if_7^\gamma + f_5^\gamma \left(-1 + \beta^2 \right) \right) \right) \right) + \frac{\frac{1}{2} \hat{s} g_Z g_{WWZ} (a_f + v_f)}{\hat{s} - m_Z^2} \\
& \left(-if_6^Z \left(-1 + \beta^2 \right) + \beta \left(f_3^Z \left(-1 + \beta^2 \right) + if_4^Z \left(-1 + \beta^2 \right) \right) \right. \\
& + \left. \left. \beta \left(2if_7^Z + f_5^Z \left(-1 + \beta^2 \right) \right) \right) \right) \\
\mathcal{M}_{-,+,+,-} & = s_\theta \left(-g_{WW\gamma} g_e \beta + \frac{\frac{1}{2} \hat{s} g_Z g_{WWZ} (a_f + v_f) \beta}{\hat{s} - m_Z^2} - \frac{g_W^2 (c_\theta - \beta)}{1 - 2c_\theta \beta + \beta^2} \right) \\
& + s_\theta \left(g_{WW\gamma} g_e \left(if_6^\gamma + f_1^\gamma \beta \right) - \frac{\frac{1}{2} \hat{s} g_Z g_{WWZ} (a_f + v_f) \left(if_6^Z + f_1^Z \beta \right)}{\hat{s} - m_Z^2} \right) \\
\mathcal{M}_{-,+,+0} & = \frac{(1-c_\theta) \left(2g_{WW\gamma} g_e \beta - \frac{\hat{s} g_Z g_{WWZ} (a_f + v_f) \beta}{\hat{s} - m_Z^2} + \frac{g_W^2 (1 + 2c_\theta - 2\beta - \beta^2)}{1 - 2c_\theta \beta + \beta^2} \right)}{\sqrt{2-2\beta^2}} \\
& + \frac{(1-c_\theta)}{\sqrt{2} \left(1 - \beta^2 \right)^{3/2}} \left(-g_{WW\gamma} g_e \left(-if_6^\gamma \left(-1 + \beta^2 \right) + \beta \left(f_3^\gamma - f_3^\gamma \beta^2 \right) \right. \right. \\
& + \left. \left. if_4^\gamma \left(-1 + \beta^2 \right) + \beta \left(f_5^\gamma + 2if_7^\gamma - f_5^\gamma \beta^2 \right) \right) \right) + \frac{\frac{1}{2} \hat{s} g_Z g_{WWZ} (a_f + v_f)}{\hat{s} - m_Z^2} \\
& \left(-if_6^Z \left(-1 + \beta^2 \right) + \beta \left(f_3^Z - f_3^Z \beta^2 + if_4^Z \left(-1 + \beta^2 \right) \right) \right. \\
& + \left. \left. \beta \left(f_5^Z + 2if_7^Z - f_5^Z \beta^2 \right) \right) \right) \\
\mathcal{M}_{-,+,+,+} & = -\frac{(1-c_\theta) g_W^2 s_\theta}{1 - 2c_\theta \beta + \beta^2} \\
\mathcal{M}_{+,-,-,0} & = -\frac{(1-c_\theta) \beta \sqrt{2-2\beta^2}}{\left(\hat{s} - m_Z^2 \right) \left(1 - \beta^2 \right)} \left(-g_{WW\gamma} g_e m_Z^2 + \frac{1}{2} \hat{s} \left(2g_{WW\gamma} g_e \right. \right. \\
& + \left. \left. g_Z g_{WWZ} (a_f - v_f) \right) \right)
\end{aligned}$$

$$\begin{aligned}
& + \frac{(1-c\theta)}{\sqrt{2}(1-\beta^2)^{3/2}} \left(-g_{WW\gamma}g_e \left(-if_6^\gamma(-1+\beta^2) + \beta(f_3^\gamma(-1+\beta^2) \right. \right. \\
& - if_4^\gamma(-1+\beta^2) + \beta(f_5^\gamma + 2i\widetilde{f}_7^\gamma - f_5^\gamma\beta^2) \left. \left. \right) \right) + \frac{\frac{1}{2}\hat{s}gz g_{WWZ}(a_f - v_f)}{\hat{s} - m_Z^2} \\
& \left(if_6^Z(-1+\beta^2) + \beta(f_3^Z - f_3^Z\beta^2 + if_4^Z(-1+\beta^2) \right. \\
& + \beta(-2i\widetilde{f}_7^Z + f_5^Z(-1+\beta^2)) \left. \left. \right) \right) \\
\mathcal{M}_{+,-,-,+} & = s_\theta \left(-g_{WW\gamma}g_e + \frac{\frac{1}{2}\hat{s}gz g_{WWZ}(v_f - a_f)}{\hat{s} - m_Z^2} \right) \beta \\
& + g_{WW\gamma}g_e s_\theta (-if_6^\gamma + f_1^\gamma\beta) + \frac{\frac{1}{2}\hat{s}gz g_{WWZ}s_\theta(a_f - v_f)(-if_6^Z + f_1^Z\beta)}{\hat{s} - m_Z^2} \\
\mathcal{M}_{+,-,0,-} & = \frac{\sqrt{2}(1-c\theta) \left(-g_{WW\gamma}g_e m_Z^2 + \frac{1}{2}\hat{s}(2g_{WW\gamma}g_e + gzg_{WWZ}(a_f - v_f)) \right) \beta}{(\hat{s} - m_Z^2) \sqrt{1-\beta^2}} \\
& + \frac{(1-c\theta)}{\sqrt{2}(1-\beta^2)^{3/2}} \left(-g_{WW\gamma}g_e \left(-if_6^\gamma(-1+\beta^2) + \beta(f_3^\gamma - f_3^\gamma\beta^2 \right. \right. \\
& - if_4^\gamma(-1+\beta^2) + \beta(2i\widetilde{f}_7^\gamma + f_5^\gamma(-1+\beta^2)) \left. \left. \right) \right) + \frac{\frac{1}{2}\hat{s}gz g_{WWZ}(a_f - v_f)}{\hat{s} - m_Z^2} \\
& \left(if_6^Z(-1+\beta^2) - \beta(f_3^Z - f_3^Z\beta^2 - if_4^Z(-1+\beta^2) \right. \\
& + \beta(2i\widetilde{f}_7^Z + f_5^Z(-1+\beta^2)) \left. \left. \right) \right) \\
\mathcal{M}_{+,-,0,0} & = \frac{s_\theta \left(-g_{WW\gamma}g_e m_Z^2 + \frac{1}{2}\hat{s}(2g_{WW\gamma}g_e + gzg_{WWZ}(a_f - v_f)) \right) \beta (3 - \beta^2)}{(\hat{s} - m_Z^2) (1 - \beta^2)} \\
& + \frac{s_\theta \beta}{(1 - \beta^2)^2} \left(g_{WW\gamma}g_e (f_1^\gamma - 2f_3^\gamma - 4f_2^\gamma\beta^2 + 2f_3^\gamma\beta^2 - f_1^\gamma\beta^4) \right. \\
& \left. + \frac{\frac{1}{2}\hat{s}gz g_{WWZ}(a_f - v_f) (f_1^Z - 2f_3^Z - 4f_2^Z\beta^2 + 2f_3^Z\beta^2 - f_1^Z\beta^4)}{\hat{s} - m_Z^2} \right) \\
\mathcal{M}_{+,-,0,+} & = \frac{\sqrt{2}(1+c\theta) \left(-g_{WW\gamma}g_e m_Z^2 + \frac{1}{2}\hat{s}(2g_{WW\gamma}g_e + gzg_{WWZ}(a_f - v_f)) \right) \beta}{(\hat{s} - m_Z^2) \sqrt{1-\beta^2}} \\
& + \frac{(1+c\theta)}{\sqrt{2}(1-\beta^2)^{3/2}} \left(-g_{WW\gamma}g_e \left(if_6^\gamma(-1+\beta^2) + \beta(f_3^\gamma - f_3^\gamma\beta^2 \right. \right. \\
& - if_4^\gamma(-1+\beta^2) + \beta(f_5^\gamma - 2i\widetilde{f}_7^\gamma - f_5^\gamma\beta^2) \left. \left. \right) \right) + \frac{\frac{1}{2}\hat{s}gz g_{WWZ}(a_f - v_f)}{\hat{s} - m_Z^2} \\
& \left(-if_6^Z(-1+\beta^2) + \beta(f_3^Z(-1+\beta^2) + if_4^Z(-1+\beta^2) \right.
\end{aligned}$$

$$\begin{aligned}
& + \beta \left(2i\widetilde{f}_7^Z + f_5^Z(-1 + \beta^2) \right) \Big) \Big) \\
\mathcal{M}_{+,-,+,-} & = s_\theta \left(-g_{WW\gamma}g_e + \frac{\frac{1}{2}\hat{s}g_Z g_{WWZ}(v_f - a_f)}{\hat{s} - m_Z^2} \right) \beta \\
& + g_{WW\gamma}g_e s_\theta (if_6^\gamma + f_1^\gamma \beta) + \frac{\frac{1}{2}\hat{s}g_Z g_{WWZ}s_\theta(a_f - v_f)(if_6^Z + f_1^Z \beta)}{\hat{s} - m_Z^2} \\
\mathcal{M}_{+,-,+,0} & = -\frac{\sqrt{2}(1 + c_\theta) \left(-g_{WW\gamma}g_e m_Z^2 + \frac{1}{2}\hat{s}(2g_{WW\gamma}g_e + g_Z g_{WWZ}(a_f - v_f)) \right) \beta}{\left(\hat{s} - m_Z^2 \right) \sqrt{1 - \beta^2}} \\
& + \frac{(1 + c_\theta)}{\sqrt{2}(1 - \beta^2)^{3/2}} \left(\frac{\frac{1}{2}\hat{s}g_Z g_{WWZ}(a_f - v_f)}{\hat{s} - m_Z^2} \right) \left(if_6^Z(1 - \beta^2) \right. \\
& + \beta \left(f_3^Z - f_3^Z \beta^2 + if_4^Z(-1 + \beta^2) + \beta \left(f_5^Z + 2i\widetilde{f}_7^Z - f_5^Z \beta^2 \right) \right) \\
& - g_{WW\gamma}g_e \left(if_6^\gamma(-1 + \beta^2) - \beta \left(f_3^\gamma(1 - \beta^2) - if_4^\gamma(1 - \beta^2) \right) \right. \\
& \left. + \beta \left(2i\widetilde{f}_7^\gamma + f_5^\gamma(1 - \beta^2) \right) \right) \Big) \Big)
\end{aligned} \tag{D.0.10}$$

E The fitting procedures of the observables and their SM values in WZ^\pm productions at the LHC

E.1 The SM values of the asymmetries and the corresponding polarizations

In Table E.1, we show the SM estimates (with 1σ MC error) of the polarization asymmetries of Z and W and their corresponding polarizations along with the other asymmetries for our selection cuts (sel . cut) given in Eq. (7.1.2) and optimized cuts (opt . cut) given Table 7.3. A number of events of $N \simeq 9.9 \times 10^6$ satisfy our selection cuts which give the same error ($\delta A_i = 1/\sqrt{N}$) for all asymmetries, and hence they are given in the top row. As the optimized cuts for W are same for all asymmetries, the errors for them are also given in the top row. For the optimized cuts of Z observables, however, the number of events vary and hence the MC error are given to each asymmetry. The CP -odd polarizations p_y , T_{xy} , T_{yz} and their corresponding asymmetries are consistent with zero in the SM within MC error.

Table E.1. The SM values with MC error of the polarization asymmetries of Z and W and their corresponding polarizations along with the other asymmetries in ZW^\pm production in the $e^+e^-\mu^+ + \cancel{E}_T$ channel are shown for event selection cuts (sel. cut) given in Eq. (7.1.2) and optimized cuts (opt. cut) given Table 7.3.

	Z		W^+		Z		W^-	
	sel. cut	opt. cut	sel. cut	opt. cut	sel. cut	opt. cut	sel. cut	opt. cut
\mathcal{O}	± 0.0003		± 0.0003	± 0.0007	± 0.0003		± 0.0003	± 0.0007
δA_i								
A_x	-0.0196	-0.0150 ± 0.0008	-0.2303	-0.0550	$+0.0074$	-0.0046 ± 0.0010	-0.0826	-0.0001
P_x	$+0.1192 \pm 0.0018$	$+0.0912 \pm 0.0049$	$+0.3071 \pm 0.0004$	0.0733 ± 0.0009	-0.0450 ± 0.0018	$+0.0280 \pm 0.0061$	$+0.110 \pm 0.00041$	$+0.00013 \pm 0.0009$
A_y	$+0.0003$	$+0.0004 \pm 0.0007$	-0.0007	-0.0005	-0.0013	-0.0021 ± 0.0007	0.0	$+0.0007$
P_y	-0.0018 ± 0.0018	-0.0024 ± 0.0146	$+0.0009 \pm 0.0004$	$+0.0006 \pm 0.0009$	$+0.0079 \pm 0.0018$	$+0.0127 \pm 0.0042$	0.0 ± 0.0004	-0.0009 ± 0.0009
A_z	-0.0040	$+0.0502 \pm 0.0025$	$+0.1337$	$+0.6615$	$+0.0316$	$+0.0482 \pm 0.0019$	$+0.1954$	$+0.7381$
P_z	$+0.0243 \pm 0.0018$	-0.3051 ± 0.0152	-0.1783 ± 0.0004	-0.8820 ± 0.0009	-0.1921 ± 0.0018	-0.2930 ± 0.0115	-0.2605 ± 0.0004	-0.9841 ± 0.0009
A_{xy}	-0.0017	$+0.0005 \pm 0.0007$	-0.0011	-0.0006	$+0.0008$	$+0.0014 \pm 0.0007$	$+0.0013$	-0.0003
T_{xy}	-0.0033 ± 0.0006	$+0.00096 \pm 0.0013$	-0.0021 ± 0.0006	-0.0012 ± 0.0013	$+0.0015 \pm 0.0006$	$+0.0027 \pm 0.0013$	$+0.0025 \pm 0.0006$	-0.0006 ± 0.0013
A_{xz}	$+0.0196$	$+0.0914 \pm 0.0004$	$+0.0048$	-0.0063	$+0.0961$	$+0.0547 \pm 0.0006$	$+0.0010$	-0.0136
T_{xz}	$+0.0377 \pm 0.0006$	$+0.1758 \pm 0.0008$	$+0.0092 \pm 0.0006$	-0.0121 ± 0.0013	$+0.1849 \pm 0.0006$	$+0.1052 \pm 0.0011$	$+0.0019 \pm 0.0006$	-0.0262 ± 0.0013
A_{yz}	$+0.0002$	-0.0001 ± 0.0004	$+0.0003$	-0.0005	-0.0017	-0.0016 ± 0.0003	$+0.0001$	-0.0001
T_{yz}	$+0.0004 \pm 0.0006$	-0.0002 ± 0.0008	$+0.0006 \pm 0.0006$	-0.0009 ± 0.0013	-0.0033 ± 0.0006	-0.0031 ± 0.0006	$+0.0002 \pm 0.0006$	-0.0002 ± 0.0013
$A_{x^2-y^2}$	-0.0878	-0.0925 ± 0.0019	-0.0266	-0.1326	-0.0935	-0.0899 ± 0.0012	-0.0923	-0.1588
$T_{xx}-T_{yy}$	-0.3378 ± 0.0011	-0.3559 ± 0.0073	-0.1023 ± 0.0011	-0.5102 ± 0.0027	-0.3597 ± 0.0011	-0.3459 ± 0.0046	-0.3551 ± 0.0011	-0.6110 ± 0.0027
A_{zz}	-0.0137	$+0.0982 \pm 0.0024$	$+0.0519$	$+0.1406$	$+0.0030$	$+0.0863 \pm 0.0048$	$+0.1046$	$+0.2547$
T_{zz}	-0.0298 ± 0.0006	$+0.2138 \pm .0052$	$+0.1130 \pm 0.0006$	$+0.3061 \pm 0.0015$	$+0.0065 \pm 0.0006$	$+0.1879 \pm 0.0104$	$+0.2277 \pm 0.0006$	$+0.5546 \pm 0.0015$
$A_{f/b}$	$+0.6829$	$+0.4475 \pm 0.0009$	$+0.4699$	$+0.2627$	$+0.6696$	$+0.2791 \pm 0.0025$	$+0.2060$	$+0.3174$
	sel. cut		opt. cut		sel. cut		opt. cut	
$A_{\Delta\phi}$	-0.3756 ± 0.0003		-0.4151 ± 0.0022		-0.3880 ± 0.0003		-0.4208 ± 0.0025	

E.2 Fitting procedure for obtaining observables as a function of couplings

The SM+aTGC events are generated for about 100 set of couplings

$$\{c_i\} = \{\Delta g_1^Z, \lambda^Z, \Delta \kappa^Z, \widetilde{\lambda}^Z, \widetilde{\kappa}^Z\}$$

in both processes. The values of all the observables are obtained for the set couplings in the optimized cuts (Table 7.3) and then those are used for numerical fitting to obtain the semi-analytical expression of all the observables as a function of the couplings. For the cross sections the following CP -even expression is used to fit the data:

$$\sigma(\{c_i\}) = \sigma_{SM} + \sum_{i=1}^3 c_i \times \sigma_i + \sum_{i=1}^5 (c_i)^2 \times \sigma_{ii} + \frac{1}{2} \sum_{i=1}^3 \sum_{j(\neq i)=1}^3 c_i c_j \times \sigma_{ij} + c_4 c_5 \times \sigma_{45}. \quad (\text{E.2.1})$$

For asymmetries, the numerator and the denominator are fitted separately and then used as

$$A_j(\{c_i\}) = \frac{\Delta \sigma_{A_j}(\{c_i\})}{\sigma_{A_j}(\{c_i\})}. \quad (\text{E.2.2})$$

The numerator ($\Delta \sigma_A$) of CP -odd asymmetries are fitted with the CP -odd expression

$$\Delta \sigma_A(\{c_i\}) = \sum_{i=4}^5 c_i \times \sigma_i + \sum_{i=1}^3 (c_i c_4 \times \sigma_{i4} + c_i c_5 \times \sigma_{i5}). \quad (\text{E.2.3})$$

The denominator (σ_{A_j}) of all the asymmetries and the numerator ($\Delta \sigma_A$) of CP -even asymmetries are fitted with the CP -even expression given in Eq. (E.2.1).

We use MCMC method to fit the coefficients of the cross sections with positivity demand, i.e., $\sigma(\{c_i\}) \geq 0$. We use 80 % data to fit the coefficients of the cross sections, and then the fitted expressions are validated against the rest 20 % of the data and found to be matching within 2σ MC error. We generated 10^7 events to keep the MC error as small as possible even in the tightest optimized cuts. For example, the A_{zz} in ZW^+ has the tightest cut on m_{3l} (see Table 7.3) and yet have very small (0.2 %) MC error (see Table E.1). In Fig. E.1 fitted values of observables are compared against the simulated data for the cross section in two diagonal bins (*top-panel*) and the polarization asymmetries A_z and A_{xz} (*bottom-panel*) in ZW^+ production in $e^+e^-\mu^+\nu_\mu$ channel as representative. The fitted values seem to agree with the simulated data used within the MC error.

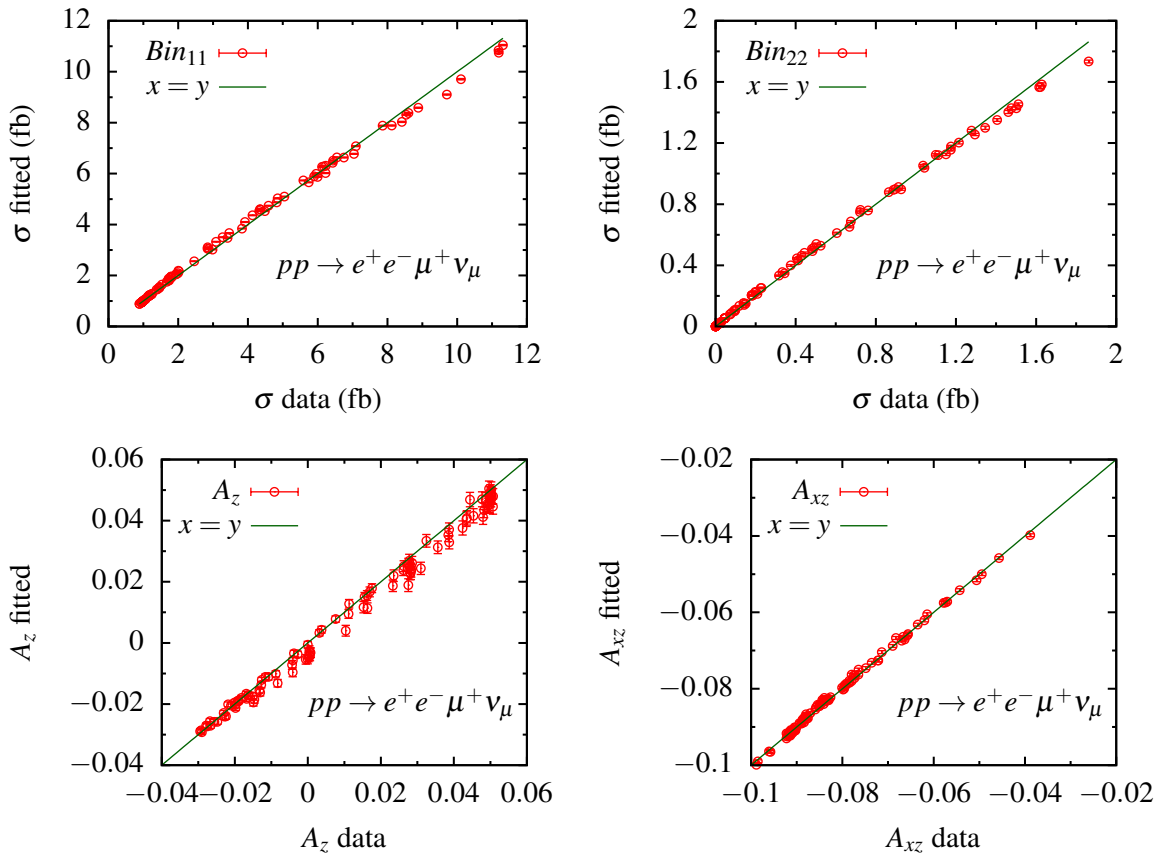


Figure E.1. The simulated data (in x -axis) vs. fitted values (in y -axis) for the cross section in the two diagonal bins (*top-panel*) and the polarization asymmetries A_z and A_{xz} (*bottom-panel*) in WZ^+ production in $e^+e^-\mu^+\nu_\mu$ channel at the LHC at $\sqrt{s} = 13$ TeV.

F HEP packages that are used in this thesis

We have used various high energy physics (HEP) packages for modelling the anomalous couplings, implementing to event generators, and for analysing events. Below, we give brief descriptions of them and their role in my thesis.

FeynRules The FeynRules [204] is a Mathematica based HEP package, where one generates model files for various event generators and get the Feynman rules by implementing the SM or BSM Lagrangian. One has to provide the FeynRules with the required information such as the gauge symmetry, particles, parameters, etc., to describe the QFT model, contained in the model file with ‘fr’ extension. The FeynRules then calculate the set of Feynman rules in momentum space associated with the given Lagrangian. The FeynRules can provide output for various other packages such as, CalcHep [253], FeynArts [254], Sherpa [255], UFO (Universal FeynRules output), Whizard [256] etc for physics analysis.

MadGraph5 The MadGraph5 [190] package named as MADGRAPH5_aMC@NLO is a Monte-Carlo event generator for scattering and decay processes in a QFT model. One imports the UFO model files in a given model in the MadGraph5 interface and generates events of a given process with/without kinematical cuts on the final state particles. This can calculate the cross section and generates events at up to NLO in QCD.

MATRIX The MATRIX [229] can calculate cross section up to NNLO in QCD for some specific processes already implemented. One can get distributions of various kinematical variables of the final state particles at LO, NLO and NNLO in QCD and compare the QCD corrections over the ranges of the variables. This package has no features of generating events of a process.

GetDist The package `GetDist` [205, 206] is a Python based package which performs Bayesian statistics of Monte-Carlo samples. It produces 1D, 2D, even 3D marginalised plots on the parameter space of interest from the Monte-Carlo samples, e.g., MCMC correlated samples, and gives simultaneous confidence limits on the parameters.

MadAnalysis5 The `MadAnalysis5` [236] is a package for analysing events generated by a Monte-Carlo event generator (`MadGraph5`). The `MadAnalysis5` which uses the package `ROOT/python`, can give a cut flow analysis and produces nice plots containing several event files. The package has an expert mode, where one can perform some cut based analysis for casting some analysis performed at the LHC to derive confidence level exclusions on the signals. It can perform detector simulations using hadronized events generated by `MadGraph5` and `Pythia`.

Uses of the packages in the thesis We calculated Feynman rules and produced UFO model files for `MadGraph5` using the `FeynRules` package with aTGC Lagrangian in all the processes from chapters 3-7. We generated LO model files for processes in e^+e^- collider used in chapters 3, 4 & 6, while we generated NLO in QCD model files for processes at the LHC as used in chapters 5 & 7. Using the UFO models files generated in `FeynRules`, we generated events in `MadGraph5` for e^+e^- collider and the LHC over the range of aTGC and beam energy, and obtained different angular observables from the events. We used these events to get differential distributions using the package `MadAnalysis5` and used in chapters 5 & 7. The package `MATRIX` is used to calculate NLO and NNLO cross sections and distributions of kinematical variables in chapters 5 & 7. The package `GetDist` is used in all chapters 3-7 to obtain posterior 1D and 2D marginalised plots and simultaneous confidence limits on the aTGC.

Bibliography

- [1] S. Glashow, *Partial Symmetries of Weak Interactions*, *Nucl. Phys.* **22** (1961) 579–588.
- [2] S. Weinberg, *A Model of Leptons*, *Phys. Rev. Lett.* **19** (1967) 1264–1266.
- [3] A. Salam, *Weak and Electromagnetic Interactions*, *Conf. Proc. C* **680519** (1968) 367–377.
- [4] M. Gell-Mann, *Quarks*, *Acta Phys. Austriaca Suppl.* **9** (1972) 733–761.
- [5] H. Fritzsch, M. Gell-Mann, and H. Leutwyler, *Advantages of the Color Octet Gluon Picture*, *Phys. Lett. B* **47** (1973) 365–368.
- [6] D. J. Gross and F. Wilczek, *Ultraviolet Behavior of Nonabelian Gauge Theories*, *Phys. Rev. Lett.* **30** (1973) 1343–1346.
- [7] D. Gross and F. Wilczek, *Asymptotically Free Gauge Theories - I*, *Phys. Rev. D* **8** (1973) 3633–3652.
- [8] H. Politzer, *Reliable Perturbative Results for Strong Interactions?*, *Phys. Rev. Lett.* **30** (1973) 1346–1349.
- [9] S. Weinberg, *Nonabelian Gauge Theories of the Strong Interactions*, *Phys. Rev. Lett.* **31** (1973) 494–497.
- [10] CMS Collaboration, S. Chatrchyan *et al.*, *Observation of a new boson at a mass of 125 GeV with the CMS experiment at the LHC*, *Phys. Lett.* **B716** (2012) 30–61, [arXiv:1207.7235](https://arxiv.org/abs/1207.7235) [hep-ex].
- [11] ATLAS Collaboration, G. Aad *et al.*, *Observation of a new particle in the search for the Standard Model Higgs boson with the ATLAS detector at the LHC*, *Phys. Lett.* **B716** (2012) 1–29, [arXiv:1207.7214](https://arxiv.org/abs/1207.7214) [hep-ex].

- [12] **ATLAS** Collaboration, *ATLAS Summary plot for exotics*,
https://atlas.web.cern.ch/Atlas/GROUPS/PHYSICS/CombinedSummaryPlots/EXOTICS/ATLAS_Exotics_Summary/ATLAS_Exotics_Summary_201905.png, (May 2019) .
- [13] **ATLAS** Collaboration, *ATLAS Summary plot for SUSY*,
https://atlas.web.cern.ch/Atlas/GROUPS/PHYSICS/CombinedSummaryPlots/SUSY/ATLAS_SUSY_Summary/ATLAS_SUSY_Summary_201907.png, (July 2019) .
- [14] **CMS** Collaboration, *CMS Summary plot for exotics*,
https://twiki.cern.ch/twiki/pub/CMSPublic/SummaryPlotsEXO13TeV/EXO_barchart_Jan19.png, (January 2019) .
- [15] **CMS** Collaboration, *CMS Summary plot for long lived particle*,
https://twiki.cern.ch/twiki/pub/CMSPublic/SummaryPlotsEXO13TeV/CMS_LLIP_barchart.png, (July 2019) .
- [16] **CMS** Collaboration, *CMS Summary plot for Beyond-two-generations (B2G)*,
https://twiki.cern.ch/twiki/pub/CMSPublic/PhysicsResultsB2G/barplot_DIB_RES_VHF.png, (July 2019) .
- [17] **ATLAS** Collaboration, M. Aaboud *et al.*, *Search for resonances in diphoton events at $\sqrt{s}=13$ TeV with the ATLAS detector*, *JHEP* **09** (2016) 001, [arXiv:1606.03833](https://arxiv.org/abs/1606.03833) [[hep-ex](#)].
- [18] **CMS** Collaboration, V. Khachatryan *et al.*, *Search for Resonant Production of High-Mass Photon Pairs in Proton-Proton Collisions at $\sqrt{s}=8$ and 13 TeV*, *Phys. Rev. Lett.* **117** no. 5, (2016) 051802, [arXiv:1606.04093](https://arxiv.org/abs/1606.04093) [[hep-ex](#)].
- [19] **CMS** Collaboration, A. M. Sirunyan *et al.*, *Search for resonances in the mass spectrum of muon pairs produced in association with b quark jets in proton-proton collisions at $\sqrt{s}=8$ and 13 TeV*, *JHEP* **11** (2018) 161, [arXiv:1808.01890](https://arxiv.org/abs/1808.01890) [[hep-ex](#)].
- [20] P. W. Higgs, *Broken Symmetries and the Masses of Gauge Bosons*, *Phys. Rev. Lett.* **13** (1964) 508–509.
- [21] G. Guralnik, C. Hagen, and T. Kibble, *Global Conservation Laws and Massless Particles*, *Phys. Rev. Lett.* **13** (1964) 585–587.

- [22] F. Englert and R. Brout, *Broken Symmetry and the Mass of Gauge Vector Mesons*, *Phys. Rev. Lett.* **13** (1964) 321–323.
- [23] P. W. Higgs, *Spontaneous Symmetry Breakdown without Massless Bosons*, *Phys. Rev.* **145** (1966) 1156–1163.
- [24] R. A. Diaz and R. Martinez, *The Custodial symmetry*, *Rev. Mex. Fis.* **47** (2001) 489–492, [arXiv:hep-ph/0302058](https://arxiv.org/abs/hep-ph/0302058) [hep-ph].
- [25] M. Thomson, *Modern particle physics*. Cambridge University Press, New York, 2013.
- [26] A. J. Buras, J. R. Ellis, M. K. Gaillard, and D. V. Nanopoulos, *Aspects of the Grand Unification of Strong, Weak and Electromagnetic Interactions*, *Nucl. Phys.* **B135** (1978) 66–92.
- [27] P. Langacker, *Grand Unified Theories and Proton Decay*, *Phys. Rept.* **72** (1981) 185.
- [28] B. S. Balakrishna, A. L. Kagan, and R. N. Mohapatra, *Quark Mixings and Mass Hierarchy From Radiative Corrections*, *Phys. Lett.* **B205** (1988) 345–352.
- [29] K. S. Babu and R. N. Mohapatra, *Top quark mass in a dynamical symmetry breaking scheme with radiative b quark and tau lepton masses*, *Phys. Rev. Lett.* **66** (1991) 556–559.
- [30] Y. Fujimoto, T. Miura, K. Nishiwaki, and M. Sakamoto, *Dynamical generation of fermion mass hierarchy in an extra dimension*, *Phys. Rev.* **D97** no. 11, (2018) 115039, [arXiv:1709.05693](https://arxiv.org/abs/1709.05693) [hep-th].
- [31] C. A. Scrucca, M. Serone, and L. Silvestrini, *Electroweak symmetry breaking and fermion masses from extra dimensions*, *Nucl. Phys.* **B669** (2003) 128–158, [arXiv:hep-ph/0304220](https://arxiv.org/abs/hep-ph/0304220) [hep-ph].
- [32] A. Ahmed, A. Carmona, J. Castellano Ruiz, Y. Chung, and M. Neubert, *Dynamical origin of fermion bulk masses in a warped extra dimension*, *JHEP* **08** (2019) 045, [arXiv:1905.09833](https://arxiv.org/abs/1905.09833) [hep-ph].
- [33] C. T. Hill and E. H. Simmons, *Strong dynamics and electroweak symmetry breaking*, *Phys. Rept.* **381** (2003) 235–402, [arXiv:hep-ph/0203079](https://arxiv.org/abs/hep-ph/0203079) [hep-ph]. [Erratum: *Phys. Rept.* 390,553(2004)].

- [34] B. Bellazzini, C. Csáki, and J. Serra, *Composite Higgses*, *Eur. Phys. J.* **C74** no. 5, (2014) 2766, [arXiv:1401.2457 \[hep-ph\]](#).
- [35] P. Langacker, *Structure of the standard model*, *Adv. Ser. Direct. High Energy Phys.* **14** (1995) 15–36, [arXiv:hep-ph/0304186 \[hep-ph\]](#).
- [36] R. D. Peccei and H. R. Quinn, *CP Conservation in the Presence of Instantons*, *Phys. Rev. Lett.* **38** (1977) 1440–1443. [,328(1977)].
- [37] S. Weinberg, *A New Light Boson?*, *Phys. Rev. Lett.* **40** (1978) 223–226.
- [38] P. W. Graham, I. G. Irastorza, S. K. Lamoreaux, A. Lindner, and K. A. van Bibber, *Experimental Searches for the Axion and Axion-Like Particles*, *Ann. Rev. Nucl. Part. Sci.* **65** (2015) 485–514, [arXiv:1602.00039 \[hep-ex\]](#).
- [39] I. G. Irastorza and J. Redondo, *New experimental approaches in the search for axion-like particles*, *Prog. Part. Nucl. Phys.* **102** (2018) 89–159, [arXiv:1801.08127 \[hep-ph\]](#).
- [40] **Super-Kamiokande** Collaboration, Y. Fukuda *et al.*, *Evidence for oscillation of atmospheric neutrinos*, *Phys. Rev. Lett.* **81** (1998) 1562–1567, [arXiv:hep-ex/9807003 \[hep-ex\]](#).
- [41] **SNO** Collaboration, Q. R. Ahmad *et al.*, *Measurement of the rate of $\nu_e + d \rightarrow p + p + e^-$ interactions produced by ^8B solar neutrinos at the Sudbury Neutrino Observatory*, *Phys. Rev. Lett.* **87** (2001) 071301, [arXiv:nucl-ex/0106015 \[nucl-ex\]](#).
- [42] **KamLAND** Collaboration, K. Eguchi *et al.*, *First results from KamLAND: Evidence for reactor anti-neutrino disappearance*, *Phys. Rev. Lett.* **90** (2003) 021802, [arXiv:hep-ex/0212021 \[hep-ex\]](#).
- [43] **Soudan-2** Collaboration, W. W. M. Allison *et al.*, *The Atmospheric neutrino flavor ratio from a 3.9 fiducial kiloton year exposure of Soudan-2*, *Phys. Lett.* **B449** (1999) 137–144, [arXiv:hep-ex/9901024 \[hep-ex\]](#).
- [44] B. T. Cleveland, T. Daily, R. Davis, Jr., J. R. Distel, K. Lande, C. K. Lee, P. S. Wildenhain, and J. Ullman, *Measurement of the solar electron neutrino flux with the Homestake chlorine detector*, *Astrophys. J.* **496** (1998) 505–526.

- [45] R. N. Mohapatra and G. Senjanovic, *Neutrino Mass and Spontaneous Parity Nonconservation*, *Phys. Rev. Lett.* **44** (1980) 912. [[231\(1979\)](#)].
- [46] E. K. Akhmedov, G. C. Branco, and M. N. Rebelo, *Seesaw mechanism and structure of neutrino mass matrix*, *Phys. Lett.* **B478** (2000) 215–223, [arXiv:hep-ph/9911364](#) [[hep-ph](#)].
- [47] R. N. Mohapatra, *Seesaw mechanism and its implications*, in *Seesaw mechanism. Proceedings, International Conference, SEESAW25, Paris, France, June 10-11, 2004*, pp. 29–44. 2004. [arXiv:hep-ph/0412379](#) [[hep-ph](#)].
- [48] J. W. F. Valle, *Neutrino physics overview*, *J. Phys. Conf. Ser.* **53** (2006) 473–505, [arXiv:hep-ph/0608101](#) [[hep-ph](#)].
- [49] R. N. Mohapatra and J. W. F. Valle, *Neutrino mass and baryon-number nonconservation in superstring models*, *Phys. Rev. D* **34** (Sep, 1986) 1642–1645.
- [50] **WMAP** Collaboration, G. Hinshaw *et al.*, *Nine-Year Wilkinson Microwave Anisotropy Probe (WMAP) Observations: Cosmological Parameter Results*, *Astrophys. J. Suppl.* **208** (2013) 19, [arXiv:1212.5226](#) [[astro-ph.CO](#)].
- [51] **Planck** Collaboration, N. Aghanim *et al.*, *Planck 2018 results. VI. Cosmological parameters*, [arXiv:1807.06209](#) [[astro-ph.CO](#)].
- [52] K. Garrett and G. Duda, *Dark Matter: A Primer*, *Adv. Astron.* **2011** (2011) 968283, [arXiv:1006.2483](#) [[hep-ph](#)].
- [53] E. Morgante, *Simplified Dark Matter Models*, *Adv. High Energy Phys.* **2018** (2018) 5012043, [arXiv:1804.01245](#) [[hep-ph](#)].
- [54] T. Lin, *Dark matter models and direct detection*, *PoS* **333** (2019) 009, [arXiv:1904.07915](#) [[hep-ph](#)].
- [55] C. H. Coimbra-Araujo and R. da Rocha, *Gravity with extra dimensions and dark matter interpretation: A straightforward approach*, *ISRN High Energy Phys.* **2013** (2013) 713508, [arXiv:1203.5736](#) [[gr-qc](#)].
- [56] C. Pongkitivanichkul, N. Thongyoi, and P. Uttayarat, *Inverse seesaw mechanism and portal dark matter*, *Phys. Rev. D* **100** (Aug, 2019) 035034.

- [57] A. D. Sakharov, *Violation of CP Invariance, C asymmetry, and baryon asymmetry of the universe*, *Pisma Zh. Eksp. Teor. Fiz.* **5** (1967) 32–35. [Usp. Fiz. Nauk 161, no. 5, 61 (1991)].
- [58] I. Aitchison and A. Hey, *Gauge Theories in Particle Physics: Volume I: From Relativistic Quantum Mechanics to QED, Third Edition*. Graduate Student Series in Physics. Taylor & Francis, 2002.
<https://books.google.sc/books?id=KnyAvAEACAAJ>.
- [59] W. Buchmuller and D. Wyler, *Effective Lagrangian Analysis of New Interactions and Flavor Conservation*, *Nucl. Phys.* **B268** (1986) 621–653.
- [60] S. Willenbrock and C. Zhang, *Effective Field Theory Beyond the Standard Model*, *Ann. Rev. Nucl. Part. Sci.* **64** (2014) 83–100, [arXiv:1401.0470](https://arxiv.org/abs/1401.0470) [hep-ph].
- [61] K. Hagiwara, S. Ishihara, R. Szalapski, and D. Zeppenfeld, *Low-energy effects of new interactions in the electroweak boson sector*, *Phys. Rev.* **D48** (1993) 2182–2203.
- [62] C. Degrande, N. Greiner, W. Kilian, O. Mattelaer, H. Mebane, T. Stelzer, S. Willenbrock, and C. Zhang, *Effective Field Theory: A Modern Approach to Anomalous Couplings*, *Annals Phys.* **335** (2013) 21–32, [arXiv:1205.4231](https://arxiv.org/abs/1205.4231) [hep-ph].
- [63] C. Degrande, *A basis of dimension-eight operators for anomalous neutral triple gauge boson interactions*, *JHEP* **02** (2014) 101, [arXiv:1308.6323](https://arxiv.org/abs/1308.6323) [hep-ph].
- [64] K. Hagiwara, R. D. Peccei, D. Zeppenfeld, and K. Hikasa, *Probing the Weak Boson Sector in $e^+e^- \rightarrow W^+W^-$* , *Nucl. Phys.* **B282** (1987) 253–307.
- [65] L. Landau, *On the angular momentum of a system of two photons*, *Dokl. Akad. Nauk SSSR* **60** no. 2, (1948) 207–209.
- [66] C.-N. Yang, *Selection Rules for the Dematerialization of a Particle Into Two Photons*, *Phys. Rev.* **77** (1950) 242–245.
- [67] J. Wudka, *Electroweak effective Lagrangians*, *Int. J. Mod. Phys.* **A9** (1994) 2301–2362, [arXiv:hep-ph/9406205](https://arxiv.org/abs/hep-ph/9406205) [hep-ph].
- [68] T. Corbett, M. J. Dolan, C. Englert, and K. Nordström, *Anomalous neutral gauge boson interactions and simplified models*, *Phys. Rev.* **D97** no. 11, (2018) 115040, [arXiv:1710.07530](https://arxiv.org/abs/1710.07530) [hep-ph].

- [69] G. J. Gounaris, J. Layssac, and F. M. Renard, *New and standard physics contributions to anomalous Z and gamma selfcouplings*, *Phys. Rev.* **D62** (2000) 073013, [arXiv:hep-ph/0003143](#) [hep-ph].
- [70] D. Choudhury, S. Dutta, S. Rakshit, and S. Rindani, *Trilinear neutral gauge boson couplings*, *Int. J. Mod. Phys.* **A16** (2001) 4891–4910, [arXiv:hep-ph/0011205](#) [hep-ph].
- [71] S. Dutta, A. Goyal, and Mamta, *New Physics Contribution to Neutral Trilinear Gauge Boson Couplings*, *Eur. Phys. J.* **C63** (2009) 305–315, [arXiv:0901.0260](#) [hep-ph].
- [72] B. Grzadkowski, O. M. Ogreid, and P. Osland, *CP-Violation in the ZZZ and ZWW vertices at e^+e^- colliders in Two-Higgs-Doublet Models*, *JHEP* **05** (2016) 025, [arXiv:1603.01388](#) [hep-ph]. [Erratum: JHEP11,002(2017)].
- [73] H. Béhusca-Maïto, A. Falkowski, D. Fontes, J. C. Romão, and J. P. Silva, *CP violation in 2HDM and EFT: the ZZZ vertex*, *JHEP* **04** (2018) 002, [arXiv:1710.05563](#) [hep-ph].
- [74] N. G. Deshpande and X.-G. He, *Triple neutral gauge boson couplings in noncommutative standard model*, *Phys. Lett.* **B533** (2002) 116–120, [arXiv:hep-ph/0112320](#) [hep-ph].
- [75] N. G. Deshpande and S. K. Garg, *Anomalous triple gauge boson couplings in $e^-e^+ \rightarrow \gamma\gamma$ for noncommutative standard model*, *Phys. Lett.* **B708** (2012) 150–156, [arXiv:1111.5173](#) [hep-ph].
- [76] A. B. Lahanas and V. C. Spanos, *Static quantities of the W boson in the MSSM*, *Phys. Lett.* **B334** (1994) 378–390, [arXiv:hep-ph/9405298](#) [hep-ph].
- [77] A. Arhrib, J. L. Kneur, and G. Moultaka, *Radiative contributions to TGC in the MSSM*, in *e^+e^- collisions at TeV energies: The physics potential. Proceedings, Workshop, Annecy, France, February 4, 1995, Gran Sasso, Assergi, Italy, June 2-3, 1995, Hamburg, Germany, August 30-September 1, 1995*, pp. 331–334. 1996. [arXiv:hep-ph/9603268](#) [hep-ph]. [331(1996)].

- [78] E. N. Argyres, A. B. Lahanas, C. G. Papadopoulos, and V. C. Spanos, *Trilinear gauge boson couplings in the MSSM*, *Phys. Lett.* **B383** (1996) 63–77, [arXiv:hep-ph/9603362](#) [hep-ph].
- [79] A. Flores-Tlalpa, J. Montano, H. Novales-Sanchez, F. Ramirez-Zavaleta, and J. J. Toscano, *One-loop effects of extra dimensions on the $WW\gamma$ and WWZ vertices*, *Phys. Rev.* **D83** (2011) 016011, [arXiv:1009.0063](#) [hep-ph].
- [80] M. López-Osorio, E. Martínez-Pascual, J. Montañó, H. Novales-Sánchez, J. J. Toscano, and E. S. Tututi, *Trilinear gauge boson couplings in the standard model with one universal extra dimension*, *Phys. Rev.* **D88** no. 1, (2013) 016010, [arXiv:1305.0621](#) [hep-ph].
- [81] M. A. Arroyo-Ureña, G. Hernández-Tomé, and G. Tavares-Velasco, *WWV ($V = \gamma, Z$) vertex in the Georgi-Machacek model*, *Phys. Rev.* **D94** no. 9, (2016) 095006, [arXiv:1610.04911](#) [hep-ph].
- [82] G. J. Gounaris, J. Layssac, and F. M. Renard, *Signatures of the anomalous $Z\gamma$ and ZZ production at the lepton and hadron colliders*, *Phys. Rev.* **D61** (2000) 073013, [arXiv:hep-ph/9910395](#) [hep-ph].
- [83] H. Czyz, K. Kolodziej, and M. Zralek, *Composite Z Boson and CP Violation in the Process $e^+e^- \rightarrow Z\gamma$* , *Z. Phys.* **C43** (1989) 97.
- [84] U. Baur and E. L. Berger, *Probing the weak boson sector in $Z\gamma$ production at hadron colliders*, *Phys. Rev.* **D47** (1993) 4889–4904.
- [85] D. Choudhury and S. D. Rindani, *Test of CP violating neutral gauge boson vertices in $e^+e^- \rightarrow \gamma Z$* , *Phys. Lett.* **B335** (1994) 198–204, [arXiv:hep-ph/9405242](#) [hep-ph].
- [86] S. Y. Choi, *Probing the weak boson sector in $\gamma e \rightarrow Ze$* , *Z. Phys.* **C68** (1995) 163–172, [arXiv:hep-ph/9412300](#) [hep-ph].
- [87] H. Aihara *et al.*, *Anomalous gauge boson interactions*, *World scientific: Advanced Series on Directions in High Energy Physics | Electroweak Symmetry Breaking and New Physics at the TeV Scale* (1997) 488–547, [arXiv:hep-ph/9503425](#) [hep-ph].

- [88] J. Ellison and J. Wudka, *Study of trilinear gauge boson couplings at the Tevatron collider*, *Ann. Rev. Nucl. Part. Sci.* **48** (1998) 33–80, [arXiv:hep-ph/9804322](#) [hep-ph].
- [89] G. Gounaris, J. Layssac, and F. Renard, *Off-shell structure of the anomalous Z and γ selfcouplings*, *Phys. Rev. D* **65** (2002) 017302, [arXiv:hep-ph/0005269](#).
- [90] U. Baur and D. L. Rainwater, *Probing neutral gauge boson selfinteractions in ZZ production at hadron colliders*, *Phys. Rev.* **D62** (2000) 113011, [arXiv:hep-ph/0008063](#) [hep-ph].
- [91] T. G. Rizzo, *Polarization asymmetries in gamma e collisions and triple gauge boson couplings revisited*, in *4th International Workshop on Linear Colliders (LCWS 99)*, pp. 529–533. 7, 1999. [arXiv:hep-ph/9907395](#).
- [92] S. Atag and I. Sahin, *ZZ gamma and Z gamma gamma couplings in gamma e collision with polarized beams*, *Phys. Rev.* **D68** (2003) 093014, [arXiv:hep-ph/0310047](#) [hep-ph].
- [93] B. Ananthanarayan, S. D. Rindani, R. K. Singh, and A. Bartl, *Transverse beam polarization and CP-violating triple-gauge-boson couplings in $e^+e^- \rightarrow \gamma Z$* , *Phys. Lett.* **B593** (2004) 95–104, [arXiv:hep-ph/0404106](#) [hep-ph]. [Erratum: *Phys. Lett.* **B608**,274(2005)].
- [94] B. Ananthanarayan, S. K. Garg, M. Patra, and S. D. Rindani, *Isolating CP-violating γZZ coupling in $e^+e^- \rightarrow \gamma Z$ with transverse beam polarizations*, *Phys. Rev.* **D85** (2012) 034006, [arXiv:1104.3645](#) [hep-ph].
- [95] B. Ananthanarayan, J. Lahiri, M. Patra, and S. D. Rindani, *New physics in $e^+e^- \rightarrow Z\gamma$ at the ILC with polarized beams: explorations beyond conventional anomalous triple gauge boson couplings*, *JHEP* **08** (2014) 124, [arXiv:1404.4845](#) [hep-ph].
- [96] P. Poulose and S. D. Rindani, *CP violating $Z\gamma\gamma$ and top quark electric dipole couplings in $\gamma\gamma \rightarrow t\bar{t}$* , *Phys. Lett.* **B452** (1999) 347–354, [arXiv:hep-ph/9809203](#) [hep-ph].
- [97] A. Senol, *ZZ γ and Z $\gamma\gamma$ anomalous couplings in γp collision at the LHC*, *Phys. Rev.* **D87** (2013) 073003, [arXiv:1301.6914](#) [hep-ph].

- [98] R. Rahaman and R. K. Singh, *On polarization parameters of spin-1 particles and anomalous couplings in $e^+e^- \rightarrow ZZ/Z\gamma$* , *Eur. Phys. J.* **C76** no. 10, (2016) 539, [arXiv:1604.06677 \[hep-ph\]](#).
- [99] R. Rahaman and R. K. Singh, *On the choice of beam polarization in $e^+e^- \rightarrow ZZ/Z\gamma$ and anomalous triple gauge-boson couplings*, *Eur. Phys. J.* **C77** no. 8, (2017) 521, [arXiv:1703.06437 \[hep-ph\]](#).
- [100] I. Ots, H. Uiho, H. Liivat, R. Saar, and R. K. Loide, *Possible anomalous ZZ gamma and Z gamma gamma couplings and Z boson spin orientation in $e^+e^- \rightarrow Z\gamma$: The role of transverse polarization*, *Nucl. Phys.* **B740** (2006) 212–221.
- [101] B. Ananthanarayan and S. D. Rindani, *CP violation at a linear collider with transverse polarization*, *Phys. Rev.* **D70** (2004) 036005, [arXiv:hep-ph/0309260 \[hep-ph\]](#).
- [102] M. Chiesa, A. Denner, and J.-N. Lang, *Anomalous triple-gauge-boson interactions in vector-boson pair production with RECOLA2*, *Eur. Phys. J.* **C78** no. 6, (2018) 467, [arXiv:1804.01477 \[hep-ph\]](#).
- [103] M. Chiesa, A. Denner, and J.-N. Lang, *Effects of anomalous triple-gauge-boson interactions in diboson production with RECOLA2*, in *14th DESY Workshop on Elementary Particle Physics: Loops and Legs in Quantum Field Theory 2018 (LL2018) St Goar, Germany, April 29-May 4, 2018*. 2018. [arXiv:1808.03167 \[hep-ph\]](#).
- [104] F. Boudjema, *Proc. of the Workshop on e^-e^+ Collisions at 500GeV: The Physics Potential*, edited by P.M. Zerwas, *DESY 92-123B* (1992) 757. <https://inspirehep.net/literature/1511359>.
- [105] B. Ananthanarayan and S. D. Rindani, *New physics in $e^+e^- \rightarrow Z\gamma$ with polarized beams*, *JHEP* **10** (2005) 077, [arXiv:hep-ph/0507037 \[hep-ph\]](#).
- [106] R. Rahaman and R. K. Singh, *Anomalous triple gauge boson couplings in ZZ production at the LHC and the role of Z boson polarizations*, *Nucl. Phys.* **B948** (2019), [arXiv:1810.11657 \[hep-ph\]](#).
- [107] K. J. F. Gaemers and G. J. Gounaris, *Polarization Amplitudes for $e^+e^- \rightarrow W^+W^-$ and $e^+e^- \rightarrow ZZ$* , *Z. Phys.* **C1** (1979) 259.

- [108] C. L. Bilchak and J. D. Stroughair, *W^+W^- Pair Production in e^+e^- Colliders*, *Phys. Rev. D* **D30** (1984) 1881.
- [109] K. Hagiwara, S. Ishihara, R. Szalapski, and D. Zeppenfeld, *Low-energy constraints on electroweak three gauge boson couplings*, *Phys. Lett.* **B283** (1992) 353–359.
- [110] J. D. Wells and Z. Zhang, *Status and prospects of precision analyses with $e^+e^- \rightarrow W^+W^-$* , *Phys. Rev. D* **D93** no. 3, (2016) 034001, [arXiv:1507.01594 \[hep-ph\]](#). [Phys. Rev.D93,034001(2016)].
- [111] G. Buchalla, O. Cata, R. Rahn, and M. Schlaffer, *Effective Field Theory Analysis of New Physics in $e^+e^- \rightarrow W^+W^-$ at a Linear Collider*, *Eur. Phys. J.* **C73** no. 10, (2013) 2589, [arXiv:1302.6481 \[hep-ph\]](#).
- [112] Z. Zhang, *Time to Go Beyond Triple-Gauge-Boson-Coupling Interpretation of W Pair Production*, *Phys. Rev. Lett.* **118** no. 1, (2017) 011803, [arXiv:1610.01618 \[hep-ph\]](#).
- [113] L. Berthier, M. Bjørn, and M. Trott, *Incorporating doubly resonant W^\pm data in a global fit of SMEFT parameters to lift flat directions*, *JHEP* **09** (2016) 157, [arXiv:1606.06693 \[hep-ph\]](#).
- [114] L. Bian, J. Shu, and Y. Zhang, *Prospects for Triple Gauge Coupling Measurements at Future Lepton Colliders and the 14 TeV LHC*, *JHEP* **09** (2015) 206, [arXiv:1507.02238 \[hep-ph\]](#).
- [115] L. Bian, J. Shu, and Y. Zhang, *Triple gauge couplings at future hadron and lepton colliders*, *Int. J. Mod. Phys.* **A31** no. 33, (2016) 1644008, [arXiv:1612.03888 \[hep-ph\]](#).
- [116] D. Choudhury and J. Kalinowski, *Unraveling the $WW\gamma$ and WWZ vertices at the linear collider: Anti-neutrino neutrino γ and anti-neutrino neutrino $\bar{q}q$ final states*, *Nucl. Phys.* **B491** (1997) 129–146, [arXiv:hep-ph/9608416 \[hep-ph\]](#).
- [117] D. Choudhury, J. Kalinowski, and A. Kulesza, *CP violating anomalous $WW\gamma$ couplings in e^+e^- collisions*, *Phys. Lett.* **B457** (1999) 193–201, [arXiv:hep-ph/9904215 \[hep-ph\]](#).

- [118] R. Rahaman and R. K. Singh, *Probing the anomalous triple gauge boson couplings in $e^+e^- \rightarrow W^+W^-$ using W polarizations with polarized beams*, *Phys. Rev. D* **101** no. 7, (2020) 075044, [arXiv:1909.05496 \[hep-ph\]](#).
- [119] S. S. Biswal, M. Patra, and S. Raychaudhuri, *Anomalous Triple Gauge Vertices at the Large Hadron-Electron Collider*, [arXiv:1405.6056 \[hep-ph\]](#).
- [120] I. T. Cakir, O. Cakir, A. Senol, and A. T. Tasci, *Search for anomalous $WW\gamma$ and WWZ couplings with polarized e -beam at the LHeC*, *Acta Phys. Polon.* **B45** no. 10, (2014) 1947, [arXiv:1406.7696 \[hep-ph\]](#).
- [121] R. Li, X.-M. Shen, K. Wang, T. Xu, L. Zhang, and G. Zhu, *Probing anomalous $WW\gamma$ triple gauge bosons coupling at the LHeC*, *Phys. Rev.* **D97** no. 7, (2018) 075043, [arXiv:1711.05607 \[hep-ph\]](#).
- [122] S. Kumar and P. Poulose, *Probing $WW\gamma$ coupling through $e^-\gamma \rightarrow \nu_e W^-$ at ILC*, *Int. J. Mod. Phys.* **A30** no. 36, (2015) 1550215, [arXiv:1501.01380 \[hep-ph\]](#).
- [123] U. Baur and D. Zeppenfeld, *Unitarity Constraints on the Electroweak Three Vector Boson Vertices*, *Phys. Lett.* **B201** (1988) 383–389.
- [124] L. J. Dixon, Z. Kunszt, and A. Signer, *Vector boson pair production in hadronic collisions at order α_s : Lepton correlations and anomalous couplings*, *Phys. Rev.* **D60** (1999) 114037, [arXiv:hep-ph/9907305 \[hep-ph\]](#).
- [125] A. Falkowski, M. Gonzalez-Alonso, A. Greljo, D. Marzocca, and M. Son, *Anomalous Triple Gauge Couplings in the Effective Field Theory Approach at the LHC*, *JHEP* **02** (2017) 115, [arXiv:1609.06312 \[hep-ph\]](#).
- [126] A. Azatov, J. Elias-Miro, Y. Reyimuaji, and E. Venturini, *Novel measurements of anomalous triple gauge couplings for the LHC*, [arXiv:1707.08060 \[hep-ph\]](#).
- [127] A. Azatov, D. Barducci, and E. Venturini, *Precision diboson measurements at hadron colliders*, *JHEP* **04** (2019) 075, [arXiv:1901.04821 \[hep-ph\]](#).
- [128] R. Roth, F. Campanario, S. Sapeta, and D. Zeppenfeld, *Anomalous couplings in WZ production beyond NLO QCD*, *PoS LHCP2016* (2016) 141, [arXiv:1612.03577 \[hep-ph\]](#).

- [129] A. Butter, O. J. P. Éboli, J. Gonzalez-Fraile, M. C. Gonzalez-Garcia, T. Plehn, and M. Rauch, *The Gauge-Higgs Legacy of the LHC Run I*, *JHEP* **07** (2016) 152, [arXiv:1604.03105 \[hep-ph\]](#).
- [130] J. Baglio, S. Dawson, and I. M. Lewis, *An NLO QCD effective field theory analysis of W^+W^- production at the LHC including fermionic operators*, *Phys. Rev.* **D96** no. 7, (2017) 073003, [arXiv:1708.03332 \[hep-ph\]](#).
- [131] H. T. Li and G. Valencia, *CP violating anomalous couplings in W jet production at the LHC*, [arXiv:1708.04402 \[hep-ph\]](#).
- [132] D. Bhatia, U. Maitra, and S. Raychaudhuri, *Pinning down anomalous $WW\gamma$ couplings at the LHC*, *Phys. Rev.* **D99** no. 9, (2019) 095017, [arXiv:1804.05357 \[hep-ph\]](#).
- [133] **L3** Collaboration, M. Acciarri *et al.*, *Search for anomalous $ZZ\gamma$ and $Z\gamma\gamma$ couplings in the process $e^+e^- \rightarrow Z\gamma$ at LEP*, *Phys. Lett.* **B489** (2000) 55–64, [arXiv:hep-ex/0005024 \[hep-ex\]](#).
- [134] **OPAL** Collaboration, G. Abbiendi *et al.*, *Search for trilinear neutral gauge boson couplings in $Z\gamma$ production at $\sqrt{s} = 189$ GeV at LEP*, *Eur. Phys. J.* **C17** (2000) 553–566, [arXiv:hep-ex/0007016 \[hep-ex\]](#).
- [135] **OPAL** Collaboration, G. Abbiendi *et al.*, *Study of Z pair production and anomalous couplings in e^+e^- collisions at \sqrt{s} between 190-GeV and 209-GeV*, *Eur. Phys. J.* **C32** (2003) 303–322, [arXiv:hep-ex/0310013 \[hep-ex\]](#).
- [136] **L3** Collaboration, P. Achard *et al.*, *Study of the $e^+e^- \rightarrow Z\gamma$ process at LEP and limits on triple neutral-gauge-boson couplings*, *Phys. Lett.* **B597** (2004) 119–130, [arXiv:hep-ex/0407012 \[hep-ex\]](#).
- [137] **DELPHI** Collaboration, J. Abdallah *et al.*, *Study of triple-gauge-boson couplings ZZZ , $ZZ\gamma$ and $Z\gamma\gamma$ at LEP*, *Eur. Phys. J.* **C51** (2007) 525–542, [arXiv:0706.2741 \[hep-ex\]](#).
- [138] **D0** Collaboration, V. M. Abazov *et al.*, *Search for ZZ and $Z\gamma^*$ production in $p\bar{p}$ collisions at $\sqrt{s} = 1.96$ TeV and limits on anomalous ZZZ and $ZZ\gamma^*$ couplings*, *Phys. Rev. Lett.* **100** (2008) 131801, [arXiv:0712.0599 \[hep-ex\]](#).

- [139] **CDF** Collaboration, T. Aaltonen *et al.*, *Limits on Anomalous Trilinear Gauge Couplings in $Z\gamma$ Events from $p\bar{p}$ Collisions at $\sqrt{s} = 1.96$ TeV*, *Phys. Rev. Lett.* **107** (2011) 051802, [arXiv:1103.2990 \[hep-ex\]](#).
- [140] **D0** Collaboration, V. M. Abazov *et al.*, *$Z\gamma$ production and limits on anomalous $ZZ\gamma$ and $Z\gamma\gamma$ couplings in $p\bar{p}$ collisions at $\sqrt{s} = 1.96$ TeV*, *Phys. Rev.* **D85** (2012) 052001, [arXiv:1111.3684 \[hep-ex\]](#).
- [141] **CMS** Collaboration, S. Chatrchyan *et al.*, *Measurement of the ZZ production cross section and search for anomalous couplings in 2 l2l' final states in pp collisions at $\sqrt{s} = 7$ TeV*, *JHEP* **01** (2013) 063, [arXiv:1211.4890 \[hep-ex\]](#).
- [142] **CMS** Collaboration, S. Chatrchyan *et al.*, *Measurement of the production cross section for $Z\gamma \rightarrow \nu\bar{\nu}\gamma$ in pp collisions at $\sqrt{s} = 7$ TeV and limits on $ZZ\gamma$ and $Z\gamma\gamma$ triple gauge boson couplings*, *JHEP* **10** (2013) 164, [arXiv:1309.1117 \[hep-ex\]](#).
- [143] **ATLAS** Collaboration, G. Aad *et al.*, *Measurements of $W\gamma$ and $Z\gamma$ production in pp collisions at $\sqrt{s}=7$ TeV with the ATLAS detector at the LHC*, *Phys. Rev.* **D87** no. 11, (2013) 112003, [arXiv:1302.1283 \[hep-ex\]](#). [Erratum: Phys. Rev.D91,no.11,119901(2015)].
- [144] **CMS** Collaboration, V. Khachatryan *et al.*, *Measurement of the $Z\gamma$ Production Cross Section in pp Collisions at 8 TeV and Search for Anomalous Triple Gauge Boson Couplings*, *JHEP* **04** (2015) 164, [arXiv:1502.05664 \[hep-ex\]](#).
- [145] **CMS** Collaboration, V. Khachatryan *et al.*, *Measurement of the $Z\gamma \rightarrow \nu\bar{\nu}\gamma$ production cross section in pp collisions at $\sqrt{s} = 8$ TeV and limits on anomalous $ZZ\gamma$ and $Z\gamma\gamma$ trilinear gauge boson couplings*, *Phys. Lett.* **B760** (2016) 448–468, [arXiv:1602.07152 \[hep-ex\]](#).
- [146] **CMS** Collaboration, A. M. Sirunyan *et al.*, *Measurements of the $pp \rightarrow ZZ$ production cross section and the $Z \rightarrow 4\ell$ branching fraction, and constraints on anomalous triple gauge couplings at $\sqrt{s} = 13$ TeV*, *Eur. Phys. J.* **C78** (2018) 165, [arXiv:1709.08601 \[hep-ex\]](#). [Erratum: Eur. Phys. J.C78,no.6,515(2018)].
- [147] **ATLAS** Collaboration, M. Aaboud *et al.*, *$ZZ \rightarrow \ell^+\ell^-\ell'^+\ell'^-$ cross-section measurements and search for anomalous triple gauge couplings in 13 TeV pp collisions with the ATLAS detector*, *Phys. Rev.* **D97** no. 3, (2018) 032005, [arXiv:1709.07703 \[hep-ex\]](#).

- [148] **ATLAS** Collaboration, M. Aaboud *et al.*, *Measurement of the $Z\gamma \rightarrow \nu\bar{\nu}\gamma$ production cross section in pp collisions at $\sqrt{s} = 13$ TeV with the ATLAS detector and limits on anomalous triple gauge-boson couplings*, *JHEP* **12** (2018) 010, [arXiv:1810.04995 \[hep-ex\]](#).
- [149] **OPAL** Collaboration, G. Abbiendi *et al.*, *Measurement of W boson polarizations and CP violating triple gauge couplings from W^+W^- production at LEP*, *Eur. Phys. J. C* **19** (2001) 229–240, [arXiv:hep-ex/0009021 \[hep-ex\]](#).
- [150] **OPAL** Collaboration, G. Abbiendi *et al.*, *Measurement of charged current triple gauge boson couplings using W pairs at LEP*, *Eur. Phys. J. C* **33** (2004) 463–476, [arXiv:hep-ex/0308067 \[hep-ex\]](#).
- [151] **DELPHI** Collaboration, J. Abdallah *et al.*, *Study of W boson polarisations and Triple Gauge boson Couplings in the reaction $e^+e^- \rightarrow W^+W^-$ at LEP 2*, *Eur. Phys. J. C* **54** (2008) 345–364, [arXiv:0801.1235 \[hep-ex\]](#).
- [152] **DELPHI, OPAL, LEP Electroweak, ALEPH, L3** Collaboration, S. Schael *et al.*, *Electroweak Measurements in Electron-Positron Collisions at W -Boson-Pair Energies at LEP*, *Phys. Rept.* **532** (2013) 119–244, [arXiv:1302.3415 \[hep-ex\]](#).
- [153] **CDF** Collaboration, T. Aaltonen *et al.*, *Limits on Anomalous Triple Gauge Couplings in $p\bar{p}$ Collisions at $\sqrt{s} = 1.96$ -TeV*, *Phys. Rev. D* **76** (2007) 111103, [arXiv:0705.2247 \[hep-ex\]](#).
- [154] **D0** Collaboration, V. M. Abazov *et al.*, *Limits on anomalous trilinear gauge boson couplings from WW , WZ and $W\gamma$ production in $p\bar{p}$ collisions at $\sqrt{s} = 1.96$ TeV*, *Phys. Lett. B* **718** (2012) 451–459, [arXiv:1208.5458 \[hep-ex\]](#).
- [155] **ATLAS** Collaboration, M. Aaboud *et al.*, *Measurement of $WW/WZ \rightarrow \ell\nu qq'$ production with the hadronically decaying boson reconstructed as one or two jets in pp collisions at $\sqrt{s} = 8$ TeV with ATLAS, and constraints on anomalous gauge couplings*, *Eur. Phys. J. C* **77** no. 8, (2017) 563, [arXiv:1706.01702 \[hep-ex\]](#).
- [156] **CMS** Collaboration, A. M. Sirunyan *et al.*, *Search for anomalous couplings in boosted $WW/WZ \rightarrow \ell\nu q\bar{q}$ production in proton-proton collisions at $\sqrt{s} = 8$ TeV*, *Phys. Lett. B* **772** (2017) 21–42, [arXiv:1703.06095 \[hep-ex\]](#).

- [157] **ATLAS** Collaboration, M. Aaboud *et al.*, *Measurements of electroweak Wjj production and constraints on anomalous gauge couplings with the ATLAS detector*, *Eur. Phys. J.* **C77** no. 7, (2017) 474, [arXiv:1703.04362 \[hep-ex\]](#).
- [158] **CMS** Collaboration, V. Khachatryan *et al.*, *Measurement of the WZ production cross section in pp collisions at $\sqrt{s} = 7$ and 8 TeV and search for anomalous triple gauge couplings at $\sqrt{s} = 8$ TeV*, *Eur. Phys. J.* **C77** no. 4, (2017) 236, [arXiv:1609.05721 \[hep-ex\]](#).
- [159] **ATLAS** Collaboration, G. Aad *et al.*, *Measurements of $W^{\pm}Z$ production cross sections in pp collisions at $\sqrt{s} = 8$ TeV with the ATLAS detector and limits on anomalous gauge boson self-couplings*, *Phys. Rev.* **D93** no. 9, (2016) 092004, [arXiv:1603.02151 \[hep-ex\]](#).
- [160] **ATLAS** Collaboration, G. Aad *et al.*, *Measurement of total and differential W^+W^- production cross sections in proton-proton collisions at $\sqrt{s} = 8$ TeV with the ATLAS detector and limits on anomalous triple-gauge-boson couplings*, *JHEP* **09** (2016) 029, [arXiv:1603.01702 \[hep-ex\]](#).
- [161] **CMS** Collaboration, S. Chatrchyan *et al.*, *Measurement of the W^+W^- Cross section in pp Collisions at $\sqrt{s} = 7$ TeV and Limits on Anomalous $WW\gamma$ and WWZ couplings*, *Eur. Phys. J.* **C73** no. 10, (2013) 2610, [arXiv:1306.1126 \[hep-ex\]](#).
- [162] **CMS** Collaboration, P. Rebello Teles, *Search for anomalous gauge couplings in semi-leptonic decays of $WW\gamma$ and $WZ\gamma$ in pp collisions at $\sqrt{s} = 8$ TeV*, in *Meeting of the APS Division of Particles and Fields*. 10, 2013. [arXiv:1310.0473 \[hep-ex\]](#).
- [163] **ATLAS** Collaboration, G. Aad *et al.*, *Measurement of W^+W^- production in pp collisions at $\sqrt{s} = 7$ TeV with the ATLAS detector and limits on anomalous WWZ and $WW\gamma$ couplings*, *Phys. Rev.* **D87** no. 11, (2013) 112001, [arXiv:1210.2979 \[hep-ex\]](#). [Erratum: *Phys. Rev.* **D88**, no. 7, 079906 (2013)].
- [164] **CMS** Collaboration, S. Chatrchyan *et al.*, *Measurement of the sum of WW and WZ production with W +dijet events in pp collisions at $\sqrt{s} = 7$ TeV*, *Eur. Phys. J.* **C73** no. 2, (2013) 2283, [arXiv:1210.7544 \[hep-ex\]](#).
- [165] **CMS** Collaboration, S. Chatrchyan *et al.*, *Measurement of the $W\gamma$ and $Z\gamma$ inclusive cross sections in pp collisions at $\sqrt{s} = 7$ TeV and limits on anomalous triple gauge*

- boson couplings*, *Phys. Rev.* **D89** no. 9, (2014) 092005, [arXiv:1308.6832](#) [[hep-ex](#)].
- [166] CMS Collaboration, A. M. Sirunyan *et al.*, *Electroweak production of two jets in association with a Z boson in proton–proton collisions at $\sqrt{s} = 13$ TeV*, *Eur. Phys. J.* **C78** no. 7, (2018) 589, [arXiv:1712.09814](#) [[hep-ex](#)].
- [167] CMS Collaboration, A. M. Sirunyan *et al.*, *Search for anomalous triple gauge couplings in WW and WZ production in lepton + jet events in proton–proton collisions at $\sqrt{s} = 13$ TeV*, *JHEP* **12** (2019) 062, [arXiv:1907.08354](#) [[hep-ex](#)].
- [168] CMS Collaboration, A. M. Sirunyan *et al.*, *Measurement of electroweak production of a W boson in association with two jets in proton–proton collisions at $\sqrt{s} = 13$ TeV*, *Eur. Phys. J. C* **80** no. 1, (2020) 43, [arXiv:1903.04040](#) [[hep-ex](#)].
- [169] CMS Collaboration, A. M. Sirunyan *et al.*, *Measurements of the $pp \rightarrow WZ$ inclusive and differential production cross section and constraints on charged anomalous triple gauge couplings at $\sqrt{s} = 13$ TeV*, *JHEP* **04** (2019) 122, [arXiv:1901.03428](#) [[hep-ex](#)].
- [170] T. Corbett, O. J. P. Éboli, J. Gonzalez-Fraile, and M. C. Gonzalez-Garcia, *Determining Triple Gauge Boson Couplings from Higgs Data*, *Phys. Rev. Lett.* **111** (2013) 011801, [arXiv:1304.1151](#) [[hep-ph](#)].
- [171] R. M. Godbole, S. D. Rindani, and R. K. Singh, *Lepton distribution as a probe of new physics in production and decay of the t quark and its polarization*, *JHEP* **12** (2006) 021, [arXiv:hep-ph/0605100](#) [[hep-ph](#)].
- [172] F. Boudjema and R. K. Singh, *A Model independent spin analysis of fundamental particles using azimuthal asymmetries*, *JHEP* **07** (2009) 028, [arXiv:0903.4705](#) [[hep-ph](#)].
- [173] C. Bourrely, J. Soffer, and E. Leader, *Polarization Phenomena in Hadronic Reactions*, *Phys. Rept.* **59** (1980) 95–297.
- [174] I. Ots, H. Uiho, H. Liivat, R. Saar, and R. K. Loide, *Possible anomalous ZZ gamma and Z gamma gamma couplings and Z boson spin orientation in $e^+ e^- \rightarrow Z$ gamma*, *Nucl. Phys.* **B702** (2004) 346–356.

- [175] J. A. Aguilar-Saavedra and J. Bernabeu, *Breaking down the entire W boson spin observables from its decay*, *Phys. Rev.* **D93** no. 1, (2016) 011301, [arXiv:1508.04592 \[hep-ph\]](#).
- [176] J. Nakamura, *Polarisations of the Z and W bosons in the processes $pp \rightarrow ZH$ and $pp \rightarrow W^\pm H$* , *JHEP* **08** (2017) 008, [arXiv:1706.01816 \[hep-ph\]](#).
- [177] R. Rahaman and R. K. Singh, *Constraining anomalous gauge boson couplings in $e^+e^- \rightarrow W^+W^-$ using polarization asymmetries with polarized beams*, [arXiv:1711.04551 \[hep-ph\]](#).
- [178] R. Rahaman and R. K. Singh, *Unravelling the anomalous gauge boson couplings in ZW^\pm production at the LHC and the role of spin-1 polarizations*, *JHEP* **04** (2020) 075, [arXiv:1911.03111 \[hep-ph\]](#).
- [179] K. Rao and S. D. Rindani, *W boson polarization as a measure of gauge-Higgs anomalous couplings at the LHC*, *Nucl. Phys.* **B940** (2019) 78–87, [arXiv:1805.06602 \[hep-ph\]](#).
- [180] S. Behera, R. Islam, M. Kumar, P. Poullose, and R. Rahaman, *Fingerprinting the Top quark FCNC via anomalous Ztq couplings at the LHeC*, *Phys. Rev.* **D100** no. 1, (2019) 015006, [arXiv:1811.04681 \[hep-ph\]](#).
- [181] F. M. Renard, *Polarization effects due to dark matter interaction between massive standard particles*, [arXiv:1802.10313 \[hep-ph\]](#).
- [182] F. M. Renard, *Z Polarization in $e^+e^- \rightarrow t\bar{t}Z$ for testing the top quark mass structure and the presence of final interactions*, [arXiv:1803.10466 \[hep-ph\]](#).
- [183] F. M. Renard, *W polarization in e^+e^- , gluon-gluon and $\gamma\gamma \rightarrow Wt\bar{b}$ for testing the top quark mass structure and the presence of final interactions*, [arXiv:1807.00621 \[hep-ph\]](#).
- [184] F. M. Renard, *Further tests of special interactions of massive particles from the Z polarization rate in $e^+e^- \rightarrow Zt\bar{t}$ and in $e^+e^- \rightarrow ZW^+W^-$* , [arXiv:1808.05429 \[hep-ph\]](#).
- [185] F. M. Renard, *Z polarization in $e^+e^- \rightarrow ZWW$ for testing special interactions of massive particles*, [arXiv:1807.08938 \[hep-ph\]](#).

- [186] J. A. Aguilar-Saavedra, J. Bernabéu, V. A. Mitsou, and A. Segarra, *The Z boson spin observables as messengers of new physics*, *Eur. Phys. J.* **C77** no. 4, (2017) 234, [arXiv:1701.03115 \[hep-ph\]](#).
- [187] J. J. Song, W. L. Chang, R. Han, and W. H. Yang, *Spin Density Matrix For Spin-3/2 Particles*, [arXiv:1911.11771 \[hep-ph\]](#).
- [188] V. Arunprasath, R. M. Godbole, and R. K. Singh, *Polarization of a top quark produced in the decay of a gluino or a stop in an arbitrary frame*, *Phys. Rev.* **D95** no. 7, (2017) 076012, [arXiv:1612.03803 \[hep-ph\]](#).
- [189] A. Velusamy and R. K. Singh, *Polarization of a vector boson produced in decay of a heavy fermion in an arbitrary frame*, *Phys. Rev.* **D98** no. 5, (2018) 053009, [arXiv:1805.00876 \[hep-ph\]](#).
- [190] J. Alwall, R. Frederix, S. Frixione, V. Hirschi, F. Maltoni, O. Mattelaer, H. S. Shao, T. Stelzer, P. Torrielli, and M. Zaro, *The automated computation of tree-level and next-to-leading order differential cross sections, and their matching to parton shower simulations*, *JHEP* **07** (2014) 079, [arXiv:1405.0301 \[hep-ph\]](#).
- [191] G. Mahlon and S. J. Parke, *Spin Correlation Effects in Top Quark Pair Production at the LHC*, *Phys. Rev.* **D81** (2010) 074024, [arXiv:1001.3422 \[hep-ph\]](#).
- [192] A. Behring, M. Czakon, A. Mitov, A. S. Papanastasiou, and R. Poncelet, *Higher order corrections to spin correlations in top quark pair production at the LHC*, *Phys. Rev. Lett.* **123** no. 8, (2019) 082001, [arXiv:1901.05407 \[hep-ph\]](#).
- [193] ATLAS Collaboration, M. Aaboud *et al.*, *Measurements of top-quark pair spin correlations in the $e\mu$ channel at $\sqrt{s} = 13$ TeV using pp collisions in the ATLAS detector*, [arXiv:1903.07570 \[hep-ex\]](#).
- [194] ATLAS, CMS Collaboration, J. Linacre, *Spin correlations in top physics at ATLAS and CMS in Run 2*, in *54th Rencontres de Moriond on Electroweak Interactions and Unified Theories (Moriond EW 2019) La Thuile, Italy, March 16-23, 2019*. 2019. [arXiv:1905.08634 \[hep-ex\]](#).
- [195] ILC Collaboration, G. Aarons *et al.*, *International Linear Collider Reference Design Report Volume 2: Physics at the ILC*, [arXiv:0709.1893 \[hep-ph\]](#).

- [196] H. Baer, T. Barklow, K. Fujii, Y. Gao, A. Hoang, S. Kanemura, J. List, H. E. Logan, A. Nomerotski, M. Perelstein, *et al.*, *The International Linear Collider Technical Design Report - Volume 2: Physics*, [arXiv:1306.6352](https://arxiv.org/abs/1306.6352) [hep-ph].
- [197] T. Behnke, J. E. Brau, B. Foster, J. Fuster, M. Harrison, J. M. Paterson, M. Peskin, M. Stanitzki, N. Walker, and H. Yamamoto, *The International Linear Collider Technical Design Report - Volume 1: Executive Summary*, [arXiv:1306.6327](https://arxiv.org/abs/1306.6327) [physics.acc-ph].
- [198] F. M. Renard, *Tests of Neutral Gauge Boson Selfcouplings With $e^+e^- \rightarrow \gamma Z$* , *Nucl. Phys.* **B196** (1982) 93–108.
- [199] F. Larios, M. A. Perez, G. Tavares-Velasco, and J. J. Toscano, *Trilinear neutral gauge boson couplings in effective theories*, *Phys. Rev.* **D63** (2001) 113014, [arXiv:hep-ph/0012180](https://arxiv.org/abs/hep-ph/0012180) [hep-ph].
- [200] O. Cata, *Revisiting ZZ and γZ production with effective field theories*, [arXiv:1304.1008](https://arxiv.org/abs/1304.1008) [hep-ph].
- [201] A. Senol, M. Köksal, and S. C. İnan, *Probe of the Anomalous Quartic Couplings with Beam Polarization at the CLIC*, *Adv. High Energy Phys.* **2017** (2017) 6970587, [arXiv:1603.01065](https://arxiv.org/abs/1603.01065) [hep-ph].
- [202] Y. Wen, H. Qu, D. Yang, Q.-s. Yan, Q. Li, and Y. Mao, *Probing triple-W production and anomalous WWW coupling at the CERN LHC and future $\mathcal{O}(100)$ TeV proton-proton collider*, *JHEP* **03** (2015) 025, [arXiv:1407.4922](https://arxiv.org/abs/1407.4922) [hep-ph].
- [203] G. Perez, M. Sekulla, and D. Zeppenfeld, *Anomalous quartic gauge couplings and unitarization for the vector boson scattering process $pp \rightarrow W^+W^+ jjX \rightarrow \ell^+ \nu_\ell \ell^+ \nu_\ell jjX$* , *Eur. Phys. J.* **C78** no. 9, (2018) 759, [arXiv:1807.02707](https://arxiv.org/abs/1807.02707) [hep-ph].
- [204] A. Alloul, N. D. Christensen, C. Degrande, C. Duhr, and B. Fuks, *FeynRules 2.0 - A complete toolbox for tree-level phenomenology*, *Comput. Phys. Commun.* **185** (2014) 2250–2300, [arXiv:1310.1921](https://arxiv.org/abs/1310.1921) [hep-ph].
- [205] A. Lewis, *GetDist: Kernel Density Estimation*, [url::http://cosmologist.info/notes/GetDist.pdf](http://cosmologist.info/notes/GetDist.pdf), *Homepage* <http://getdist.readthedocs.org/en/latest/index.html> .

- [206] A. Lewis, *GetDist: a Python package for analysing Monte Carlo samples*, [arXiv:1910.13970](#) [astro-ph.IM].
- [207] G. Moortgat-Pick *et al.*, *The Role of polarized positrons and electrons in revealing fundamental interactions at the linear collider*, *Phys. Rept.* **460** (2008) 131–243, [arXiv:hep-ph/0507011](#) [hep-ph].
- [208] V. V. Andreev, G. Moortgat-Pick, P. Osland, A. A. Pankov, and N. Paver, *Discriminating Z' from Anomalous Trilinear Gauge Coupling Signatures in $e^+e^- \rightarrow W^+W^-$ at ILC with Polarized Beams*, *Eur. Phys. J.* **C72** (2012) 2147, [arXiv:1205.0866](#) [hep-ph].
- [209] B. Ananthanarayan, M. Patra, and P. Poulose, *Signals of additional Z boson in $e^+e^- \rightarrow W^+W^-$ at the ILC with polarized beams*, *JHEP* **02** (2011) 043, [arXiv:1012.3566](#) [hep-ph].
- [210] P. Osland, A. A. Pankov, and A. V. Tsytinov, *Identification of extra neutral gauge bosons at the International Linear Collider*, *Eur. Phys. J.* **C67** (2010) 191–204, [arXiv:0912.2806](#) [hep-ph].
- [211] A. A. Pankov, N. Paver, and A. V. Tsytinov, *Distinguishing new physics scenarios at a linear collider with polarized beams*, *Phys. Rev.* **D73** (2006) 115005, [arXiv:hep-ph/0512131](#) [hep-ph].
- [212] O. Kittel, G. Moortgat-Pick, K. Rolbiecki, P. Schade, and M. Terwort, *Measurement of CP asymmetries in neutralino production at the ILC*, *Eur. Phys. J.* **C72** (2012) 1854, [arXiv:1108.3220](#) [hep-ph].
- [213] H. K. Dreiner, O. Kittel, and A. Marold, *Normal tau polarisation as a sensitive probe of CP violation in chargino decay*, *Phys. Rev.* **D82** (2010) 116005, [arXiv:1001.4714](#) [hep-ph].
- [214] A. Bartl, K. Hohenwarter-Sodek, T. Kernreiter, and O. Kittel, *CP asymmetries with longitudinal and transverse beam polarizations in neutralino production and decay into the $Z0$ boson at the ILC*, *JHEP* **09** (2007) 079, [arXiv:0706.3822](#) [hep-ph].
- [215] K. Rao and S. D. Rindani, *Probing CP-violating contact interactions in $e^+e^- \rightarrow HZ$ with polarized beams*, *Phys. Lett.* **B642** (2006) 85–92, [arXiv:hep-ph/0605298](#) [hep-ph].

- [216] A. Bartl, H. Fraas, S. Hesselbach, K. Hohenwarter-Sodek, T. Kernreiter, and G. A. Moortgat-Pick, *CP-odd observables in neutralino production with transverse e^+ and e^- beam polarization*, *JHEP* **01** (2006) 170, [arXiv:hep-ph/0510029 \[hep-ph\]](#).
- [217] S. Groote, J. G. Korner, B. Melic, and S. Prelovsek, *A survey of top quark polarization at a polarized linear e^+e^- collider*, *Phys. Rev.* **D83** (2011) 054018, [arXiv:1012.4600 \[hep-ph\]](#).
- [218] M. S. Amjad *et al.*, *A precise characterisation of the top quark electro-weak vertices at the ILC*, *Eur. Phys. J.* **C75** no. 10, (2015) 512, [arXiv:1505.06020 \[hep-ex\]](#).
- [219] B. Ananthanarayan, M. Patra, and P. Poulose, *W physics at the ILC with polarized beams as a probe of the Littlest Higgs Model*, *JHEP* **11** (2009) 058, [arXiv:0909.5323 \[hep-ph\]](#).
- [220] B. Ananthanarayan, M. Patra, and P. Poulose, *Probing strongly interacting W's at the ILC with polarized beams*, *JHEP* **03** (2012) 060, [arXiv:1112.5020 \[hep-ph\]](#).
- [221] S. Kumar, P. Poulose, and S. Sahoo, *Study of Higgs-gauge boson anomalous couplings through $e^-e^+ \rightarrow W^-W^+H$ at ILC*, *Phys. Rev.* **D91** no. 7, (2015) 073016, [arXiv:1501.03283 \[hep-ph\]](#).
- [222] S. D. Rindani and P. Sharma, *Decay-lepton correlations as probes of anomalous ZZH and gammaZH interactions in $e^+e^- \rightarrow ZH$ with polarized beams*, *Phys. Lett.* **B693** (2010) 134–139, [arXiv:1001.4931 \[hep-ph\]](#).
- [223] S. S. Biswal and R. M. Godbole, *Use of transverse beam polarization to probe anomalous VVH interactions at a Linear Collider*, *Phys. Lett.* **B680** (2009) 81–87, [arXiv:0906.5471 \[hep-ph\]](#).
- [224] S. D. Rindani and P. Sharma, *Angular distributions as a probe of anomalous ZZH and gammaZH interactions at a linear collider with polarized beams*, *Phys. Rev.* **D79** (2009) 075007, [arXiv:0901.2821 \[hep-ph\]](#).
- [225] G. Heinrich, S. Jahn, S. P. Jones, M. Kerner, and J. Pires, *NNLO predictions for Z-boson pair production at the LHC*, *JHEP* **03** (2018) 142, [arXiv:1710.06294 \[hep-ph\]](#).
- [226] F. Cascioli, T. Gehrmann, M. Grazzini, S. Kallweit, P. Maierhöfer, A. von Manteuffel, S. Pozzorini, D. Rathlev, L. Tancredi, and E. Weihs, *ZZ production at*

- hadron colliders in NNLO QCD*, *Phys. Lett.* **B735** (2014) 311–313, [arXiv:1405.2219 \[hep-ph\]](#).
- [227] M. Grazzini, S. Kallweit, and D. Rathlev, *ZZ production at the LHC: fiducial cross sections and distributions in NNLO QCD*, *Phys. Lett.* **B750** (2015) 407–410, [arXiv:1507.06257 \[hep-ph\]](#).
- [228] S. Kallweit and M. Wiesemann, *ZZ production at the LHC: NNLO predictions for $2\ell 2\nu$ and 4ℓ signatures*, *Phys. Lett.* **B786** (2018) 382–389, [arXiv:1806.05941 \[hep-ph\]](#).
- [229] M. Grazzini, S. Kallweit, and M. Wiesemann, *Fully differential NNLO computations with MATRIX*, *Eur. Phys. J.* **C78** no. 7, (2018) 537, [arXiv:1711.06631 \[hep-ph\]](#).
- [230] F. Cascioli, P. Maierhöfner, and S. Pozzorini, *Scattering Amplitudes with Open Loops*, *Phys. Rev. Lett.* **108** (2012) 111601, [arXiv:1111.5206 \[hep-ph\]](#).
- [231] A. Denner, S. Dittmaier, and L. Hofer, *Collier: a fortran-based Complex One-Loop Library in Extended Regularizations*, *Comput. Phys. Commun.* **212** (2017) 220–238, [arXiv:1604.06792 \[hep-ph\]](#).
- [232] T. Gehrmann, A. von Manteuffel, and L. Tancredi, *The two-loop helicity amplitudes for $q\bar{q}' \rightarrow V_1 V_2 \rightarrow 4$ leptons*, *JHEP* **09** (2015) 128, [arXiv:1503.04812 \[hep-ph\]](#).
- [233] S. Catani, L. Cieri, D. de Florian, G. Ferrera, and M. Grazzini, *Vector boson production at hadron colliders: hard-collinear coefficients at the NNLO*, *Eur. Phys. J.* **C72** (2012) 2195, [arXiv:1209.0158 \[hep-ph\]](#).
- [234] S. Catani and M. Grazzini, *An NNLO subtraction formalism in hadron collisions and its application to Higgs boson production at the LHC*, *Phys. Rev. Lett.* **98** (2007) 222002, [arXiv:hep-ph/0703012 \[hep-ph\]](#).
- [235] F. Caola, K. Melnikov, R. Röntsch, and L. Tancredi, *QCD corrections to ZZ production in gluon fusion at the LHC*, *Phys. Rev.* **D92** no. 9, (2015) 094028, [arXiv:1509.06734 \[hep-ph\]](#).
- [236] E. Conte, B. Fuks, and G. Serret, *MadAnalysis 5, A User-Friendly Framework for Collider Phenomenology*, *Comput. Phys. Commun.* **184** (2013) 222–256, [arXiv:1206.1599 \[hep-ph\]](#).

- [237] E. N. Argyres, G. Katsilieris, A. B. Lahanas, C. G. Papadopoulos, and V. C. Spanos, *One loop corrections to three vector boson vertices in the Standard Model*, *Nucl. Phys.* **B391** (1993) 23–41.
- [238] J. Papavassiliou and K. Philippides, *Gauge invariant three boson vertices in the Standard Model and the static properties of the W*, *Phys. Rev.* **D48** (1993) 4255–4268, [arXiv:hep-ph/9310210](#) [hep-ph].
- [239] G. Gounaris, J. Layssac, G. Moultaqa, and F. M. Renard, *Analytic expressions of cross-sections, asymmetries and W density matrices for $e^+ e^- \rightarrow W^+ W^-$ with general three boson couplings*, *Int. J. Mod. Phys.* **A8** (1993) 3285–3320.
- [240] ATLAS Collaboration, M. Aaboud *et al.*, *Measurement of $W^\pm Z$ production cross sections and gauge boson polarisation in pp collisions at $\sqrt{s} = 13$ TeV with the ATLAS detector*, *Eur. Phys. J.* **C79** no. 6, (2019) 535, [arXiv:1902.05759](#) [hep-ex].
- [241] A. Vauth and J. List, *Beam Polarization at the ILC: Physics Case and Realization*, *Int. J. Mod. Phys. Conf. Ser.* **40** (2016) 1660003.
- [242] G. Moortgat-Pick, *Physics aspects of polarized e^+ at the linear collider*, in *1st International Positron Source Workshop*. 7, 2006. [arXiv:hep-ph/0607173](#).
- [243] W. J. Stirling and E. Vryonidou, *Electroweak gauge boson polarisation at the LHC*, *JHEP* **07** (2012) 124, [arXiv:1204.6427](#) [hep-ph].
- [244] J. Baglio and N. Le Duc, *Fiducial polarization observables in hadronic WZ production: A next-to-leading order QCD+EW study*, *JHEP* **04** (2019) 065, [arXiv:1810.11034](#) [hep-ph].
- [245] J. Baglio and L. D. Ninh, *Polarization observables in WZ production at the 13 TeV LHC: Inclusive case*, *Commun. Phys.* **30** no. 1, (2020) 35–47, [arXiv:1910.13746](#) [hep-ph].
- [246] S. Buddenbrock, A. S. Cornell, Y. Fang, A. Fadol Mohammed, M. Kumar, B. Mellado, and K. G. Tomiwa, *The emergence of multi-lepton anomalies at the LHC and their compatibility with new physics at the EW scale*, *JHEP* **10** (2019) 157, [arXiv:1901.05300](#) [hep-ph].

- [247] M. Grazzini, S. Kallweit, D. Rathlev, and M. Wiesemann, *$W^\pm Z$ production at the LHC: fiducial cross sections and distributions in NNLO QCD*, *JHEP* **05** (2017) 139, [arXiv:1703.09065 \[hep-ph\]](#).
- [248] CMS Collaboration, V. Khachatryan *et al.*, *Measurement of the WZ production cross section in pp collisions at $\sqrt{s} = 13$ TeV*, *Phys. Lett.* **B766** (2017) 268–290, [arXiv:1607.06943 \[hep-ex\]](#).
- [249] M. Grazzini, S. Kallweit, D. Rathlev, and M. Wiesemann, *$W^\pm Z$ production at hadron colliders in NNLO QCD*, *Phys. Lett.* **B761** (2016) 179–183, [arXiv:1604.08576 \[hep-ph\]](#).
- [250] ATLAS Collaboration, M. Aaboud *et al.*, *Measurement of the $W^\pm Z$ boson pair-production cross section in pp collisions at $\sqrt{s} = 13$ TeV with the ATLAS Detector*, *Phys. Lett.* **B762** (2016) 1–22, [arXiv:1606.04017 \[hep-ex\]](#).
- [251] S. Kumar, P. Poulose, R. Rahaman, and R. K. Singh, *Measuring Higgs self-couplings in the presence of VVH and VVHH at the ILC*, *Int. J. Mod. Phys.* **A34** no. 18, (2019) 1950094, [arXiv:1905.06601 \[hep-ph\]](#).
- [252] E. da Silva Almeida, A. Alves, N. Rosa Agostinho, O. J. P. Éboli, and M. C. Gonzalez–Garcia, *Electroweak Sector Under Scrutiny: A Combined Analysis of LHC and Electroweak Precision Data*, *Phys. Rev.* **D99** no. 3, (2019) 033001, [arXiv:1812.01009 \[hep-ph\]](#).
- [253] A. Pukhov, *CalcHEP 2.3: MSSM, structure functions, event generation, batchs, and generation of matrix elements for other packages*, [arXiv:hep-ph/0412191 \[hep-ph\]](#).
- [254] T. Hahn, *Generating Feynman diagrams and amplitudes with FeynArts 3*, *Comput. Phys. Commun.* **140** (2001) 418–431, [arXiv:hep-ph/0012260 \[hep-ph\]](#).
- [255] S. Höche, S. Kuttimalai, S. Schumann, and F. Siegert, *Beyond Standard Model calculations with Sherpa*, *Eur. Phys. J.* **C75** no. 3, (2015) 135, [arXiv:1412.6478 \[hep-ph\]](#).
- [256] W. Kilian, T. Ohl, and J. Reuter, *WHIZARD: Simulating Multi-Particle Processes at LHC and ILC*, *Eur. Phys. J.* **C71** (2011) 1742, [arXiv:0708.4233 \[hep-ph\]](#).